Solvent Mediated Reactive Crystallisation of Calcium Carbonate

The Effects of Non-aqueous Solvents on the Structure of Calcium Sulphonate Overbased Detergents

Thokozile Alice Kathyola

Submitted in accordance with the requirements for the degree of
Doctor of Philosophy

The University of Leeds
School of Chemical and Process Engineering

October, 2018

The candidate confirms that the work submitted is his/her own and that appropriate credit has been given where reference has been made to the work of others.

Acknowledgements

First and foremost I would like to thank my supervisors Sven L.M. Schroeder, Fiona C. Meldrum, Rik M.D. Brydson and Elizabeth A. Willneff. Thanks to my industrial supervisor Peter J. Dowding and mentor Colin J. Willis. Thanks Infineum UK, Ltd. and EPSRC Centre for Doctoral Training in Complex Particulate Products and Processes for funding the PhD. I am also grateful to Diamond Light Source for the multiple beamtime awards.

Various teams were involved in different aspects of the project, most especially the development of analytical techniques. The collaborative work includes a pertinent University of Leeds, Infineum UK and Diamond Light Source collaboration. Development and application of the XAS/Mid-IR process analytical technology was carried out by a team which included Sin-Yuen Chang, Elizabeth Willneff, Colin Willis, Arturs Pugejs, Paul Wilson, Peter Dowding, Giannantonio Cibin, Anna Kroner, Elizabeth Shotton, and Sven Schroeder. Sin-Yuen Chang and I contributed equally to the development of this setup.

Other notable collaborations were with the Leeds electron microscopy and spectroscopy (LEMAS) centre and the Meldrum Group. The electron microscopy work was carried out with the aid of Rob Hooley, Stuart Micklethwaite, Zabeada Aslam, Andy Brown and Rik Brydson. Rob Hooley and I contributed equally to the transmission electron microscopy work presented in this thesis. Thanks to Yi-Yeoun Kim and Fiona C. Meldrum for providing guidance and literature on relevant calcium carbonate aqueous systems. I would also like to thank Faith Bamiduro, Wei Ding, Andre Botha for their assistance with some data collection/interpretation.

Last but not least, I would like to thank my family and friends. I possibly could not have completed this PhD journey without their constant and unwavering support. These include: Janet Kathyola, Damson Kathyola, Vitumbiko Kathyola, Tiwonge Maganga, Esther Maganga, Wongani Maganga, Christina Mitchell, Oluwatoyin Job, Vincent Job, Monika Patel, Thandiwe Chirwa, Tapiwa Banda, Talumba Mkali, Kondwani Shawa, Pamela Sauzande, Henry Sauzande, Malikie Bailah-Leigh, Chifundo Banda and Yumna Islam.

"Education never ends, Watson. It is a series of lessons, with the greatest for the last."

— *Sir Arthur Conan Doyle*

Abstract

Lubricant additives have been extensively used since the 1920s to reduce friction, wear and corrosion in combustion engines. One important class of these additives is overbased detergents, generally defined as colloidal dispersions of inorganic metal carbonates such as calcium carbonate ($CaCO_3$), sterically stabilised by organic oil-soluble surfactants. Since overbased detergents were introduced in circa 1952, their chemical composition and manufacturing processes have been extensively developed to meet industrial demand for these products. However, the relationship between solvents, surfactants and process parameters and the structure and performance of the $CaCO_3$ component in the detergents is still unclear.

A literature review of the synthesis of overbased detergents revealed that the structure of the $CaCO_3$ core in the detergent, as well as the mechanism by which this structure evolved from the precursor during synthesis, was not very well defined. To address this, several analytical techniques, including X-ray absorption spectroscopy (XAS) and mid-infrared (mid-IR) spectroscopy, were used to determine time-resolved transformations that occur during synthesis. A novel continuous-flow liquid-jet process analytical technology (PAT) system for simultaneous *in situ/operando* XAS and mid-IR was developed and used to characterise Ca species in multiphase multicomponent model systems as well as in the industrial overbasing process.

Crucially, as a consequence of this work, it was confirmed for the first time that chemical interactions between the non-aqueous solvents and reagents dictate the reaction kinetics and mechanisms of formation of the carbonate core in the detergent. Complementary spectroscopy, diffraction and microscopy results show that different $CaCO_3$ polymorphs are obtained by varying solvent compositions. Additionally, it was confirmed that the metastable $CaCO_3$ core in the detergent is precipitated *via* a diffusion-limited reaction pathway. The reaction includes the formation of calcium methoxide ($Ca(OCH_3)_2$) and calcium di-methylcarbonate ($Ca(OCOOCH_3)_2$) intermediates. Both $CaCO_3$ and $Ca(OCOOCH_3)_2$ have been identified in the final detergent product. Ultimately, these results show that the structure of the detergent core can be influenced by the polarity and concentration of the solvents used. This should aid in the future development of specially tailored overbased detergents with physicochemical properties tuned to meet the requirements of the end application.

Table of Contents

List of Tables

List of Figures

Abbreviations

ACC	Amorphous calcium carbonate
ADP	Atomic distribution parameter
$CaCO_3$-α	Calcite
$CaCO_3$-β	Aragonite
$CaCO_3$-γ	Vaterite
CQA	Critical quality attributes
DLS	Dynamic light scattering
EDX	Energy dispersive X-ray spectroscopy
EELS	Electron energy-loss spectroscopy
EXAFS	Extended X-ray absorption fine structure
FT	Fourier transform
FY	Fluorescence yield
G(r)	Pair distribution function
LCF	Linear combination fitting
Mid-IR	Mid-infrared spectroscopy
PAT	Process analytical technology
SANS	Small-angle neutron scattering
SAXS	Small-angle X-ray scattering
SEM	Scanning electron microscopy
STEM	Scanning transmission electron microscopy
S(Q)	Total scattering structure function
TBN	Total base number
TEM	Transmission electron microscopy
TEY	Total electron yield
TGA	Thermogravimetric analysis
WAXS	Wide-angle X-ray scattering
XAS	X-ray absorption spectroscopy
XANES	X-ray absorption near-edge structure
XPDF	X-ray pair distribution function
XPS	X-ray photoelectron spectroscopy
PXRD	Powder X-ray diffraction

Chapter 1:
Introduction

1.1. Background

Lubricant additives are agents that improve the properties of lubricating fluids with the aim of reducing the friction and wear of mechanical equipment, which in turn has an effect on equipment performance and durability. The use of lubricants, in the form of animal fats, dates back as far as 1400 B.C. (1). The use of petroleum-based lubricants came about in 1859, which was followed a century later (circa 1930) with the established use of additives. The development and extensive use of petroleum-based lubricants was initially promoted by the introduction of more compact and powerful motor engines coupled with military demands during World War II (1, 2). The main type of lubricant additives are deposit control, film-forming and polymeric agents. These agents include detergents, dispersants, corrosion inhibitors, and viscosity modifiers (1, 3). The specific applications of these additives have become more defined over the years with the increasing demand for and manufacture of complex fast-running high performance engines.

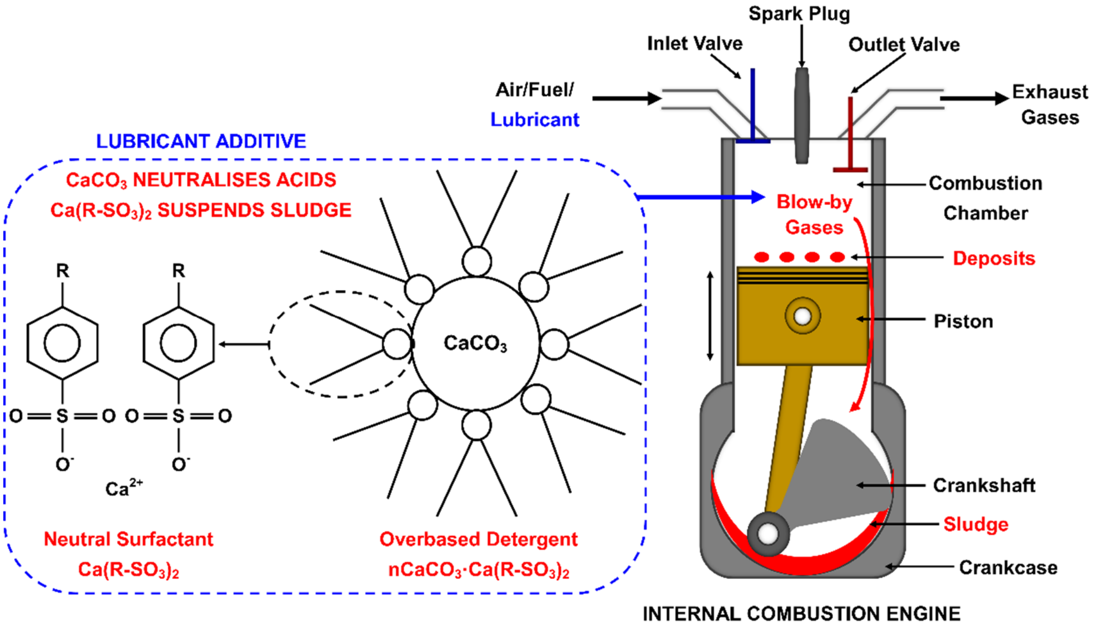

Figure 1.1. Schematic representations of a neutral calcium sulphonate surfactant, an overbased calcium sulphonate detergent and an internal combustion engine.

This project focuses on overbased detergents that are used in combustion engine oil lubricants (Figure 1.1). These detergents mainly consist of a metal carbonate inorganic core, which is stabilised by an organic surfactant (commonly sulphonate) layer. The early development of lubricant detergents dates from the 1940s, with the introduction of calcium carboxylate, sulphonate, phosphonate and finally phenate detergents, through to the production of overbased and salicylate detergents in the 1950s and lastly sodium detergents circa 1980 (1). The niche area of overbased detergents was initially developed around 1952 with the production of basic sulphonate detergents of alkaline earth metals such as barium, calcium, and magnesium (1, 4). Subsequent development and optimisation of the 'overbasing process' was driven by the need to minimise interference of the basic sulphonates on anti-oxidants and to increase total base numbers (TBN) (3, 4). Current developments in the field involve the modification of the metal core and/or surfactant layer of the overbased detergents. A fine example of these new types are calixarate overbased detergents, which are essentially phenates with complex molecular structures (5, 6). Calixarates combine the desirable properties of both conventional phenates and sulphonates with respects to high stability and TBN values.

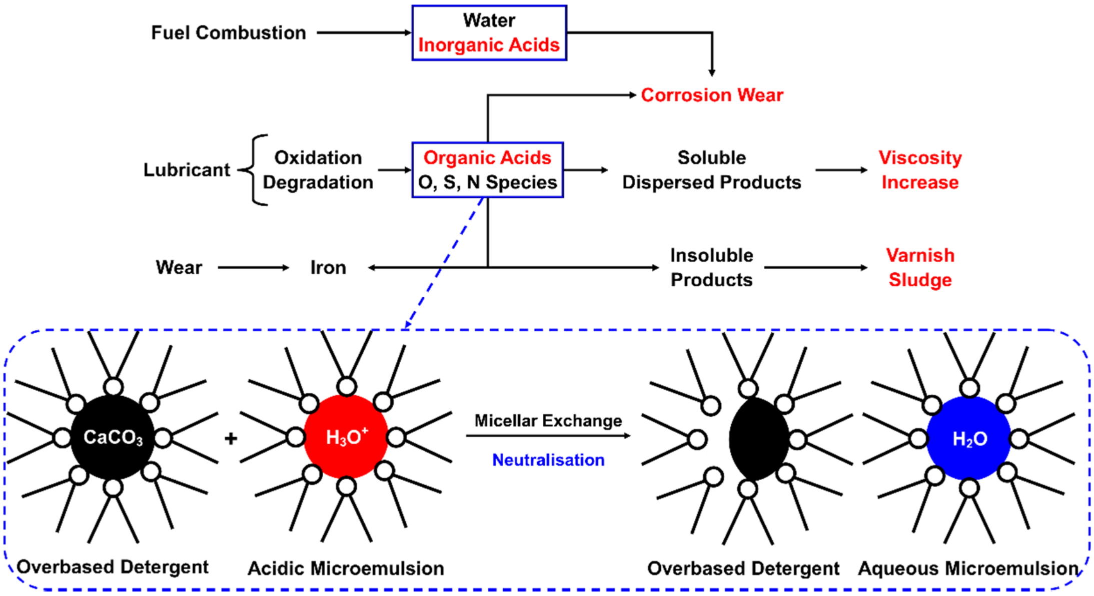

Figure 1.2. Schematic showing lubricant degradation pathways/products (7) and neutralisation of acids by overbased detergents (8).

Overbased detergents exhibit multi-functionality in lubricants as both deposit control and film forming agents (1-3, 7). They have three main functions that mitigate lubricant degradation (Figure 1.2) in internal combustion engines (5, 9, 10). First, they reduce corrosive wear by neutralising the organic and inorganic acidic materials. These acids are produced as products/by-products of the oxidative degradation of the lubricant and the reaction of water with 'blow-by' gases such as SO_2 and NO_x formed in combustion processes. It has been proposed that the acid neutralisation results from the collision of and micellar exchange between the overbased detergents and microemulsions containing highly acidic aqueous solutions (Figure 1.2) (8). Secondly, they act similar to dispersants and prevent the formation of deposits such as varnish lacquer (sludge) on high temperature surfaces in the engine. Thirdly, they act as anti-wear, extreme pressure and friction-reducing additives. The roles of the detergent constituents can be defined in relation to the overall multiple functions of the detergents. For instance, the surfactants are said to play two major roles i.e. corrosion inhibitor and micelle stabiliser (11). The type and structure of the surfactant strongly influence the overall structure of the particles in the overbased reverse micelles and the basicity of these micelles, which in turn impacts on performance (5, 12). The complexity of these detergent components and how this affects the overall performance of lubricants, was one of the major driving forces in the inception, development and completion of this project.

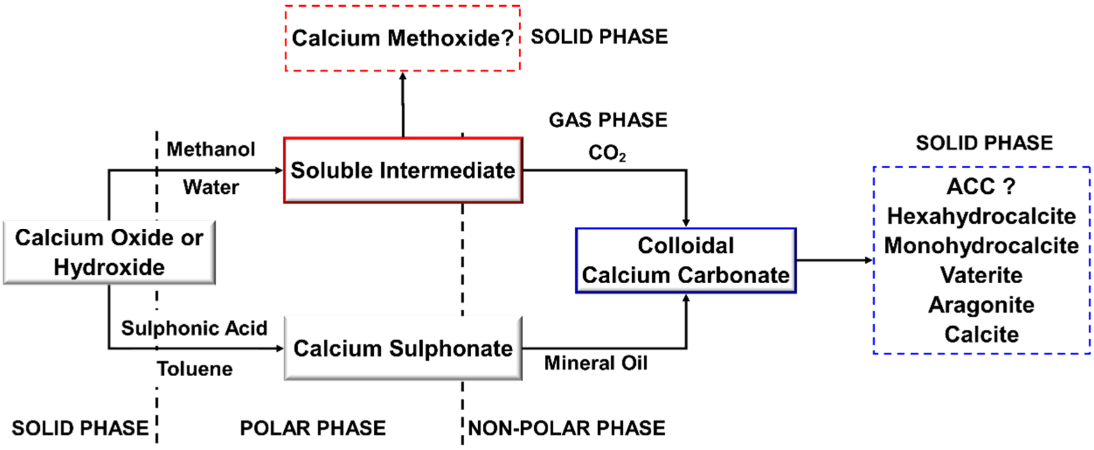

Figure 1.3. A modified illustration of the complex gas/polar liquid/non-polar liquid/solid phase overbasing process (7). Possible structures for the 'soluble intermediate' and calcium carbonate core of the overbased detergent product have been included.

Overbased detergents are sub-micron particles of about 2 to 20 nm (3, 5, 7, 12-14), which are reported to consist of: (i) a carbonate/borate core (of either barium, calcium or magnesium) that makes up 20 to 30 weight percent (wt%) of the total colloidal particle mass; (ii) 5 to 10 wt% of an aqueous metal hydroxide; and (iii) 18 to 30 wt% of an organic surfactant layer. Generally, the colloidal particles are the result of a complex multiphase multicomponent reaction (overbasing process – Figure 1.3) (7), which involves the carbonation of an inorganic metal oxide/hydroxide in the presence of an organic acid/surfactant and promoter in a non-aqueous hydrocarbon environment (12, 13, 15). Two aspects of particular interest in this project are the microstructures of the transient soluble intermediate and of the calcium carbonate ($CaCO_3$) core of overbased calcium sulphonate detergents (Figure 1.3). Whereas the occurrence of the intermediate has been suggested in a number of previous studies (3, 7, 13, 16), it has not been explored to the same extent as the carbonate core. The core has often been assumed to be amorphous $CaCO_3$ (ACC) (7, 13). However, some studies using analytical techniques such as transmission electron microscopy (TEM) and X-ray absorption spectroscopy (XAS) seem to suggest the existence of discrete crystallinity in the micellar core (10, 17-19).

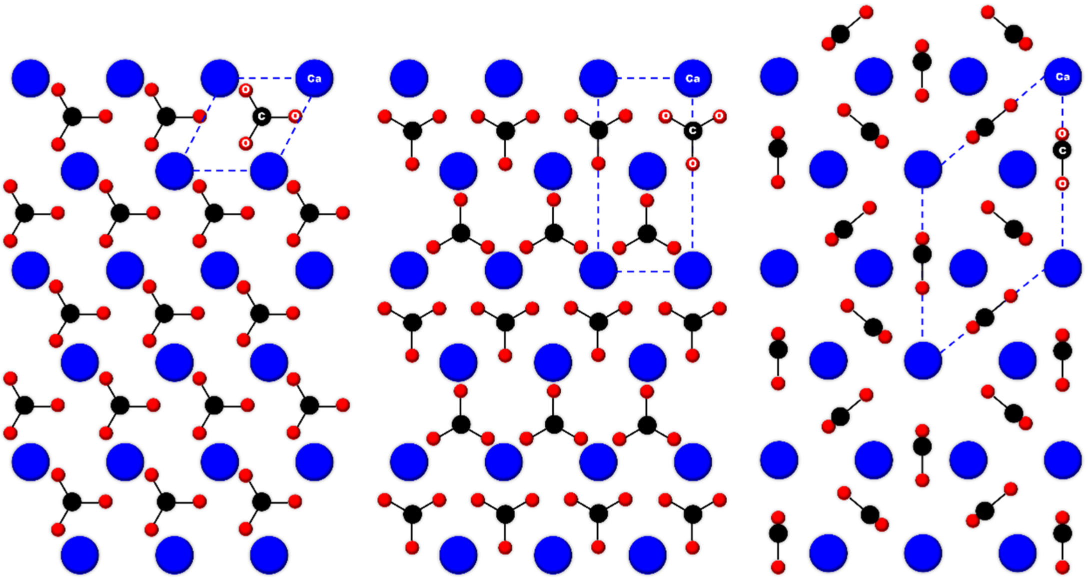

Calcite
Rhombohedral (*R-3c*)

Aragonite
Orthorhombic (*Pmna*)

Vaterite
Hexagonal ($P6_3/mmc$)

Figure 1.4. Schematic representations of (a) calcite ($CaCO_3$-α) (20); (b) aragonite ($CaCO_3$-β) (21); and (c) vaterite ($CaCO_3$-γ) (22) single layers onto the basal plane (23). Dashed (blue) lines highlight the unit cell.

The $CaCO_3$ in the core of overbased detergents is one of the most prominent minerals which exists in six different polymorphic forms. These polymorphs are: three anhydrous crystalline forms – calcite ($CaCO_3$-α), aragonite ($CaCO_3$-β) and vaterite ($CaCO_3$-γ) (Figure 1.4); two hydrates – monohydrocalcite ($CaCO_3 \cdot H_2O$) and ikaite ($CaCO_3 \cdot 6H_2O$); and ACC – which exists in both anhydrous and hydrated forms (24, 25). The three anhydrous polymorphs (Figure 1.4) are the most studied with varying morphologies and physicochemical properties. In order of decreasing thermodynamic stability, rhombohedral ($CaCO_3$-α), orthorhombic ($CaCO_3$-β) and hexagonal ($CaCO_3$-γ) (21, 24, 26, 27). Hence, in theory, altering the crystal structure of the $CaCO_3$ will change the physicochemical properties of the particles and in turn should affect the performance of the final product. The metal core of overbased detergents, the $CaCO_3$, strongly determines the ability of the lubricant additive to neutralise acids (its basicity), which is represented in terms of the TBN. It has been found that when calcium hydroxide is fully carbonated, the resulting $CaCO_3$ core becomes crystalline (usually $CaCO_3$-α). These crystalline particles, unlike the presumably amorphous ones, tend to agglomerate and sediment out of the hydrocarbon lubricating oil during the carbonation reaction. This in turn compromises the stability of the system and thus reduces the TBN of the final product (9, 13, 28).

1.2. Aims and Objectives

On the basis of the current developments in the fundamental science of overbased calcium detergents and their applications, the proposed research question was:

"What is the impact of varying solvents and process parameters on the microstructure of the calcium carbonate component in overbased detergents?"

To address this question, the three aims of this project were to (i) examine the influence of non-aqueous solvents and reagent concentrations on the short and long-range structure of $CaCO_3$; (ii) develop a robust *in situ/operando* process analytical technology (PAT) setup for monitoring variations in the structure of the carbonate core during the overbasing process; and (iii) identify transient reaction intermediates to understand the mechanism by which $CaCO_3$ is formed in non-aqueous systems. In order to achieve these aims, the objectives included:

- Replicating a lab-scale overbasing process with the aim of optimising it by varying process conditions, reagent types and compositions.
- Comparing the formation of $CaCO_3$ in the complex non-aqueous system used to make overbased detergents with less complex but relatively similar aqueous system to further understand the mechanisms of formation and reagent interactions.
- Analysing the resultant detergent particles using various established and new analytical techniques to determine the optimal combination of techniques and related operating conditions for the complete characterisation of the particles.

1.3. Report Outline

This thesis consists of nine chapters (summarised in Figure 1.5). Chapter 1 is the project introduction, which includes a background to lubricant additives and overbased detergents, the related research question and the project aims and objectives. Chapter 2 consists of a literature review on the synthesis and analysis of calcium overbased detergents. The review is followed by chapter 3, which summarises the optimal synthesis and analytical methods that were applied throughout this research project.

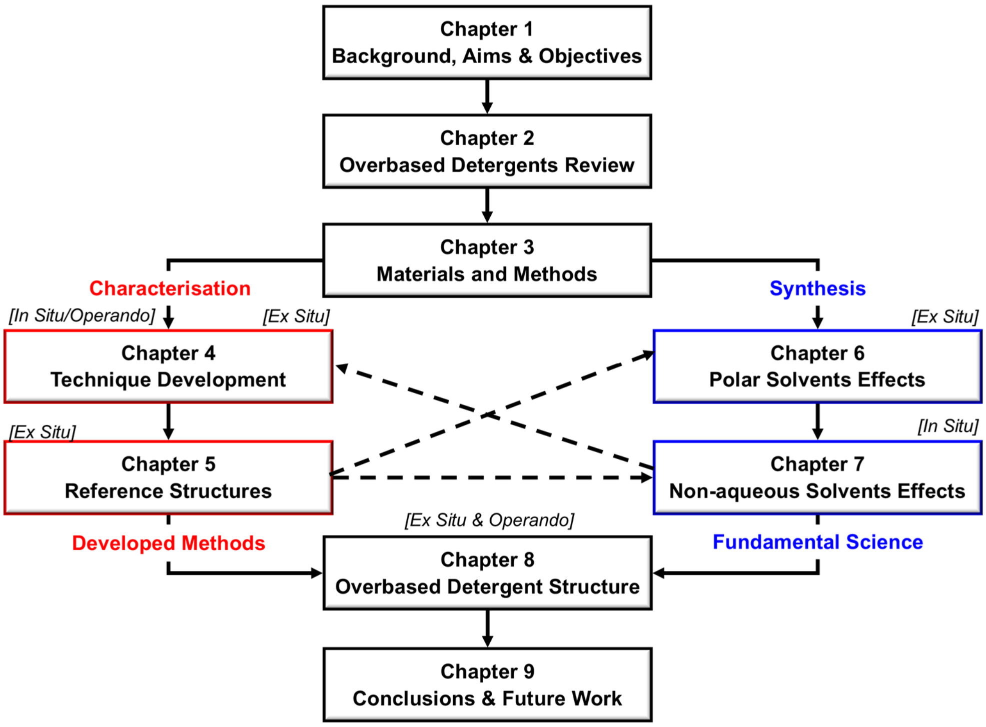

Figure 1.5. Diagrammatic representation of the thesis outline highlighting the nine chapters from the introduction through to the conclusions.

The four subsequent results chapters are split into the two categories i.e. characterisation and synthesis (Figure 1.5). Chapter 4 details the development of a novel cell and process analytical technology (PAT) setup that allows for simultaneous *in situ* and *operando* XAS and Mid-IR analysis. Concurrently, Chapter 5 focuses on establishing complementary data analysis methods, which have been applied *ex situ* to six reference $CaCO_3$ precursors and polymorphs. Chapters 6 and 7 combine the aforementioned techniques/methods and apply them to the *ex* and *in situ* analysis of non-aqueous solvents effects. The abridged *ex situ* study in Chapter 5, on the influence of methanol (and water) on $CaCO_3$ precipitation, acts as an introduction to Chapter 7. This penultimate results chapter culminates the previously attained methods and knowledge with regards to the reactive crystallisation of $CaCO_3$ in single, binary and ternary solvent systems based on the overbasing process (Figure 1.3). Ultimately, the collective results on $CaCO_3$ polymorphism and reaction pathways inform the elucidation of the structure of overbased calcium sulphonate detergents in Chapter 8. All of the results are summarised in Chapter 9 along with recommendations for future work.

Chapter 2:
Literature Review

2.1 Introduction

The primary focus of this literature review is the synthesis and characterisation of overbased detergents. As previously discussed in the introduction (section 1.1), there are different types of metals and surfactants used in the preparation of these detergents. However, overbased calcium sulphonate detergents (studied in this project) are the most commercially used and studied. This review aims to provide an overview of previous research and highlight areas that are essential to process and product optimisation. These areas include experimental and analytical techniques, which were used in the development of techniques/methods (chapters 4 and 5) and in the *ex situ* (chapter 6), *in situ* (chapter 7) and *operando* (chapter 8) experiments. This chapter is split into two main sections. The first section (section 2.2) details the role of the different reagents/components (section 2.2.1) and proposed reaction mechanisms (section 2.2.2) involved in complex multiphase multicomponent overbasing process (section 2.2.3). Section 2.2 also highlights pertinent issues that could contribute to process and product optimisation if understood. Subsequently, section 2.3 discusses previously used analytical techniques with regards to the morphology (section 2.3.1) and structure (section 2.3.2) of the nano-sized detergent particles.

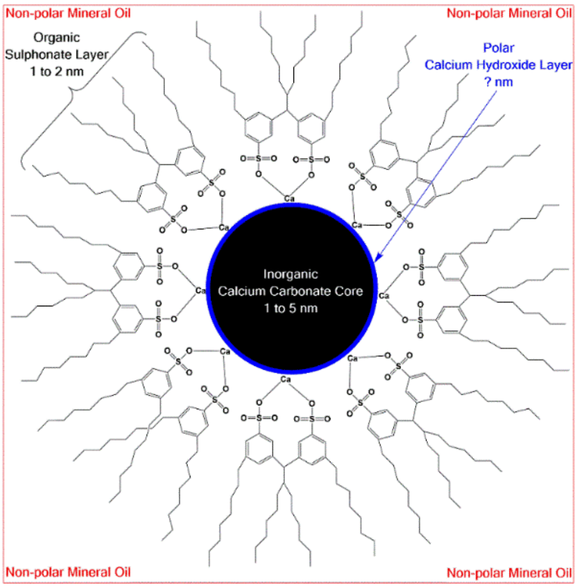

Figure 2.1. Schematic of an overbased calcium sulphonate detergent highlighting the calcium carbonate ($m\cdot CaCO_3$) core, calcium hydroxide ($n\cdot Ca(OH)_2$) inner-layer and calcium sulphonate ($Ca(R\text{-}SO_3)_2$) stabilising outer-layer.

2.2 Synthesis of Overbased Detergents

Overbased calcium sulphonate detergents (Figure 2.1) are colloidal dispersions that result from the carbonation of a multiphase dispersion containing an inorganic metal oxide/hydroxide, organic acid/surfactant and alcohol promoter (all dispersed in a hydrocarbon medium). The general preparation procedure involves two main stages: (i) the *in situ* formation of the surfactant, which is achieved by neutralising the organic acid with the metal oxide/hydroxide; and (ii) the conversion of the metal oxide/hydroxide to a metal carbonate salt by bubbling *via* a reaction with carbon dioxide.

The general preparation procedure for overbased detergents, also known as the overbasing process, involves two reactive stages. First, the *in situ* formation of the surfactant, which is achieved by neutralising the organic acid with the metal oxide/hydroxide. Second, the conversion of the metal oxide/hydroxide to a metal carbonate salt by bubbling through carbon dioxide through the system. There are a number of patents that provide detailed procedures of how to prepare these overbased detergents. Some of the most notable and perhaps the most relevant to this project are those involving barium, magnesium and calcium based detergents (4, 16, 29-31). Noticeable differences exist between most of these patents with respect to the constituents used, process parameters and final product properties. However, they all involve the preparation of a metal carbonate *via* the reaction of a metal oxide/hydroxide and CO_2 and the stabilisation of these metal carbonate particles with surfactants. Importantly, these patents have served as the basis for some of the preparation procedures used in industry and in the published literature for overbased calcium sulphonate detergents (12, 13).

Prior to the review of the different preparation methods, as a way of understanding the fundamental science that governs the overbasing processes, there is a need to define the roles of the constituents involved in this complex polyphasic reaction system. The constituents/reagents play different roles in determining the ultimate structure (represented in Figure 2.1) and performance of the overbased detergents.

2.2.1 Roles of Reagents and Solvents

There are normally seven gas, liquid and solid components involved in the overbasing process. These are (i) an alkaline metal or metal oxide/hydroxide; (ii) carbon dioxide; (iii) an acid and/or surfactant; (iv) a promoter; (v) water; (vi) a hydrocarbon solvent;

and (vii) a base mineral oil. Each of these reagents and solvents play a different role in determining the size, structure, stability and performance of the detergents. Elucidating the interactions of the different components, in terms of reactivity, miscibility and solubility. This analysis is an essential in terms of product/process optimisation and the development of process analytical technology (PAT).

Metal Oxide/Hydroxide and Carbon Dioxide. Most processes involve the conversion of a metal oxide (M-O) or hydroxide (M-OH) to a metal carbonate (M-CO_3) salt *via* a reaction with carbon dioxide (CO_2). The resulting carbonate makes up the majority of the overbased detergent core, which accounts for 20 to 30 weight percent (wt%) of the total colloidal particle mass, and is responsible for the neutralisation of acids present engines from combustion and oxidation (7). The alkaline-earth metals are usually preferred for the preparation of commercial overbased detergents, with calcium and magnesium being the most common (1, 7). Even though barium detergents were the first to be introduced, their use has decreased over the years amidst concerns over their toxicity (1). As calcium detergents are the focal point in this project, it is important to highlight the fact that the synthesis involved in the preparation of this type of detergents is slightly different from the others with respect to the conversion of the oxide/hydroxide.

During the synthesis of calcium-based detergents, the carbonation reaction is stopped before the stoichiometric amount of CO_2 has been introduced into the system (7). This results in the incomplete conversion of the calcium hydroxide ($Ca(OH)_2$) to calcium carbonate ($CaCO_3$). This has been found to be necessary to ensure the stability of the detergent particles. The complete carbonation of $Ca(OH)_2$ is said to lead to the crystallisation of the amorphous $CaCO_3$ to calcite or vaterite (7, 13). Crystalline $CaCO_3$ exhibits low solubility in non-aqueous overbased systems such that it tends to agglomerate and sediment out of the system (1, 9). It is therefore necessary to stop the when there is still 5 to 10 wt% of $Ca(OH)_2$ present in the detergent core and the $CaCO_3$ is not in any of its anhydrous crystalline forms. This is not necessary in magnesium systems where the carbonation process stops automatically after the formation of the carbonate salt (7, 32).

The Acid/Surfactant. The surfactants used in the overbasing process are amphiphilic with a polar head group, which binds to the metal cation (barium, calcium or magnesium) of the carbonate core, and a lipophilic tail with one or two hydrophobic alkyl chains ranging from C_9 to C_{60} (9). The main groups of surfactants that are currently used are sulphonates, phenates, salicylates and phosphates, where alkylbenzene sulphonates and sulphurised alkyl phenates are the most commonly used and studied (5, 7, 9). One of the probable reasons why sulphonates are preferred is that they were the first surfactants to be used in the production of overbased detergents in 1952 (4) and are thus the most established. Another reason is that they tend to produce detergents with very desirable total base number (TBN), thermal stability, detergency, and rust inhibition (5).

Different surfactants exhibit different steric stabilisation levels, where this has been principally attributed to their molecular structures (7, 33). For example, it has been discovered that alkylbenzene sulphonates exhibit higher levels of stabilisation by forming thicker shells around the micellar core when compared to sulphurised alkyl phenates (33). This difference is probably due to the more flexible nature of the monodentate sulphonates as compared to phenates, whose anion is a bidentate ligand with a sulphur-bridged phenate (33). The ability of a surfactant to adequately stabilise the detergent particles (an important property in synthesis) has a knock-on effect on the corrosion inhibition performance of the overbased detergent. For example, sulphonates tend to produce detergents with higher TBN numbers (with a maximum of 500), whereas the maximum for phenates and salicylates is about 300 (5). This is the only property that makes sulphonate detergents stand out from phenates, salicylates and phosphates; these other surfactants are better or fairly equal with respect to detergency, anti-oxidant effect, hydrolytic, oxidation and thermal stability (5).

Another important aspect of surfactants that is related to their molecular structure and their role in the synthesis of overbased detergents is their ability to control the size of the metal carbonate core. The size of the metal detergent core is thought to be determined by the difference in the rates of $CaCO_3$ particle growth and surfactant adsorption onto these particles (13). Furthermore, the size also depends on (a) the type of surfactant – sulphonate cores tend to be bigger than phenate ones, and (b) the concentration of the surfactant – the core size decreases with increasing surfactant concentration (7). Considering the previously discussed point that different surfactants form stabilising layers of different thickness, it is safe to state that the surfactant also determines the overall size of the final detergent particle.

Water. In all overbasing processes, water is a common by-product of the acid neutralisation and calcium hydroxide carbonation reactions. However, it has been discovered that water determines whether, and to what extent the carbonation reaction occurs. If too little is present in the system the reaction will not occur and if there is too much over-carbonation occurs, which leads to destabilisation of the colloidal particles (16). The destabilisation is evident by the hazy appearance of the formulation and by the agglomeration and subsequent sedimentation of the inorganic cores of the detergents. The water in the reaction appears to solubilise the calcium hydroxide in the pre-carbonation micelles and increase the uptake of carbon dioxide (13).

Water has also been found to affect (a) the number of colloidal carbonate particles present at the end of the overbasing process – a 0.1 difference in the volume of water shows a double increase in the number up to a critical volume after which the number decreases; and (b) the size of these particles – the water forms a layer on the surface of the core and aids in providing growing carbonate particles with dissolved calcium hydroxide. An increase in the volume therefore leads to an increase in the size of the detergent core (13, 34, 35).

For these reasons, the oxide/hydroxide overbasing process has been modified to include at least 0.1 wt% of water at the start of the process and remove 60 to 80 % of the water present at the end (16). A patent, whose main focus is controlling the concentration of water in the overbasing system, states that the amount of water required in a system is highly dependent on the molecular weight of the surfactant (16). For example, a surfactant with a molecular weight of ≤600 limits the range of the water required to about 0.1 to 0.5 wt% (16). On the other hand, if the surfactant has a molecular weight of 800 or 900 then the range changes to 0.5 to 0.8 wt%. In other patents, the amount of water has been limited to no more than 10 wt% of the total liquids in the system, which should account for 0.1 to 10 volume percent of the alcohol promoter used (31, 36).

Methanol. Compared to the other constituents, the role of the promoter is the least studied and understood (34). In the overbasing process, promoters are generally considered to be catalysts that promote the carbonation reaction and thus the formation of the desired metal carbonate product (1, 34). There is a wide range of polar short alkyl chain molecules that are considered viable promoters. These include lower alcohols such as methanol, ethanol and isopropanol, alkyl phenols such as nonyl phenol, and amines such as ethylene diamine and ethanolamine (16). Recent processes, however, have shown a preference for alcohols, and in particular methanol. In one patent, the amount of alcohol required in the system has been represented as a volume ratio of the alcohol to the hydrocarbon solvent (36). The patent stated that the alcohol to hydrocarbon solvent ratio should be less or equal to 1, and preferably between 0.1 and 0.6. Two primary functions have been attributed to these promoters over the years. These include (1) the formation of soluble intermediates and (2) the facilitation of dynamic micellar exchanges during the overbasing process (7, 13).

In some cases, overbased colloidal dispersions have been considered to form *via* hydrocarbon-soluble intermediates between the metal or metal oxide/hydroxide with the promoter such as alkoxides (7). Another proposed case, in which the soluble intermediates are involved, is the formation of water-soluble carbamates in systems where ammonia or an amine is present as the main or auxiliary promoter (7, 16, 30). The carbamates are the result of the ammonia or amine reacting with carbon dioxide (CO_2) and are said to either cause the metal oxide/hydroxide to react with the CO_2 present or react with the metal base directly to form the carbonate (7, 16, 30). A prime example, where the use of amines as auxiliary promoters is mandatory, is the case of magnesium carbonate formation using the oxide/hydroxide method (7).

The idea that methanol facilitates dynamic micellar exchanges has been mainly driven by studies involving the effects of lower alcohols on the stability of micelles and the formation of the micelles around metals carbonates (13, 34, 37). Roman *et al.* (13) hypothesised that methanol facilitated the exchange of calcium hydroxide between un-nucleated and nucleated micelles in their overbasing system, which promoted the growth of the particles. This hypothesis was made on the basis of a study by Jao and Kreuz, (37) who showed that lower alcohols had the ability to affect the stability of the surfactant shell by loosening it. These studies were later followed by a study which compared the amount of methanol with the amount of colloidal and non-colloidal calcium carbonate particles (34). The study showed that, up to about a certain volume of methanol, the number of colloidal calcium carbonate particles increased with the amount of methanol. However, beyond this critical volume the surfactant layer around calcium carbonate destabilised.

The role of the promoter in facilitating micellar exchange can further be supported by the difference in the sizes of the calcium carbonate cores synthesised in a study by

Markovic *et al.* (12) The authors used two different methods (one of which has been highlighted in section 2.2.2) to produce detergents with $CaCO_3$ cores of about 2.5 and 7.5 nm. One of the main differences between the two procedures was the use of both methanol and nonyl phenol in the formation of the larger particles. It is suggested that the nonyl phenol further promotes the dynamic exchange, leading to an increase of the growth rate of the $CaCO_3$ particles.

Non-polar Hydrocarbon Solvents. The base oil and hydrocarbon solvent are both considered diluents i.e. their main function is to dissolve the colloidal detergent particles. All overbasing processes involve a non-volatile base oil, which in most cases is a refined mineral lubricating oil. Other oils that can be used include vegetable oils such as corn and castor oil, animal oils such as lard oil, and synthetic oils such as polypropylene (29). In most of the overbasing processes, apart from the solvent-free process (4) used only for barium-based detergents, there is also a volatile hydrocarbon solvent present in the system. These solvents include alkanes such as hexane, heptane, and octane and alkenes such as benzene, toluene, and xylene (29).

No effects of changing the solvent have been noted although xylene has been preferentially used in most detergent preparation processes reported in patents and publications (4, 13, 16, 29-31). Notably, toluene has been used in cases where the solvent serves as a medium that aids in the analysis of the overbased detergents (12). One of the advantages of using toluene, as highlighted by Markovic *et al.*, (12) is that it can be obtained in both hydrocarbon and deuterated forms. This is particularly essential in SANS analysis because the neutron beam used in this technique has the ability to distinguish between hydrogen and deuterium atoms, which in turn leads to the determination of the size and structure of the particles.

Furthermore, in its role as a diluent, the solvent has been found to modify the viscosity of the system, which not only aids in the mixing of the reaction mixture but also the carbonation reaction (29, 34). An interesting relationship has been discovered between the volume of the solvent and the rate of the overbasing reaction. Belle *et al.* (34) found that increasing the amount of xylene in their system decreased the viscosity and in turn increased the dissolution and diffusion of carbon dioxide. It is important to note that this increase in the carbon dioxide gas uptake did not have any influence on the number of micelles containing calcium hydroxide that were carbonated.

2.2.2 Mechanisms of Detergent Formation

Two of the least understood issues related to the synthesis of overbased detergents is the mechanism by which calcium hydroxide ($Ca(OH)_2$) is converted to calcium carbonate ($CaCO_3$) and the reverse micelle structure is formed using the oxide/hydroxide synthetic process. The mechanism has been continuously discussed over the years and has been presented in the form of four different models (7, 13, 38). The main differences between these models (discussed below) are in the routes by which the $Ca(OH)_2$ is transformed into $CaCO_3$ (direct conversion or through an intermediate), the polymorphic form of the $CaCO_3$ (amorphous or calcite), and when the surfactants form the micelle (before or after $CaCO_3$ formation).

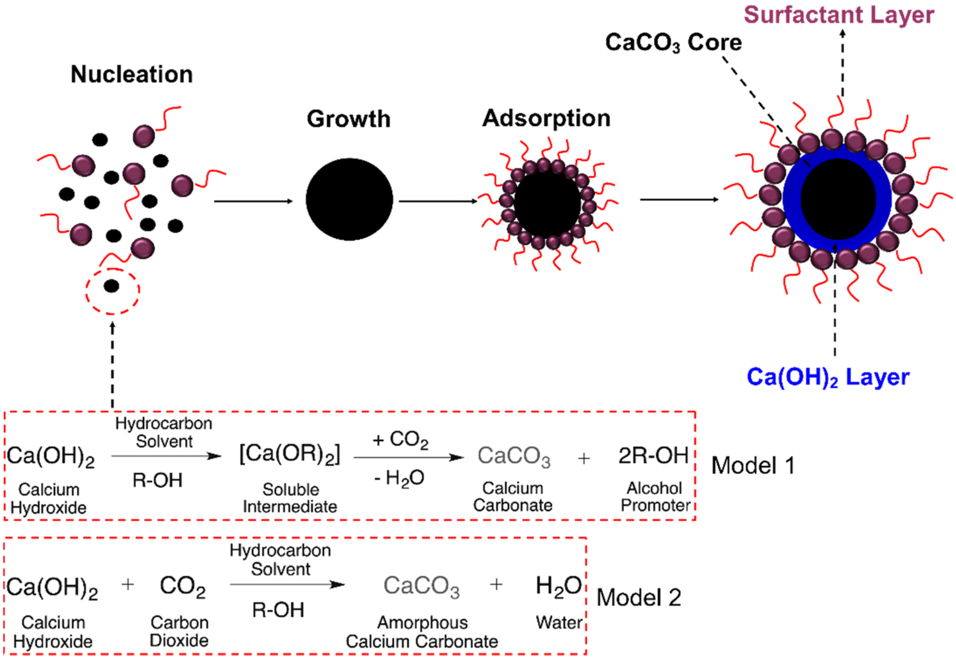

Figure 2.2. Schematic of two possible mechanisms for the formation of calcium overbased detergents – The soluble intermediates model (1) presented by Marsh (7); and the direct carbonation model (2) presented by Jao and Kreuz (13, 38).

The first model (the soluble intermediates model), presented by Marsh in 1987 (7), states that the $CaCO_3$ is the result of the carbonation of hydrocarbon-soluble metal intermediates ($Ca(OR)_2$) which are the result of a reaction between the $Ca(OH)_2$ and an alkanol or alcohol promoter (R-OH) (Figure 2.2). In most recent cases, the soluble intermediates involved in this process are alcoholates as lower alcohols such as methanol are the preferred choice for the promoter (13). Furthermore, Marsh proposed that the surfactant is formed *in-situ* simultaneously with the formation of the $Ca(OR)_2$ and later is adsorbed onto the amorphous $CaCO_3$ particles (Figure 2.2). The final structure and size of the reverse micelles are both said to be functions of the surfactant structure (chain length and shape of molecule) and the packing order of these molecules when they adsorb to the carbonate (this has been detailed in section 2.2.1) (13, 33). However, this hypothesis has been disputed as there was no concrete evidence supporting the existence of alcoholates and the model did not account for changes in particle size that occur when process parameters are altered (13, 39).

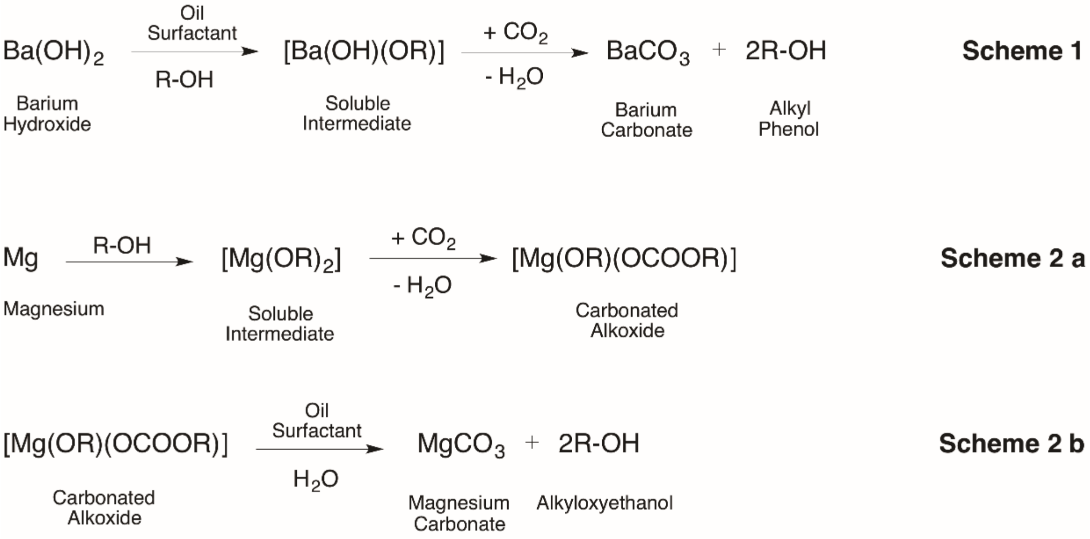

Figure 2.3. Reaction schemes for the formation of overbased detergents containing barium (scheme 1) (4) and magnesium (schemes 2 a and b) (29) carbonate cores, which involve soluble intermediates (7).

Notably, the soluble intermediates concept that governs this first model has been proposed previously for overbased detergents formed using the *solvent-free* (4) and *alkoxide* (29) synthetic processes (discussed in section 2.2.3). These two processes were employed, prior to the development of the *oxide/hydroxide* synthetic process, in the production of barium carbonate ($BaCO_3$) and magnesium carbonate ($MgCO_3$) respectively. In the solvent-free process, barium hydroxide ($Ba(OH)_2$) reacts with an alkyl phenol (R-OH) promoter in the presence of the surfactant to form an intermediate (Ba(OH)(OR)) soluble in the lubricant oil, which transformed into $BaCO_3$ after carbonation (Figure 2.3 scheme 1). On the other hand, the alkoxide process involves two separate stages where the first stage (Figure 2.3 scheme 2a) involves the reaction of magnesium (Mg) with alkyloxyethanol (R-OH) to form a soluble alkoxide intermediate ($Mg(OR)_2$) which *via* carbonation is converted to the carbonated alkoxide (Mg(OR)(OCOOR)). In the final stage (Figure 2.3 scheme 2a), this carbonated alkoxide (that is dispersed in the lubricant oil) undergoes hydrolysis in the presence of the surfactant and water and results in the formation of the desired $MgCO_3$.

The second (the direct carbonation model presented in Figure 2.2) and third (the pre-existing micelle model presented in Figure 2.4) models have been accredited to Jao and Kreuz (13). However, a review of the specified work by these two authors (38) seems to suggest that they did not address the issue of the mechanisms but instead focused on developing a robust method for analysing overbased detergents using fluorescence probes. Interestingly, a further look in the literature revealed that these models, especially the pre-existing micelle model, could result from the analytical work on calcium sulphonate overbased detergents done by Kandori *et al.*(35, 40) who address the issues of the mechanisms repeatedly in their publications.

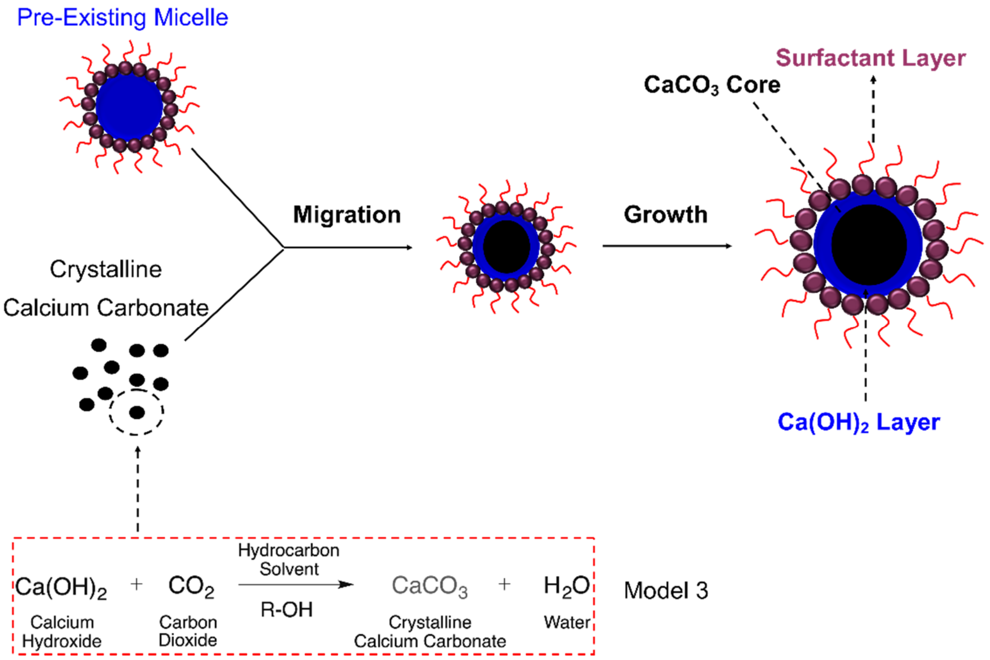

Figure 2.4. Schematic of a possible mechanism for the formation of calcium overbased detergents – The pre-existing micelle model (3) first presented by Jao and Kreuz (13, 38).

Supposedly, the models state that the detergent particles are either the result of (a) the direct transformation of $Ca(OH)_2$ to amorphous $CaCO_3$ (ACC) *via* the carbonation reaction, which is then followed by surfactant adsorption (Model 2 in Figure 2.2); or (b) the pre-carbonation formation of water-in-oil reverse micelles which are later filled by crystalline calcium carbonate (Model 3 in Figure 2.4) (13). Their first hypothesis is said to suffer from the lack of an indisputable explanation of how micro-sized hydroxide particles can directly transform to nano-sized carbonate particles of less than 10 nm.(13) On the other hand, their second hypothesis inadvertently provides an explanation for the ultimate size of the overbased reverse micelles by suggesting the pre-existence of the micelles but does not address where the carbonation reaction occurs.

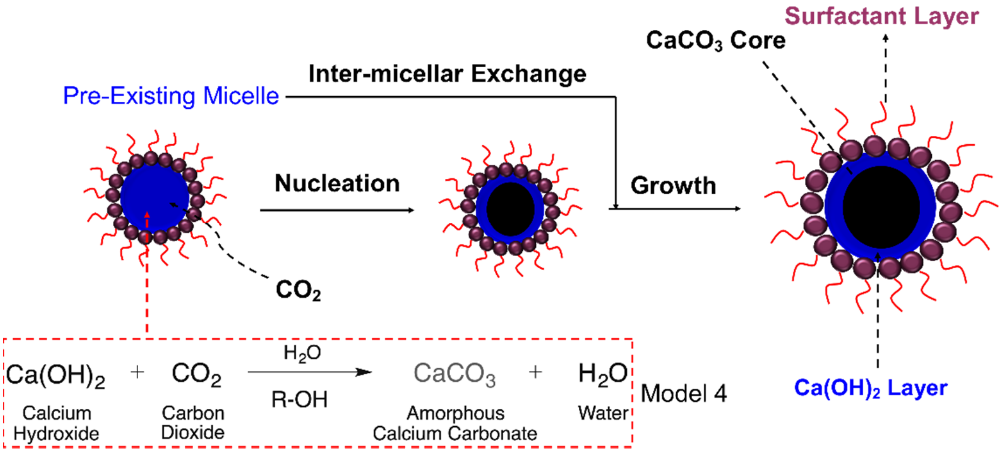

Figure 2.5. Schematic of a possible mechanism for the formation of calcium overbased detergents – The modified pre-existing micelle model (4) proposed by Roman *et al.* (13).

Finally, a fourth model (which will be termed the “modified pre-existing micelle model”) proposed by Roman *et al.* (13) is presented in Figure 2.5. This is based on the previous three models, the major role of water in the system and a multi-step analysis procedure. The authors found that reverse micelles of about 0.86 nm containing $Ca(OH)_2$, methanol and water in the core were present in the system following the neutralisation of the sulphonic acid and prior to the carbonation reaction. During carbonation, the CO_2 dissolves into non-polar hydrocarbon solvent, diffuses into the polar core (as can be seen in Figure 2.6), and reacts with the $Ca(OH)_2$ to give amorphous $CaCO_3$. The nuclei of the $CaCO_3$ were reported to be about 0.72 nm and the final core sizes about 3 nm, an increase which is due to inter-micellar dynamic exchange of $Ca(OH)_2$ with the pre-existing un-nucleated micelles. However, they do propose possible scenarios where more surfactant is adsorbed onto the carbonates after the growth stage and during distillation of methanol and water.

In conclusion, it is interesting to note that when Marsh (7) discusses the soluble intermediates model, he refers to the existence of microemulsions containing the polar solvent and water before carbonation, which seems in line with the third and fourth pre-existing micelles models. In consideration of this observation alone, one can say that the biggest issue that needs to be addressed in relation to the particle formation mechanism is the conversion of the calcium hydroxide to the calcium carbonate. However, an analytical study of calcium sulphonate detergents by Tavacoli *et al.* (41), using the small-angle neutron scattering (SANS) technique, revealed that there were no microemulsions present in the system pre-carbonation. These results contradict the small-angle X-ray scattering (SAXS) results obtained by Roman *et al.* (13), which they used to form their model, that show the existence of these micelles. Thus, in this project, it would be beneficial to explore different analytical techniques that would help in determining the real mechanism involved in the formation of overbased detergent particles. Some of these techniques have been discussed in section 2.3.

2.2.3 The Overbasing Process

Over the years, multiple manufacturing processes have been developed for the production of overbased detergents, and in particular detergent particles with barium, magnesium and calcium carbonate cores. The most prominent ones have been the *solvent-free*, *alkoxide* and *oxide/hydroxide processes* (4, 29, 30). The *solvent-free process* was the first of the three to be developed. It was introduced in 1952 (4) and was solely used for the production of barium-centric detergents. The reason this process was not used for the other alkaline earth metals was because the required conditions for the production of the carbonate were not ideal to induce the necessary intermediary reaction between an alkyl phenol promoter and the magnesium and calcium hydroxides (7). Hence, despite the simplicity, high efficiency and low cost of this process it was replaced by more complex processes such as the *alkoxide* and *oxide/hydroxide* ones.

The *alkoxide process* (29) was introduced in 1964 and was considered for many years as the most practical way to make magnesium overbased detergents (7). Unlike its predecessor, this process involved the use of a volatile hydrocarbon solvent such as hexane, heptane, toluene or xylene and the initial metal reagent was pure magnesium instead of the metal hydroxide (7, 29). The use of these solvents contributed to a relative increase in the complexity and cost of the overbasing process, partially due to the need for the additional distillation step to remove the volatile solvent. Furthermore, the high costs were also probably due to the fact that the alkoxide process was carried out in two separate batch reactions, one for the formation of the oil soluble intermediate and the other for the formation if the detergents (7). Subsequently, with the aim of addressing the relatively high costs of this *alkoxide process* and the inflexibility in application of the solvent-free process before it, the optimised oxide/hydroxide method was introduced.

The *oxide/hydroxide process* (30) was introduced in 1970, and is currently the most widely used method for the synthesis of overbased detergents. This process can successfully and efficiently be used for the production of overbased detergents for all of the three metals, but it is mostly related to the production of calcium-centric detergents (7, 12, 13, 30) At its inception, the *oxide/hydroxide process* was considered to be revolutionary with respect to the production of overbased detergents using the economically sustainable calcium (30). It overcame the persistent issues that were encountered by previous methods, such as the inability of calcium compounds to react sufficiently with acids, promoters and carbon dioxide to produce the detergents (30).

Further comparisons with the preceding processes show that this overbasing method is much like the *alkoxide process* in terms of the use of volatile hydrocarbon solvents and the inclusion of a distillation stage for the removal of these solvents (7). However, unlike the alkoxide method, the metal precursor in the *oxide/hydroxide process* is a metal oxide or hydroxide like in the *solvent-free process*. Furthermore, it is an improvement from the *alkoxide process* because it can be carried out in one batch reaction (7), which cumulatively should have a favourable effect on the total cost of the process. Another notable difference in the *oxide/hydroxide process* as compared with its predecessors is the use of lower alcohols such as methanol, ethanol or isopropanol as the promoter (30). One aspect that all three processes share is the use of filtration or centrifugation at the end to remove unreacted and non-colloidal material.

The *oxide/hydroxide process* has undergone significant development over the years with respect the type, amount or ratios of components used and the process conditions. However, the general procedure has remained the same with four main stages (7):

1) *Neutralisation* of the acid by the metal hydroxide to form the surfactant in the presence of the polar and hydrocarbon solvents
2) *Carbonation* of the system to convert they hydroxide to the metal carbonate
3) *Stripping* of the solvents from the system, which leaves the detergents dispersed in the lubricant oil added
4) *Filtration* or *centrifugation* of unreacted and non-colloidal material to give the final product

The first example of the successful application of the oxide/hydroxide process is presented by Markovic *et al.* (12) in their paper on the first case of analysis of overbased calcium sulphonate detergents using small-angle neutron scattering (SANS). In this publication, Markovic *et al.* present a preparation method that generates reverse micelles containing calcium carbonate ($CaCO_3$) particles with an average size of 2.5 nm. The process initially involves charging the reaction vessel with 217 g of alkyl aryl sulphonic acid (for the *in-situ* preparation of the sulphonate surfactant), 219 g toluene (hydrocarbon solvent), and 124 g of methanol (polar solvent). The mixture is stirred until homogenous, before adding 140 g of calcium hydroxide ($Ca(OH)_2$) and setting the temperature to 25 °C. Carbon dioxide (CO_2) is then bubbled through the reaction mixture to convert the $Ca(OH)_2$ to $CaCO_3$. Temperature control during the carbonation reaction is crucial since the reaction is very exothermic. The temperature must be kept below 30 °C to ensure that the $Ca(OH)_2$ remains soluble (7). The carbonation reaction is closely followed by the addition of a hydrocarbon mineral oil. A two-stage distillation process is carried out to remove all of the methanol, water (generated during the carbonation), and toluene, where the latter stage is carried out under vacuum and below 150 °C. The resultant mixture is then filtered under pressure to remove residual solids.

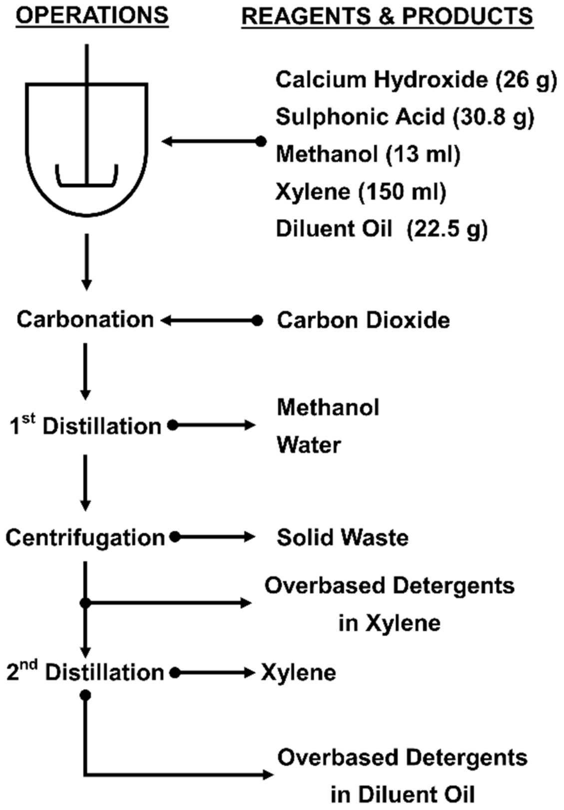

Figure 2.6. Modified summary of the experimental procedure and materials used in the preparation of overbased calcium sulphonate detergents presented by Roman *et al.* (13).

The second example is presented by Roman *et al.* (13) in their paper on in-process analysis of the overbased calcium sulphonate detergents using various analytical techniques (discussed further in section 2.3). The experimental procedure and materials used have been summarised in Figure 2.6. This specific process, much like the one presented by Markovic *et al.*, follows the general procedure with the four main stages and resulted in particles with similar sized calcium carbonate cores of about 3 nm. However, this procedure has two solvent stripping stages before (1st distillation) and after (2nd distillation) the removal of the residual solids by centrifugation. In the first stage the methanol and water are removed, whereas the second stage involved the removal of the hydrocarbon solvent xylene.

2.3. Characterisation of Overbased Detergents

There has been continuous development and exploration of the chemical, physical and surface analytical techniques for characterising overbased detergents, most of which has focused on calcium sulphonate detergents. Some of the earliest analytical work (in 1984) involved characterising overbased calcium sulphonate detergents using SANS (12). This helped determine the structure and size of the detergent particles (*cf.* Figure 2.1) that are still widely referenced today in various publications (9).

This characterisation was followed by further analysis of various overbased detergents using SANS (7, 32, 39, 41, 42) and other techniques such as fluorescence polarisation (35, 37, 38, 43), Powder X-ray diffraction (PXRD) (40), transmission electron microscopy (TEM) (10, 13, 19, 40, 44-48), dynamic light scattering (DLS) (13, 35, 40, 44, 48) X-ray absorption spectroscopy (XAS) (10, 13, 18, 19), electron energy loss spectroscopy (EELS) (19, 45, 46), small-angle X-ray scattering (SAXS) (13, 42, 47), mid-infrared (mid-IR) spectroscopy (13, 41), energy dispersive X-ray (EDX) spectroscopy (19), X-ray photoelectron spectroscopy (XPS) (10), time-of-flight secondary ion mass spectroscopy (ToF-SIMS) (10), and rheometry (41). These techniques will be discussed in this section in terms of determination of the size, structure and content of the detergent particles.

It is important to note, that most of the work surrounding the characterisation of calcium sulphonate detergents has been done by Martin, Mansot, Roman and their co-workers (10, 13, 17-19, 34, 45, 46, 48, 49). Most of their work is on the post-production analysis of the micelles using various analytical techniques such as TEM, XAS, EELS, SAXS, FTIR, EDX, XPS and ToF-SIMS. An exception to this post-production approach is the work by Roman *et al.* (13), which looks into the products of all the four stages involved in synthesis of overbased calcium sulphonate detergents. The authors provided a detailed account of the synthetic process for the overbased detergents (discussed previously in section 2.2.3) and combined the multiple steps in the process with complimentary analytical techniques. Their aim was to not only characterise the detergent particles but to also determine the mechanism by which the particles are formed (*cf.* section 2.2.2). Hopefully, this at-line approach can be adopted in the later parts of this project and be used in the development of a robust *in situ* analysis procedure.

Considering the extensive analytical work that Martin, Mansot, Roman and their co-workers have done separately and together in a space of two decades since 1986, the subsequent focus in this section will mostly be on their methods and findings. Their work will be continuously linked to other notable works that have utilised similar analytical techniques and obtained complimentary or opposing results.

2.3.1 Detergent Particle Structure

The structure of an overbased detergent particle (i.e. a carbonate core stabilised by a concentric organic surfactant shell) was first proposed by Markovic *et al.* (12) on the basis of their SANS analysis. This has subsequently been further refined by the SANS data of Tavacoli *et al.* (41), who showed that there is a quantifiable layer of water around the carbonate core. It has also been proposed that both calcium hydroxide and methanol are present at the surface of the carbonate core. However, these have not yet been quantified (10, 34). XPS and ToF-SIMS were used to determine the presence of the calcium hydroxide, but only ToF-SIMS was able to locate it on the surface (10). On the other hand, the location of the methanol has been extrapolated from its effects on the stability of the surfactant layer using techniques such as fluorescence polarisation (34, 37). It is important to note however, that it has been suggested that due to the amorphous-like nature of the carbonate core, there is a distinct possibility that there is some calcium hydroxide and maybe water and methanol present inside the core.(10, 17) Other techniques such as EDX have also been used to determine the composition of these detergents (19).

Particle size is one of the well-studied morphological aspects of overbased detergents. This has been determined previously, principally for overbased calcium sulphonate detergent systems, using analytical techniques such as SANS, SAXS, TEM and DLS. The size of overbased detergents is generally described in terms of the carbonate core and the stabilising surfactant shell. The core diameter is usually around 3 nm, whereas the surfactant shell thickness is about 2 nm (7).

SANS was one of the first techniques used to characterise the carbonate core and the surfactant layer (12). In this study by Markovic *et al.*, the authors were able to determine the size of the core and surfactant layer of two overbased calcium sulphonate systems, whose main difference was the use of the auxiliary promoters nonyl phenol and calcium chloride in the second system (12). It was found that the diameter of the calcium carbonate ($CaCO_3$) cores were 4.4 nm and 13.4 nm in the first and second systems respectively, while the surfactant layer thickness remained the same for both systems at 1.9 nm. The surfactant layer thickness has been found (using SANS) to remain constant with the type of surfactant used regardless of changes in its amount and/or the addition of components such as promoters to the overbasing reaction system (12). In contrast, the carbonate core is very sensitive to these changes and the rate of surfactant adsorption. SANS studies have also revealed that there is a water layer around the carbonate particle with a mean thickness of 0.5 nm (41).

Most studies today tend to use TEM and DLS separately and together to determine the size of these particles. Generally, both of these techniques can be considered limited in the sense that with conventional TEM (CTEM) the only dimension that can be determined is the core size whereas DLS gives a hydrodynamic diameter of the whole particle estimated using the Stokes-Einstein equation. For this reason, numerous studies on these overbased detergents have used both techniques to fully characterise overbased detergents made from various surfactants including sulphonates (13, 35, 40, 44, 48).

With CTEM, it is possible to determine the size of the detergent core from the resulting micrographs. From these images, it is also possible to discern but not quantitatively determine the presence of the surfactant shell from the absence of coalescence between the particles (19). Moreover, energy-filtered TEM (EFTEM) has been found to be more accurate in determining the core size as was shown by Mansot *et al.* (19). These authors analysed overbased calcium alkyl benzene sulfonate detergents with both CTEM and EFTEM. The resulting images showed that EFTEM gave a specific core size of 15 nm as opposed to the range obtained using CTEM of 10 to 20 nm. Even though there isn't much variation in these results, EFTEM has been proven to be the better option as it was possible to determine the thickness of the surfactant layer (45, 46). The shell thickness can be determined from high resolution images obtained from carbon plasmon loss electron spectroscopic imaging (ESI). The results from two studies using ESI by Martin *et al.* in 1989 (45) and 1990 (46) have proven that regardless of the size of the detergent core, if the surfactant used is the same, then the thickness of the organic shell remains the same. In their case they used alkyl aryl sulphonate, the same as Markovic *et al.* (12), and found the mean thickness to be about 2 nm.

Other notable techniques are fluorescence polarisation and SAXS, which can be used to determine the size of the colloidal carbonate dispersions and the micelles present in a system prior to carbonation (13, 38, 42, 47, 50, 51). In conclusion, the techniques discussed in this sub-section have been used to determine the influence of certain parameters in the overbasing process by determining the size of particles as a function of time (SAXS) (13), surfactant concentration (SANS) (7), and water volume (SANS and TEM) (35, 41).

2.3.2 Detergent Core Structure

As for the local structure of the calcium carbonate core, the predominant techniques that have successfully been used are XAS and EELS (in conjunction with EFTEM). XAS has been used extensively to determine the local structure of inorganic metal core of overbased sulphonate detergents from that of calcite. Most of this work was done by Martin, Mansot and their co-workers (together and separately) (10, 17-19). It was also used in the formulation of the modified pre-existing model for the formation of calcium-based detergents proposed by Roman *et al.* (13).

In their first publication in 1986, Martin *et al.* (17) looked into determining the local structure of overbased detergents using extended X-ray absorption fine structure (EXAFS) and X-ray absorption near edge structure (XANES). This is one of the first instances where these X-ray absorption techniques were used to analyse the calcium carbonate core of these types of micelles. The authors analysed the detergents along with a standard sample of calcite (prepared in a similar medium) at the calcium K-edge. They worked on the assumption that the micelle core was amorphous calcium carbonate (ACC), based on previous a TEM analysis, and on the basis of the extensively studied structure of calcite. Following an evaluation of their XANES and EXAFS results, they determined that much like aragonite (52) the micelles did not display a strong peak at ~20 eV in the XANES, which is present in calcite. This peak was associated with the collinear calcium and carbonate atoms and thus its absence suggested distortion in the local structure of the micellar calcium carbonate (17). This misalignment of the carbonyl groups was also observed in a later XANES study by

Cizaire *et al.* (10) who also concluded that the core consisted of ACC. Interestingly, despite the slight resemblance of the XAS data of the overbased detergents to that of aragonite, the two have never been compared.

Further, from the EXAFS data collected by Martin *et al.* (17) there was a noticeable absence of a peak at about 4040 eV in the micelles that was strongly present in the calcite data. This absence was attributed to the core being amorphous, which was further supported by the plots from the radial distribution function (RDF) statistical modulation of the EXAFS data of the two systems. The RDF results of the overbased detergents presented only one distinct modulation due to the Ca-O bond but there was no evidence of the Ca-Ca modulation present in the calcite RDF results. Martin *et al.* (17) concluded their study by showing *via* simulations that the first coordination shell of micellar core consisted of 7.5 oxygen atoms at 2.38 Å as opposed to 6.0 atoms at 2.35 Å as occurs in calcite.

Three years later, Mansot *et al.*(18) presented more Ca K-edge EXAFS data of calcite and overbased detergents. However, in this instance, they analysed samples taken every 15 minutes during the calcium carbonate synthesis to monitor how the local structure changed over time. They found that, over time, the RDF results showed only one peak for the overbased detergents at 2.41 Å (as was also observed by Martin *et al.*) (17). They took this as evidence of an amorphous structure. However, it is important to note that a second peak, which does occur in calcite, did not appear following over-carbonation when most of the material present in the reaction system was crystalline (at > 90 minutes).

The authors also looked at the total base number (TBN), the number of oxygen atoms and Ca-O bond distances as a function of time. The basicity of the micelles was seen to increase over time up to about 90 minutes, when most of the cores were crystalline, after which it declined. As for the number of oxygen atoms, there was an observable increase from 4.8 ± 0.5 atoms at the initial 15 minutes to 5.7 ± 0.5 atoms at 90 minutes (which is considered as the time carbonation terminates). On the other hand, the Ca-O distance remained relatively steady over time at 2.41 ± 0.02 Å. Ultimately, the number of atoms obtained in this study was less than that of calcite (6.0 atoms) as well as the 7.5 that was formerly obtained in the previous study *via* simulation by Martin *et al.* (17) Based on these collective results, the authors offer the first postulation of the presence of water, methanol and calcium hydroxide in the mineral core, which they suggest contributes to the disorder of the local structure (18).

In conclusion, most of the aforementioned analytical studies on the detergents provide evidence of disorder in the local structure of the $CaCO_3$ core, which suggests that it is amorphous. Nevertheless, there are some significant limitations in these studies. These limitations include: (a) the lack of comparison of the detergent core structure with $CaCO_3$ structures other than calcite; (b) the failure to address variations in amorphous calcium carbonate (ACC) that are partially dependent on process conditions and reagents (25); and (c) the lack of consideration of the effects of the presence of various components in the detergents particles such as H_2O and $Ca(OH)_2$ on the results. Notably, EXAFS has been extensively used to characterise the structure of crystalline and amorphous $CaCO_3$ polymorphs (53-61). Structural elucidation of these polymorphs using EXAFS has been inconclusive due to limited accuracy in estimating inelastic and multiple scattering contributions (62, 63). This is evident through inconsistencies in fitting the EXAFS beyond the first Ca-O shell (55, 56, 59, 64, 65). As such, the application of X-ray pair distribution function (XPDF) to look at the average short- and medium-range order has been proposed. However, most of the comprehensive XPDF studies are limited to characterising variations in ACC (61, 66, 67).

2.4 Conclusions

A comprehensive literature review on the synthesis and characterisation of calcium overbased detergents, in particular sulphonate systems, was conducted. Some interesting research areas were identified with regards to the synthesis of the particles. One of these areas is the mechanism of the formation of the detergent particles (*cf.* section 2.2.2), which has been investigated several times since the late 1980s. However, none of the four proposed models have yet been proven (7, 9, 13). Interestingly, one of these models (*cf.* Figure 2.2) (7) includes a possible soluble metal-organic intermediate suggesting that the role of the solvents, such as water and methanol, could be important in defining the mechanism of the reaction (*cf.* section 2.2.1). In terms of characterisation, one of the main issues that was identified was the lack of comparison between the overbased detergents and other forms of $CaCO_3$ aside from calcite. This interest stems from the fact that vaterite has been identified as one of the compounds present in the sediment collected at the end of the overbasing process (7, 13). Additionally, some spectral features in the XAS of the overbased detergents are similar to those in the aragonite spectrum (17). Based on these findings form the literature, the synthesis and characterisation methods were determined in this thesis. Figure 2.7 summarises the overbasing process and the techniques that have been chosen to determine the structures of the reactants, (possible) intermediates and products.

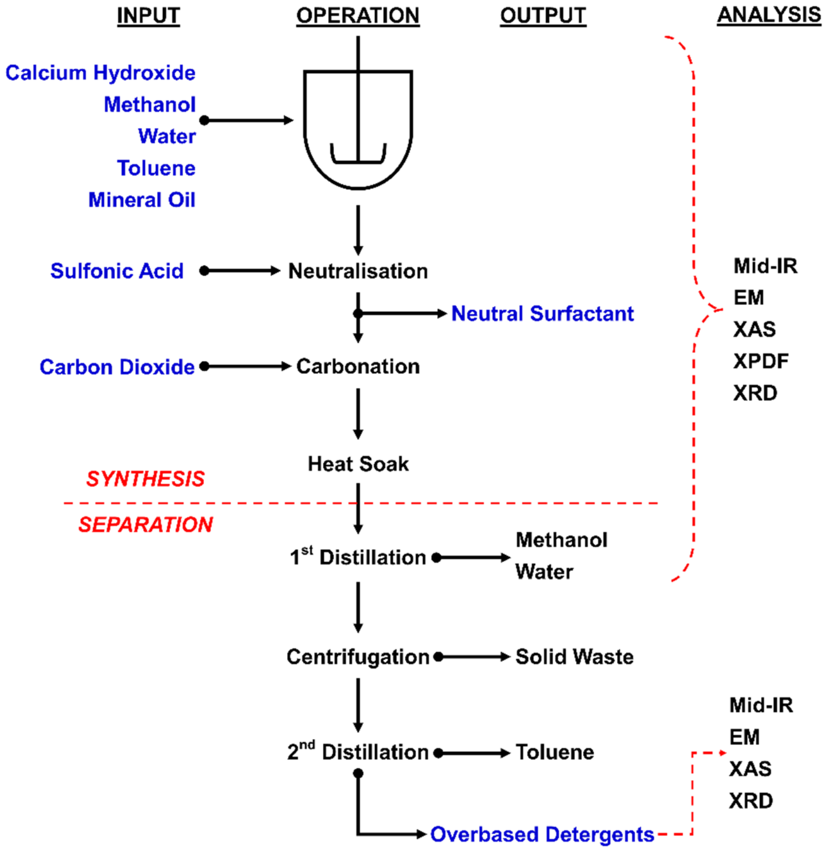

Figure 2.7. Summary of the overbasing process based on methods proposed by Markovic *et al.* (12), Roman (13) and Alcock (15). The reagents, solvents and products of interest have been highlighted. Selected microscopy, scattering and spectroscopy analytical techniques have been included.

Chapter 3:
Research Methodology

3.1 Introduction

This chapter details the materials, synthesis methods and analytical techniques used in the various *ex situ*, *in situ* and *operando* studies discussed in chapters 4 to 8. The methods proposed in this chapter are based on processes and techniques currently being employed for the preparation of study overbased sulphonate detergents (discussed in chapter 2). The chapter consists of three main sections (Figure 3.1): (i) section 3.2 lists the materials used in the various synthesis methods; (ii) section 3.3 details the methods used for synthesising functionalised calcium-containing compounds e.g. calcium carbonate polymorphs and calcium sulphonate detergents; and (ii) section 3.4 gives a brief overview of the analytical procedures, ranging from electron microscopy to X-ray spectroscopy, which were used to obtain the results in chapters 5 to 8.

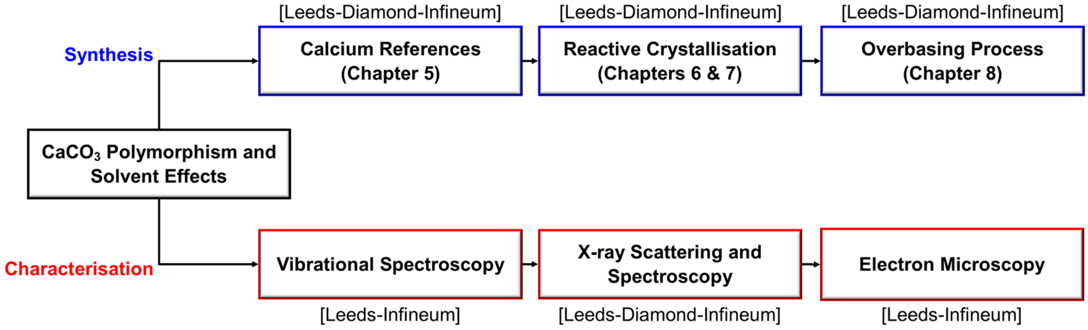

Figure 3.1. Summary of the research methodology utilised in the project with particular focus on spectroscopy, scattering and microscopy techniques. Collaborations have also been highlighted.

3.2 Materials

Powders. geological calcium oxide (Alfa Aesar), geological calcium hydroxide (94%, L'hoist, UK), synthetic calcium methoxide (≥99%; Sigma Aldrich), anhydrous calcium chloride (96%; ACROS Organics), and three anhydrous calcium carbonate polymorphs – synthetic calcite (≥99%; Sigma Aldrich), geological aragonite (Alfa Aesar), synthetic aragonite, synthetic vaterite and amorphous calcium carbonate (ACC) – were analysed as references in this study. The calcium hydroxide was also extensively used in the synthesis methods detailed in section 3.2.2. Other materials used for synthesis were sodium hydroxide (≥99%; Fisher Chemical), sodium carbonate (≥99%; Fisher Chemical) and calcium chloride dihydrate (≥99%; Sigma Aldrich).

Oil-based Materials. calcium sulphonate surfactant (Infineum, UK), overbased sulphonate detergents (Infineum, UK), akylbenzene sulphonic acid (Infineum, UK) and mineral oil (Infineum, UK).

Dispersions. Commercial nanolimes (Nanorestore Plus®; CSGI) containing 5g/L of calcium hydroxide dispersed in ethanol and isopropanol.

Gases. carbon dioxide (99.9%; BOC), helium (99.9%; BOC) and nitrogen (99.9%; BOC).

Solvents. Methanol (99.9%; Fisher Scientific), ethanol (99.8%; Fisher Scientific), isopropanol (99.8%; Fisher Scientific) and toluene (99.8%; Fisher Scientific) and deionised water. Table 3.1 shows the solubility of calcium hydroxide and carbon dioxide in the various solvents at different temperatures. These will be discussed in chapter 7.

Table 3.1. Solubility of calcium hydroxide ($Ca(OH)_2$) and carbon dioxide (CO_2) from 20 to 30 °C in water, methanol, ethanol, isopropanol and toluene. Relative solvent polarities have been included.

Solvent	Relative Polarity	Solubility					
		$Ca(OH)_2$ (g/100 ml)			CO_2 (ml/ml)		
		20 °C	25 °C	30 °C	20 °C	25 °C	30 °C
H_2O	1.000	0.165	0.159	0.153	0.930	0.826	0.742
CH_3OH	0.762	-	0.008	-	4.205	3.837	3.83
CH_3CH_2OH	0.654	-	-	-	2.973	2.706	2.60
$CH_3CH_2CH_2OH$	0.546	-	-	-	2.180	-	1.95
$C_6H_5CH_3$	0.099	-	-	-	2.426	2.305	-

3.3 Synthesis Methods

3.3.1 Calcium Carbonate References

Aragonite Precipitation. The aragonite was synthesised using a variation of the method proposed by Kitamura *et al.* (68). 1.61 M of sodium carbonate (in 126 ml of water) was added to 0.21 M calcium hydroxide (in 82 ml of water) *via* dropwise addition. The reaction mixture was continuously stirred at a rate of 255 rpm and maintained at a temperature of 70 ± 1 °C. The dropwise addition and stirring were maintained for 30 and 60 minutes respectively. The resulting white precipitate was filtered, washed with water and ethanol, and dried under vacuum for 24 hours.

Vaterite Precipitation. The vaterite was synthesised using the method proposed by Shivkumara *et al.* (69). 1 M of sodium carbonate (in 20 ml of water) was added a solution of glycine (12 g in 200 ml of water). The mixture was stirred for 30 minutes before 0.03 M of calcium chloride dihydrate (in 20 ml of water) was added. The mixture was further stirred for 60 minutes after which the white precipitate was filtered, washed with water and ethanol, and dried under vacuum for 24 hours.

Amorphous Calcium Carbonate (ACC) Precipitation. The ACC sample (provided by Muling Zeng (University of Leeds)) was synthesised using a variation of the method proposed by Koga *et al.* (70). The method involved mixing equivolumes (5 ml) of aqueous solutions of 1 M calcium chloride dihydrate and a mixture of 1 M sodium carbonate and 30 mM sodium hydroxide. The reaction between the two solutions was allowed to proceed for 10 seconds, after which the mixture was vacuum filtered and rinsed multiple times with ethanol. The resulting white precipitate was then submerged in liquid nitrogen for 15 minutes, which was subsequently followed by vacuum drying for 24 hours.

3.3.2 Calcium Methoxides, Esters and Sol-gels

Reactor System. All experiments were reproducibly carried out using either a 250 ml Quickfit™ Dreschel bottle or a Radley's Carousel 6 Plus Reaction Station™ equipped with six 250 ml round-bottomed flasks. Each 250 ml vessel contained cylindrical PTFE stir bar (6 x 25 mm) and was connected to a CO_2 gas cylinder *via* PTFE tubing and a gas flowmeter. The temperature and stirring rate were maintained at 28 ± 1 °C and 400 rpm respectively by a hotplate stirrer equipped with a thermocouple and a digital temperature indicator/controller. The temperature and agitation rate were determined based on the overbasing methods proposed by Markovic *et al.* (12) and Alcock. (15).

Calcium Hydroxide Methoxylation (Chapter 6). $Ca(OH)_2$ was mixed with pure CH_3OH (100 mol%) for 24 hours. An inert environment was maintained in the reaction vessel, by the constant addition of nitrogen (at 33 ml/min), to prevent any reactions with atmospheric CO_2. The product was vacuum filtered before characterisation.

Calcium Carbonate Precipitation (Chapter 6). $CaCO_3$ was synthesised by carbonating a colloidal dispersion of $Ca(OH)_2$ (0.05 moles) in 4 moles of pure (100 mol%) and diluted (90 mol%) CH_3OH. CO_2 was bubbled through the dispersions at a rate of 33 ml/min for a duration of 40 minutes. Agitation and heating were maintained for 20 minutes after CO_2 addition was stopped to allow for complete reaction. The waxy white precipitate product from the 100 mol% system was vacuum filtered before characterisation but since the 90 mol% product was a sol-gel (Figure A.1 in Appendix A) no filtration was required.

3.3.3 Calcium Carbonate in Non-aqueous Systems

Calcium Carbonate Precipitation (Chapter 7). The dispersions were prepared by mixing calcium hydroxide (4.2 or 60 g) with 750 ml of solvent. Solvent ratios of the binary and ternary solvent systems were determined based on the overbasing process. The reactive crystallisation processes were carried out in a 1 L glass baffled reactor using a conventional lab-scale setup (Figure 3.2) under a constant N_2 (30 ml/min) environment. The dispersion was carbonated for a duration of 20 to 60 minutes using 95 wt% of the required stoichiometric amount of carbon dioxide.

3.3.4 Calcium Sulphonate Overbased Detergents

***Ex situ* Calcium Sulphonate Surfactant and Detergent References (Chapter 8).** The overbasing process, based on literature (*cf.* section 2.2.3) (12, 13), was carried out in two stages (synthesis and separation – Figure 3.2). The first stage consisted primarily of the synthesis of the particles and the second stage involved the removal of the solvents and solid sediments from the colloidal dispersion. The detergent synthesis and isolation can be separated into six steps i.e.

(Step 1) Neutralisation – Reaction of sulphonic acid ($R–SO_3H$) with calcium hydroxide ($Ca(OH)_2$) to produce calcium sulphonate ($Ca(R–SO_3)_2$) surfactant:

$$2R\text{-}SO_3H + Ca(OH)_2 \longrightarrow Ca(R\text{-}SO_3)_2 + 2H_2O$$

Firstly, the reactor was set to reflux (Figure 3.2) and charge it with toluene (240 ml), methanol (177 ml), water (14 ml), and mineral oil (about 6% of the required total). Calcium hydroxide (114 g) was then added to the vessel, which was then followed by the addition of the sulphonic acid (170 g) and smaller amount of toluene in semi-batch mode. The temperature during this process ranged from 28.0 to 40 °C (12) and the system was operated at stirrer speeds ranging from 0 to 400 rpm depending on the material being added and its associated viscosity, which could lead to insufficient mixing and hot spots if not accounted for properly. Following the completion of the neutralisation process, an aliquot of the dispersion was taken to isolate the non-carbonated calcium sulphonate surfactant.

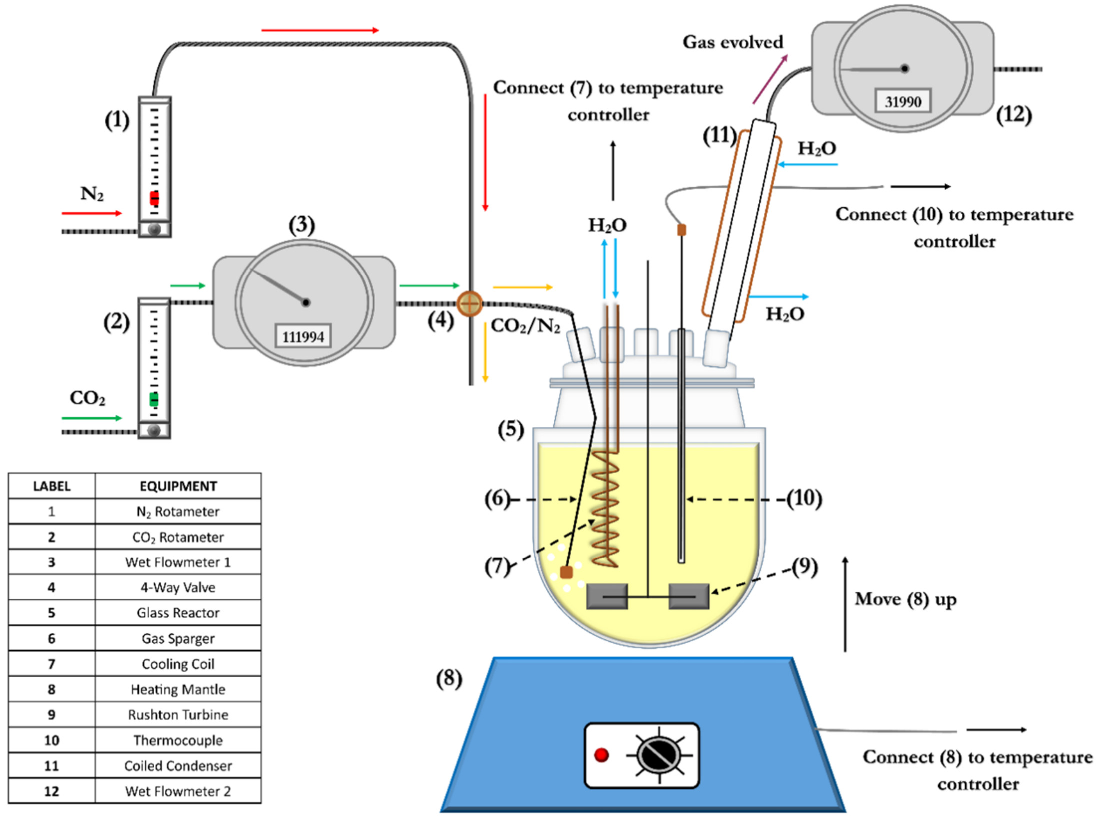

LABEL	EQUIPMENT
1	N_2 Rotameter
2	CO_2 Rotameter
3	Wet Flowmeter 1
4	4-Way Valve
5	Glass Reactor
6	Gas Sparger
7	Cooling Coil
8	Heating Mantle
9	Rushton Turbine
10	Thermocouple
11	Coiled Condenser
12	Wet Flowmeter 2

Figure 3.2. Schematic of the conventional lab setup (in reflux mode) for the synthesis of calcium sulphonate neutral surfactants and overbased detergents.

(Step 2) Carbonation – Reaction of $Ca(OH)_2$ with carbon dioxide (CO_2) to form overbased sulphonate ($nCaCO_3{\cdot}Ca(R{-}SO_3)_2$) detergent:

$$Ca(R\text{-}SO_3)_2 + (n + x)Ca(OH)_2 + nCO_2 \xrightarrow{CH_3OH} nCaCO_3{\cdot}Ca(R\text{-}SO_3)_2 + xCa(OH)_2 + nH_2O$$

The second step initially required setting a carbon dioxide (CO_2) flowrate that ensures a 3 hour reaction. To account for the exothermic nature of the carbonation reaction, a cooling coil connected to a temperature controller was inserted in the vessel to maintain the reaction temperature at about 28.0 °C. After the reaction was completed, the temperature in the reactor was raised again.

(Step 3) Heat Soak – Heating of the post-carbonation mixture to allow for reaction completion and growth of the carbonate particles and to reduce the formation of sludge and sedimentation. During this time, a second charge of 56% of the mineral oil is added to the reactor.

(Step 4) Polar Distillation – The reactor setup was changed to distillation configuration (as can be seen in Figure 3.3) to remove the polar (water and methanol) solvents. This involved increasing the temperature above the boiling point of the two solvents i.e. greater than 100 °C. The remaining mineral oil was added during distillation. Subsequently, the dispersion was diluted with a specified amount of toluene, ensuring the methanol to toluene ratio is within the 0.1 to 0.6 range (36).

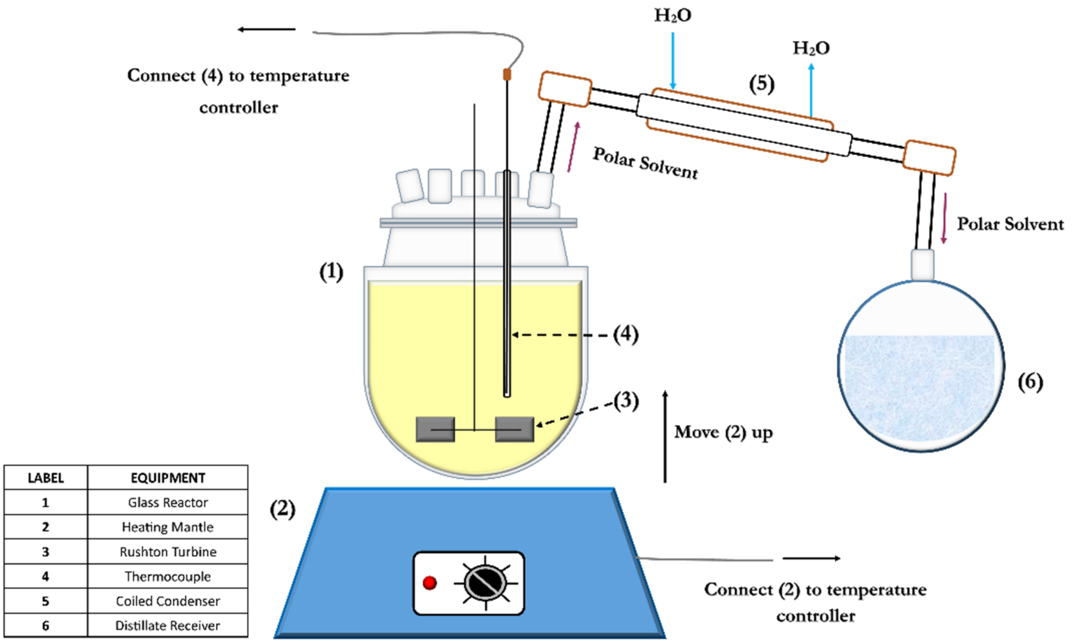

LABEL	EQUIPMENT
1	Glass Reactor
2	Heating Mantle
3	Rushton Turbine
4	Thermocouple
5	Coiled Condenser
6	Distillate Receiver

Figure 3.3. Schematic of the of the conventional lab setup (in distillation mode) for the removal of the polar and non-polar solvents from the oil dispersion containing calcium sulphonate neutral surfactants and overbased detergents.

(Step 5) Centrifugation – the non-polar (toluene) solvent removed from the post-carbonation dispersion in a three step distillation, the first step is to centrifuge the entire reaction mixture for an hour in order to remove all residual solids from incomplete carbonation of $Ca(OH)_2$ and $CaCO_3$ crystallisation. The sediment-free fluid containing suspended detergent particles is then put back into the reactor.

(Step 6) Non-polar Distillation – The hydrocarbon solvent and some water is distilled using the same setup as for the methanol distillation (Figure 3.3) but with the addition of a vacuum and re-insertion of the gas sparger for a nitrogen purge. This distillation is achieved by increasing the reactor temperature from ambient to a temperature greater than 130.0 °C (15).

***Operando* Calcium Sulphonate Overbased Detergent Synthesis (Chapter 8).** The overbased sulphonate ($nCaCO_3 \cdot Ca(R\text{–}SO_3)_2$) detergents were synthesised *operando* using a modified overbasing process similar to the methods used by Markovic *et al.* (12) and Alcock (15). Essentially, the amount of sulphonic acid ($R\text{–}SO_3H$) and calcium hydroxide ($Ca(OH)_2$) were reduced to prevent blockages the X-ray absorption spectroscopy sample loop (*cf.* Figure 4.2). Only the synthesis steps were monitored due to the time constraints of X-ray absorption spectroscopy experiments. Initially, methanol (280.0 g), water (27.0 g), toluene (517.0 g), and mineral oil (21.8 g) were loaded into a 1 L baffled glass reactor and stirred (at 400 rpm). Calcium hydroxide (4.2 g) was then added to the vessel. Neutralisation (step 1) was initiated by the addition of the sulphonic acid (170 g) and toluene (100 g) in semi-batch mode. The subsequent stage, carbonation (step 2), involved the second addition of calcium hydroxide (4.2 g). Approximately 95 wt% of the required stoichiometric amount of carbon dioxide was then flowed through the system for an hour at 57 ml/min at 28 +/- 2 °C. After carbonation, during heat soak (step 3), the temperature in the reactor was raised to 60 +/-2 °C max to improve product yield and filtration properties.

3.4 Analytical Methods

3.4.1 Electron Microscopy

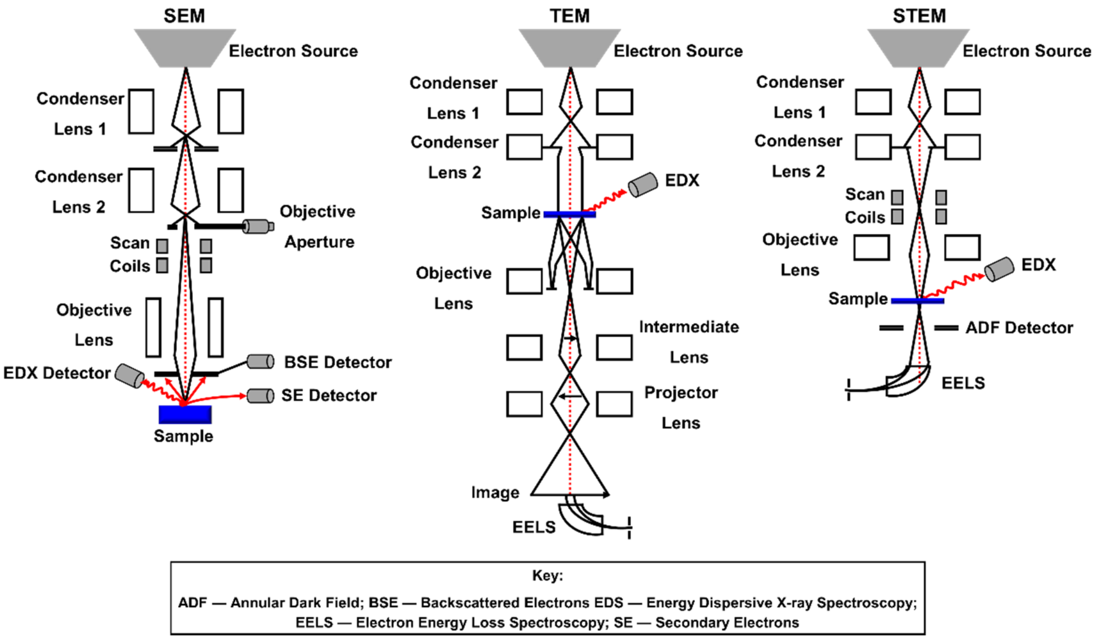

Figure 3.4. Simplified schematic highlighting the differences between scanning electron microscopy (SEM), transmission electron microscopy (TEM) and scanning transmission electron microscopy (STEM) (72).

Background. Electron microscopy utilises high-energy electrons to determine the structure of complex materials at micro- and nano-scale. It is usually used to elucidate morphology (e.g. shape and size), topography (e.g. surface deformations), composition (e.g. elements) and crystallinity (e.g. atomic structure (dis)order) (71). Figure 3.4 (72) shows the three types of electron microscopy used in this project; scanning electron microscopy (SEM), transmission electron microscopy (TEM) and scanning transmission electron microscopy (STEM). All three types involve the same basic steps to obtain images/micrographs and spectra (71, 72) i.e. (i) an electron beam is accelerated to a high energy from the electron source towards a sample; (ii) the beam is condensed and aligned to produce either a focussed probe (SEM and STEM) or a parallel beam (TEM); (iii) the incident beam interacts with the sample, which results in several signals (Figure 3.5) including electron scattering, transmission and absorption; and (iv) the signals are detected to give a micrograph or spectrum (in the case of energy dispersive X-ray spectroscopy (EDX) and electron energy-loss spectroscopy (EELS).

SEM is typically used for surface analysis, whereby the electrons probe (a few nm in size) raster scans over a region of the sample and images are serially generated from backscattered electrons (BSE) and secondary electrons (SE) (Figure 3.5) (72). TEM and STEM require thin (<100 nm) samples to allow for electron transmission (71). The main difference between the two techniques is that conventional TEM utilises a parallel beam that images a region of interest as a whole, whereas STEM involves a fine focused beam (~0.1 nm) that raster scans across the sample imaging in a serial manner (71). The main advantage of using STEM for sensitive samples such as calcium carbonate and overbased detergents is that there is the potential for less radiation damage through superior dose control and efficient imaging (73).

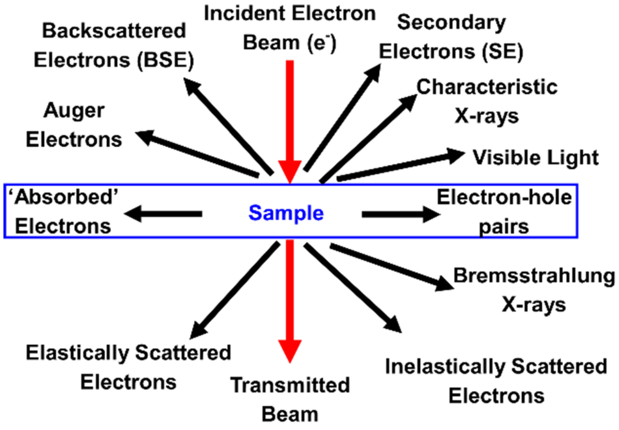

Figure 3.5. Summary of the signals generated when a high-energy electron beam interacts with a thin sample (71, 72).

Scanning Electron Microscopy (SEM). SEM was used to determine the morphologies of synthetic calcium methoxide (chapter 5), crystalline carbonates (chapter 5) and the post-carbonation products (chapter 6). The powdered samples were coated with 15 nm of iridium and analysed using a Hitachi SU8230 microscope operated at 2.0 kV. The images were processed and analysed using the ImageJ software (74). Cryo-SEM was used to characterise the 90 mol% sol-gel (chapter 6). The gel was frozen in liquid nitrogen, cleaved and analysed using a Thermo Fisher Scientific Helios G4 CX DualBeam™ microscope operated at 1.0 kV.

Transmission Electron Microscopy (TEM). The morphology and crystallinity of the overbased detergents were studied using low-dose TEM and STEM. The colloidal detergent oil dispersions were purified *via* dialysis in hexane (17, 19, 45, 46). A few drops of the diluted sample were deposited onto ultrathin (~3 nm) amorphous carbon support films (Agar Scientific), prior to ozone cleaning in a Hitachi Zone SEM. All TEM and STEM measurements were performed on a FEI Titan^3 Themis operated at 300 kV, using a FEI double tilt low background analytical holder. Conventional TEM imaging used a Gatan OneView CCD camera with beam currents of 0.5 to 1 nA. STEM measurements were taken with a 10 pA probe current at a camera length of 460 mm, the probe convergence angle was 10 mrad. This gave collection angles of 7 mrad for bright field imaging, and 17 to 100 mrad for annular dark field (ADF) imaging. STEM images were acquired using a pixel size of 81.7 pm and a dwell time of 10 μs. The resulting total fluence per scan was 9.4×10^5 $e^- nm^{-2}$ which is ~3% of the measured damage threshold of calcite nanoparticles (73). The bright field collection angle of 7 mrad provides phase contrast images with a moderate electron collection efficiency of 25%, allowing for lattice resolution imaging (75). The collection angles of the ADF detector provide contrast for crystalline and amorphous scattering, where bright features are indicative of crystalline scattering, or thickness based scattering from amorphous materials.

3.4.2 X-ray Scattering/Diffraction

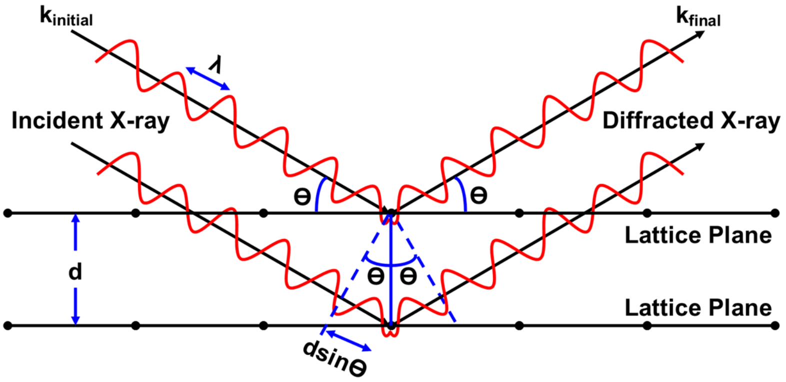

Figure 3.6. Schematic illustrating diffraction/scattering of two parallel incident X-ray beams. Highlighted are the wavelength (λ), scattering angle (θ), incident ($k_{initial}$) and scattered (k_{final}) wavefactors and lattice spacing (d).

Background. X-ray scattering/diffraction is a commonly used analytical technique for determining the atomic structure of complex solid materials. Powder X-ray diffraction (PXRD) has conventionally been used to elucidate the average long-range structure of ordered crystalline compounds such as calcite, aragonite and vaterite. PXRD data is defined by the constructive interferences of scattered X-rays passing through a sample (illustrated in Figure 3.6). PXRD data can be represented by Bragg's Law (76) that states:

$$n\lambda = 2d\sin\theta \qquad [3.1]$$

Where n is a positive integer, λ is the wavelength of the incident wave, d is the spacing between lattice planes and θ is the scattering angle. λ can also be written in terms of momentum transfer (Q) (77-79) i.e.

$$\lambda = \frac{4\pi\sin\theta}{Q} \qquad [3.2]$$

Since Q is a function of the incident ($k_{initial}$) and scattered (k_{final}) wavefactors (Figure 3.6), equation 3.2 can also be represented as (77-79):

$$\lambda = \frac{4\pi\sin\theta}{k_{initial} - k_{final}} \qquad [3.3]$$

Notably, conventional PXRD is limited to determining the long-range structure of ordered crystalline materials based on the intensities and positions of Bragg peaks (79). Disordered, non-crystalline and nano-sized materials, such as amorphous calcium carbonate (ACC) and overbased detergents, tend to display non-definitive broad diffuse maxima (61, 80, 81). As such, these materials are typically analysed using techniques that provide short-range order information e.g. extended X-ray absorption fine structure (EXAFS). However, diffuse X-ray scattering also provides information about short to medium-range local structure (up to ~20 Å) (77-79). Most laboratory facilities use Cu-Kα radiation sources where λ = 1.54 Å and the maximum Q is ~8 Å (79), which limits the accuracy of the diffuse scattering information. Conversely, high energy X-ray synchrotron sources utilise relatively shorter wavelengths and thus provide more accurate structural information.

Two-dimensional experimental diffraction data can be calibrated and integrated to produce the one-dimensional total scattering structure function S(Q), which is defined as (67, 77, 78):

$$S(Q) = \frac{\frac{1}{N}\frac{d\sigma_X}{d\Omega}(Q) - \sum c_i |f_i(Q)|^2}{|\sum c_i f_i(Q)|^2} + 1 \qquad [3.4]$$

Where the terms $(1/N)(d\sigma_x/d\Omega)$ are collectively defined as the scattering cross-section and for an atom i c_i and f_i are the atomic concentration and X-ray form factor respectively. The intensity of S(Q) is a function of scattering from Bragg peaks (long-range structure), elastic diffuse scattering (static local structure) and inelastic scattering from moving atoms (atom dynamics) (77-79). Fourier transformation of the S(Q) diffuse scattering gives the X-ray pair distribution function (XPDF) G(r), which is defined by the following equation (67, 77, 78):

$$G(r) = \frac{2}{\pi} \int_{Q_{min}}^{Q_{max}} Q[S(Q) - 1] \sin(Qr)\, dQ \qquad [3.5]$$

Where Q_{min} is the cut-off point for small-angle X-ray scattering and Q_{max} is the upper limit (usually about 20 $Å^{-1}$) for the medium-range (77, 78). Notably, the peaks observed in XPDF plots provide information about the average local structure such as interatomic distances (peak positions), coordination number (integrated peak intensity) and static/dynamic atom disorder (peak width).

Powder X-ray Diffraction (PXRD) Measurements (Chapters 5 to 8). PXRD was performed using a PANalytical X'Pert-Pro powder X-ray diffractometer with Cu-Kα radiation (λ = 1.54056 Å) operated at 40 kV and 40 mA. Powdered samples were placed on a zero-background silicon sample holder and scanned over a 2θ range of 5 to 80° at a scan rate of 0.08° min^{-1} and step size of 0.03°. PXRD data were processed and analysed using the PANalytical HighScore Plus software (82) and model structures from the American Mineralogist Crystal Structure Database (AMCSD) and Inorganic Crystal Structure Database (ICSD) (83).

Total X-ray Scattering Measurements (Chapter 5). High-energy total X-ray scattering data were collected at Diamond Light Source on beamline I15-1 (Energy = 77 keV; Wavelength = 0.161699 Å) up to a scattering wavevector (Q) of 50 $Å^{-1}$. Two-dimensional experimental diffraction data were calibrated and integrated using DAWN (84) to produce S(Q). The XPDF G(r) plots were then obtained by Fourier transformation of S(Q) using GudrunX (85). Theoretical XPDF Fourier transforms were calculated using PDFgui (86) and crystallographic model structures obtained from AMCSD (87) and ICSD (83). These structures included the nine summarised in Table 3.2. For each structure refinement, the fitting range was fixed at 0.5 – 15 Å while variables associated with the experimental data and reference crystal structure were allowed to float. These variables included the data scale (d_{scale}) and resolution (Q_{damp}) factors, as well as the crystal structure lattice constants (a, b and c) and isotropic atomic displacement parameters (similar to Debye-Waller factors in EXAFS). The refined XPDF plots were used to calculate bond distances (r) of neighbouring atoms using the Gaussian function in Fityk (88).

Table 3.2. Summary of lattice parameters of model crystallographic structures used for XPDF analysis of calcium oxide (CaO), hydroxide ($Ca(OH)_2$), methoxide ($Ca(OCH_3)_2$), calcite ($CaCO_3$-α), aragonite ($CaCO_3$-β) and vaterite ($CaCO_3$-γ).

Compound	**Space Group**	**Lattice Parameters** a	 b	 c	**Reference**
CaO	Cubic – *Fm-3m*	4.81	4.81	4.81	Wong-Ng *et al.* (89)
$Ca(OH)_2$	Hexagonal – *P-3m1*	3.59	3.59	4.88	Busing and Levy (90)
$Ca(OCH_3)_2$	Hexagonal – *P-3m1*	3.64	3.64	8.31	Staeglich and Weiss (91)
$CaCO_3$-α	Rhombohedral – *R-3c*	4.98	4.98	17.02	Markgraf and Reeder (20)
$CaCO_3$-β	Orthorhombic – *Pnma*	5.74	4.96	7.97	Pilati *et al.* (92)
$CaCO_3$-γ	Orthorhombic – *Pbnm*	4.13	7.15	8.48	Meyer (93)
	Orthorhombic – *Ama2*	8.47	7.16	4.13	Le Bail *et al.* (94)
	Hexagonal – *P6₅22*	7.29	7.29	25.30	Wang and Becker (27)
	Monoclinic – *C1_2*	12.17	7.12	25.32	Demichelis *et al.* (95)

3.4.3 Mid Infrared (Mid-IR) Spectroscopy

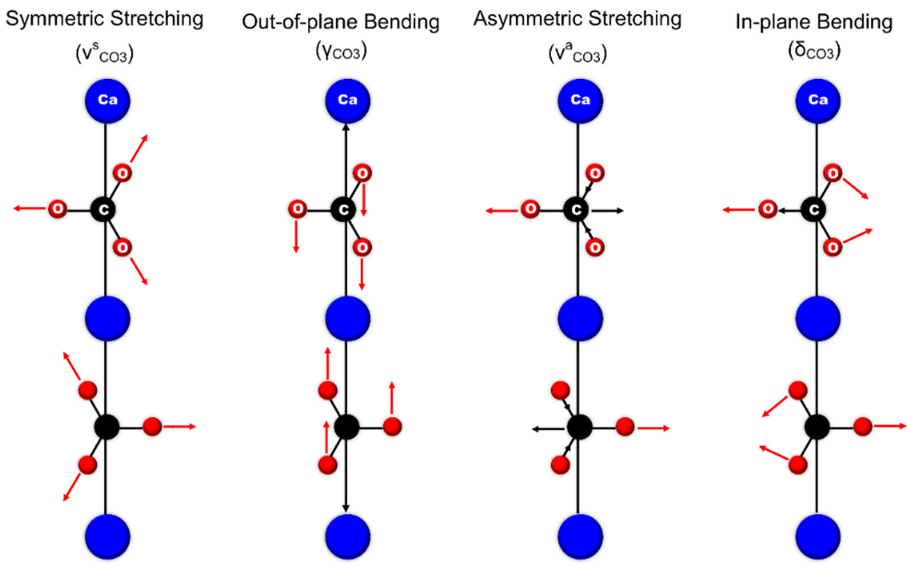

Figure 3.7. Schematic of the four fundamental vibrational frequencies – symmetric stretching (ν^s), asymmetric stretching (ν^a), in-plane bending (δ) and out-of-plane bending (γ) – of the CO_3^{2-} in calcite ($CaCO_3$-α) (23).

Background. Mid-IR spectroscopy is an analytical technique used to characterise molecular structures of gas, liquid and solid materials based on their interactions with infrared radiation in the 4000 to 400 cm^{-1} electromagnetic region. Infrared radiation absorption is due to the vibrational motion of molecules. Notably, an isolated trigonal

CO_3^{2-} anion (point group: *6-2m*) has six permissible modes of vibration of which only three to four are observable in IR and Raman spectra (96, 97). The vibrational frequencies observed pertain to (i) non-degenerate symmetric stretching (ν^s_{CO3}) at 1063 cm^{-1} (Raman only); (ii) non-degenerate out-of-plane bending (γ_{CO3}) at 879 cm^{-1} (IR/Raman); (iii) double-degenerate asymmetric stretching (ν^a_{CO3}) at 1415 cm^{-1} (IR/Raman); and (iv) double-degenerate in-plane bending (δ_{CO3}) at 680 cm^{-1} (IR/Raman). Crystallisation leads to the lowering of the CO_3^{2-} site symmetry and thus leads to the splitting of double-degenerate features and appearance of IR inactive peaks (96, 97). Figure 3.7 shows the four fundamental vibrations of the CO_3^{2-} anion present in calcite (23), which has a site symmetry of *32* (*cf.* section 5.3).

There are various configurations that can be used to obtain mid-IR data depending on the properties of the sample such as thickness/size, homogeneity and reflectivity (98). Considering the multiple variables involved in the systems studied in this project (chapters 5 to 8), e.g. size (nano- to micro-scale) and phase (gas, liquid and solid), the attenuated total reflectance (ATR) configuration (Figure 3.8) was chosen. The main advantages of ATR are easy sample preparation, spectral reproducibility and a higher sensitivity to surfaces (98). This final attribute makes it an ideal analytical technique for determining subtle differences in the composition of the nano-sized overbased detergents as a function of time. As can be seen in Figure 3.8, the ATR configuration requires the sample to be in contact with the crystal because the penetration depth (D_p) of the evanescent wave is limited. Total reflection of the IR beam is dependent on the IR incidence angle (Θ_i) being greater than critical angle ($\Theta_c = \sin^{-1}(n_2/n_1)$) i.e. the refractive index of the crystal (n_1) has to be greater than that of the sample (n_2) (98, 99). The experiments in this thesis utilised zinc selenide (ZnSe) crystals with n_1 – 2.42, Θ_i – 45 degrees and D_p – 40 μ (maximum) (98).

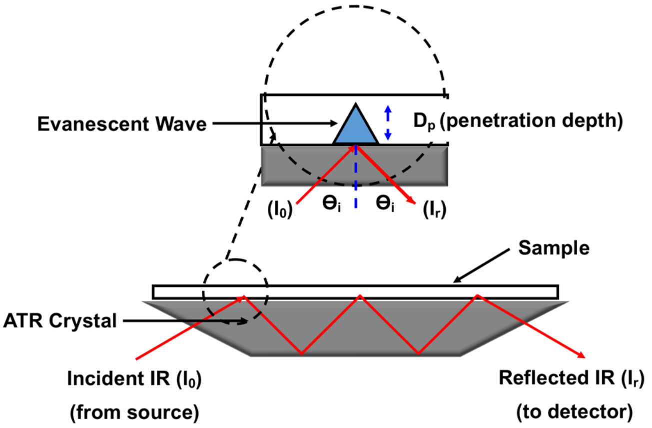

Figure 3.8. Schematic of the attenuated total reflectance (ATR) mid-IR spectroscopy configuration.

***Ex situ* Mid-IR Measurements (Chapters 5 to 8).** Fourier transform mid-IR spectra were collected for powdered samples using Perkin Elmer Spectrum 100 and Thermo Fisher Nicolet 10 iS10 spectrometers each equipped with a ZnSe attenuated total reflectance (ATR) crystal. All spectra are an average of 4 scans obtained at a resolution of 4 cm^{-1} and scan speed of 0.1 cms^{-1} from 4000 to 650 cm^{-1}. Background spectra of a powder-free ATR crystal surface were collected and subtracted from each spectrum using the Perkin Elmer Spectrum 10 and Thermo Fisher OMNIC software.

In-line Mid-IR Measurements (Chapters 7 and 8). ATR mid-IR spectra were collected from 4000 to 650 cm^{-1}. A Bruker Alpha FTIR spectrometer equipped with a DPR 210 ZnSe probe (Hellman Analytics) was used for the *in situ/operando* time-resolved measurements of the various aqueous and/or non-aqueous dispersions. The *in situ/operando* FTIR spectra were acquired from 64 scans each. All experiments were performed at a resolution of 4 cm^{-1}. The measurements were controlled and processed remotely on a computer using the OPUS 7.0 software and analysed using Fityk 1.3.1 curve fitting software (100).

3.4.4 X-ray Absorption Spectroscopy (XAS)

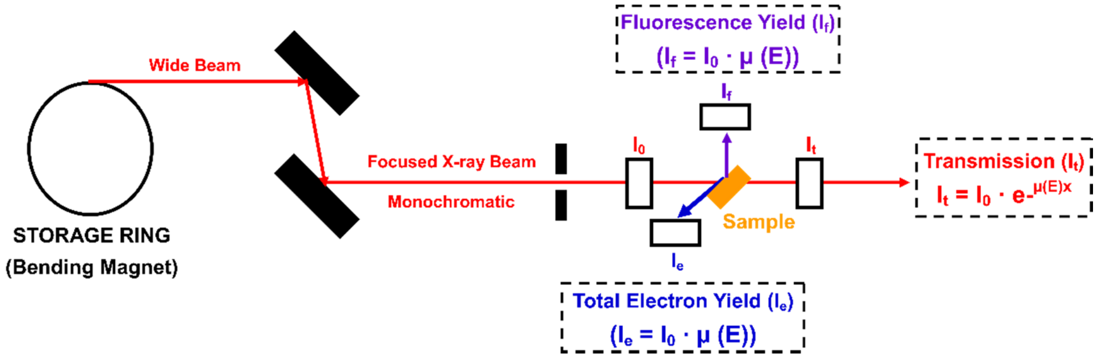

Figure 3.9. Schematic of X-ray absorption spectroscopy (XAS) synchrotron setup. Highlighted are the three X-ray absorption detection modes: transmission (I_t), fluorescence yield (I_f; FY) and total electron yield (I_e; TEY).

Background. X-ray absorption spectroscopy (XAS) is based on measuring the absorption coefficient ($\mu(E)$) for a specific sample as a function of photon energy (E) (101, 102). $\mu(E)$ decreases inversely with E and can be approximated based on sample density (ρ), atomic number (Z) and atomic mass (A) (103). However, this coefficient is more generally defined in terms of incident beam intensity (I_0), transmission intensity (I_t) or fluorescence yield (I_f; FY) or electron yield (I_e; TEY), and sample thickness (x) (Figure 3.9) (63). The detection mode used for measurements is usually determined by sample thickness and homogeneity (63). The solid calcite XAS spectrum in Figure A.2 (Appendix A) shows that transmission and FY are more prone to distortions and reduction of the edge intensity/fine structure amplitude than TEY when probing concentrated and non-homogenous samples. These variations are due to increased sample thickness, which leads to less transmitted X-rays (transmission mode) and 'self-absorption effects' (FY mode) (103, 104). Hence, in this project, solid reference *ex situ* spectra (chapters 5 to 8) were obtained in TEY mode and *in situ/operando* (chapters 7 and 8) analysis was performed on dilute dispersions using FY. Notably, the feasibility of *in situ/operando* TEY measurements on concentrated dispersions was also explored (Figure B.3 in Appendix B). Optimisation of the TEY setup is currently underway as part of a follow-on project.

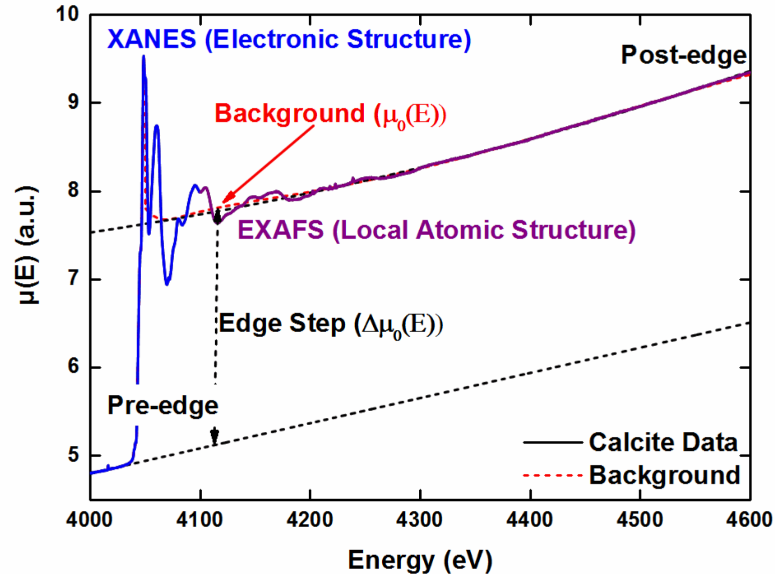

Figure 3.10. A Ca K-edge X-ray absorption spectrum of solid calcite ($CaCO_3$-α) highlighting the X-ray absorption near-edge structure (XANES) and extended X-ray absorption fine structure (EXAFS) regions.

The photon energy can be tuned to obtain μ(E) at a sample-dependent absorption edge, which in this case is the Ca K-edge (~4038.5 eV). Spectral variations in μ(E) beyond the edge (Figure 3.10) are dependent on the excitation and/or ejection of core shell electrons into unoccupied orbitals or vacuum continuum. An XAS spectrum (Figure 3.9) is typically composed of two regions i.e. the X-ray absorption near-edge structure (XANES) and extended X-ray absorption fine structure (EXAFS). The XANES region is defined by the oxidation state of the element being probed and its coordination chemistry (63). It is usually evaluated qualitatively in terms of electron transitions(Figure 3.11a). The main features in the Ca K-edge XANES region (Figure 3.11b) are determined by electronic transitions from the 1s (K) core state to the unoccupied 4p (N) states (105). Notably, ejection of photoelectrons into the continuum leads to occurrence of EXAFS. The EXAFS region provides information about local structure and bonding in crystalline and non-crystalline materials (63). Information about the coordination number of neighbouring atoms, bond distances and the degree of disorder can be obtained quantitatively.

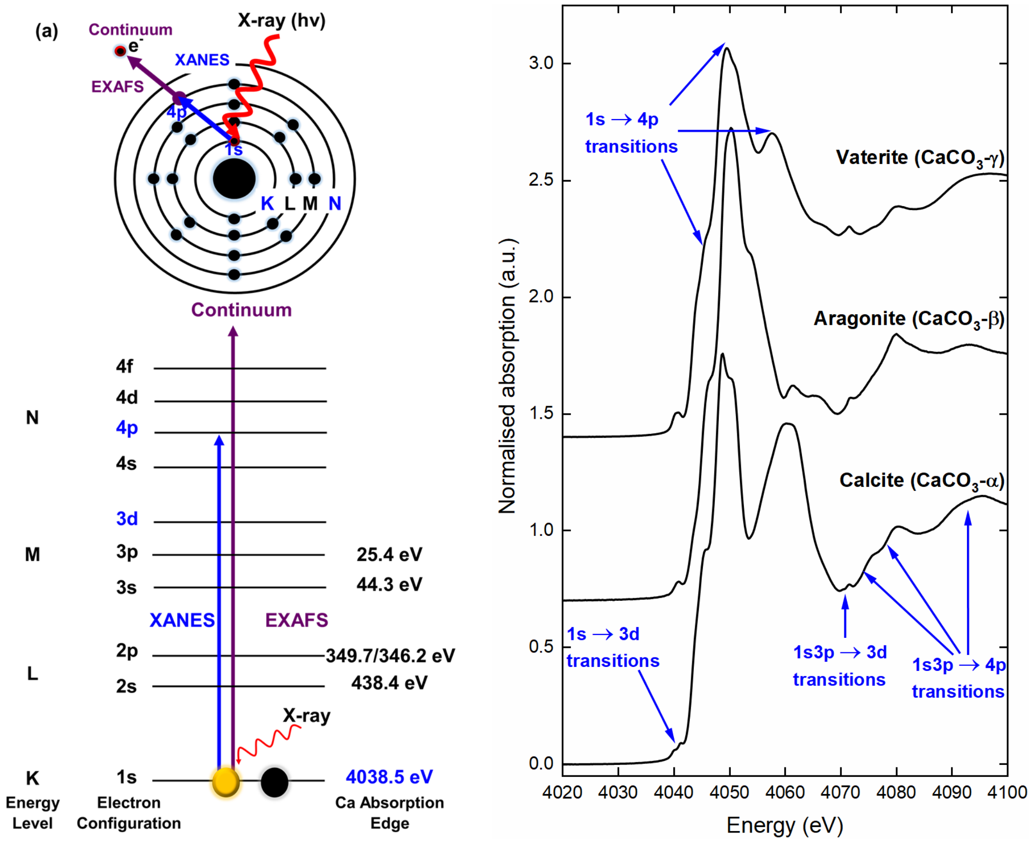

Figure 3.11. (a) Schematic showing the electronic transitions (1s to 4p) that contribute to the XANES in relation to the features observed in the (b) Ca K-edge spectra of crystalline $CaCO_3$ polymorphs.

The EXAFS region is defined by constructive and destructive interferences of the absorbing (Ca) atom photoelectron waves and backscattering from neighbouring atoms (e.g. O and C in $CaCO_3$) (Figure 3.12). EXAFS can be defined in terms of the structure function χ (E) (62, 63):

$$\chi(E) = \frac{\mu(E) - \mu_0(E)}{\Delta\mu_0(E)} \qquad [3.6]$$

Where μ(E) is the absorption coefficient, $\mu_0(E)$ is the background function and $\Delta\mu_0(E)$ is the edge step (Figure 3.10). However, the EXAFS is typically defined in terms of the photoelectron wave factor (k) which is defined as (62, 63):

$$k = \sqrt{\frac{2m\,(E - E_0)}{\hbar^2}} \qquad [3.7]$$

Where E_0 is the absorption edge energy, m is the electron mass, and ħ is Planck's constant. Assuming the EXAFS is dominated by single scattering contributions (Figure 3.11b), the EXAFS equation is usually written as (63, 107):

$$\chi(k) = \sum_j \frac{S_0^2 N_j f_i(k) e^{-\sigma_j^2 k^2} e^{-2R_j/\lambda(k)}}{k(\Delta r + R_j)^2} \sin\left[2k\left(\Delta r + R_j\right) + \delta_j(k)\right] \qquad [3.8]$$

The EXAFS oscillations (χ (k)), as shown in equation 3.8, are a function of the coordination number of neighbouring atoms (N_{atom}), the distances of these neighbours from the absorber atom (R), and the degree of thermal or static disorder present around the absorber atom (defined by the Debye-Waller factors (σ^2)) (107). Whereas these parameters provide information about the crystal structure, the other parameters in the equation pertain to the photoelectron in relation to the absorber and backscattering atoms (19). Where S_0^2 is the amplitude reduction factor, f (k) is the backscattering amplitude of the neighbouring atoms, and δ (k) is the phase shift of the ejected and backscattered photoelectron (19, 63). It is important to note that the EXAFS x-axis R is a sum of the real interatomic distances (r; the XPDF x-axis) and δ(k) due to scattering (101, 102, 108).

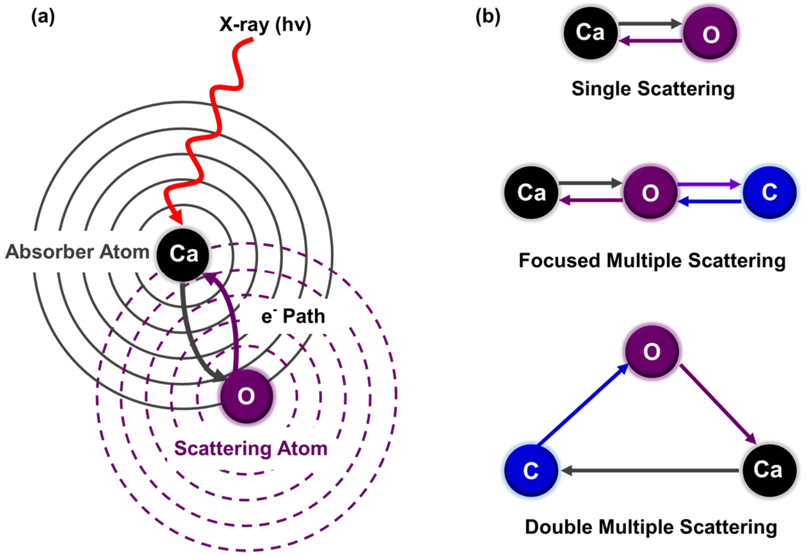

Figure 3.12. Schematic showing (a) the photoelectron scattering event that defines the extended X-ray absorption fine structure (EXAFS) and (b) examples of simple scattering paths (63, 106).

Notably, XAS is very sensitive to changes in process chemistries because it probes local molecular structure around X-ray absorbing atoms and can thus be applied to both ordered and disordered materials, including gas, liquid and solid systems. Unlike PXRD, its structure sensitivity is not limited by lack of crystallinity. It is also much less impacted by the presence of solvents or other media that may mask the desired information as is the case with IR and Raman spectroscopy (109, 110). It provides both qualitative and quantitative element specific information about the physical and chemical attributes of a material. For example, in the case of crystallizing systems, information that can be obtained includes kinetic and mechanistic information of nucleation, crystallisation or dissolution, crystal structure and polymorphic form, nanoparticle size, solid composition and solute concentration (109, 111, 112). XAS requires an X-ray source with tuneable photon energy, which is currently available almost exclusively at synchrotron radiation facilities. This has limited the use of XAS on industrial systems and hence its consideration as a PAT tool. However, affordable portable bench-top XAS systems using laboratory X-ray sources are now becoming available (113), opening up a realistic potential for using XAS under manufacturing conditions.

XAS Data Collection. XAS experiments were carried out at B18, a beamline at Diamond Light Source, using the Ca K-edge (4038.5 eV) (114). A Si (111) double crystal monochromator was used and the 3 GeV synchrotron facility was operated at a current of 300 mA. The beam size was 800 μm in height and 600 μm in width.

Table 3.3. Summary of reference interatomic distances (r_{ref}) and coordination numbers ($N_{O/C/Ca}$) for the model crystallographic structures used for the EXAFS analysis of calcium oxide (CaO), hydroxide ($Ca(OH)_2$), methoxide ($Ca(OCH_3)_2$), calcite ($CaCO_3$-α), aragonite ($CaCO_3$-β) and vaterite ($CaCO_3$-γ).

Compound	**Space Group**	**1st Shell**		**2nd Shell**		**3rd Shell**		**4th Shell**	
		N_O	r_{ref} (Å)	$N_{O/C/Ca}$	r_{ref} (Å)	$N_{O/C}$	r_{ref} (Å)	N_{Ca}	r_{ref} (Å)
CaO	*Fm-3m* (89)	6 O	2.41	12 Ca	3.41	8 O	4.17	6 Ca	4.82
$Ca(OH)_2$	*P-3m1*(90)	6 O	2.37	6 Ca	3.59	12 O	4.29	2 Ca	4.88
$Ca(OCH_3)_2$	*P-3m1* (91)	-	-	-	-	-	-	-	-
$CaCO_3$-α	*R-3c* (20)	6 O	2.36	6 C	3.21	6 O	3.46	6 Ca	4.05
$CaCO_3$-β	*Pnma* (92)	9 O	2.51	3 C	2.92	3 C	3.24	6 Ca	3.89
$CaCO_3$-γ	*Pbnm* (93)	6 O	2.44	3 C	2.82	3 C	3.25	6 Ca	4.13
	Ama2 (94)	6 O	2.28	3 O	2.82	3 C	3.26	6 Ca	4.13
	P6$_5$22 (27)	6 O	2.36	3 O	3.15	3 C	3.24	6 Ca	4.22
	C_2 (95)	6 O	2.31	3 O	2.74	3 C	3.19	6 Ca	4.16

***Ex situ* XANES and EXAFS Measurements (Chapters 5 to 8).** Total electron yield (TEY) Ca K-edge X-ray absorption spectra for calcium-containing solids and oil-based samples were collected from 4000 – 4600 eV. For each reference sample, a total of 10 spectra were acquired. Measurements were acquired at room temperature under a helium environment. Background subtraction and normalization to an edge-step height of 1 (*cf.* Figure 3.9) of the experimental data was done using Athena. This program, along with Artemis and Hephaestus, is available as part of the free Demeter software package for analysis of XAS data (62). Fourier transform (FT) extended X-ray absorption fine structure (EXAFS) were extracted over a k-range of 3-10 Å^{-1} with a k-weight of 3. Theoretical EXAFS scattering paths were calculated using ATOMS and FEFF6 in Artemis. Theoretical Fourier transforms were obtained by fixing $S0_2$ at 0.7 and floating R, N_{atom}, σ_2 and zero-energy correction (ΔE_0) values for all coordination shells around a central, X-ray absorbing, Ca atom. Experimental EXAFS data were fit using the crystal structure models summarised in Table 3.3.

***In situ* and *Operando* XANES Measurements (Chapters 7 and 8)**. XANES spectra were collected every minute during each stage of the reactive crystallisation and overbasing process for a duration of ~1 hour and ~4.5 hours respectively. 10 scans were taken before and after carbonation. These *in situ* XAS data were collected in fluorescence yield (FY) using a 4-element SII Vortex silicon-drift detector with XSPRESS3 electronics. All experimental data were processed and analysed using Athena (62). Linear combination fitting (LCF) was performed on the *in situ* spectra over a range of 4020 to 4090 eV. *Ex situ* spectra of the calcium hydroxide, calcite, aragonite, vaterite, amorphous calcium carbonate and calcium di-methylcarbonate, neutral calcium sulphonate surfactant and overbased calcium sulphonate detergent reference samples were used as standards for the LCF.

Chapter 4:
Development of *In Situ/Operando* Spectroscopic Techniques

4.1 Introduction

Process analytical chemistry (PAC) tools monitor changes in the physicochemical properties during industrial synthetic processes *operando* and are part of any process analytical technology (PAT) strategy (109, 115). PAT tools provide crucial information about the relationship between reagents and in-process materials with the desired product (109, 115). Specifically, PAT identifies, measures and monitors critical quality attributes (CQA) of a process in relation to the quality and performance of the final product. Analytical techniques such as mid-infrared (mid-IR), Raman, and ultraviolet-visible (UV-vis) spectroscopies as well as powder X-ray diffraction (PXRD) are the main *in situ/operando* PAT analysis tools across the fine chemicals and oil industries (109, 111, 116). The information provided by X-ray absorption spectroscopy (XAS) fills gaps in the information provided by these techniques. This combined with other strengths of the technique outlined below for probing complex chemical systems make XAS a potential PAT tool in R&D.

The work described in this chapter is concerned with the development of a new PAT system for simultaneous *in situ/operando* XAS and mid-IR monitoring of multiphase multicomponent processes. The three main components of this system are: (i) a conventional glass reactor for lab-based synthetic reactions equipped with the capability to control temperature, gas flow and mixing; (ii) a bespoke liquid-jet cell for on-line XAS measurements (117); and (iii) a commercial in-line mid-IR attenuated total reflectance (ATR) probe. The system permits real-time probing of bulk solutions/dispersions using XAS and mid-IR to determine changes in local atomic environments due to reactions and/or changes in process conditions. Data documenting the real-time evolution of Ca speciation during the synthesis of calcium carbonate ($CaCO_3$) and overbased calcium sulfonate detergents are presented in chapters 6 and 7 respectively. The studies highlights the sensitivity of XAS to the crystal structure of calcium-containing materials in dilute dispersions, which becomes evident through the *in situ/operando* X-ray absorption near-edge structure (XANES) in the spectra. The work presented here is a result of collaborative work with various people from the University of Leeds, Diamond Light Source and Infineum UK Ltd. Notably, Sin-Yuen Chang (Leeds/Diamond) and Giannatonio Cibin (Diamond), Elizabeth A. Willneff (Leeds) and Sven L.M. Schroeder (Leeds/Diamond) were instrumental in the development of the XAS liquid-jet cell. Whereas Colin J. Willis, Paul Wilson and Peter J. Dowding from Infineum helped incorporate the lab-scale reactor system and mid-IR into the setup.

4.2 XAS Liquid-jet Cell

Substantial progress has been made with *in situ* XAS instrumentation for probing heavy elements such as gold, palladium and platinum (mostly in catalysis (103, 118) and electrochemistry (112, 119-125)) with hard (> 5 keV) X-rays or low atomic elements (e.g. carbon, oxygen and nitrogen) (126, 127) with soft (< 1 keV) X-rays. End stations for tender X-rays (1-5 keV) suitable for probing elements such as calcium, magnesium and titanium are well less developed. One of the identified challenges that has hampered the advancement of tender X-ray experiments is the lack of flexibility of existing soft and hard X-ray beamlines to accommodate energy ranges above 2 keV (soft X-rays) and less than 5 keV (hard X-rays) (128). This is in part due to sample environment, whereby the sample chambers for soft and hard X-ray facilities are designed for vacuum and air environments respectively. This has made it difficult to perform *in situ* XAS studies at the Ca K-edge on $CaCO_3$ (129). Notably, Politi *et al.* (57) and Zhang *et al.* (130) have performed *in situ* Ca K-edge XAS experiments on amorphous calcium carbonate (ACC) and calcium phosphate respectively.

In situ XAS experiments rely on suitable sample cells for introduction of the sample into the incident X-ray beam and detection of emitted photons or electrons in the case of FY or TEY measurements respectively. Transmission XAS is difficult for *in situ* experiments at soft/tender X-ray energies because of the combination of lower energy X-rays with concentrated sample environments attenuates too much of the incident X-ray beam. Various sample cells for the analysis of liquids and solutions/dispersions under reaction conditions with X-rays have been reported in the literature. The most prevalent cell types were the droplet and liquid flow cells (126, 127, 131-135). For example, a levitating droplet cell has been used to study of the formation of $CaCO_3$ with WAXS (131) and Au nanoparticles by XAFS/SAXS (132). However, limitations such droplet instability, insufficient reactant gas diffusion, and beam induced radiation damage and/or crystallisation were identified. To overcome some of these problems liquid-jet flow cells have also been developed to study, for example, Au nanoparticle formation with SAXS (133), XAS of Au nanoparticles (134) and XAS of water at the O K-edge (126). The liquid-jet reduces the risk of beam damage by continuously introducing fresh sample to the focal point of the incident X-ray beam and tries to closely mimic the true sample environment by using a separate reaction vessel for e.g. control of mixing and temperature.

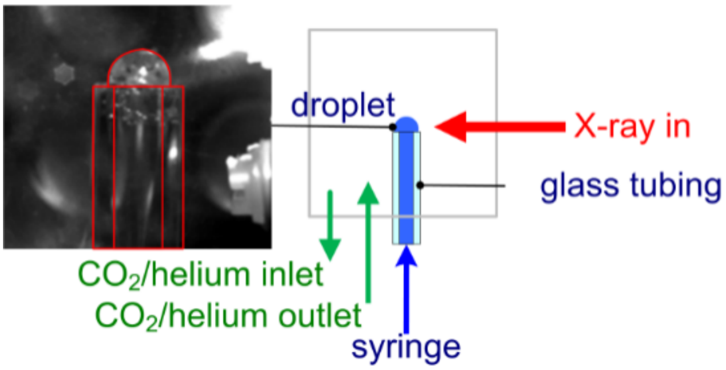

Figure 4.1. Picture/schematic of the droplet configuration of the cell developed for *in situ/operando* X-ray absorption spectroscopy measurements – courtesy of Sin-Yuen Chang (117).

In this project, the first prototype was a droplet cell (Figure 4.1) (117, 121, 124). However, the control of non-aqueous dispersions involving volatile solvents was not trivial and made more difficult by the introduction of additional variables. The challenges included control of non-ambient temperatures and saturation of the gas phase with solvent to counteract evaporation of solvent from the droplet. The multiphase gas-liquid-solid systems studied were difficult to achieve and/or maintain in a droplet. It was also challenging to maintain the desired phase interaction/miscibility when in some cases the liquid comprised of two immiscible solvents and ensure reactant gas diffused into the droplet. In light of these challenges, we chose to build a continuous-flow cell informed by previous liquid-jet instrumentation. The cell presented here was built for *in situ* and *operando* fluorescence yield (FY) and (potentially) total electron yield (TEY) XAS measurements with hard and tender X-rays on aqueous and non-aqueous dispersions. The same sample cell is also suitable for *ex situ* characterisation of solids (Figure B.2 in Appendix B) in all three detection modes.

Liquid-jet Cell Components. The cell consists of three main components (Figure 4.2): (a) a stainless steel ConFlat 6-way cube sample chamber (40 x 40 x 40 mm^3) with a controlled He environment accommodates sample flow in the vertical direction from top to bottom, transmission of the X-ray beam in the horizontal direction from right (I_0) to left (I_t) and fluorescence-yield (I_f) XAS *via* a detector placed perpendicular to the path of the X-ray beam; (b) a glass tube (inner diameter = 0.8 mm) to create the liquid-jet which is collected by (c) a glass funnel (diameter = 25 mm) for recycling back to the reactor.

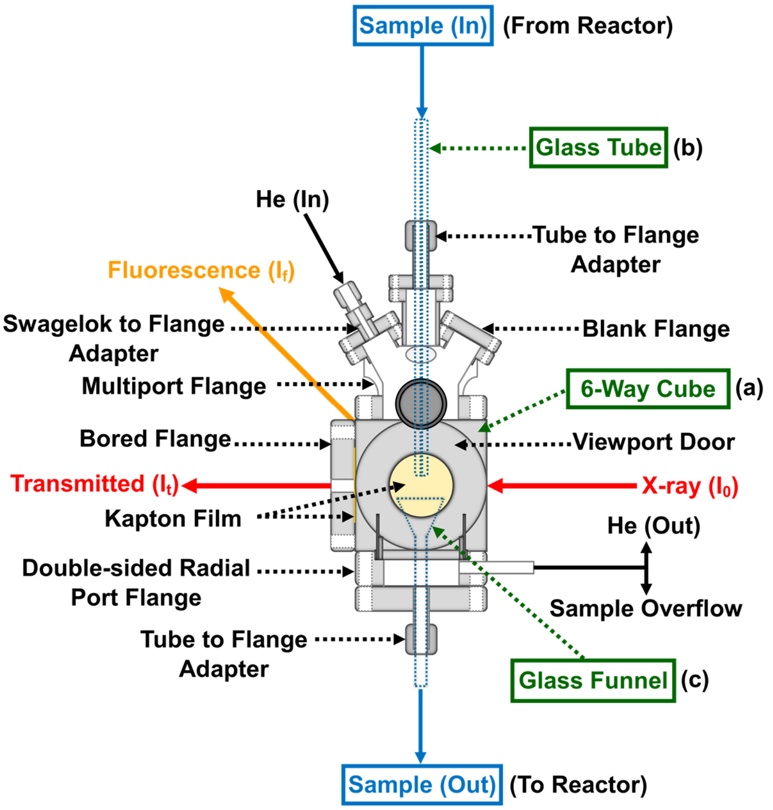

Figure 4.2. Detailed schematic of the liquid-jet cell used in the XAS PAT setup – shows the main cell components including the (a) stainless steel 6-way cube, (b) glass tube and (c) funnel (green). The entry and exit of the sample fluid (blue) and X-ray beam (red) are also highlighted.

The liquid-jet cell was connected to the reaction vessel *via* Viton^{TM} tubing attached to the ends of the glass tube and funnel. Viton^{TM} tubing was chosen to connect the baffled reactor to the sample-loop because it is sufficiently robust to tolerate the pressures induced by the high fluid flow and exposure to organic solvents over an extended period of time. The flow rate of sample through the liquid-jet sampling loop was regulated by digital flow controllers (FIC 3 and 5 in Figure 4.3) attached to the two peristaltic pumps. For the systems studied in this paper, a flowrate greater than 280 ml/min was required to create a steady liquid-jet stream ideal for XAS measurements. The high flowrate also ensured high turnover of the sample at the X-ray beam which minimised the potential for beam damage or X-ray radiation-induced reactions. All experiments were carried out under N_2 (reactor) and He (cell) environments. Notably, solid samples were brushed onto carbon adhesive tape (Agar scientific) that was loaded onto a stainless steel tube. This steel tube was interchangeable with the glass tube in the liquid-jet experimental setup for the *in situ* FY measurements.

Cell Design Considerations. The main factors which informed the design of the liquid-jet cell (Figure 4.2) are addressed individually below.

- Easy assembly, reproducibility and portability of the cell: The cell was constructed primarily from commercially available parts such as ConFlat (CF) vacuum parts, Kapton™ film and glassware. All flanges were sealed with Viton O-rings. A standard commercially available CF cube (Figure 4.2) was chosen as the central component of the sample chamber. The horizontal holes of the cube permitted the entry of the X-ray beam and exit of a transmitted beam (x-direction) and FY (z-direction) *via* kapton film windows. The only bespoke item in the cell was the glass funnel used to collect the liquid-jet stream. The liquid-jet was designed for operation at the endstation of beamline B18 at Diamond Light Source (UK) but its small size makes it portable. The use of standard parts permits modification to accommodate variations in sample geometry, which might be required for the cell to be used at other endstations such as the tender X-rays beamline 8-BM at the Brookhaven National Laboratory (128).
- Suitable for process conditions without significant modification: The cell should be able to accommodate actual reaction conditions without any or minimal modification. The process under investigation comprised alkali solutions and organic solvents. As such corrosion resistant materials were required for the cell components. With this in mind, stainless steel and borosilicate glass were chosen for wetted parts. However, the solids concentrations used in the process posed a risk of blockage in the glass tube (Figure 4.2b) and Viton ™ tubing connecting the external reactor to the in situ XAS cell. Therefore, the concentration of solids was reduced and the sample was recycled to the external reactor *via* a wide-mouth glass funnel (Figure 4.2c) to minimize blockage of wetted components after the liquid-jet. This concentration was also optimal for FY acquisition of X-ray absorption spectra because it was below the level at which self-absorption effects could distort the spectral features.
- Multi-modal use in terms of sample type, detection mode and X-ray energy range: Both solid samples and gas-liquid-solid dispersions could be analysed using XAS by exchanging the inlet tube (Figure 4.2b) used to introduce the sample into the X-ray beam. A glass tube was used to create a liquid-jet

(Figure 4.2b) from solid/liquid dispersions, while a steel tube was used as a sample stage onto which solid samples could be mounted with adhesive carbon tape (Figure A2 in Appendix A). The means of detecting the XAS spectrum was also flexible. Solid samples could in principle (depending on the sample composition) be analysed in all three detection modes i.e. transmission, FY and TEY (Figure A.2 in Appendix A). Liquid phase samples could be analysed with FY or TEY XAS. Furthermore, the cell design, including the geometry of the multiple ports in the sample cube, choice of window materials and ability to change the composition of the gas-phase in the sample cube, made it possible to collect XANES spectra of elements with X-ray absorption edges spanning the hard to tender region.

- Controlled sample environment: This was required to accommodate transmission of lower energy X-rays down to 4 keV (Ca K-edge) and ensure stability of the sample composition over time as it was recycled back to the reactor through the sample chamber and *via* the liquid-jet. The environment in the sample chamber could not contaminate the sample and had to minimize evaporation of volatile organic solvents. To achieve these aims, the sample cube was designed to accommodate gas flows of pure He or He saturated with organic solvent. Helium was chosen as the carrier gas because it only weakly absorbs X-rays and therefore would not reduce the incident beam intensity.
- Negligible radiation damage and disruption to the conventional synthesis process: The entire cell design was built around a continuous flow process for recycling the stock sample solution in the X-ray beam. Continual replenishment of the sample in the X-ray beam minimized the possibility of radiation damage to the sample. The volume of sample removed from the external vessel for introduction into the sample chamber was small relative to the total volume of solution in the vessel. This minimized the extent to which the process conditions were altered by XAS measurements with the liquid-jet from those of the conventional process.

4.3 *In Situ/Operando* XAS and Mid-IR PAT System

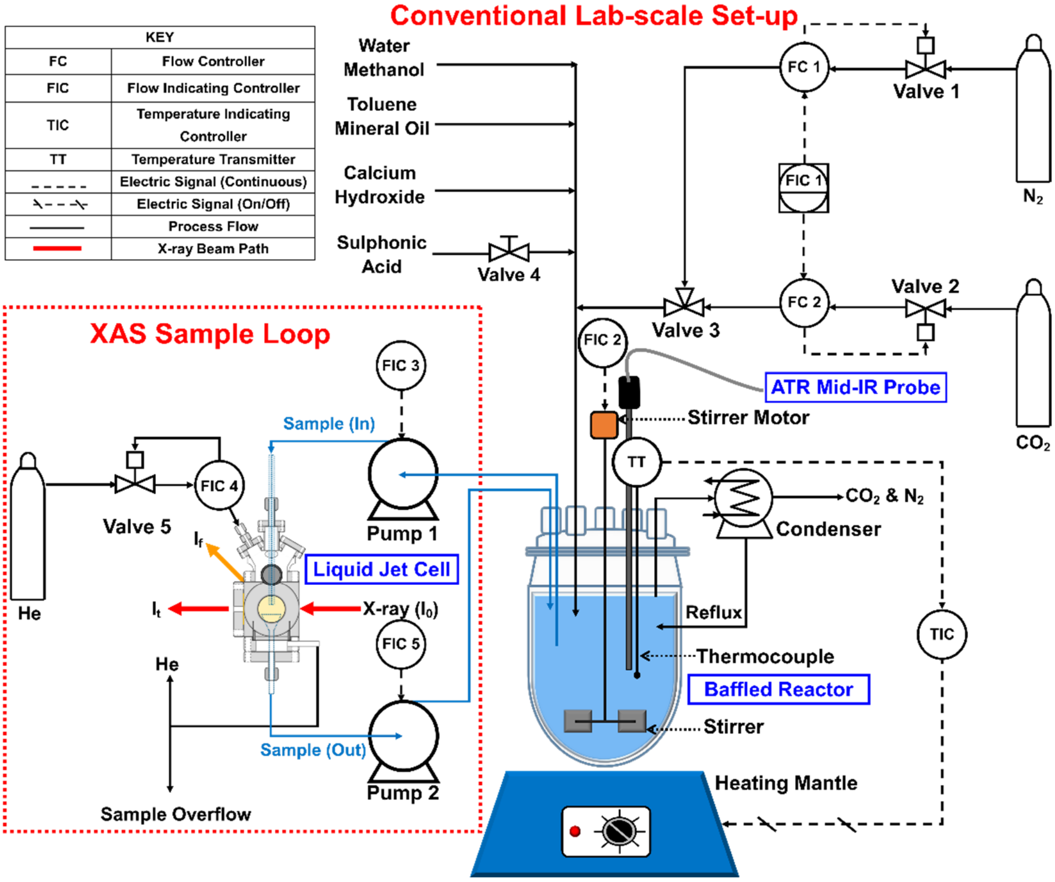

Figure 4.3. Piping and instrumentation diagram (P&ID) of the continuous-flow liquid-jet PAT experimental setup for simultaneous *in situ/operando* mid-infrared (mid-IR) and X-ray absorption spectroscopy (XAS) measurements.

Continuous-flow Liquid-jet PAT System. The PAT setup (Figure 4.3) consists of three main components i.e. the 1 L baffled reactor, liquid-jet cell (Figure 4.2) and mid-IR ATR probe. The baffled reactor contained the polyphasic dispersion in which the reactive crystallisation processes took place (detailed in sections 3.3.3 and 3.3.4). To monitor chemical state changes of calcium during the overbasing process with XAS in real-time with minimal disruption to the synthesis, a sampling loop *via* the liquid-jet cell was introduced to the baffled reactor (Figure 4.3). Aliquots of the polyphasic dispersion were continuously pumped from the baffled reactor into the liquid-jet cell at a flowrate of ~320 ml/min using two peristaltic pumps for the entire duration of the experiment (~4.5 hours). The inclusion of the sample loop made it possible to use apparatus typically used for the lab-scale industrial overbasing process with only minor modifications to the synthesis process and eliminated the need to design a reactor system specifically for XAS measurements. This is particularly important because product composition is highly dependent on the experimental setup. If a significantly modified synthesis method and setup had been used, the XAS results would have been unrepresentative of the industrial process.

Reactor System and Process Control. The calcium carbonate ($CaCO_3$) reactive crystallisation processes (*cf.* sections 3.3.3 and 3.3.4) were carried out in a 1 L glass baffled reactor using a conventional lab-scale setup (Figure 4.3) under a constant N_2 (30 ml/min) environment. The sample fluid flow to and from the reactor (Figure 4.3– FIC 3 and 5) was controlled by two peristaltic pumps (Watson Marlow 520Du and 520S). High fluid flowrates (~320 ml/min) through the liquid-jet sample loop were required to circumvent phase separation. It was essential that fluctuations in the temperature of the reaction mixture were minimised, especially during the neutralisation (step 1) and carbonation (step 2) stages of the overbasing process. The exothermic reactions of acid and CO_2 with calcium hydroxide could potentially lead to a runaway reaction. Temperature variations were minimised through control measures which included slow carbonation over an extended period of time and the dropwise addition of sulphonic acid (by manually opening valve 4 shown in Figure 4.3). The reactor was heated by a 1 L Cole Palmer electrothermal heating mantle. Temperature was controlled through a feedback loop consisting of a thermocouple (Figure 4.3– TT) and a digital West N4400 temperature controller (Figure 4.3 – TIC).

The contents of the reactor were mixed at high speed (400 rpm), by a Heidolph Hei-Torque Precision 100 digital overhead stirrer (Figure 4.3– FIC 2), to ensure even heat distribution in the reactor. This was aided by customised pseudo-baffles in the form of four equally-spaced depressions in the glass reactor that emulate fin-type baffles. This customised baffle configuration was chosen over conventional wall-mounted baffles to maintain the mechanical integrity of the baffles as fluid viscosity increases. The balanced axial and radial flow created by these pseudo-baffles and the Rushton turbine also promoted the mixing of the gas-liquid-solid phases and thus the formation of the desired products.

All gas flows were regulated with flow controllers labelled FC 1, FC 2 and FIC 4 in Figure 4.3. The reactor vessel was continuously flushed with gaseous N_2 to prevent the reaction between $Ca(OH)_2$ and atmospheric CO_2. A glass spiral reflux condenser prevented evaporation of volatile solvents and vented CO_2 and N_2 gas which had been bubbled through the reactor. The XAS cell was flushed with He because it has a low X-ray absorption cross-section.

4.4 Conclusions

A novel process analytical technology (PAT) system was developed for *in situ/operando* X-ray absorption (XAS) studies of multiphase multicomponent crystallisation processes. The PAT setup is a combination of a conventional lab-scale reaction vessel with a continuous-flow liquid-jet XAS cell. It permits real-time probing of bulk solutions/dispersions by XAS (on-line) to determine the changes in local/electronic structure as a function of process conditions. The PAT configuration also accommodates an attenuated total reflection (ATR) probe in the reaction vessel, which allows for complementary in-line infrared spectroscopy. The synthesis of calcium carbonate ($CaCO_3$) via the carbonation of calcium hydroxide ($Ca(OH)_2$) in aqueous and non-aqueous environments has been successfully monitored *in situ/operando* at the Ca K-edge. The results of these experiments are presented and discussed in chapters 7 and 8.

Chapter 5:

Structure Elucidation of Reference Calcium Compounds

5.1 Introduction

This chapter deals with the elucidation of the short- and long-range structures of the three crystalline calcium carbonate polymorphs: calcite ($CaCO_3$-α), aragonite ($CaCO_3$-β) and vaterite ($CaCO_3$-γ) and the precursors used for their synthesis Figure 5.1). Predicting and controlling performance of these $CaCO_3$ products requires a thorough understanding of the relationship with molecular and microstructure, which in turn depends critically on the synthesis route (24, 136). Calcium oxide (CaO) and hydroxide ($Ca(OH)_2$) are widely used precursors in the synthesis of $CaCO_3$ (Figure 5.1). Calcium methoxide ($Ca(OCH_3)_2$) is also a potential precursor in $CaCO_3$ synthesis although it is more widely used as a catalyst in transesterification processes (137-139). The structural information obtained from this study can be used to tailor the interfacial properties of $CaCO_3$ into more sophisticated formulations. Herein, a comprehensive study on the electronic and local structure of calcium oxide, hydroxide, methoxide and carbonate using multiple microscopy, spectroscopy and scattering techniques is presented. This is the first reported case of $Ca(OCH_3)_2$ XANES, EXAFS and XPDF data.

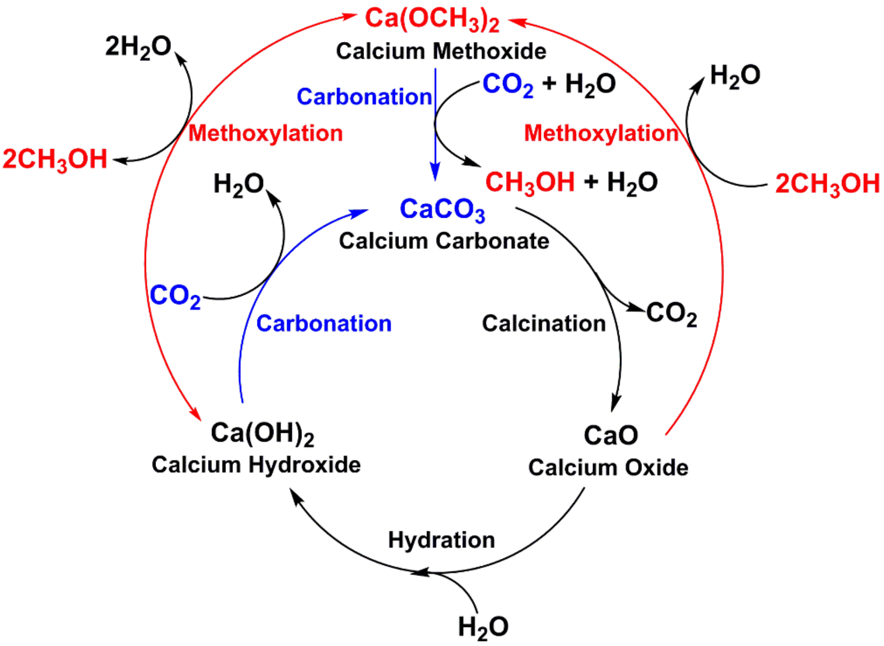

Figure 5.1. A sequence of reaction mechanisms highlighting the formation of calcium methoxide and carbonate from calcium oxide and hydroxide *via* methoxylation and carbonation reactions.

5.2 Scanning Electron Microscopy (SEM)

SEM was used to determine the microstructures of the probable crystalline products from the methoxylation and carbonation of calcium oxide (CaO) and hydroxide ($Ca(OH)_2$). The SEM micrographs in Figures 5.2 to 5.4 show remarkable morphological differences between calcium methoxide ($Ca(OCH_3)_2$), calcite ($CaCO_3$-α), aragonite ($CaCO_3$-β) and vaterite ($CaCO_3$-γ). The SEM micrograph in Figure 5.2a shows that the $Ca(OCH_3)_2$ studied consists of clusters of plate-like sub-micron particles. The particle size ranges from 80 to 160 nm with a mean size of 11 nm (Figure 5.2b). The observed morphology is consistent with previous results (139, 140). Notably, it has been demonstrated (139) that the shape of the methoxide particles is highly dependent on synthesis conditions. This could account for the spherical particles observed by other authors (138).

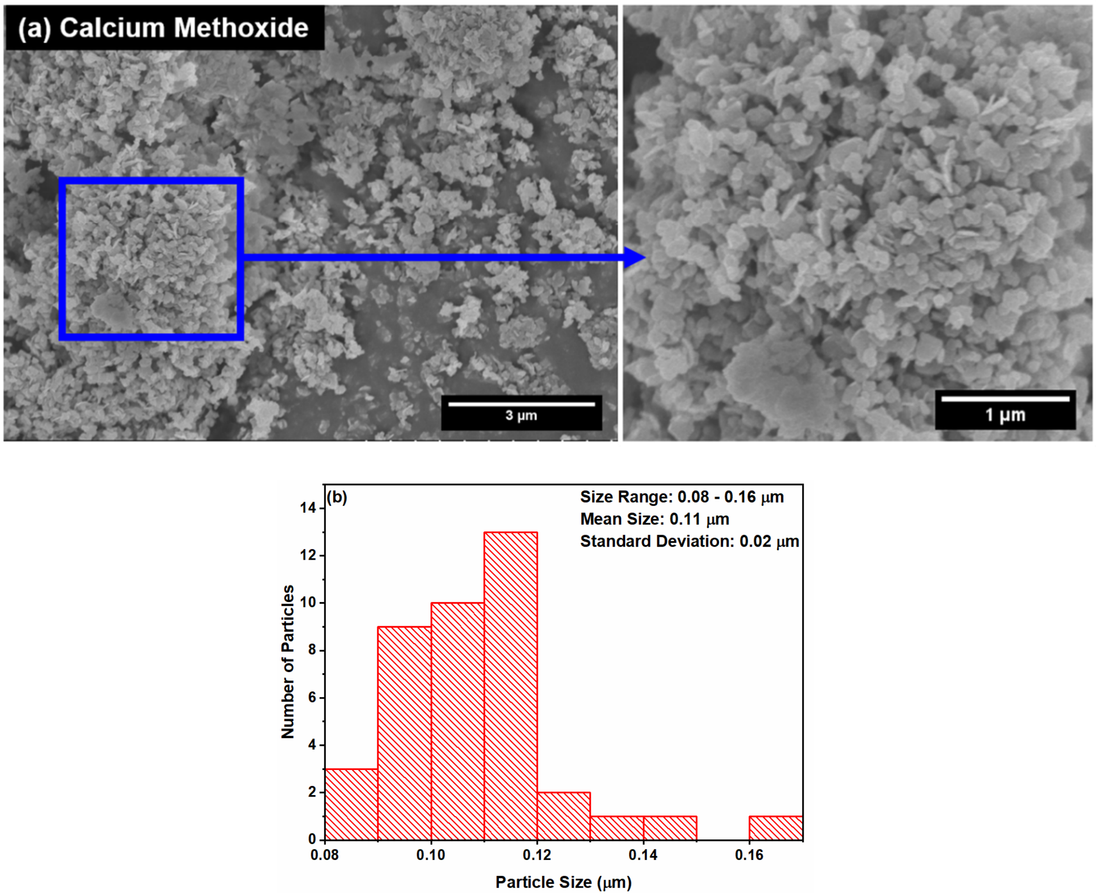

Figure 5.2. (a) SEM micrographs showing the plate-like $Ca(OCH_3)_2$ particles and (b) plot showing the particle size distribution (based on 40 particles).

The SEM micrographs for the $CaCO_3$ polymorphs show that (in order of decreasing thermodynamic stability) the particles vary from rhombohedral $CaCO_3$-α (Figure 5.3a) to needle-like $CaCO_3$-β (Figure 5.3b) to porous polycrystalline $CaCO_3$-γ spheres (Figure 5.4a). The observed morphologies are in agreement with previous SEM studies (69, 136). The preferential formation of needle-like $CaCO_3$-β (11 ± 2.62 μm) particles over the rhombohedral $CaCO_3$-α (6.07 ± 2.41 μm) was highly dependent on the temperature (50 ° C) and slow addition of carbonate ions during synthesis (*cf.* section 3.3.1) (68).

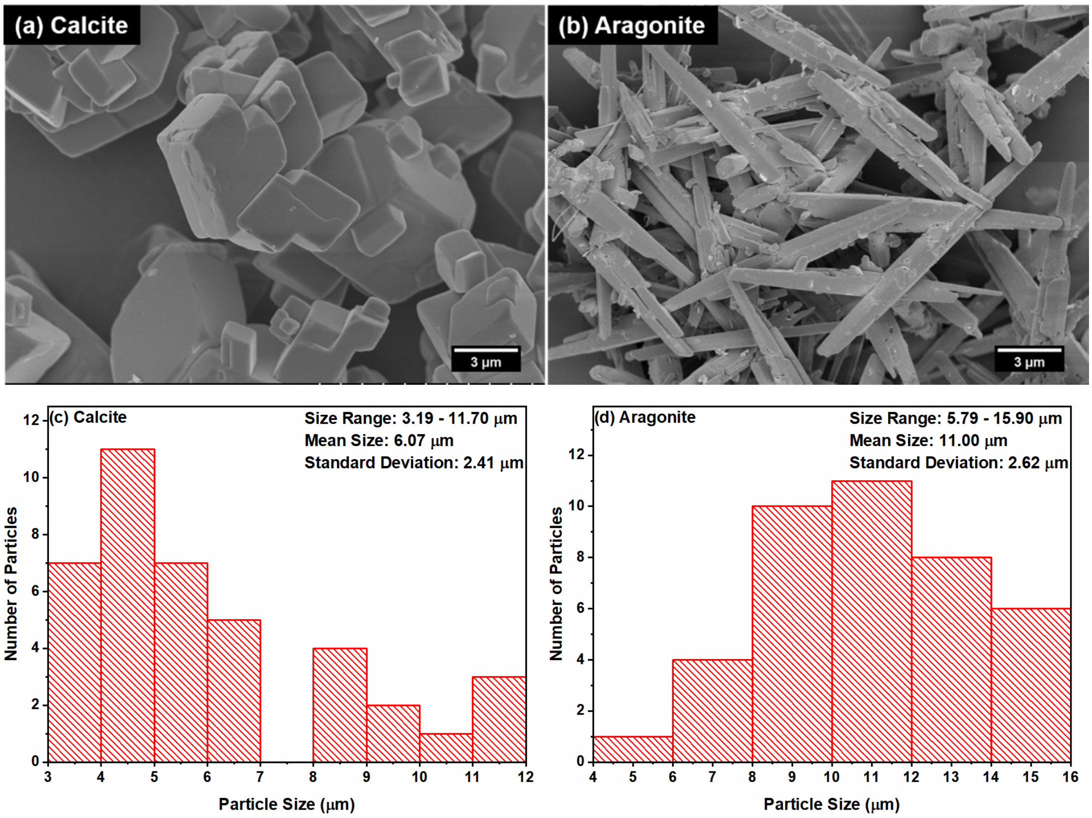

Figure 5.3. SEM micrographs showing (a) rhombohedral $CaCO_3$-α and (b) needle-like $CaCO_3$-β particles. Complementary particle size distribution plots (based on 40 particles) have been included (c and d).

Conversely, the formation of the porous $CaCO_3$-γ spheres (Figure 5.4a) at ambient temperature was governed the presence of pH-variant glycine (69). The $CaCO_3$-γ particles are relatively smaller (3.35 ± 0.65 μm – Figure 5.4b) than the other two polymorphs (Figure 5.3). A closer examination of the surfaces shows that the $CaCO_3$-γ particles have pores, ranging from 130 to 340 nm (Figure 5.4c), in between nano-sized agglomerated spherical particles. Such porous vaterite particles are used in drug delivery, regenerative medicine and personal care products (141, 142). Notably, the precipitation of hexagonal, plate-like, flower-like and rosette-shaped $CaCO_3$-γ crystals have also been reported (142-144). Essentially, much like its crystal structure (discussed in the subsequent section), the true morphology of $CaCO_3$-γ is contentious with the spherical shape being the most common.

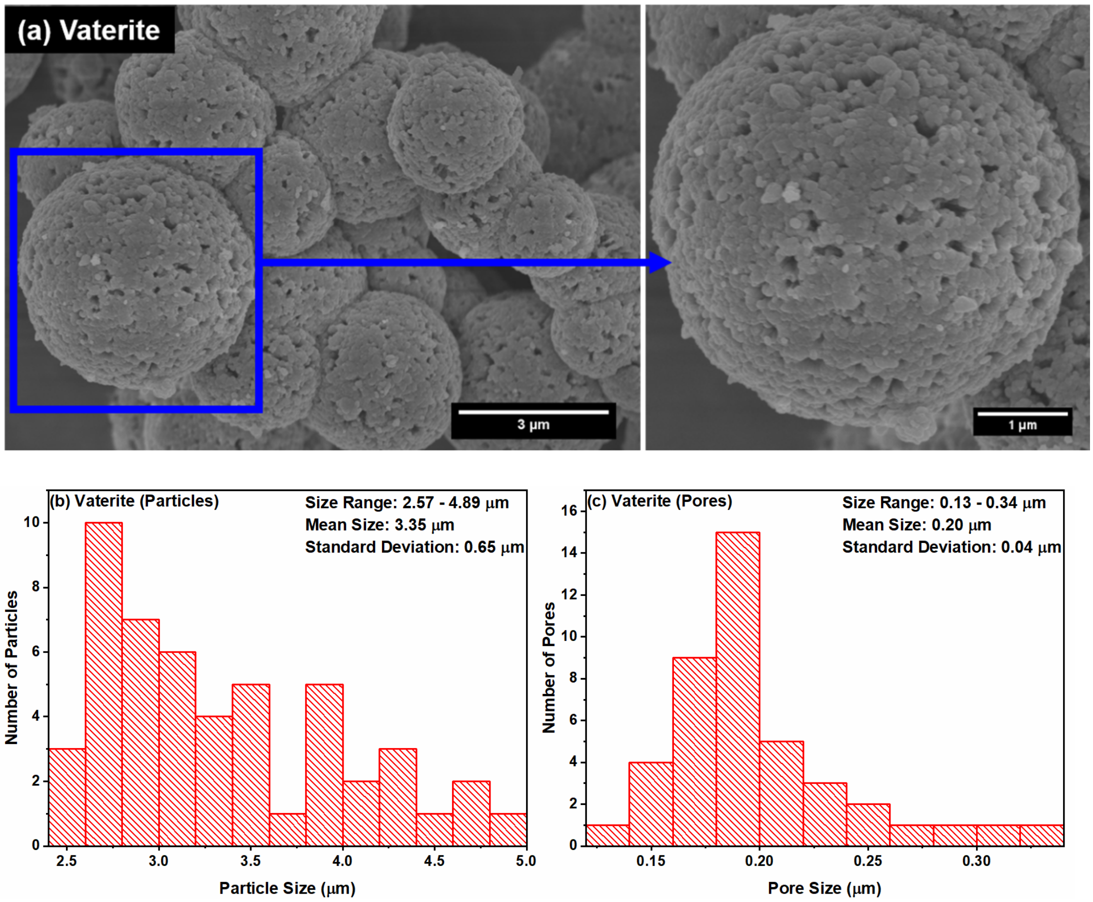

Figure 5.4. (a) SEM micrographs showing the porous spherical $CaCO_3$-γ particles. Complementary size distribution plots for (b) the particles (based on 40 particles) and (c) pores have been included.

5.3 Mid Infrared (Mid-IR) Spectroscopy

The varying anion site symmetries and crystal space groups for the six different calcium compounds were determined using Mid-IR. Figure 5.5 shows the mid-IR spectra for the precursors i.e. CaO, $Ca(OH)_2$ and $Ca(OCH_3)_2$. As expected, the CaO spectrum (Figure 5.5a) shows no characteristic peaks since the diatomic molecule is homonuclear with an IR inactive anion. However, there are some minor impurity peaks observed due to CaO conversion to $Ca(OH)_2$ and $CaCO_3$. Remarkable differences can be observed between the $Ca(OH)_2$ (Figure 5.5b) and $Ca(OCH_3)_2$ (Figure 5.5c) spectra. The most intense peaks for both materials are due to an O-X stretch, where the hydroxyl ν_{OH} vibration appears at 3641 cm^{-1} and the primary alcohol methoxy ν_{OCH3} occurs at 1044 cm^{-1}. Whereas the ν_{OH} stretching is the only evident contribution from the polyatomic $Ca(OH)_2$ (145) (excluding the $CaCO_3$ impurity peaks), the $Ca(OCH_3)_2$ spectrum shows comparatively more features because of the -CH_3 group.

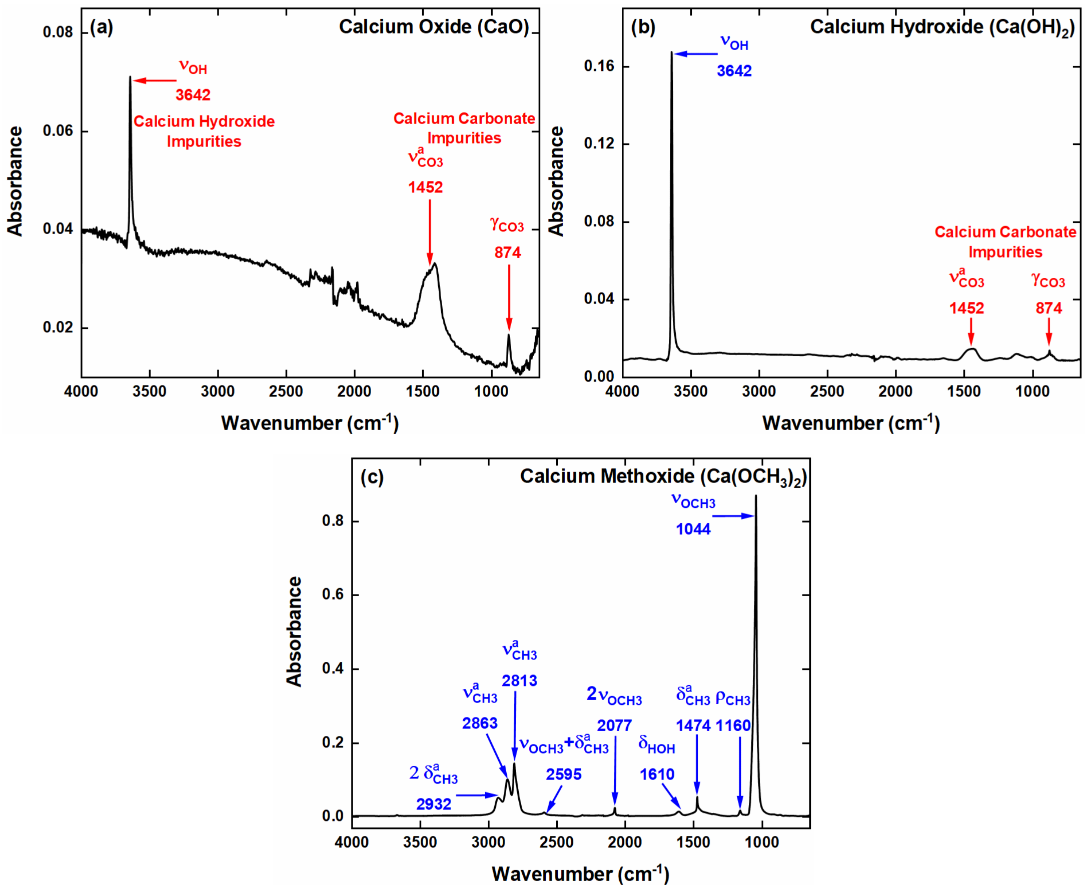

Figure 5.5. Mid-IR plots highlighting the peaks due to symmetric stretching (ν^s), asymmetric stretching (ν^a), in-plane bending (δ), out-of-plane bending (γ) and rocking (ρ) vibrational modes for (a) CaO, (b) $Ca(OH)_2$ and (c) $Ca(OCH_3)_2$.

All of the $Ca(OCH_3)_2$ peaks detected in the 1100 to 3000 cm^{-1} region (Figure 5.5c and Table 5.1) have previously been characterised in other methoxide IR studies (138, 140, 146-149). The distinct triplet features between 2800 to 2950 cm^{-1} can be assigned to two CH_3 asymmetric stretches (ν^a_{CH3}) and one in-plane deformation overtone ($2\cdot\delta^a_{CH3}$). Notably, the δ^a_{CH3} deformation (1474 cm^{-1}) not only contributes to the triplet as an overtone but also appears as part of a combination band with the ν_{OCH3} stretch at 2595 cm^{-1}. As highlighted by Lutz (147), there is some uncertainty about which vibrations account for this combination band. However, the absence of the weak δ^s_{CH3} peak at about 1410 cm^{-1} in Figure 5.5c eliminates the ρ_{CH3} (1160 cm^{-1}) + δ^s_{CH3} combination. The remaining minor features in the $Ca(OCH_3)_2$ spectrum include a δ_{HOH} adsorbed water deformation (1610 cm^{-1}) and $2\cdot\nu_{OCH3}$ overtone (2070 cm^{-1}). Unambiguous structure elucidation of the $Ca(OCH_3)_2$ from the IR data alone is precluded by the multiple overtones and combination bands coupled with non-equivalent CH bonds in the methyl group (150). However, the OCH_3^- anion has been assigned a site symmetry of *3m* and a hexagonal space group of *P-3m1* (91), with the aid of Powder X-ray Diffraction (PXRD) (147). $Ca(OH)_2$ has the same space group but an OH^- point group of *-32/m*. The CaO and O^- assignments are *Fm-3m* and *m-3m* respectively.

Table 5.1. Mid-IR vibrational frequencies (cm^{-1}) for CaO, $Ca(OH)_2$ and $Ca(OCH_3)_2$. Includes the anion point groups, crystal space groups and crystal systems.

Assignments	**CaO**	**$Ca(OH)_2$**	**$Ca(OCH_3)_2$**
ν_{OH}	3642	3642	-
$2 \cdot \delta^a_{CH3}$	-	-	2932
ν^a_{CH3}	-	-	2863
ν^a_{CH3}	-	-	2813
$\nu_{CO} + \delta^a_{CH3}$	-	-	2595
$2 \cdot \nu_{CO}$	-	-	2077
δ_{HOH}	-	-	1610
δ^a_{CH3}	-	-	1474
ρ_{CH3}	-	-	1160
ν_{CO}	-	-	1044
Anion Site Symmetry	*m-3m*	*-32/m*	*3m*
Space Group	*Fm-3m*	*P-3m1*	*P-3m1*
Crystal System	Cubic	Hexagonal	Hexagonal

Compared to the methoxide, structural identification/discrimination of $CaCO_3$-α, $CaCO_3$-β and $CaCO_3$-γ (Figure 5.6 and Table 5.2) from IR spectra is relatively more precise. Crystallisation leads to the lowering of the CO_3^{2-} site symmetry from *6-2m* (for an isolated trigonal CO_3^{2-} anion) to *32* in $CaCO_3$-α, *m* in $CaCO_3$-β, and *1* + *2* in $CaCO_3$-γ (Table 5.2) (96, 97). Consequently, the IR inactive ν^s_{CO3} is discernible in the spectra (Figure 5.6) and the double-degenerate ν^a_{CO3} and δ_{CO3} modes are split. Owing to a minor deviation in the order of symmetry of crystalline $CaCO_3$-α from that of the isolated CO_3^{2-} ion (Table 5.2), the $CaCO_3$-α ν^s_{CO3} peak observed at 1090 cm^{-1} (Figure 5.6a) has previously been reported to be IR inactive (96, 151, 152). A comparison of the synthetic calcite with a geological sample (not shown here) validated the presence of a broad and weak ν^s_{CO3} feature in both spectra. The wavenumber of this $CaCO_3$-α ν^s_{CO3} feature is expectedly found to be the difference between both the $\nu^s_{CO3} + \nu^a_{CO3}$ (2512 cm^{-1}) and $\nu^s_{CO3} + \delta_{CO3}$ (1796 cm^{-1}) combination bands and the respective double-degenerate modes. Thorough inspection of previous literature spectra (151, 152) reveals what looks like the ν^s_{CO3} feature at ~1087 cm^{-1}, which the authors did not address. It cannot be discounted that the appearance of this ν^s_{CO3} feature and the ν^a_{CO3} shoulder at 1402 cm^{-1} in the calcite IR could be a factor of the pressure (153) exerted by the attenuated total reflectance (ATR) pressure arm.

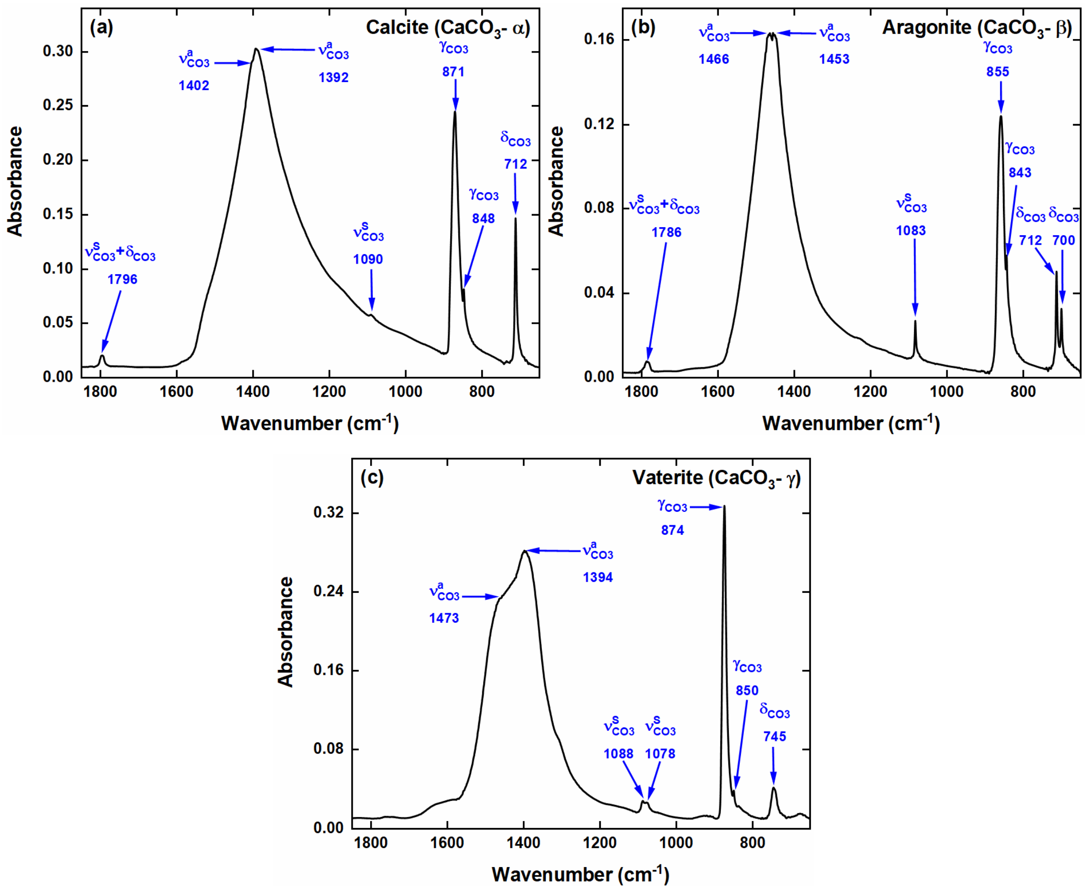

Figure 5.6. Mid-IR plots highlighting the peaks due to symmetric stretching (ν^s), asymmetric stretching (ν^a), in-plane bending (δ) and out-of-plane bending (γ) vibrational modes for (a) $CaCO_3$-α, (b) $CaCO_3$-β and (c) $CaCO_3$-γ.

In terms of $CaCO_3$-γ, there is an apparent split in this ν^s_{CO3} mode which is evidenced by two features at 1078 and 1088 cm^{-1} (Figure 5.6c). Sato and Matsuda (154) report a similar observation in their IR spectra with two features at 1070 and 1085 cm^{-1}. Complementary Raman data show a third peak at 1090 cm^{-1} (23, 155-157). The ν^s_{CO3} splitting in both IR and Raman spectra seems to be independent of degeneracy. Therefore, it can been postulated that these varied oscillations are due to the presence of CO_3^{2-} ions with two or three different environments in the vaterite structure (23, 96, 157). This hypothesis consequently eliminates the proposed orthorhombic *Pbnm* (93) and hexagonal *P6$_3$/mmc* (143, 154, 156, 158, 159) and *P6$_3$22* (22, 160, 161) crystal structures with equivalent CO_3^{2-} ions (Table C.1 in Appendix C). Figure 5.3b also shows that the other non-degenerate mode (γ_{CO3}) is coupled with a satellite peak at about 847 ± 4 cm^{-1} in all three $CaCO_3$ spectra. The assignment of this satellite is yet to be fully resolved with theories spanning from multi-layer coupling of adjacent CO_3^{2-} ions to 1-3% ^{13}C isotope contributions (153). Most of these explanations have been discounted on account of the lack of realistic numerical evidence. However, the possibility a multiphonon mode resulting from the combination of the γ_{CO3} with a zone boundary phonon has been proposed (153) and is yet to be fully explored. Coincidentally, this satellite peak seems to appear at a similar frequency of the γ_{CO3} of an aqueous bicarbonate (HCO_3^-) ion (843 cm^{-1}) (162). Further investigation of the multiphonon and lattice modes, which are not covered in this study, is required to resolve this debate.

Table 5.2. Mid-IR vibrational frequencies (cm^{-1}) of a free carbonate anion (CO_3^{2-}), $CaCO_3$-α, $CaCO_3$-β and $CaCO_3$-γ. Includes the anion point groups, crystal space groups and crystal systems.

Assignments	**Anion**	**Calcium Compounds**		
	CO_3^{2-} (97)	**$CaCO_3$-α**	**$CaCO_3$-β**	**$CaCO_3$-γ**
$\nu^{s}_{CO3} + \nu^{a}_{CO3}$	-	2512	-	-
$\nu^{s}_{CO3} + \delta_{CO3}$	-	1796	1786	-
ν^{a}_{CO3}	1415	1392	1457	1473;1394
ν^{s}_{CO3}	-	1090	1083	1088; 1078
γ_{CO3}	879	871; 848	855; 843	874; 850
δ_{CO3}	680	712	712; 700	745
CO_3^{2-} Site Symmetry	*6-2m*	*32*	*m*	*1 + 2*
Space Group	-	*R-3c*	*Pmna*	$P6_{5}22$
Crystal System	Trigonal	Trigonal	Orthorhombic	Hexagonal

Finally, the reduction in CO_3^{2-} symmetry to *m* in $CaCO_3$-β results in the splitting of δ_{CO3} into two non-degenerate modes at 700 and 712 cm^{-1} (Figure 5.3b and Table 5.2). The formation of the pseudo-hexagonal *Pmna* aragonite structure also causes the splitting of ν^{a}_{CO3} at ~1457 cm^{-1}. This second split is absent in published aragonite IR/Raman spectra. Conversely, the IR of $CaCO_3$-γ doesn't show a δ_{CO3} split but an un-resolved ν^{a}_{CO3} split is present at 1394 and 1473 cm^{-1}. These results confirm the degradation of symmetry in vaterite and are in agreement with observations reported in previous studies (152, 154). Ultimately, the Mid-IR results confirm the structures of calcium oxide, hydroxide, methoxide, calcite and aragonite as cubic (*Fm-3m*), hexagonal (*P-3m1*), hexagonal (*P-3m1*), rhombohedral (*R-3c*) and orthorhombic (*Pmna*). The vaterite results are comparatively inconclusive but they support the presence of non-equivalent CO_3^{2-} ions (23, 157). This discounts all the centrosymmetric models (Table C.1 in Appendix C) proposed prior to the Wang and Becker (27) $P6_{5}22$ hexagonal structure (point group: *1 + 2*). The other remaining possible candidates include the hexagonal, monoclinic and monoclinic models proposed by Demichelis *et al.* (95, 163) and Mugnaioli *et al.* (164). These structures will further be explored using the X-ray analytical techniques.

5.4 X-ray Scattering/Diffraction

Significant differences due to Bragg diffraction and diffuse scattering from the six calcium compounds can be observed in the powder X-ray diffraction (PXRD) and Scattering function (S(Q)) plots (Figures 5.7 and 5.8). Complementary miller indices and space groups for all six materials were determined from previously proposed model crystallographic structures (including those in Table 3.2 and C.1 in Appendix C). The crystal structures of CaO, $Ca(OH)_2$, $Ca(OCH_3)_2$, $CaCO_3$-α, $CaCO_3$-β and $CaCO_3$-γ were established to be cubic (*Fm-3m*) (89), hexagonal (*P-3m1*) (90), hexagonal (*P-3m1*) (91), rhombohedral (*R-3c*) (20), orthorhombic (*Pmna*) (92) and hexagonal (*P6₃/mmc*) (159) respectively. All of the assignments are in agreement with the mid-IR results (Tables 5.1 and 5.2), except for the previously excluded $CaCO_3$-γ structure with equivalent CO_3^{2-} ions. Also, much like the mid-IR, the CaO and $Ca(OH)_2$ patterns (Figure 5.7) revealed traces of $CaCO_3$ impurities.

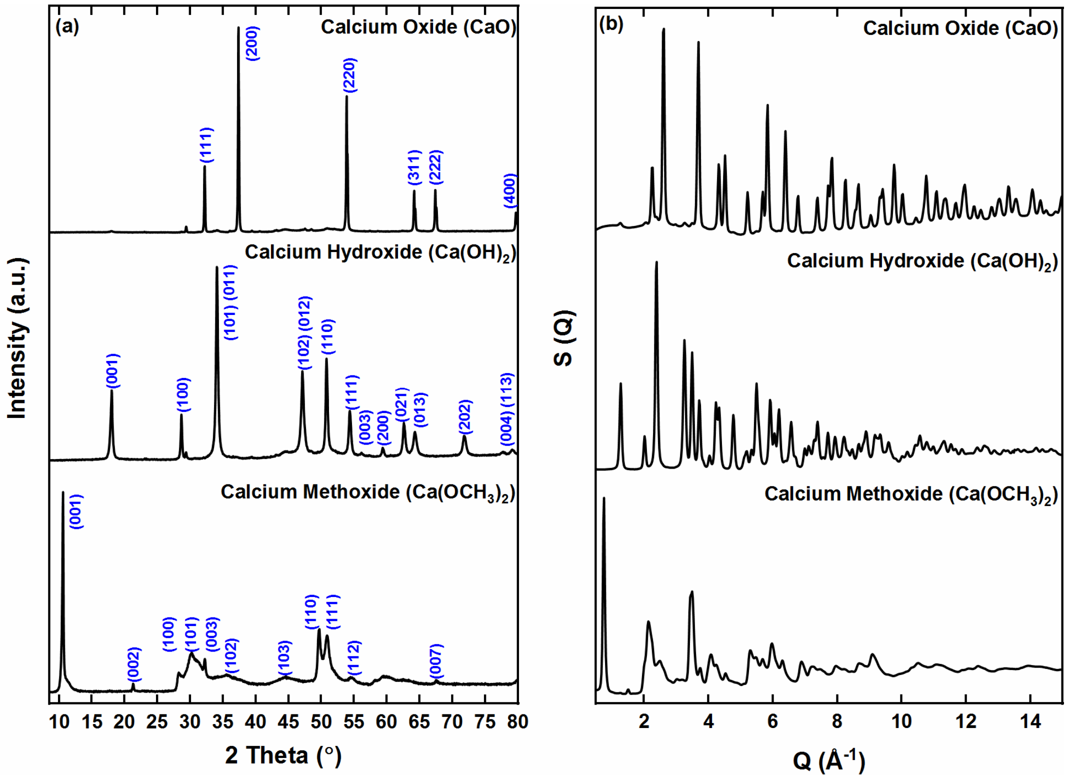

Figure 5.7. (a) Indexed PXRD and (b) S(Q) plots showing the Bragg diffraction and diffuse scattering for CaO (*Fm-3m*) (89), $Ca(OH)_2$ (*P-3m1*) (90), $Ca(OCH_3)_2$ (*P-3m1*) (91, 147).

A qualitative analysis of the two sets of S(Q) data (Figure 5.7b and 5.8b) reveals that there are relatively considerable reductions in the diffraction features for $Ca(OCH_3)_2$ and $CaCO_3$-γ beyond 10 $Å^{-1}$. These reductions could be a function of (i) positive optical orientation – anions are arranged parallel to the c-axis (27, 91); (ii) loose packing of ions – evidenced by relatively low densities of 1.75 g/cm^3 ($Ca(OCH_3)_2$)

(147) and 2.65 g/cm^3 ($CaCO_3$-γ) (165); and (iii) non-collinear arrangement of the anions – $CaCO_3$-γ is said to have two to three different CO_3 environment (27, 95, 163-165). Indexing of the $CaCO_3$-γ S(Q) and PXRD patterns (Figure 4.5) reveals that the hexagonal *P6₃/mmc* structure is the only model structure that fits most of the observed peaks.

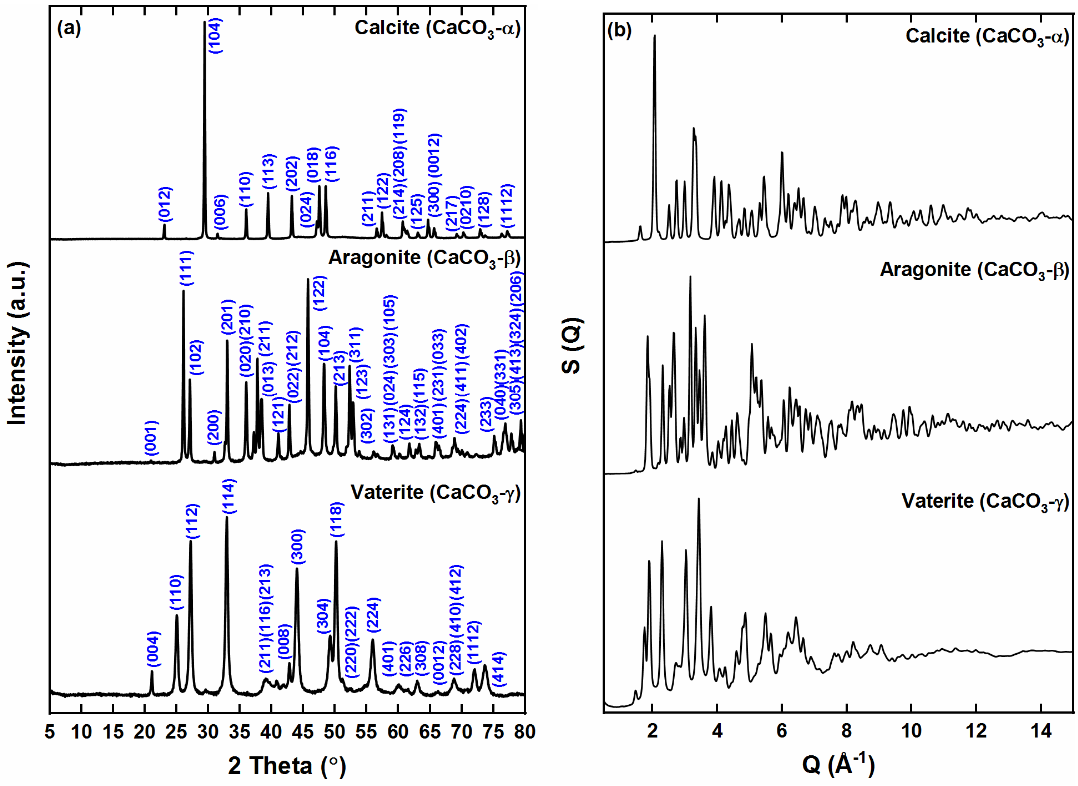

Figure 5.8. (a) Indexed PXRD and (b) S(Q) plots showing the Bragg diffraction and diffuse scattering for $CaCO_3$-α (*R-3c*) (20), $CaCO_3$-β (*Pmna*) (92) and $CaCO_3$-γ (*P6₃/mmc*) (159).

The *P6₃/mmc* structure was first proposed by Kamhi (1963) (158) who noted the presence of weak reflections pertaining to a possible vaterite superstructure. Some of these superstructure peaks (Figure 5.8) at d-spacings of 2.32, 2.28, 2.16 and 1.54 have been assigned (159) to the 211, 205, 213 and 401 planes respectively. The peak assignments are based on Meyer's (1969) (159) revised *P6₃/mmc* 2-layer model, which accounts for displacement of the CO_3 group. Notably, most *ab initio* attempts at determining the superstructure have resulted in models (Table C.1 in Appendix C) that incorporate Kamhi's hexagonal unit cell (164). However, the resulting diffraction data exclude the weak superstructure reflections (94) and/or introduce new peaks not present in any experimental data (27). It has been observed the recent *ab initio* models (starting from the *P6₅22* structure by Wang and Becker (2009) (27)) agree more with contentious structural information obtained from short-range order techniques such as

Raman and solid-state nuclear magnetic resonance (NMR) spectroscopy than the *$P6_3/mmc$* structure (157, 163, 165).

A similar variation between long and short range data has been observed with $LiPF_6$ (166). The PXRD results concluded that the structure was rhombohedral (*R-3*) but Raman countered this with a cubic structure (*Fm-3m*). In this instance, the authors suggested that the discrepancy could be due to the fact that the $LiPF_6$ is metastable/transient at the measured temperature. Since $CaCO_3$-γ readily converts to the more stable $CaCO_3$-α structure at room temperature (167), marginal disorder in the system can only be detected using techniques that probe the local structure. Therefore, resolution of the 'true' $CaCO_3$-γ structure requires complementary analysis of the short and medium-range given by X-ray pair distribution function (XPDF) and extended X-ray absorption fine structure (EXAFS) (section 4.3.5). Ideally, the unlikely $CaCO_3$-γ model structures should be eliminated based on subtle differences observed in the quantitative local structure data obtained from the two techniques. Additionally, XPDF and EXAFS have the capability to confirm the previously proposed lattice/molecular parameters for the $Ca(OCH_3)_2$ *P-3m1* structure (91, 147).

5.5 X-ray Absorption Near-Edge Structure (XANES)

Comparable to the mid-IR, PXRD and S (Q), the normalised Ca K-edge XANES spectra (Figure 5.9) for the six calcium-containing compounds exhibit discernible differences. The absorption bands in the spectra are due to single/double-electron dipole transitions from 1s/1s3p core states to unoccupied 3d and 4p state in the valence region (168). The 1s → 3d transitions (labelled A_1 and A_2 in Figure 5.9) arise at ~4040 eV, followed by 1s → 4p electronic transitions (labelled B – D_2) in the range from 4045 to 4060 eV. An additional feature visible at ~4050 eV (labelled C_1) arises from scattering of the photoelectron emitted from the central Ca absorber off of oxygen neighbours in the first Ca-O shell (169, 170). The double-electron transitions from 1s3p excitation to the 3d and 4p orbitals result in shake-up satellite peaks (171-174) (labelled E – F_3), which mirror the single electron transitions in the photon energy range from 4065 eV to 4105 eV. Previous studies (172, 175) suggested that the onset energy of the main 1s3p → 4p satellite peak (labelled F_2) can be estimated (ΔE_{approx}) using the 'Z+1 approximation'. In Ca, this satellite peak is thus expected to appear at +28.3 eV relative to the Ca K-edge energy (E_0), which corresponds to the scandium KM_{23}-edge energy (or scandium 3p binding energy) (172). More precise energy differences (ΔE_{calc}) of +23.6 and +35.6 eV for the 1s3p → 3d (labelled ‘E’) and 1s3p → 4p (labelled ‘F_2’) transitions respectively have also been proposed based on the Hartree-Fock model (171). The experimental onset energies (ΔE_{exp}) for the six calcium compounds in this study correlate with the ΔE_{calc} values more than the $\Delta E_{approx.}$ (Table 5.3). This correlation has also been observed in the XANES spectra of hydrated Ca^{2+} ions (172).

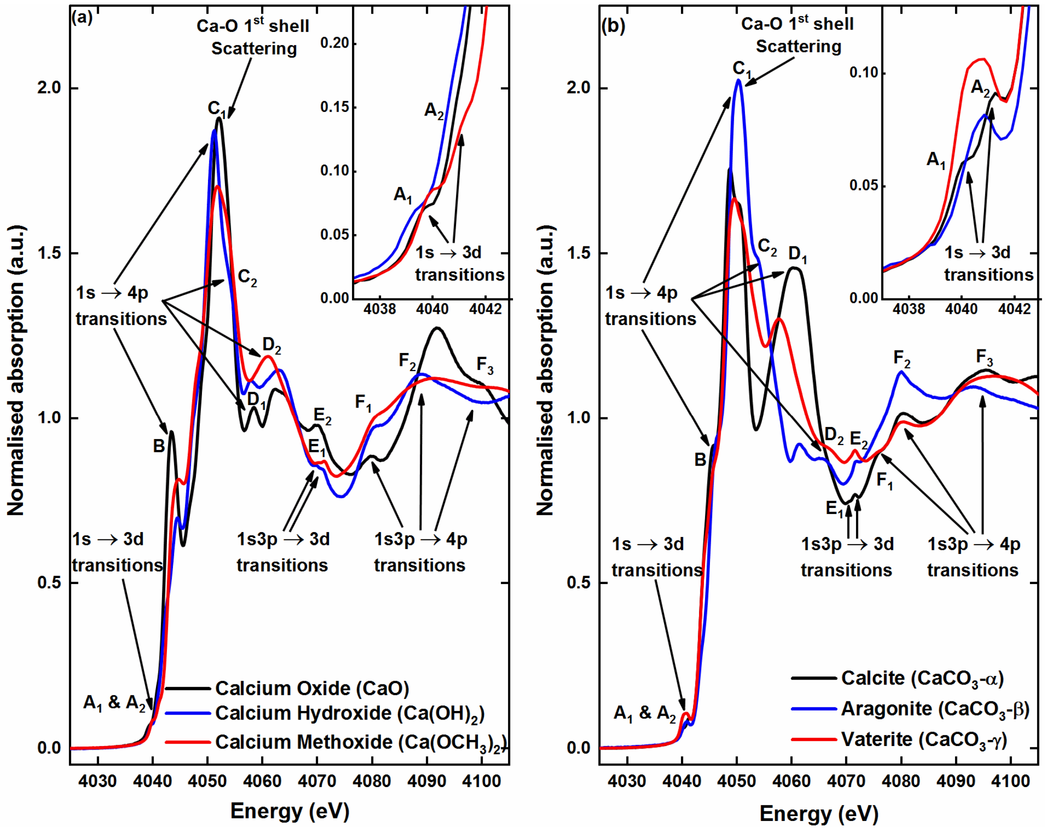

Figure 5.9. Ca K-edge XANES spectra showing features due 1s/1s3p to 3d and 1s/1s3p to 4p electron transitions for (a) CaO, $Ca(OH)_2$ and $Ca(OCH_3)_2$; and (b) $CaCO_3$-α, $CaCO_3$-β and $CaCO_3$-γ.

Comparison of the XANES spectra for CaO, $Ca(OH)_2$ and $Ca(OCH_3)_2$ (Figure 5.9a) shows that the 1s → 3d transitions occur as two small peaks (A_1 and A_2) in the pre-edge region. This transition is symmetry-forbidden in centrosymmetric systems unless, through thermal or crystallographic disorder, 3d and 4p molecular orbitals are allowed to overlap (106, 170). Since CaO and $Ca(OH)_2$ are centrosymmetric, with space groups of *Fm-3m* and *P-3m1* respectively, the presence of a weak A_1-A_2 pre-edge doublet representing a forbidden transition suggests that some crystallographic disorder is present in the system. Similarly, the occurrence of the weak A_1 and A_2 peaks in the $Ca(OCH_3)_2$ spectrum suggests the presence of an inversion centre, which supports the assignment of a hexagonal *P-3m1* space group for the methoxide (91, 147).

Table 5.3. Experimental onset energies (ΔE_{exp}) relative to the Ca K-edge energy (E_0) for the 1s/1s3p to 3d and 4p electronic transitions in the XANES spectra of CaO, $Ca(OH)_2$, $Ca(OCH_3)_2$, $CaCO_3$-α, $CaCO_3$-β and $CaCO_3$-γ.

Region	**Transition**	**Peak**	**Calcium Compounds**					
			CaO	**$Ca(OH)_2$**	**$Ca(OCH_3)_2$**	**$CaCO_3$-α**	**$CaCO_3$-β**	**$CaCO_3$-γ**
Pre-edge, ΔE_{exp} (eV)	1s → 3d	A_1	-12.7	-11.5	-11.7	-8.7	-9.4	-8.8
	1s → 3d	A_2	-11.2	-10.4	-10.7	-7.4	-	-
	1s → 4p	B	-8.6	-6.7	-7.1	-3.0	-4.0	-3.7
Edge, E_0 (eV)	1s → 4p	C_1	4052.0	4051.2	4051.7	4048.7	4050.2	4049.5
Post-edge, ΔE_{exp} (eV)	1s → 4p	C_2	-	3.1	-	1.7	3.5	1.6
	1s → 4p	D_1	6.3	6.7	-	11.7	11.0	8.1
	1s → 4p	D_2	10.2	11.7	9.2	-	14.9	17.1
	1s3p → 3d	E_1	17.5	18.7	18.3	21.8	-	-
	1s3p → 3d	E_2	18.1	19.8	19.5	22.8	21.5	22
	1s3p → 4p	F_1	27.7	29.6	29.1	27.1	25.3	26.3
	1s3p → 4p	F_2	39.6	37.3	39.9	31.7	29.6	30.9
	1s3p → 4p	F_3	48.0	-	-	46.5	42.5	46.3

Beyond 4040 eV, the three samples without CO_3 anions display similar features with varying intensities due to the other single/double-electron transitions. However, it is evident from the relatively lower intensity of peak C_1, stronger singlet D_2 and weaker F_1 to F_3 features in the $Ca(OCH_3)_2$ XANES that its structural orientation is influenced by the presence of the large CH_3 group (~1/2 of the a-axis). All three of these samples have an oxygen coordination number (N_O) of 6 around the central absorbing atom (*cf.* Table 3.3). Therefore, it is unlikely that the reduced intensity of feature C_1 in $Ca(OCH_3)_2$ arises through different interactions with neighbouring oxygen atoms. Rather, it appears more likely that weaker interactions between Ca 4p states in the absorbing Ca atom and Ca 3d and 4s states in neighbouring Ca atoms contribute to the reduced intensity (176, 177). The strength of these interactions is inversely proportional to the Ca-Ca atomic distance which increases from CaO (3.40 Å) to $Ca(OH)_2$ (3.58 Å) to $Ca(OCH_3)_2$ (3.64 Å) (91, 108). The bond distance differences will be explored further in the XPDF and EXAFS calculations (section 5.6).

In order to fully understand the significance of having the D_2 singlet (at ~4060 eV) in the $Ca(OCH_3)_2$ XANES post-edge region as opposed to a (D_1 and D_2) doublet, the non-carbonated samples (Figure 5.9a) were compared to $CaCO_3$ polymorphs (Figure 5.9b). Much like the methoxide, the centrosymmetric $CaCO_3$-α (*R-3c* space group) also displayed a pre-edge doublet (A_1 and A_2) at ΔE_{exp} values of -8.7 and -7.4 eV and a strong post-edge singlet (D_1) at +11.7 eV (Table 4.4). This $CaCO_3$-α 1s → 4p post-edge feature has previously been associated with the strongly ordered collinear arrangement of planar CO_3 groups in the rhombohedral crystal structure (17, 19, 52). Further analysis of the crystal structures of the six samples shows that the anions in

CaO, $Ca(OH)_2$, $CaCO_3$-α and $CaCO_3$-β are all arranged perpendicularly to the c-axis. Loose packing of Ca^{2+} and CO_3^{2-} ions in the $CaCO_3$-α hexagonal layers (only 1/3 of the octahedra are occupied) is the only distinguishing attribute. It can thus be deduced that the loose packing coupled with collinearity of the CO_3 ions allows for stronger interactions between the absorbing Ca 4p states and neighbouring Ca 4p and C σ^* states, which collectively contribute to the intensity of the calcite D_1 singlet (176, 177). This hypothesis, however, only half applies to the methoxide where the size of the OCH_3^- polyatomic anion (where CH_3 size = ~1.8 Å) leads to loose packing in the unit cell (a = b = 3.64 Å and c = 8.31 Å) but doesn't allow for collinearity (91). A comparison with the $CaCO_3$-γ structure shows that, in the absence of collinearity, having the anions arranged parallel to the c-axis also leads to a prominent peak at ~4060 eV. Notably, such an atomic arrangement for the OCH_3^- group in $Ca(OCH_3)_2$ has been previously proposed (91).

Figure 5.9b further highlights the differences that can be observed in the electronic structure of materials with the same chemical formula ($CaCO_3$) but varying crystal orientation (previously confirmed by mid-IR, PXRD and S(Q)). The most notable variation in the XANES pre-edge region (~4040 eV) is the relatively high intensity of the $CaCO_3$-γ 1s → 3d peak (A_1). It has been observed from previous studies that non-centrosymmetric/enantiomorphic systems, such as amorphous calcium carbonate (ACC), exhibit a single peak (54, 58, 61). Additionally, the amplitude of this peak has been found to be a non-linear function of the displacement of the absorbing atom (calcium in this case) from the centre of symmetry (168). As can be seen in the Figure 5.9b inset, the singlet amplitude increases with increasing system disorder from $CaCO_3$-β (at -9.4 eV) to $CaCO_3$-γ (at -8.8 eV). The decrease in order from $CaCO_3$-α to $CaCO_3$-γ can be qualified by the Debye-Waller factors (σ^2) and bond lengths (R) calculated in the EXAFS region (55, 56, 59, 64, 65) (section 5.6). Conclusively, the enantiomorphic nature observed in the $CaCO_3$-γ XANES excludes the proposed orthorhombic *Pbnm* (93) and hexagonal $P6_3/mmc$ (143, 154, 156, 158, 159) and $P6_322$ (22, 160, 161) crystal structures. This is in agreement with the mid-IR results (section 4.3.2) pertaining to non-equivalent CO_3^{2-} ions.

Finally, another distinguishing feature in the $CaCO_3$ XANES spectra (Figure 5.9b) is the intense peak (C_1) at about 4050 eV. This 1s → 4p peak is collectively due to Ca 4p interactions with neighbouring Ca 3d and 4s states and C π^* states and the scattering of the first shell neighbouring atoms (oxygen) (170, 176-178). The intensity and onset energy E_0 (Table 5.3) of this peak is sensitive to the coordination number (N_{atom}) of the first shell (*cf.* Table 3.3) i.e. both parameters increase from $CaCO_3$-α and $CaCO_3$-γ (N_O = 6) to $CaCO_3$-β (N_O = 9) (54, 169, 170). The $N_{O/C/Ca}$ for the six compounds have been quantified and compared in the subsequent section on the EXAFS region.

5.6 X-ray Pair Distribution Function (XPDF) and Extended X-ray Absorption Fine Structure (EXAFS)

Fourier transform (FT) XPDF (G(r)) and Ca K-edge EXAFS for the three non-carbonated precursors and $CaCO_3$ polymorphs were simulated using the model crystal structures summarised in Tables 3.2 and 3.3. Both techniques determined atom pair contributions (with respect to Ca) and interatomic distances up to 5 Å (short-range). The EXAFS also provided the coordination numbers ($N_{O/C/Ca}$) of the scattering atoms. The capability of the two techniques to determine short-range structure was demonstrated using compounds with established structures i.e. CaO (*Fm-3m*) (89), $Ca(OH)_2$ (*P-3m1*) (90), $CaCO_3$-α (*R-3c*) (20) and $CaCO_3$-β (*Pnma*) (92). The refinement/fitting methods were then used to confirm the proposed structures for $Ca(OCH_3)_2$ (*P-3m1*) (91) and $CaCO_3$-γ (*Pbnm*, *Ama2*, *P6₅22* and *C1*) (27, 93, 94, 163).

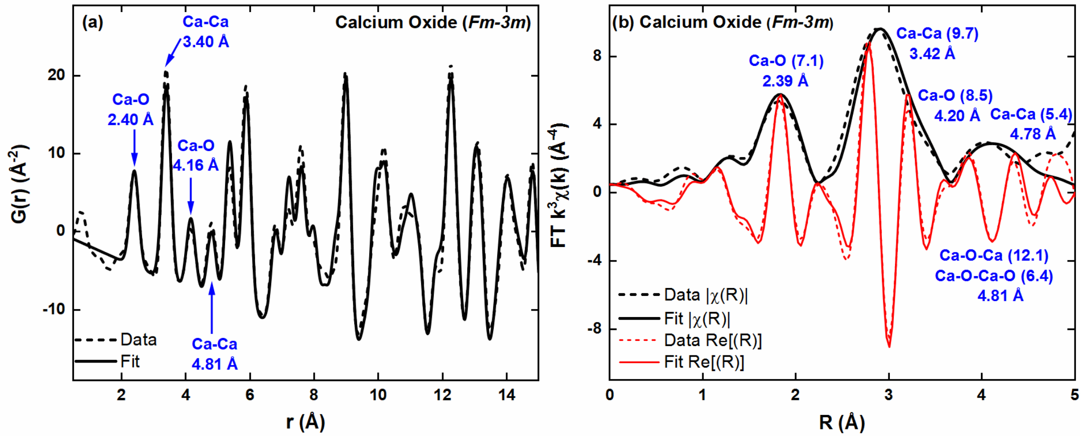

Figure 5.10. (a) XPDF (G(r)) and (b) Ca K-edge k^3-weighted Fourier transform (FT) magnitude(|X(R)|) and real (Re[(R)]) EXAFS for CaO (*Fm-3m*) (89). All plots show atom pair contributions and calculated interatomic distances (r). The EXAFS also shows the coordination numbers ($N_{O/C/Ca}$) in parentheses.

Calcium Oxide, Hydroxide and Methoxide. Theoretical CaO XPDF and EXAFS (Figure 5.10) were determined using the established *Fm-3m* (89) structure. The initial four coordination spheres in CaO consist of O, Ca, O and Ca atoms respectively. The calculated interatomic distances of 2.40 ± 0.01 Å, 3.40 ± 0.01 Å, 4.16 ± 0.03 Å and

4.81 ± 0.02 Å agree with the crystallographic model and literature values (89, 108). Conversely, higher variations were observed with the calculated coordination numbers ($N_{O/C/Ca}$) (Figure 5.10b) compared to the model values (*cf.* Table 3.3) with a maximum deviation of ~2.3 atoms for the Ca-Ca sphere (3.42 Å). Notably, multiple scattering contributions (Ca-O-Ca and Ca-O-Ca-O) were included in the EXAFS fit of the fourth coordination sphere (Figure 5.10b). Linear multiple scattering effects are prominent in the CaO EXAFS at about 4.81, 6.81 and 8.34 Å (108). These effects, coupled with a high Debye temperature, result in enhanced peaks in the medium-range region of the CaO EXAFS up to ~9 Å (108). The quantitative analysis in this study has been limited to 5 Å since the other compounds don't display distinctive peaks beyond this threshold (Figures 5.11 to 5.13). However, future EXAFS analysis of all eleven coordination spheres (108) in CaO is necessary in order to understand the poorly understood XPDF medium-range.

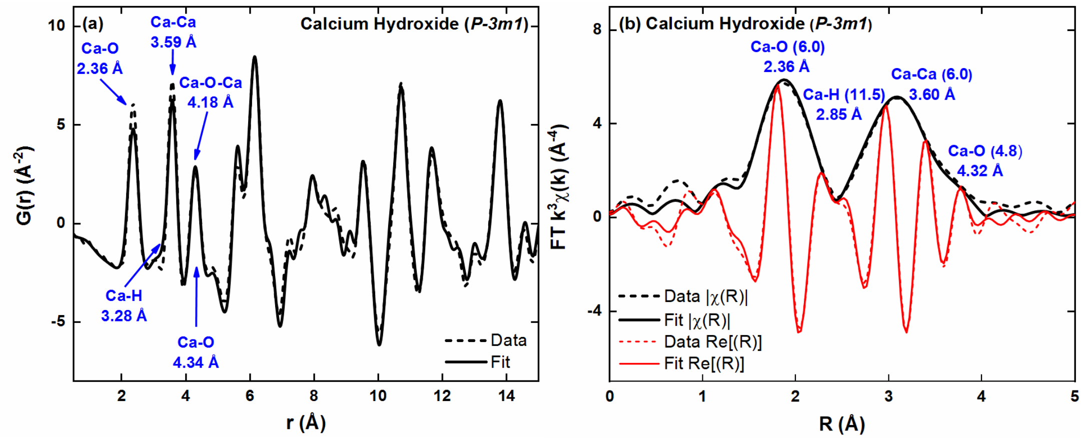

Figure 5.11. (a) XPDF (G(r)) and (b) Ca K-edge k^3-weighted Fourier transform (FT) magnitude(|X(R)|) and real (Re[(R)]) EXAFS for $Ca(OH)_2$ (*P-3m1*) (90). All plots show atom pair contributions and calculated interatomic distances (r). The EXAFS also shows the coordination numbers ($N_{O/C/Ca}$) in parentheses.

Similar to CaO, the initial two prominent peaks in the $Ca(OH)_2$ XPDF and EXAFS (Figure 5.11) are due to O (2.36 ± 0.01 Å) and Ca (3.59 ± 0.01 Å) atoms respectively. The calculated N_O and N_{Ca} values of 6 atoms for the two coordination spheres (Figure 5.8b) are consistent with the crystallographic model values (90). Reasonably good XPDF fits were obtained in the short- and medium-range with R-factors of 20.7 (CaO) and 16.0 % ($Ca(OH)_2$). Minimal variations of less than 0.1% were observed for the input lattice parameters (a, b and c) and isotropic atomic distribution parameters (ADPs; $U_{11/22/33}$). Three factors were considered with regards to achieving better fits with lower R-factor values. The first consideration was the inclusion of scattering contributions due to the $CaCO_3$/$Ca(OH)_2$ impurities observed in the mid-IR (section

5.3) and PXRD/S(Q) (section 5.4). However, the XPDF contributions from the impurities were negligible, since they account for ≤6 wt% of the samples.

The second consideration was the inclusion of anisotropic ADPs ($U_{12/13/23}$) in addition to the $U_{11/22/33}$ isotropic values. ADPs account for thermal/static displacements, much like the EXAFS Debye-Waller factors (σ^2). Varying anisotropic ADPs has been shown to improve PDF refinements but with minimal effect on the z-direction displacements for materials with stacking disorder (e.g. CdSe nanoparticles) (86, 179). In this study, the use of anisotropic ADPs led to no considerable improvements in the refinement of the ordered CaO, $Ca(OH)_2$, $CaCO_3$-α and $CaCO_3$-β. This agrees with the XANES (Figure 5.9), which showed minimal effects of local X-ray polarisation anisotropy (180, 181) on the symmetry-forbidden 1s → 3d transitions (labelled A_1 and A_2) at ~4040 eV. A complementary quantitative XANES analysis might be beneficial in understanding the electronic structures of these calcium compounds, most especially for the relatively disordered $CaCO_3$-γ.

The final and most likely explanation for the fit variations is the relatively higher scattering contribution of Ca atoms (atomic number, Z = 20) compared to the O (Z= 8), C (Z = 6) and H (Z = 1). Since PDFs extracted from total X-ray scattering data are a function of the electron density around a central atom (e.g. Ca), high Z scatterers tend to dominate the FT XPDF (80, 182). Conversely, neutrons probe the nuclei of the molecules, which results in more accurate predictions of atomic distributions involving light scatterers such as H and O (182). Busing and Levy (90) demonstrated the capabilities of neutron diffraction by calculating the r values for the O-H (~0.94 Å) and H-H (~ 2.20 Å) bonds in $Ca(OH)_2$. The low scattering contributions from these bonds are evident in Figure 5.11a. Both the first peak at 2.36 Å (which mainly considers the Ca-O) and the shoulder (Ca-H) at ~3.00 Å have been underestimated. Also, marginally higher R-factor values were obtained when $Ca(OH)_2$ structures with un-defined H positions were used. The influence of the H atom in the $Ca(OH)_2$ scattering was further exemplified by the EXAFS (Figure 5.11b).The inclusion of scattering contributions from the ~12 H atoms at 2.85 Å improved the $Ca(OH)_2$ EXAFS fit (Figure 5.11b). There was an observable decrease in the R-factor from 5.1 to 1.4 %.

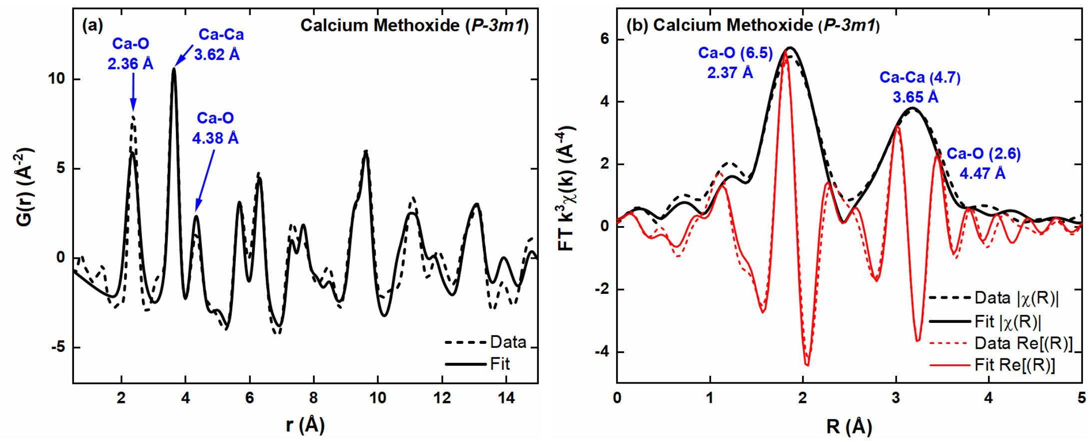

Figure 5.12. (a) XPDF (G(r)) and (b) Ca K-edge k^3-weighted Fourier transform (FT) magnitude(|X(R)|) and real (Re[(R)]) EXAFS for $Ca(OCH_3)_2$ (*P-3m1*) (91). All plots show atom pair contributions and calculated interatomic distances (r). The EXAFS also shows the coordination numbers ($N_{O/C/Ca}$) in parentheses.

Compared to the $Ca(OH)_2$ *P-3m1* model (90), the proposed *P-3m1* $Ca(OCH_3)_2$ structure (91) does not account for H positions. The absence of the hydrogens not only affected the short-range order in the XPDF and EXAFS (Figure 5.12), but also the medium-range i.e. beyond 6 Å in the XPDF. Interpretation of the medium-range region is still in the infancy stages and so it is difficult to confidently determine the single/multiple scattering contributions. However, more robust refinement methods such as Reverse Monte Carlo (RMC) have successfully been applied to relevant systems such as amorphous calcium carbonate (ACC) (67). Irrespective of the missing hydrogens, it was possible to obtain a new refined structure for the $Ca(OCH_3)_2$ based on the proposed model (91) and the XPDF data (Figure 5.12a). This refined structure was exported from PDFgui (86) and applied to the EXAFS to give a reasonably good fit.

The interatomic distances for the Ca-O (2.36 ± 0.01 Å) and Ca-Ca (3.64 ± 0.02 Å) obtained in both the XPDF and EXAFS (Figure 5.12) are reasonably close to the predicted values of about 2.24 and 3.64 Å (91). However, the refined values for both the Ca-O distances and c-axis are greater than the predictions (91). This suggests the possibility of loose packing in the unit cell. Further refinement with the inclusion of H atoms is required to obtain a more accurate model. Additionally, the EXAFS (Figure 5.9b) shows that the $Ca(OCH_3)_2$ first coordination sphere N_O value of about 6 is similar to that of $Ca(OH)_2$ (Figure 5.11b) This result correlates with the similarity of the XANES spectra (Figure 5.9a) and *P-3m1* space groups of the two compounds. Furthermore, the relatively lower N_{Ca} value (4.7) for the Ca scatters (Figure 5.12b) suggests different stacking in the $Ca(OCH_3)_2$ crystal structure compared to $Ca(OH)_2$. This could relate to the disorder that was observed in the $Ca(OCH_3)_2$ PXRD/S(Q) (Figure 5.7) and XANES (Figure 5.9a) data, which was linked to the presence of the large CH_3 group (~1/2 of the a-axis).

Calcite, Aragonite and Vaterite. Application of both XPDF and EXAFS to the crystalline $CaCO_3$ polymorphs proved to be beneficial with regards to screening model crystal structures and elucidating scattering contributions from the low Z atoms. XPDF refinement of $CaCO_3$-α (Figure 5.13a) and $CaCO_3$-β (Figure 5.14a) data, using the *R-3c* (20) and *Pnma* (92) models respectively, resulted in reasonably good fits with R-factors of 20.9 and 18.2 %. Similar to the CaO and $Ca(OH)_2$, the interatomic distances calculated from the XPDF and EXAFS (Figures 5.13 and 5.14) are in agreement with crystallographic models (*cf.* Table 3.3) (20, 92) and literature values (55, 56, 64, 183). The coordination number of the first oxygen coordination sphere is most notable difference between the EXAFS for $CaCO_3$-α (Figure 5.13b) and $CaCO_3$-β (Figure 5.14b). The calculated N_O values are about 6 and 9 for $CaCO_3$-α and $CaCO_3$-β respectively. Notably, the $CaCO_3$-β N_O is a sum of oxygens from two environments (24, 55, 56, 58, 64, 183).

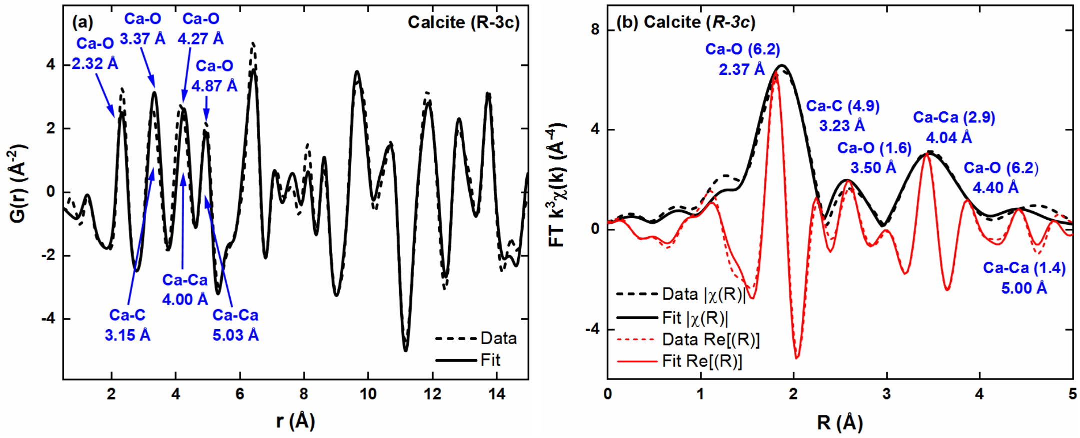

Figure 5.13. (a) XPDF (G(r)) and (b) Ca K-edge k^3-weighted Fourier transform (FT) magnitude(|X(R)|) and real (Re[(R)]) EXAFS for $CaCO_3$-α (*R-3c*) (20). All plots show atom pair contributions and calculated interatomic distances (r). The EXAFS also shows the coordination numbers ($N_{O/C/Ca}$) in parentheses.

Comparatively, the refinement of the $CaCO_3$-γ was more intricate since its crystal structure is yet to be fully determined. The previous mid-IR (*cf.* section 5.3) and XANES (*cf.* section 5.5) analyses eliminated most of the models in Table C.1 (Appendix C) with equivalent CO_3^{2-} ions and/or centres of symmetry, including the orthorhombic *Pbnm* (93) and *Ama2* (94) structures used in Figure 5.15. There are major variations between the short-range experimental data and theoretical fits in both XPDF and EXAFS (Figure 5.15). Notably, the pseudo-hexagonal nature of the *Ama2* (94) model improves the XPDF fit in the medium-range region (Figure 5.15c). Ultimately, it can be concluded that $CaCO_3$-γ does not have a centrosymmetric orthorhombic structure with equivalent carbonates based on the underestimation of the first coordination sphere Ca-O peaks in both the XPDF and EXAFS.

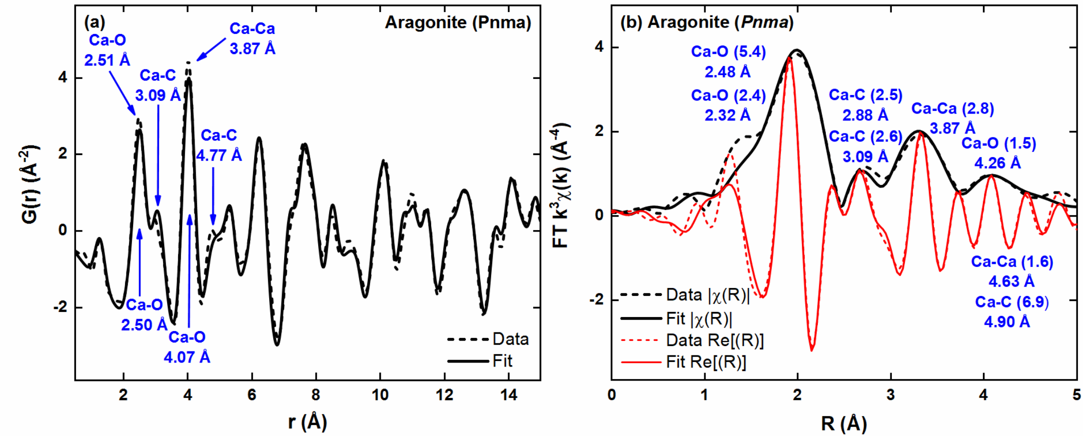

Figure 5.14. (a) XPDF (G(r)) and (b) Ca K-edge k^3-weighted Fourier transform (FT) magnitude(|X(R)|) and real (Re[(R)]) EXAFS for $CaCO_3$-β (*Pnma*) (92). All plots show atom pair contributions and calculated interatomic distances (r). The EXAFS also shows the coordination numbers ($N_{O/C/Ca}$) in parentheses.

Significant improvements in the theoretical $CaCO_3$-γ XPDF and EXAFS were achieved when the hexagonal ($P6_522$) (27) and monoclinic (*C1*) (163) models were used (Figure 5.16). Both structures consist of non-equivalent CO_3^{2-} ions and a hexagonal unit cell (164) based on the $P6_3/mmc$ model (159), which is associated with the long-range diffraction data (*cf.* section 5.4). EXAFS fitting (Figures 5.16 b and d) revealed that the first peak is a function of overlapping scattering effects from two oxygen environments. The first and second Ca-O coordination spheres consist of about 6 (2.35 ± 0.01 Å) and 3 (2.95 ± 0.01 Å) oxygen atoms respectively. The overlap of these two Ca-O spheres supports the theory of non-equivalent carbonates and could account for variations in reported coordination numbers that range from 6 to 8 (55, 163, 165). Notably, a similar Ca-O overlap was observed in the $CaCO_3$-β EXAFS (Figure 5.14b) with about 3 and 6 oxygen atoms at 2.32 and 2.48 Å respectively. The relatively higher interatomic distance of the second $CaCO_3$-γ Ca-O compared to $CaCO_3$-β alludes to disorder in the $CaCO_3$-γ structure. Disorder was also observed in the long-range PXRD/S(Q) data (*cf.* section 5.4) and XANES (*cf.* section 5.5).

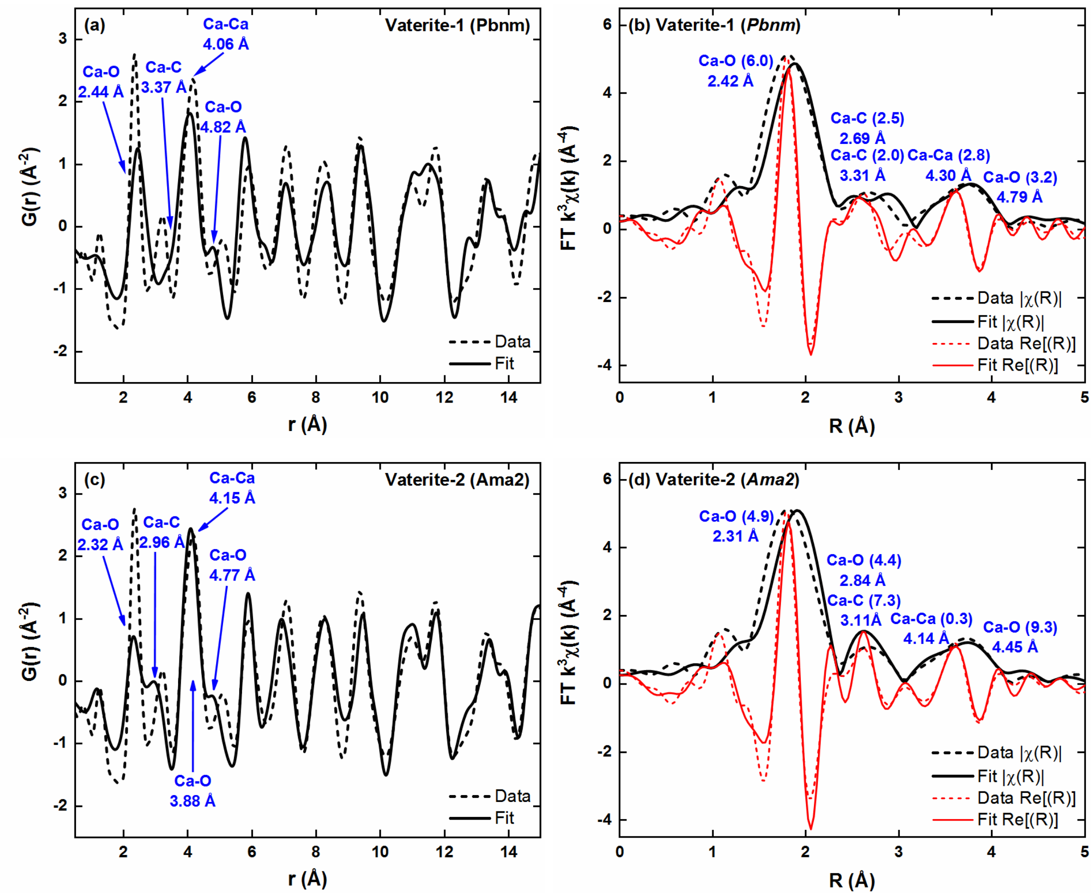

Figure 5.15. XPDF (G(r)) and Ca K-edge k^3-weighted Fourier transform (FT) magnitude(|X(R)|) and real (Re[(R)]) EXAFS for (a and b) orthorhombic vaterite-1 ($CaCO_3$-γ; *Pbnm*) (93) and (c and d) orthorhombic vaterite-2 ($CaCO_3$-γ; *Ama2*) (94). All plots show atom pair contributions and calculated interatomic distances (r). The EXAFS also shows the coordination numbers ($N_{O/C/Ca}$) in parentheses.

A closer inspection of the first two peaks in the $CaCO_3$-γ XPDF shows that the *C1* model (Figure 5.16c) fits better than the *$P6_522$* (Figure 5.16a). This is supported by the complementary Re[(R)] EXAFS spectra (Figures 5.16 b and d), which shows subtle improvements for the initial three Ca-O, Ca-O and Ca-C coordination spheres. Furthermore, neither model fits the XPDF medium-range (> 6Å) completely. Since the scattering contributions to the medium-range are not well understood, it is difficult to correlate the fit variations to the models. However, it has been suggested that at least two structures co-exist in $CaCO_3$-γ crystals (95, 184). Perhaps combining two or more model structures might improve the XPDF fit. Ultimately, it can be concluded that the $CaCO_3$-γ structure has non-equivalent CO_3^{2-} ions (23, 157). This is based on the relatively good XPDF and EXAFS fits obtained with hexagonal (*$P6_522$*) (27) and monoclinic (*C1*) (163). Out of the twenty-three vaterite models (Table C.1 in Appendix C), the 6-layered *C1* structure (163) (Figure 5.16a) fit the EXAFS and XPDF data better.

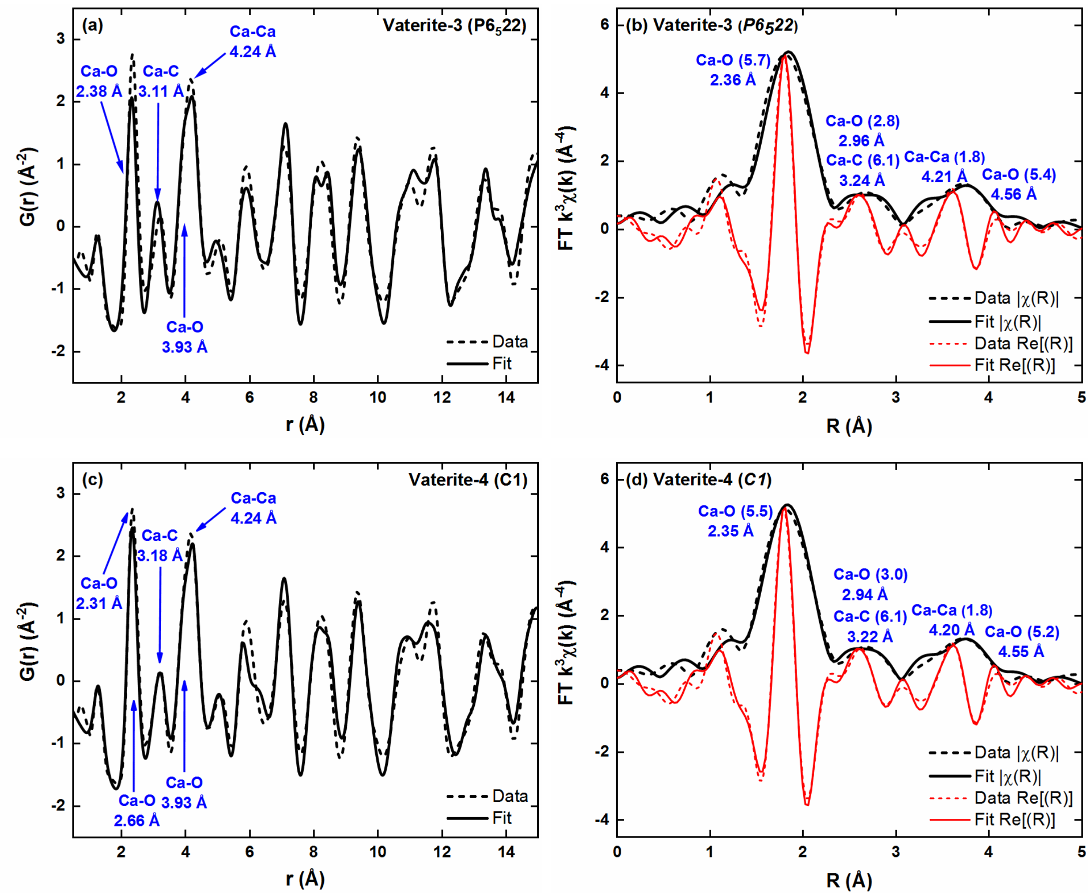

Figure 5.16. XPDF (G(r)) and Ca K-edge k^3-weighted Fourier transform (FT) magnitude(|X(R)|) and real (Re[(R)]) EXAFS for (a and b) hexagonal vaterite-3 ($CaCO_3$-γ; *P6$_5$22*) and (c and d) monoclinic vaterite-4 ($CaCO_3$-γ; *C1*) (163). All plots show atom pair contributions and calculated interatomic distances (r). The EXAFS also shows the coordination numbers ($N_{O/C/Ca}$) in parentheses.

5.7 Conclusions

A comprehensive structural analysis of $CaCO_3$ polymorphs and their precursors – calcium oxide (CaO), hydroxide ($Ca(OH)_2$) and methoxide ($Ca(OCH_3)_2$) – using a variety of analytical techniques was presented. Variations in the morphology and short- to long-range molecular structures were determined. Remarkable morphological differences were observed with plate-like $Ca(OCH_3)_2$, rhombohedral calcite ($CaCO_3$-α), needle-like aragonite ($CaCO_3$-β) and porous spherical vaterite ($CaCO_3$-γ). Diffraction and spectroscopic analysis of CaO, $Ca(OH)_2$, $Ca(OCH_3)_2$, $CaCO_3$-α and $CaCO_3$-β confirmed their crystal structures to be cubic (*Fm-3m*) (89), hexagonal (*P-3m1*) (90), hexagonal (*P-3m1*) (91), rhombohedral (*R-3c*) (20) and orthorhombic (*Pmna*) (92) respectively. Conversely, the 'true' structure of $CaCO_3$-γ was more ambiguous. Long-range PXRD and S(Q) data correlated with the hexagonal *P6$_3$/mmc* structure (159), which does not account for the presence of non-equivalent CO_3^{2-} ions determined from Mid-IR and XANES analysis. XPDF and EXAFS analysis of the $CaCO_3$-γ local structure showed that the most probable structure is the non-centrosymmetric 6-layered *C1* monoclinic model (163), with non-equivalent carbonates. Notably, the medium-range XPDF highlighted the possibility of two structures in $CaCO_3$-γ as has been reported previously (95, 184). Further quantitative analysis is required to prove this theory. The results highlight the sensitivity of XPDF and EXAFS to variations between proposed crystal structure models especially with metastable vaterite, whose crystal symmetry, unit cell dimensions and orientation of the carbonate ions are controversial.

Chapter 6:

Formation of Calcium Methoxides, Esters and Sol-gels

6.1 Introduction

The work described in this chapter is concerned with the function of methanol (CH_3OH) and water (H_2O) in the reactive crystallisation of the $CaCO_3$ core of overbased detergents. CH_3OH is generally considered as a 'promoter' in the synthesis of overbased calcium sulphonate detergents prepared *via* the *oxide/hydroxide* process (7). The exact role of CH_3OH, beyond being a dispersant and/or co-surfactant, is not fully understood – much like the mechanism and kinetics of calcium carbonate ($CaCO_3$) formation (7, 13, 34). One proposed theory is that CH_3OH interacts with calcium oxide (CaO) or hydroxide ($Ca(OH)_2$) to form a more soluble intermediate (7). However, the methoxylation process has not been extensively researched because it is generally assumed that the oxide and hydroxide do not dissolve in or react with CH_3OH. However, studies have shown that both CaO and $Ca(OH)_2$ are slightly soluble in CH_3OH with solubility values of 0.4 and 0.1 g/L respectively (137). Prolonged exposure of the bases to CH_3OH results in the formation of calcium hydroxide methoxide ($Ca(OH)(OCH_3)$) and/or calcium methoxide ($Ca(OCH_3)_2$) (140, 146, 148, 149, 185-187). The formation of calcium methoxides, ethoxides and isopropoxides has also been observed in cement treatment (149, 188) and stone conversation (189-191). In this case, the synthesis of the two methoxide salts from $Ca(OH)_2$ can be defined by the following reactions (140, 148, 185):

Formation of Calcium Hydroxide Methoxide:

$$\mathrm{Ca(OH)_2(s) + CH_3OH(l) \longleftrightarrow Ca(OH)(OCH_3)(s) + H_2O\ (l)} \qquad [6.1]$$

Formation of Calcium Methoxide:

$$\mathrm{Ca(OH)(OCH_3)\ (s) + CH_3OH\ (l) \longleftrightarrow Ca(OCH_3)_2(s) + H_2O\ (l)} \qquad [6.2]$$

There are notable differences in the reported ratios of the two methoxide salts in the final product with $Ca(OH)(OCH_3)$ ranging from ~92 wt% (185) to trace amounts (140). This controversy mostly stems from the fact that $Ca(OCH_3)_2$ readily converts to $Ca(OH)_2$ upon reaction with H_2O – possibly *via* ($Ca(OH)(OCH_3)$) and/or its hydrate forms. Morphological and structural studies (138-140, 148, 149, 186) of the methoxylation products agree with the experimental (sections 5.2 to 5.4) and literature

(91, 146, 147, 192) reference data for $Ca(OCH_3)_2$. Whereas these results suggest that the di-substituted methoxide is the major product, the formation of $Ca(OH)(OCH_3)$ as the dominant product in a ternary system with a non-polar hydrocarbon solvent cannot be discounted. The preferential transformation of $Ca(OH)_2$ to a mono-substituted calcium salt in alkenes, at an optimal carbonation temperature (~25 °C), has been demonstrated with phenol (193, 194). Notably, the two phenate salts exhibited different solubility properties in non-polar solvents such as toluene and xylene (both used in the overbasing process). The di-substituted phenate salt was found to be soluble in these solvents but the mono-substituted salt was insoluble. There is no literature data on the solubility of either methoxide salt in hydrocarbons, but $Ca(OCH_3)_2$ is reported to be slightly more soluble in methanol (0.4 g/L) than both CaO and $Ca(OH)_2$ (185).

The reactive nature of CH_3OH suggests that the mechanism of formation for calcium detergents could possibly be similar to that of magnesium detergents in the *alkoxide process* (7) (discussed in section 2.2.3). Investigations into the carbonation of $CaO/Ca(OH)_2$ methanolic colloidal dispersions reveal that prior to the formation of $CaCO_3$ (mainly vaterite) a transient carbonated calcium methoxide complex is formed (195). The existence of such complexes in the overbasing process has previously been mentioned (3, 7), but it has never been investigated. Three routes have been proposed (195-197) for the precipitation of $CaCO_3$ in this gas-liquid-solid system:

Route I – *via* Calcium Hydroxide:

$$\mathrm{Ca(OH)_2(s) + CO_2(g) \xrightarrow{CH_3OH\,(l)} CaCO_3(s) + H_2O\,(l)} \qquad [6.3]$$

Route II – *via* Calcium Hydroxide Methoxide:

$$\mathrm{Ca(OH)(OCH_3)\,(s) + CO_2(g) \longrightarrow Ca(OH)(OCOOCH_3)\,(s)} \qquad [6.4]$$

$$\mathrm{Ca(OH)(OCOOCH_3)\,(s) \longrightarrow CaCO_3(s) + CH_3OH\,(l)} \qquad [6.5]$$

Route III – *via* Calcium Methoxide:

$$\mathrm{Ca(OCH_3)_2\,(s) + 2CO_2(g) \longrightarrow Ca(OCOOCH_3)_2\,(s)} \qquad [6.6]$$

$$\mathrm{Ca(OCOOCH_3)_2\,(s) + H_2O\,(l) \longrightarrow CaCO_3(s) + CH_3OH\,(l) + CO_2(g)} \qquad [6.7]$$

The first route (equation 6.3) involves the expected reaction of $Ca(OH)_2$ with carbon dioxide (CO_2). This route is based on the assumptions that either $Ca(OH)_2$ doesn't react with CH_3OH or the methoxide salts revert to the base (as shown in equations 6.1

and 6.2). The second (equations 6.4 and 6.5) and third (equations 6.6 and 6.7) routes are two-step reaction sequences, which involve the carbonation of the two methoxide salts to form the equivalent mono- and di-substituted carbonate ester intermediates (195-197). Both calcium methyl hydroxide carbonate ($Ca(OH)(OCOOCH_3)$) and calcium di-methylcarbonate ($Ca(OCOOCH_3)_2$) have separately been reported as intermediates (195, 197). The structures of both carbonate esters are yet to be resolved, as most of the previous studies focused on characterising the final $CaCO_3$ product. Interestingly, the post-carbonation products from routes two and three have a tendency to form a sol-gel overtime (195-197). It has been observed that the presence of ≤20 wt% of H_2O (in routes two and three) seems to increase the rate of both gel and $CaCO_3$ formation. Gelation was observed almost immediately in systems with 10 to 20 wt% H_2O but the most stable and translucent gels were obtained in the presence of 0.2 wt% (195). For commercial products such as aerogels/xerogels dry methanol is recommended (197). However, in the case of overbased detergents, gel formation is undesirable thus ≤10 wt% of H_2O is included in the process (3, 16) (discussed in section 2.3.3.3).

Herein, the carbonation of $Ca(OH)_2$ colloidal dispersions in pure (100 mol%) and slightly diluted (10 mol% of H_2O) CH_3OH systems were investigated. The main aims were to (i) prove the existence of transient calcium methoxide salts and carbonate esters; (ii) elucidate the structures of these metal-organic complexes and the resulting $CaCO_3$ sol-gel/precipitates; and (iii) determine the main reaction pathway for the formation of $CaCO_3$ in a methanolic systems. The *ex situ* analytical results on various calcium compounds presented in this chapter combined with the results from chapter 5 informed the interpretation of results from the *in situ/operando* analysis of complex multiphase-multicomponent systems (chapter 7) and the complete overbasing process (chapter 8).

6.2 Calcium Methoxide Salts

Mid-infrared (mid-IR) spectroscopy was used to determine the effects of mixing calcium hydroxide ($Ca(OH)_2$) with pure methanol (CH_3OH) in an inert environment. The experimental procedure is detailed in section 3.3.2. The resulting spectrum (Figure 6.1) shows the same characteristic peaks for $Ca(OH)_2$ and calcium methoxide ($Ca(OCH_3)_2$) that were identified previously (*cf.* Figures 5.5 b and c). Unreacted $Ca(OH)_2$ is easily identified by a sharp OH stretch (ν_{OH}) at 3641 cm^{-1}. The previously assigned calcite ($CaCO_3$-α) impurity peaks present in the hydroxide IR spectrum (*cf.* Figure 5.5b/Table 5.1) at 1452 (ν^a_{CO2}) and 874 (γ_{CO2}) cm^{-1} are also present. Formation of the methoxide salt is evident in Figure 6.1 by the appearance of the methoxy stretching (ν_{OCH3} – 1053 cm^{-1}), asymmetric methyl stretching (ν^a_{CH3} – 2841 and 2785 cm^{-1}), asymmetric methyl in-plane bending (δ^a_{CH3} – 1467 cm^{-1}) and methyl rocking (ρ_{CH3} – 1162 cm^{-1}) vibrations. The minor methoxide $2 \cdot \delta^a_{CH3}$ (2922 cm^{-1}) and $2 \cdot \nu_{OCH3}$ (2090 cm^{-1}) overtones and $\nu_{OCH3} + \delta^a_{CH3}$ combination band (2593 cm^{-1}) can also be observed.

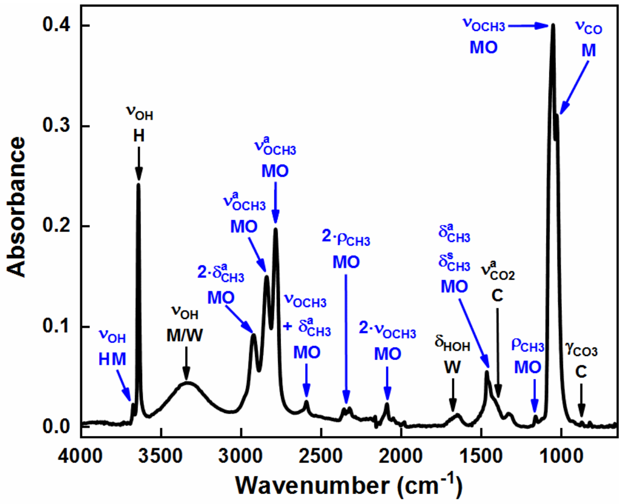

Figure 6.1. Mid-IR plot for the product from the methoxylation of $Ca(OH)_2$. Vibrations due to $Ca(OH)_2$ (H), $CaCO_3$-α (C), CH_3OH (M), $Ca(OH)(OCH_3)$ (HM), $Ca(OCH_3)_2$ (MO) and H_2O (W) have been highlighted.

Notably, there are extra peaks in Figure 6.1 that can be assigned to other compounds apart from the solid reactant ($Ca(OH)_2$) and main product ($Ca(OCH_3)_2$). These include residual liquid CH_3OH (peaks at ~3339 (ν_{OH}) and 1031(ν_{CO}) cm^{-1}) and liquid water (H_2O) (peaks at ~3339 (ν_{HOH}) and 1642(δ_{HOH}) cm^{-1}). Additionally, there is a weak peak at 3674 cm^{-1} which has previously (140) been attributed to a calcium hydroxide methoxide ($Ca(OH)(OCH_3)$) ν_{OH} stretch. The +33 cm^{-1} shift in the ν_{OH} stretch from the $Ca(OH)_2$ to $Ca(OH)(OCH_3)$ is indicative of stronger bonding in the methoxide hydroxyl group. This shift can be linked to the different electronegativities of the OH^- (2.78) and OCH_3^- (2.48) (198, 199) and their effects on the electron density of neighbouring anions. The more electronegative OH^- pulls more electrons from the other OH^- in $Ca(OH)_2$ than the OCH_3^- does in $Ca(OH)(OCH_3)$. Thus the lower wavenumber of the hydroxide ν_{OH} stretch is due to destabilisation of the neighbouring OH bond. Ultimately, the presence of IR vibrations from both methoxide salts confirms the proposed two-step methoxylation reaction (equations 6.1 and 6.2) (140, 185). The di-substituted methoxide is the main product in line with previous $Ca(OH)_2$ methoxylation studies (140, 149). Notably, this result disagrees with Berner's (185) conclusion that the mono-substituted methoxide constitutes ~92 wt% of the final product.

6.3 Calcium Methyl Carbonate Esters

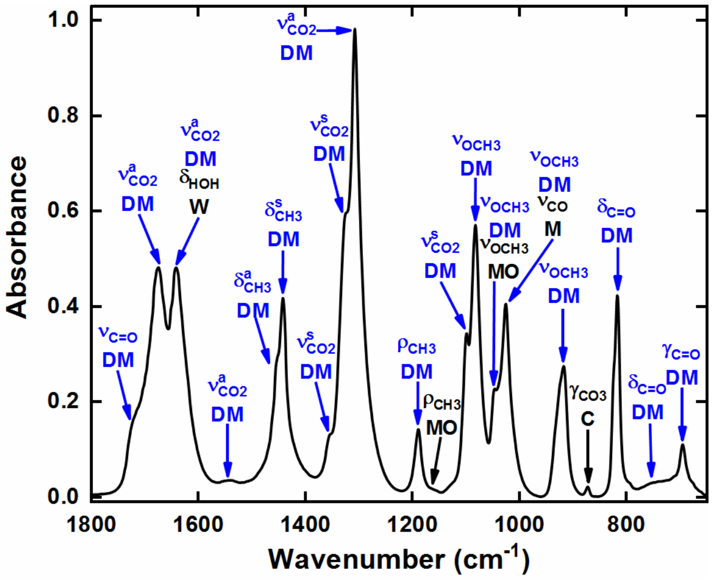

Figure 6.2. Mid-IR plot for the initial post-carbonation product from the 100 mol% $Ca(OH)_2$ methanolic dispersion. Vibrations due to CH_3OH (M), $Ca(OCH_3)_2$ (MO), $Ca(OCOOCH_3)_2$ (DM) and H_2O (W) have been highlighted.

Mid Infrared (Mid-IR) Spectroscopy. The reactive crystallisation of calcium carbonate ($CaCO_3$) from calcium hydroxide ($Ca(OH)_2$) in pure methanol (CH_3OH; 100 mol%) was investigated. The experimental procedure is detailed in section 3.3.2. The mid-IR for the initial (15 min) post-carbonation product (Figure 6.2) shows multiple vibrations (summarised in Table 6.1) in the 1800 to 650 cm^{-1} region. The precipitation of $CaCO_3$ directly from $Ca(OH)_2$ (route I – equation 6.3) was excluded by the appearance of multiple non-characteristic $CaCO_3$ stretching and deformation features. As previously discussed in section 5.3 (Figure 5.3b), calcite ($CaCO_3$-α), aragonite ($CaCO_3$-β) and vaterite ($CaCO_3$-γ) display only about 7 features in this IR region. This is also the case for monohydrocalcite ($CaCO_3 \cdot H_2O$) (162), ikaite ($CaCO_3 \cdot 6H_2O$) (162) and amorphous $CaCO_3$ (ACC) (152, 200, 201). Notably, the features at ~1453, 878 and 696 cm^{-1} in Figure 6.2 could ambiguously be attributed to one or two $CaCO_3$ polymorphs. Analysis of the product after 60 hours in open air (Figure 6.3) shows that it converts to $CaCO_3$-α with traces of aragonite ($CaCO_3$-β). In this instance, precipitation is a function of atmospheric relative humidity.

Table 6.1. Mid-IR vibrations (cm^{-1}) for the methoxycarbonyl anion ($CH_3OCO_2^-$) (150) and the post-carbonation product from the 100 mol% CH_3OH (M) system at 15 minutes (initial) and 60 hours (aged). Vibrations due to $Ca(OH)_2$ (H), $Ca(OCH_3)_2$ (MO), $Ca(OCOOCH_3)_2$ (DM), $CaCO_3$-α (C), $CaCO_3$-β (A) and $CaCO_3$-γ (V) have been assigned.

Assignments	Anion $CH_3OCO_2^-$	100 mol% CH_3OH Product			
		Initial (15 min)		Aged (60 h)	
ν_{OH}	-	3642	H	-	-
ν_{OH}	-	3295	M or W	-	-
ν^a_{CH3}	2990 ± 40	2987; 2953; 2913	M/DM	2926	M
ν^s_{CH3}	2920 ± 80	2893;2856	DM/MO?	2856	DM/MO?
$2 \cdot \nu^s_{CO2}$	-	2013	DM	-	-
$\nu^s_{CO3} + \delta_{CO3}$	-	-	-	1796	C
$\nu_{C=O}$	1750 ± 50	1730;1720; 1700	DM	-	-
ν^a_{CO2}	-	1677; 1642	DM	-	-
δ_{HOH}	-	1640	W	-	-
δ^a_{CH3}	1450 ± 15	1453; 1445	M/DM	-	-
δ^s_{CH3}	1435 ± 15	1442; 1431	DM	-	-
ν^a_{CO3}	-	-	-	1402; 1397	C
ν^s_{CO2}	-	1358	DM	-	-
ν^s_{CO2}	-	1329	DM	-	-
ν^a_{CO2}	1255 ± 60	1309; 1308	DM	-	-
ρ_{CH3}	1185 ± 35	1190	DM	-	-
ρ_{CH3}		1160	MO	-	-
ν_{OCH3}/ν^s_{CO3}	975 ± 125	1100; 1089; 1083; 1070	DM	1080	A
ν_{OCH3}		1049; 1045; 1030	MO	-	-
ν_{CO}		1025	M	-	-
ν_{OCH3}		924; 918; 908	DM	-	-
ν_{OCH3}/γ_{CO3}		873	DM	873; 857; 848	C and A
$\delta_{C=O}$	715 ± 115	825; 818; 816; 735	DM	-	-
$\gamma_{C=O}/\delta_{CO3}$	635 ± 130	696; 692	DM	713	C

The occurrence of a $Ca(OH)_2$ methoxylation reaction (equations 6.1 and 6.2), in conjunction with carbonation, is evident in Figure 6.2. There are weak to medium ρ_{CH3} (1160 cm^{-1}) and ν_{OCH3} (1049 cm^{-1}) contributions due to a methoxide salt. The absence of the $Ca(OH)(OCH_3)$ ν_{OH} stretch at ~3674 cm^{-1} (identified in Figure 6.1) alludes to the formation of mainly $Ca(OCH_3)_2$. Notably, $Ca(OCH_3)_2$ formed at a faster rate (<40 min; Figure 6.2) in the carbonated environment than the inert methoxylation system (24 h; Figure 6.1). The rate increase can be attributed to a forward shift in the reaction equilibrium (equations 6.1 and 6.2) due to: (i) a conversion of the methoxide to a carbonated species as suggested in equation 6.6; and/or (ii) the methoxylation being catalysed by carbonic acid (H_2CO_3), which is formed *via* a reaction of the CO_2 with an OH^- from CH_3OH and H_2O.

Ultimately, these results suggest that the $CaCO_3$-α (Figure 6.3) is precipitated *via* the third reaction route in equation 6.5 as suggested by Buzagh (195) and Plank *et al.* (196). Therefore, the majority of the peaks observed in Figure 6.2 must be from the calcium di-methylcarbonate ($Ca(OCOOCH_3)_2$) ester. This transient ester intermediate is yet to be characterised. Hence, the post-carbonation IR (Figures 6.2 and D.1) was compared to spectra obtained for various metal-organic/organic compounds with similar chemical structures. These reference compounds included: calcium formate ($Ca(COOH)_2$) (202), calcium acetate monohydrate ($Ca(COOCH_3)_2$) (202, 203), calcium propionate monohydrate ($Ca(COOCH_2CH_3)_2$) (204), potassium methyl carbonate ($K(OCOOCH_3)$) (205), lithium methyl carbonate ($Li(OCOOCH_3)$) (206, 207), dimethyl carbonate ($CO(OCH_3)_2$) (208) and dimethyl dicarbonate ($O(COOCH_3)_2$) (209). This comparative analysis resulted in peak assignments for the initial post-carbonation product summarised in Table 6.1.

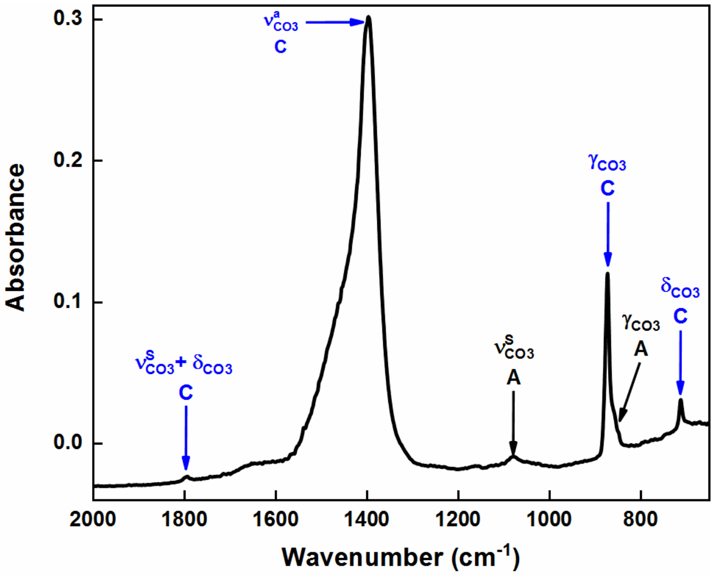

Figure 6.3. Mid-IR plot for the aged (60 hours) post-carbonation product from the 100 mol% $Ca(OH)_2$ methanolic dispersion. Vibrations due to $CaCO_3$-α (C) and $CaCO_3$-β (A) have been highlighted.

Characteristic ester peaks due to C=O and C(=O)-O stretching were identified in the initial post-carbonation IR (Figure 6.2) at 1682 ± 35 ($\nu_{C=O}$), 1308 (ν^a_{CO2}), 1100 (ν^s_{CO2}), and 1083 (ν^s_{CO2}) cm^{-1}. The presence of $Ca(OCOOCH_3)_2$ was confirmed by these methoxycarbonyl peaks. This was further evidenced by the appearance of methyl/methoxy vibrations (δ_{CH3} – 1454 and 1442 cm^{-1}; ρ_{CH3} – 1190; and ν_{OCH3} – 918 and 878 cm^{-1}) not present in the $Ca(OCH_3)_2$ IR (*cf.* Figure 5.3a/Table 5.1). Further comparison of the initial spectrum with the organic/metal-organic reference IR spectra revealed the possibility of conformational polymorphism and the presence of a hydrate. Both cis-cis and cis-trans conformers have been observed in the IR of dimethyl carbonate (208) and di-methylcarbonate (209), whereby the cis-cis was the more thermodynamically stable form. Hence, the observed ν^a_{CO2} (1676 and 1651 cm^{-}

^{1}) and ν^{s}_{CO2} (1083 cm^{-1}) degeneracies could possibly be due to a second $Ca(OCOOCH_3)_2$ conformer, which is most likely the cis-trans.

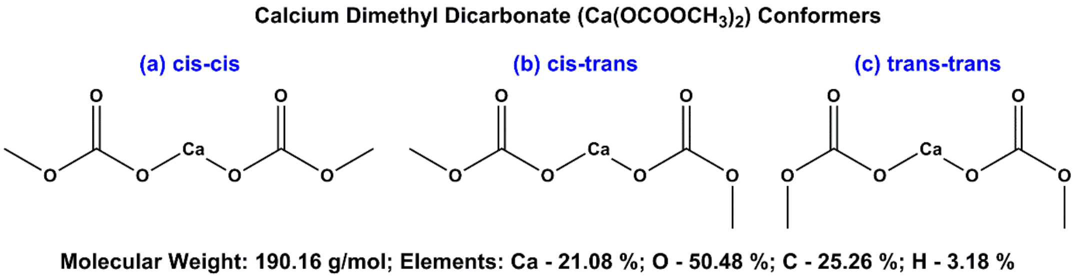

Figure 6.4. Possible conformations of $Ca(OCOOCH_3)_2$ based on variations of the methyl group ($-CH_3$) orientation.

Figure 6.4 shows three possible structures of the $Ca(OCOOCH_3)_2$ conformers based on variations in the orientation of methyl groups. Preliminary attempts to simulate the IR spectra of the conformers based on basic molecular dynamics were marginally successful. The theoretical gas phase spectra (not shown here) for the three conformers each displayed some peaks, which are present in the experimental IR (Figure 6.2). However, the probability of a hydrate (δ_{HOH} – 1642 cm^{-1}) (145) or dimerization, as observed with calcium propionate monohydrate (204) and lithium methyl carbonate (206, 207) respectively, were not considered. A more precise *ab initio* study on a pure sample is required, which will account for multiple factors including solute-solvent and solute-solute interactions.

Conclusively, the Mid-IR results confirm the presence of the $Ca(OCOOCH_3)_2$ ester and that $CaCO_3$-α is precipitated *via* route III (equation 6.7). Whereas the point symmetry of the methoxycarbonyl anion ($CH_3OCO_2^-$) has been determined as *m* (205), the crystal symmetry of $Ca(OCOOCH_3)_2$ is yet to be defined. However, its space group is most likely monoclinic (e.g. *P*21/*a*) like various hydrated carboxylic esters such as calcium propionate monohydrate (204). Refinement of X-ray scattering data on a pure sample, as demonstrated for $Ca(OCH_3)_2$ and $CaCO_3$-γ (*cf.* section 5.6), would give better indications of its symmetry. The similarity of $Ca(OCOOCH_3)_2$ to these esters will be explored further in the subsequent sub-sections.

Powder X-ray Diffraction (PXRD). Time-resolved PXRD (Figures 6.5 and D.2) was also used to confirm the presence of the $Ca(OCOOCH_3)_2$ ester (≤15 min) and show its transformation into various forms of $CaCO_3$ (~60 h). The initial PXRD pattern for the ester in Figure 6.5a was reproducibly obtained in various experiments. A similar PXRD pattern with a relatively strong peak at about 7.3° (d-spacing of 12.1 Å) has been observed for calcium propionate monohydrate (204) and this peak was assigned to a dominating -200 reflection. This reflection was also present in the other hydrated carboxylic esters studied at varying positions (from ~4.5° to 6.0°) (204). Definitive indexing of $Ca(OCOOCH_3)_2$ will require Rietveld refinement of the diffraction pattern of an isolated pure single crystal. Notably, much like the mid-IR (Figure 6.2), the PXRD patterns show that the $Ca(OCH_3)_2$ precursor is almost always present in the sample.

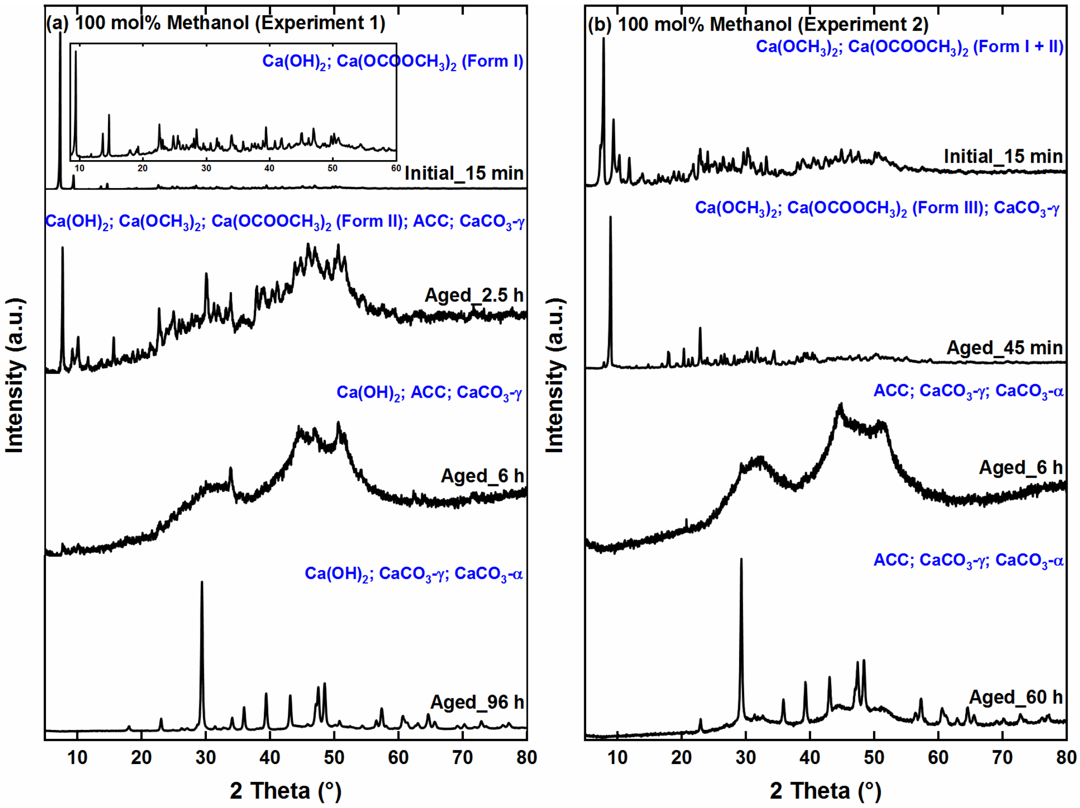

Figure 6.5. Time-resolved PXRD plots showing the products precipitated from the carbonation of the pure (100 mol%) methanolic dispersion in experiment 1 (a) and 2 (b). Features/peaks due to $Ca(OH)_2$, $Ca(OCH_3)_2$, $Ca(OCOOCH_3)_2$, ACC, $CaCO_3$-γ and $CaCO_3$-α were identified.

Inspection of the post-carbonation product PXRD (Figure 6.5a) beyond 15 mins showed a decrease in the intensity of the peak at 7.31° and the subsequent appearance of a lower intensity peak at 7.82° (d-spacing of 11.3 Å). Initially it was assumed that the second pattern was merely due to the expected loss of methanol *via* equation 6.5 as $CaCO_3$ formed. However, in an isolated case (experiment 2 in Figures 6.5b and D.2), this second peak (at ≤15 min) transformed further into a higher intensity peak at 8.92° (d-spacing of 9.91 Å) after 30 minutes in open air. A peak-to-peak comparison of the three PXRD patterns (at ≤45 min in Figures 6.5 a and b) revealed unique reflections pertaining to different forms. The three patterns were assigned to forms I, II and III of the $Ca(OCOOCH_3)_2$.

Whereas the aforementioned assignments might not be definitive and require further analysis, they do highlight the possibility of polymorphism. These transformations mirror the observations made in the mid-IR analysis about the presence of a hydrate and/or second conformer. Pseudo- and conformational polymorphism are highly debated topics especially with regards to organic pharmaceutical compounds (210). Since the $Ca(OCOOCH_3)_2$ ester has never been characterised before, it is difficult to conclude that it definitely exists in three forms. Ultimately, these results highlight that there is an inherent need to explore the structure(s) of the initial transient post-carbonation product as a function of time and synthesis environment. Various analytical techniques with the capability of distinguishing polymorphs, such as thermogravimetric analysis (TGA) and X-ray pair distribution function (XPDF), are being considered. Presently, X-ray absorption spectroscopy (XAS) has been used to determine how the intermediate electronic/local structure differs from $Ca(OH)_2$, $Ca(OCH_3)_2$ and $CaCO_3$ (detailed in section 6.3.4).

Interestingly, the observed difference between the two experiments in Figure 6.5 can be linked to the extent of carbonation as evidenced by the presence of unreacted $Ca(OH)_2$ in the first experiment (Figure 6.5a). The hydroxide seems to promote the stability of form I, thus slowing down its transformation into form II and subsequently $CaCO_3$. This stabilising role played by the $Ca(OH)_2$ could explain the observations made previously (7, 13) about its secondary role in the synthesis of overbased calcium sulphonate detergents (*cf.* section 2.2.2). It has been noted that the complete carbonation of $Ca(OH)_2$ leads to the crystallisation of the $CaCO_3$ in the form of calcite and/or vaterite (7, 13). These crystalline particles tend to destabilise the surfactant shell of the detergent particles, which affects the properties of the colloidal dispersion. As such, the extent of carbonation in the overbasing system is limited to about 90% of the required stoichiometric amount required to form $CaCO_3$ (7). Notably, similarity in the reaction behaviour of the $Ca(OCOOCH_3)_2$ intermediate and detergent particles even extends to $CaCO_3$ precipitation in the presence of acetone (3, 33, 42, 195, 211).

Finally, the formation of $CaCO_3$-α as the final product is evident in both experiments (Figure 6.5). This agrees with the mid-IR results shown in Figure 6.3. Ultimately, the time-resolved PXRD patterns show that the $Ca(OCOOCH_3)_2$ (in the presence of the $Ca(OCH_3)_2$ precursor) transforms into $CaCO_3$-α *via* a mixture of ACC and $CaCO_3$-γ. The contributions from the $CaCO_3$-γ are present as minor reflections in the PXRD patterns for forms II and III of $Ca(OCOOCH_3)_2$ and as inflections in the two broad diffused peaks characteristic of ACC (212-214). The kinetics and mechanisms involved in the formation of $CaCO_3$-α *via* this ACC/$CaCO_3$-γ have previously been explored in various alcohol-water systems (189-191, 201, 215-217). In this particular case, the most reasonable explanation is that the precipitation of ACC/$CaCO_3$-γ is kinetically favoured in the methanol-induced supersaturated system (215). This can be linked to the low solubility of both $Ca(OH)_2$ and the $CaCO_3$-α in alcohols.

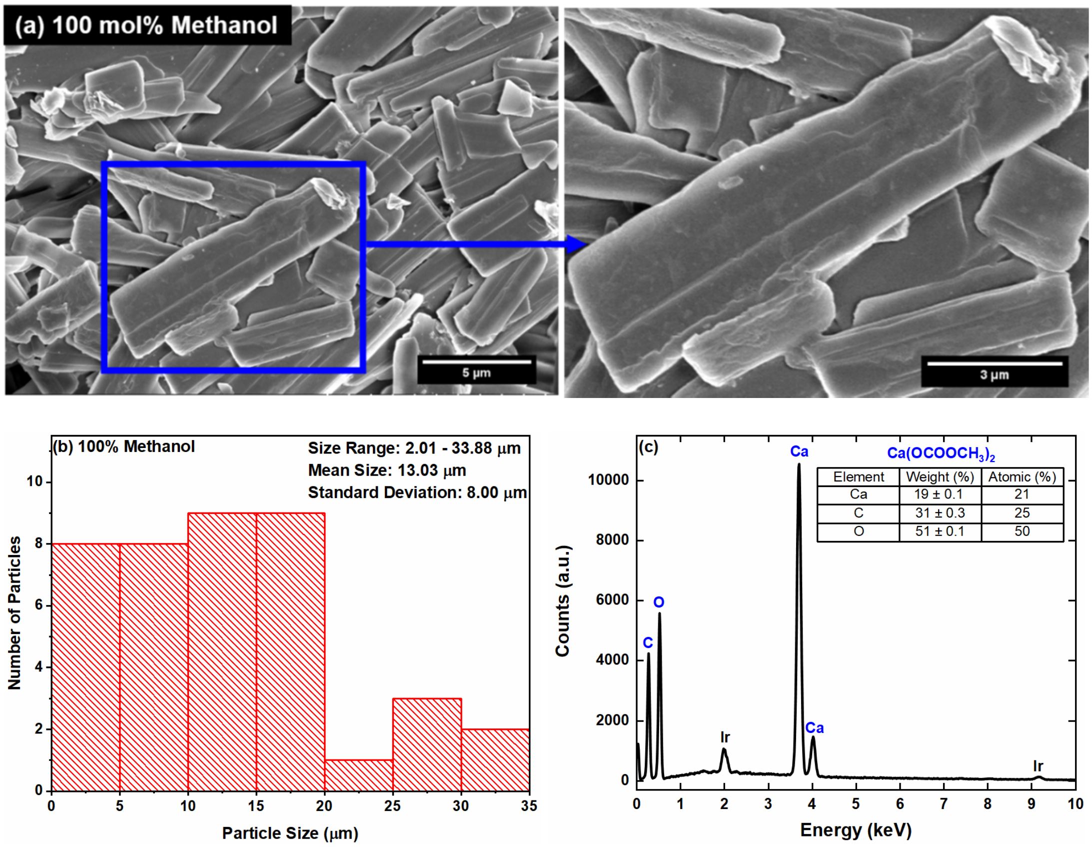

Figure 6.6. (a) SEM micrographs of rod-like $Ca(OCOOCH_3)_2$ particles synthesised from the 100 mol% $Ca(OH)_2$ methanolic dispersion and a complementary (b) particle size distribution plot (based on 40 particles) and (c) EDX spectrum.

Scanning Electron Microscopy (SEM). SEM was used to determine the morphology of the waxy white $Ca(OCOOCH_3)_2$ precipitate. Figure 6.6 shows that the powder consists of thin rectangular polydisperse rod-like crystals ranging from about 2 to 34 µm. The shape of the crystals are distinctly different from those determined previously for the three $CaCO_3$ crystalline polymorphs and $Ca(OCH_3)_2$ (*cf.* Figures 5.2 to 5.4). However, the particles are comparable to the those obtained for calcium propionate monohydrate (204). This similarity in morphology further supports the postulation that the ester is likely to have a monoclinic *P*21/*a* space group like the other hydrated carboxylic acid esters (204). Energy dispersive X-ray (EDX) spectroscopy of the particles (Figure 6.6c) revealed that the Ca to C to O ratio of the particles was about 19:31:51. The element compositions are comparable to the theoretical values of 21:25:50 (Figure 6.4) for the $Ca(OCOOCH_3)_2$, even without accounting for adventitious carbon and hydrogen contributions.

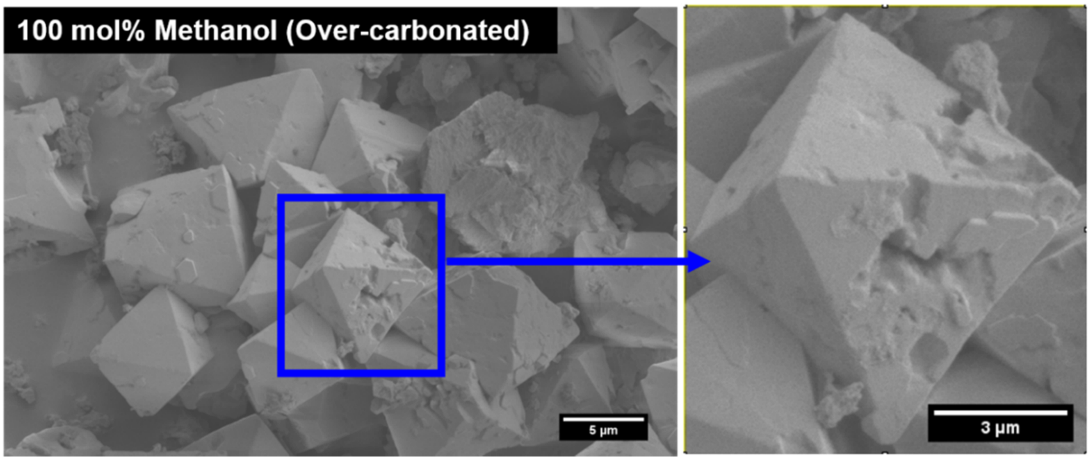

Figure 6.7. SEM micrographs highlighting how excess CO_2 in the pure methanolic dispersion results in the precipitation of polyhedral $CaCO_3$-α instead of rod-like $Ca(OCOOCH_3)_2$ particles (Figure 6.6).

In order to test the theory of $Ca(OH)_2$ acting as a stabiliser, CO_2 was bubbled through the system for a longer duration than the required 40 minutes. SEM (Figure 6.7) of the over-carbonated products shows both distinct micro-sized polyhedral crystals and clusters of mixed nano- and micro-sized particles. Mid-IR (not shown here) confirmed that the polyhedral particles are $CaCO_3$-α and that observed clusters are a mixture of the $Ca(OCOOCH_3)_2$ and ACC. The presence of $CaCO_3$-γ was not confirmed as the IR spectrum did not show a distinct in-plane bending (δ_{CO3}) vibration at 745 cm^{-1}.

X-ray absorption Near-Edge Structure (XANES). Complementary structural information about the 100 mol% CH_3OH product (now assumed to be a form of $Ca(OCOOCH_3)_2$) was obtained using XANES and EXAFS (Figure 6.8). The Ca K-edge XANES for the product (Figure 6.8a), when compared to $Ca(OH)_2$ and $Ca(OCH_3)_2$ spectra (*cf.* Figure 5.9a), shows considerable reductions in the features due to the 1s → 4p electronic transitions (from 4045 to 4060 eV; labelled B – D). As was discussed in section 4.3.4, these features are defined by: (i) interactions of Ca 4p with neighbouring Ca 3d/4s and C π* states (170, 176-178); (ii) the scattering and coordination number of the first shell neighbouring oxygen atoms; and (iii) the orientation/collinearity of the anion. Initially, it was assumed that the product (at the time of the measurement) mainly consisted of ACC due to the non-definitive 1s → 4p features and a prominent 1s → 3d dipole forbidden transition (at 4040 eV). However, a review of the Ca K-edge XANES for calcium acetate (218, 219) and calcium propionate (220) monohydrates revealed analogous non-distinctive spectral features. They all seem to have a sharp peak at 4050 eV (C) and a slight modulation at 4060 eV (D). The presence of this relatively minor D feature has been linked to hydration in the case of calcium acetate (219). This could imply that the structure of the 100 mol% CH_3OH product is $Ca(OCOOCH_3)_2·xH_2O$. However, this disregards the influence of the packing arrangement of anions on the spectrum. The non-collinear arrangement of the CO_3^{2-} ions in the anhydrous CaCO3-β contributes to the diminution of this 1s → 4p feature (*cf.* Figure 5.9b).

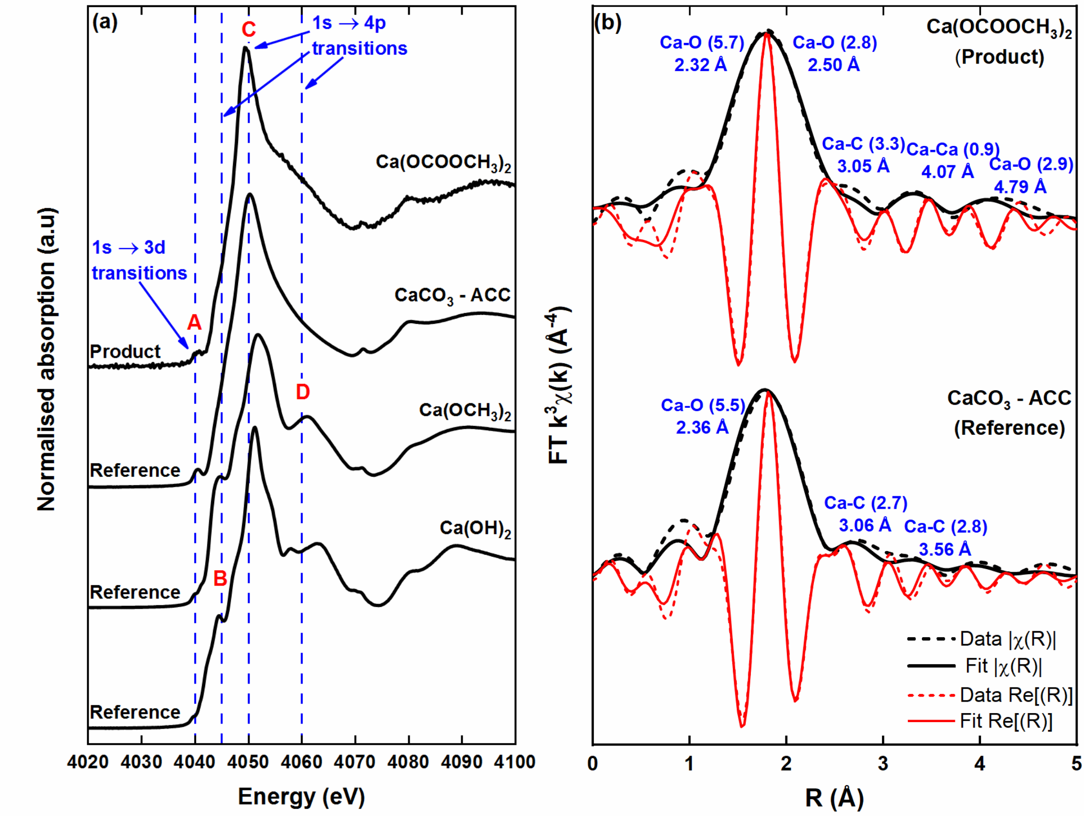

Figure 6.8. Ca K-edge (a) XANES and (b) k^3-weighted Fourier transform (FT) magnitude(|X(R)|) and real (Re[(R)]) EXAFS for $Ca(OCOOCH_3)_2$ compared to $Ca(OH)_2$, $Ca(OCH_3)_2$ and ACC – includes atom pair contributions, interatomic distances and coordination numbers ($N_{O/C/Ca}$).

Extended X-ray Absorption Fine Structure (EXAFS). As was established with the reference calcium-containing compounds in section 4.3.4, the intensity of peak C is indicative of the coordination number of the first scattering shell oxygens (N_O). A comparison of the $Ca(OCOOCH_3)_2$ XANES (Figure 6.8) with the $Ca(OH)_2$ and $Ca(OCH_3)_2$ spectra (*cf.* Figure 5.9a) suggested an N_O value of greater than 6 for the dicarbonate ester. This was confirmed by the quantitative EXAFS analysis (Figure 6.8b). Since both the ester and ACC have no known structure, various $CaCO_3$ models were tested including the structures for the 3 anhydrous polymorphs summarised in Table 3.3 (*cf.* section 3.4.4). The best models were chosen based on relative R-factor and reduced chi-square (χ^2) values (62, 63). Favourable results were obtained for the ACC (R-factor of 1.51 %) using the *C1* $CaCO_3$-γ model (95). The first Ca-O shell N_O (5.5) and R (2.36 Å) values are similar to those previously reported for synthetic ACC (59). The N_O suggests that the ACC in this study is anhydrous unlike various other biogenic and synthetic ACC samples (25, 54, 57, 58) with reported N_O values of ~8, akin to monohydrocalcite ($CaCO_3{\cdot}H_2O$). Short-range order beyond this first shell is usually not reported for stable/pure ACC samples. However, some studies (53, 54) have shown carbon contributions in the second and third shell. Levi-Kalisman *et al.* (54) report N_c values ranging of 1.5 and 3 for these two shells at 3.03 and 3.36 Å respectively. A similar fitting method of varying N was applied, which could explain the similarity to the EXAFS results in Figure 6.8b.

Conversely, the $Ca(OCOOCH_3)_2$ ester EXAFS (Figure 6.8b) showed a preference to the $CaCO_3{\cdot}H_2O$ structure producing a fit with an R-factor of 1.11 %. Two oxygen environments with a combined N_O of ~8.5 were identified at 2.32 and 2.50 Å. These oxygens could be purely due to the ester carbonyl groups, much like $CaCO_3$-β (Figure 5.14b). However, fitting of the subsequent shells revealed a partiality to oxygens from the water molecules included in the $CaCO_3{\cdot}H_2O$ model. This reiterates the possible presence of water in the molecule, as observed in the mid-IR, PXRD and XANES. A definitive confirmation of a $Ca(OCOOCH_3)_2$ hydrate will require a detailed comparative EXAFS/XPDF analysis with the calcium acetate and propionate monohydrates. Notably, the EXAFS of the ester seems to be dominated by scattering contributions from the O and C atoms with minimal contribution from the heavy Ca scatterers. This is similar to $CaCO_3$-γ (Figure 5.16d) and unlike the $Ca(OH)_2$ Figure 5.11b) and $Ca(OCH_3)_2$ (Figure 5.12b) precursors. This could explain the reasonably good fit obtained even without considering the low-scattering H atoms present in the ester. As such, determination of the crystal structure using XPDF as was demonstrated with $Ca(OCH_3)_2$ (Figure 5.12a) should be possible.

6.4 Calcium Carbonate Sol-gel

Scanning Electron Microscopy (SEM). Carbonation of the diluted (10 mol% H_2O) methanolic $Ca(OH)_2$ colloidal dispersion resulted in the formation of a translucent sol-gel (Figure A.1a in Appendix A). The initial cryo-SEM micrographs of the sol-gel (Figures 6.9 and D.1 in Appendix D) displayed a myriad of particles with varying morphologies from cubes to spheres to dendrites. Initially, it was assumed that the dendrite-like structures (Figure D.3) were similar to the polycrystalline dendrites acquired due to diffusion limited aggregation in gels (136, 221). However, repeat experiments (Figure 6.9a) revealed that the gel mainly consisted of clusters of spherical particles of about 110 nm (Figure 6.9b). Hence, the previously observed dendrite-like formations could be traces of CH_3OH crystallisation due to cryo-treatment of the gel. Similar patterns were observed upon sublimation of the sol-gel to -90 ° C, which is close to the melting point of anhydrous CH_3OH (-97.6 ° C) (222). All subsequent experiments were carried out without sublimation, but there is an obvious need to further investigate the issue of solvent crystallisation versus polymerisation.

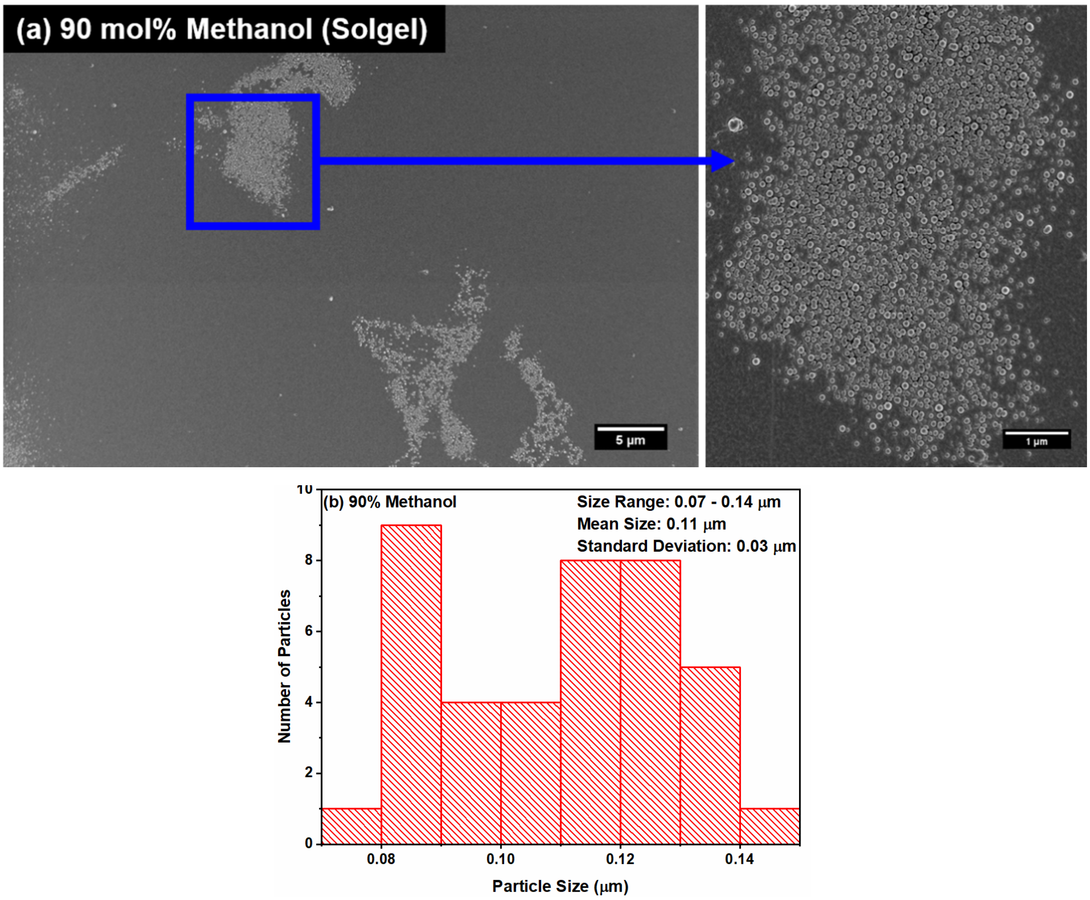

Figure 6.9. (a) Cryo-SEM micrographs of the sol-gel post-carbonation product from the 90 mol% $Ca(OH)_2$ methanolic dispersion showing clusters of spherical ACC particles; and (b) a complementary size distribution plot for the ACC particles (based on 40 particles).

In this study, gel formation *via* the aggregation route is dictated by three main processes i.e. (i) the hydrolysis of the $Ca(OCOOCH_3)_2$ ester to form $CaCO_3$ nanoparticles (equation 6.7); (ii) the aggregation of the nanoparticles; and (iii) condensation of the system to form the gel. This is similar to the gel formation process proposed by Plank *et al.* (196). Notably, the hydrolysis and condensation reactions can be catalysed by an acid (H_2CO_3) and/or a base ($Ca(OH)_2$) (223). The spherical nature of the nanoparticles observed in the SEM (Figure 6.9a) suggests that the hydrolysis and condensation occur in a high pH system (223, 224). Further condensation of the gel led to syneresis i.e. gel shrinkage and CH_3OH expulsion (225). Precipitation of $CaCO_3$ can be observed (Figure A.1 in Appendix A) during/after the syneresis process.

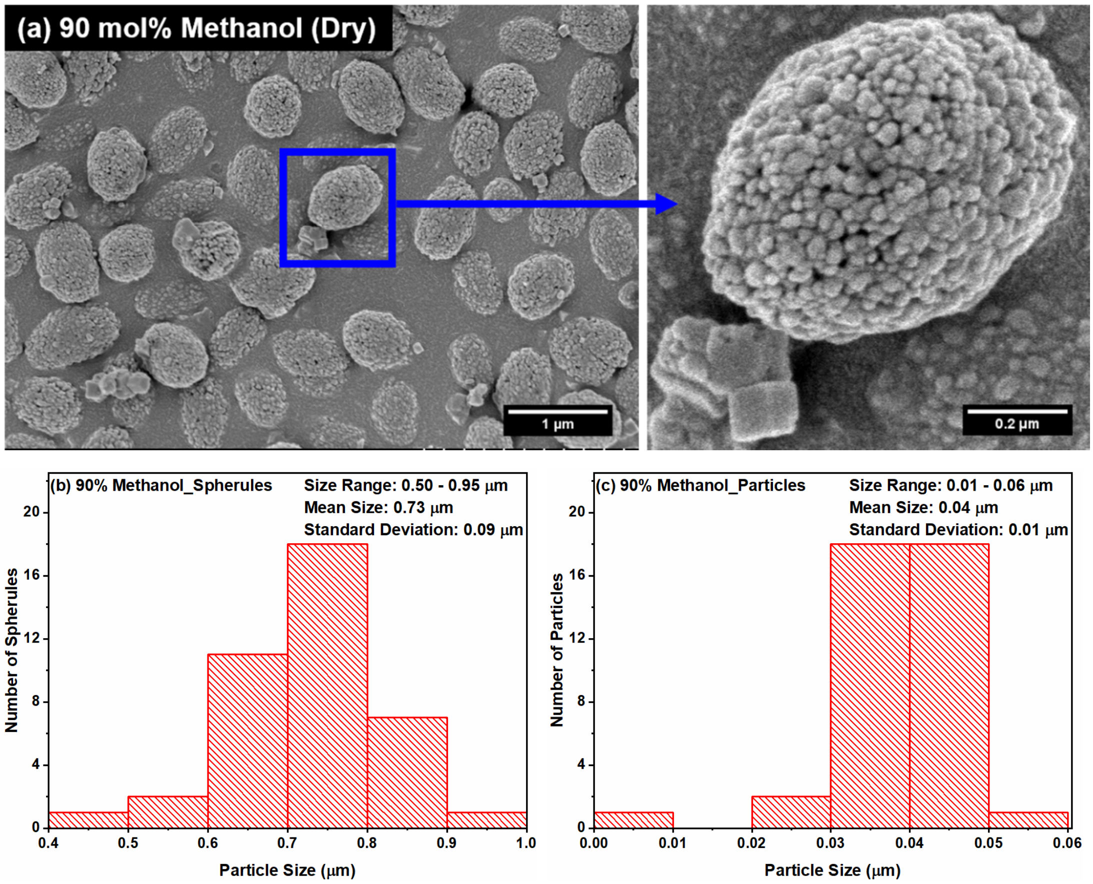

Figure 6.10. (a) SEM micrographs of the dry sol-gel (1 hour) showing $CaCO_3$-γ spherules and traces of cubic $CaCO_3$-α. Complementary size distribution plots (based on 40 particles) for the $CaCO_3$-γ (b) spherules and (c) constituent particles have been included.

The SEM of the dried precipitated powder (Figure 6.10a) shows that an hour after carbonation the product mainly consisted of $CaCO_3$-γ spherules. The morphology of these particles (precipitated in a methanolic environment) is slightly different to the porous $CaCO_3$-γ particles (precipitated in an aqueous environment) (*cf.* Figure 5.4). The ~730 nm spherules (Figure 6.10b) are essentially aggregates of smaller (~40 nm) $CaCO_3$-γ particles (Figure 6.10c). Notably, these 40 nm particles are smaller than the ACC precursors (~110 nm) that were observed in the sol-gel. This decrease in size has been observed previously in relation to the transformation of ACC to crystalline

$CaCO_3$-γ *via* a dissolution-precipitation process (190, 226, 227). Closer inspection of the SEM (Figure 6.10a) shows the growth of cubic $CaCO_3$-α particles. This sequence of polymorphic transformations (ACC→$CaCO_3$-γ→$CaCO_3$-α) appears to be in tandem with previous studies that have suggested non-classical crystal growth (190, 228). However, further SEM/TEM investigations on this particular system are required to substantiate this theory.

Mid Infrared (Mid-IR) Spectroscopy. Figure 6.11a shows the Mid-IR of the initial sol-gel product (~15 minutes) with features pertaining to CH_3OH (ν_{CO} – 1026 cm^{-1}), H_2O (δ_{HOH} – 1660 cm^{-1}), $Ca(OCOOCH_3)_2$ ($\nu_{C=O}/\nu^{a}_{CO2}$ – 1660 cm^{-1}; $\delta^{a}_{CH3}/\ \delta^{s}_{CH3}$ – 1450 cm^{-1}; ν^{s}_{CO2} – 1335 cm^{-1}; ρ_{CH3} – 1192 cm^{-1}; ν_{OCH3} – 1100 cm^{-1}; and $\delta_{C=O}$ – 825 cm^{-1}), ACC (γ_{CO3} – 860 cm^{-1}) and calcite (δ_{CO3} – 712 cm^{-1}). The discernible amounts of $CaCO_3$ in the sol-gel, compared to the $Ca(OCOOCH_3)_2$ product (Figure 6.2), were indicative of an increased conversion/precipitation rate due to the presence of the H_2O. This can be attributed to increased H_2CO_3 formation and $Ca(OH)_2$ solubility. The H_2CO_3 promotes the hydrolysis of $Ca(OCOOCH_3)_2$ (reaction 8), which was also observed in the PXRD (Figure 4b) and SEM (Figure 6b) of over-carbonated 100 mol% CH_3OH dispersions. Comparison of the initial and aged samples in Figure 6.11 confirmed that both calcite and vaterite (δ_{CO3} – 745 cm^{-1}) were formed *via* ACC. This is consistent with the previously discussed results for the pure system.

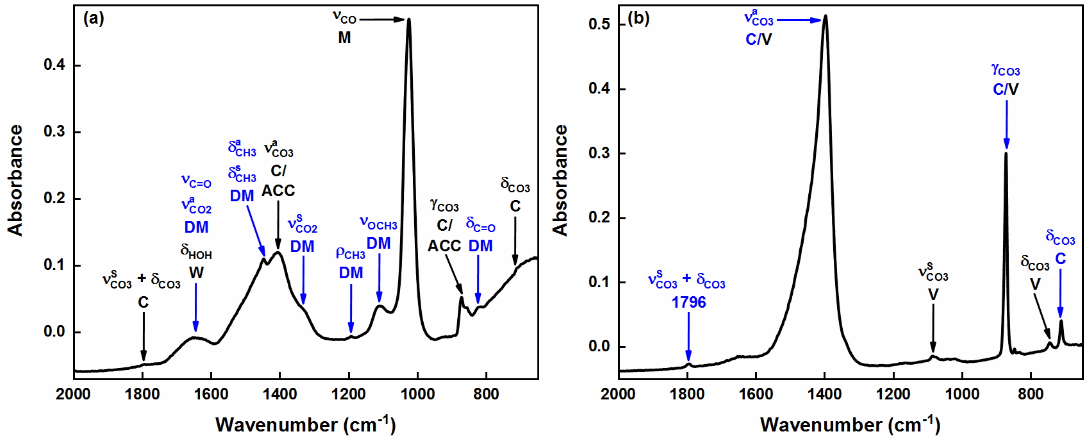

Figure 6.11. Mid-IR plots for the (a) initial (15 minutes – sol-gel) and (b) aged (60 hours – precipitate) from the 90 mol% $Ca(OH)_2$ methanolic dispersion. Vibrations due to CH_3OH (M), $Ca(OCOOCH_3)_2$ (DM), $CaCO_3$-α (C), $CaCO_3$-γ ,ACC and H_2O (W)have been highlighted.

Powder X-ray Diffraction (PXRD). The transformation from ACC to vaterite to calcite was also confirmed by time-resolved PXRD (Figure 6.12). Broad diffuse maxima were evident in the initial PXRD pattern, confirming the amorphous nature of the sol-gel. Vaterite peaks became more apparent after 90 minutes as the sol-gel underwent syneresis (i.e. gel shrinkage and CH_3OH expulsion). Beyond 105 minutes most of the product consisted of vaterite and calcite. Evidently, $CaCO_3$ precipitated at a faster in the presence of 10 mol% of H_2O than in the pure system (Figure 6.5), which only had trace amounts of vaterite even after 6 hours. The influence of H_2O on gelation and $CaCO_3$ precipitation has been discussed in more detail in section 7.3.

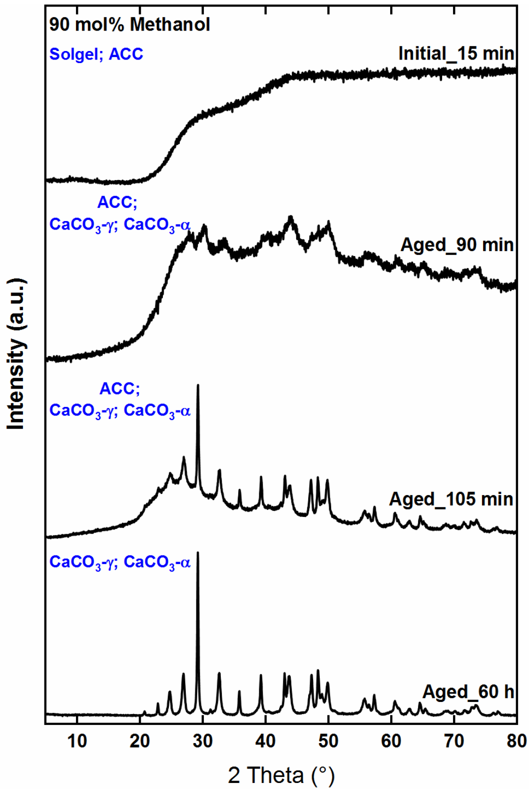

Figure 6.12. Time-resolved PXRD plot showing the post-carbonation product from the 90 mol% $Ca(OH)_2$ methanolic dispersion. Features/peaks due to ACC, $CaCO_3$-γ and $CaCO_3$-α have been identified.

X-ray absorption Spectroscopy (XAS). The absence of distinct 1s → 4p features at 4045 (B) and 4060 (D) eV in the sol-gel Ca K-edge XANES spectra (Figure 6.14a) were indicative of ACC. This was supported by similarities with the ACC reference XANES and the lack of order beyond the first oxygen shell (at 2.41 Å) in the complementary EXAFS data (Figure 6.13b). However, fitting of the EXAFS using the $CaCO_3 \cdot H_2O$ model showed that the gel was more similar to the $Ca(OCOOCH_3)_2$ than ACC (Figure 6.8b) with an N_O value of about 9. After gel syneresis (~1 hour) the 1s → 4p XANES features due to the product became more pronounced (Figure 6.13a). A comparison with the three $CaCO_3$ polymorphs (*cf.* Figure 5.9b) confirmed the presence of vaterite in the precipitate (visible in Figure A.1c in Appendix A).

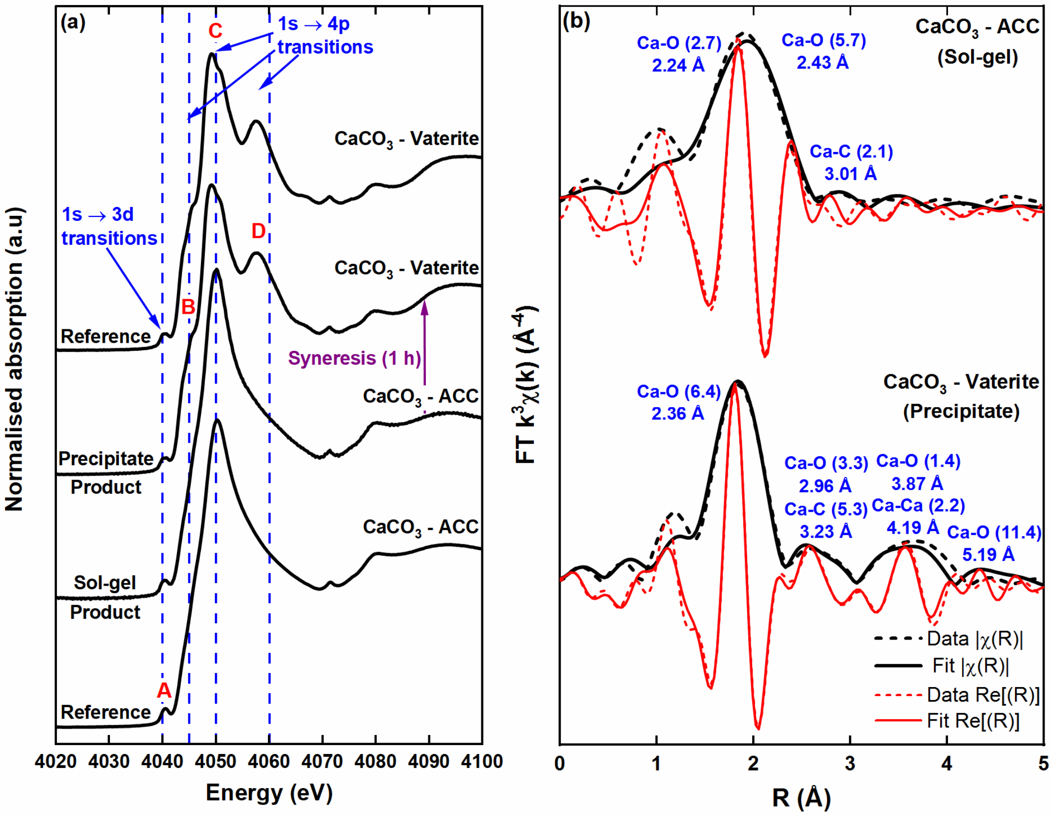

Figure 6.13. (a) Ca K-edge (a) XANES for the post-carbonation sol-gel (~15 minutes) and dried precipitate (~1 hour) products compared to ACC and $CaCO_3$-γ references; and (b) k^3-weighted Fourier transform (FT) magnitude(|X(R)|) and real (Re[(R)]) EXAFS for the sol-gel and dried precipitate – includes atom pair contributions, interatomic distances and coordination numbers ($N_{O/C/Ca}$).

6.5 Conclusions

The reactivity of methanol (CH_3OH) and its role in the carbonation of calcium hydroxide ($Ca(OH)_2$) were investigated. A methoxylation reaction was confirmed following the mixing of pure CH_3OH (100 mol%) and $Ca(OH)_2$ – calcium methoxide ($Ca(OCH)_3$) was formed *via* calcium hydroxide methoxide ($Ca(OH)(OCH)_3$). Carbonation of a pure methanolic $Ca(OH)_2$ dispersion resulted in the formation of a calcium di-methylcarbonate ($Ca(OCOOCH_3)_2$) ester. Notably, a sol-gel was formed following the carbonation of the methanolic dispersion in the presence 10 mol% water (H_2O). Time-resolved PXRD analysis in both cases showed that the $Ca(OCOOCH_3)_2$ converts to amorphous $CaCO_3$ (ACC) then vaterite ($CaCO_3$-γ) and finally calcite ($CaCO_3$-α). Whereas a rod-like morphological structure of the $Ca(OCOOCH_3)_2$ was confirmed by SEM, its atomic structure was more ambiguous. Mid-IR, PXRD and XAS structural analysis highlighted the presence of an metal-organic compound and the possibility of polymorphism and/or hydration. Confirmation of polymorphs and/or hydrates will require further structural analysis using other analytical techniques (e.g. XPDF used in section 5.6) and computational modelling.

Chapter 7:
Calcium Carbonate Synthesis in Non-aqueous Systems

7.1 Introduction

This chapter is concerned with the *in situ* analysis of the reactive crystallisation of $CaCO_3$ in non-aqueous systems using mid-infrared (mid-IR) and X-ray absorption spectroscopy (XAS) to understand the role of solvents, in particular the role of methanol (CH_3OH). The role of CH_3OH in the reactive crystallisation of $CaCO_3$ was redefined in chapter 5. It was shown that it dictates the reaction pathway for the formation of $CaCO_3$, in addition to its roles as a dispersant and co-surfactant in the overbasing process. The CH_3OH was confirmed to be reactive with the $Ca(OH)_2$ precursor to form calcium methoxide ($Ca(OCH_3)_2$). Furthermore, the presence of another intermediate – calcium di-methylcarbonate ($Ca(OCOOCH_3)_2$) – was highlighted. Notably, the reactive nature of ethanol (CH_3CH_2OH) and isopropanol ($CH_3CH_2CH_2OH$) has also been observed with $Ca(OH)_2$ nano-sized particles (nanolimes), which are used for art and stone conversation (189-191). However, none of these studies have reported a carbonated metal-organic intermediate prior to the formation of $CaCO_3$.

The function of short-chain alcohols in the precipitation of calcium carbonate ($CaCO_3$) has attracted a lot of interest in various research fields including biomimetics, conservation science (189-191) and fuel additives. Alcohols such as CH_3OH, CH_3CH_2OH and $CH_3CH_2CH_2OH$ are mainly considered as organic additives (in aqueous systems) that control $CaCO_3$ polymorphic transformations (216). The formation and stabilisation of ACC, vaterite and aragonite, instead of the thermodynamically favourable calcite, has been achieved in solvent systems with significant alcohol concentrations (189-191, 201, 215-217, 229-239). The polymorph discrimination has primarily been attributed to higher saturation levels and retardation of dissolution/(re)crystallisation reactions. Additionally, particles precipitated in these systems tend to be smaller in size with less defined morphologies. There is a general understanding of the effects of alcohols on $CaCO_3$ polymorph discrimination in aqueous systems in terms of saturation levels/the rate of dissolution-precipitation reactions. However, their role in multiphase-multicomponent systems such as the overbasing process is yet to be fully explored.

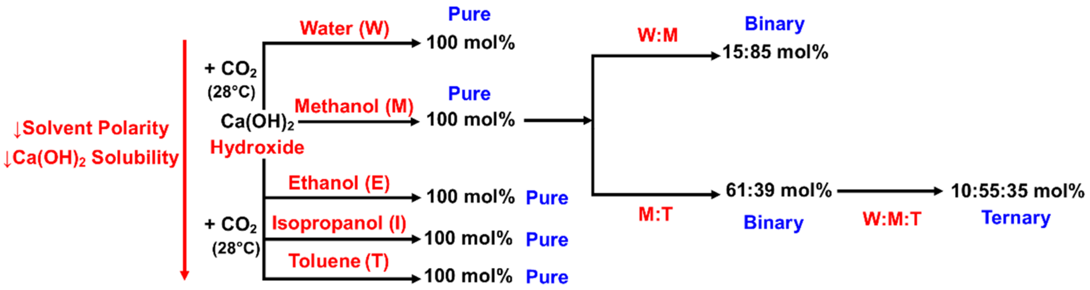

Figure 7.1. Summary of the pure, binary and ternary water, methanol, ethanol, isopropanol and toluene solvent systems studied *in situ* using in-line mid infrared (Mid-IR) and on-line X-ray absorption spectroscopy (XAS).

The work presented here extends on the previous *ex situ* study (chapter 6) on the role of methanol in the precipitation of $CaCO_3$ by looking at the time-resolved changes in Ca speciation. Herein, multiple water-methanol-toluene systems with varying solvent ratios (Figure 7.1) were investigated. Solvent ratios of the binary and ternary solvent systems were determined based on the overbasing process (13, 211). The effects of replacing the CH_3OH with CH_3CH_2OH or $CH_3CH_2CH_2OH$ were also investigated. The applicability of XAS as an on-line process analytical technology (PAT) tool is successfully demonstrated.

7.3 Influence of Water on Gelation and Precipitation

A systematic *in situ* mid-IR study (Figure 7.2) was carried to determine which water (H_2O) and methanol (CH_3OH) systems result in the formation of the sol-gel observed chapter 6. Six different dispersions with methanol content of 20 to 100 mol% were investigated. As expected the formation of the calcium di-methylcarbonate ($Ca(OCOOCH_3)_2$) ester (*cf.* section 6.3) was observed following the carbonation of calcium hydroxide ($Ca(OH)_2$ in the presence of CH_3OH. The *in situ* mid-IR of the 100 mol% system (Figure 7.2a) was compared to the filtered *ex situ* $Ca(OCOOCH_3)_2$ product (*cf.* Figure 6.3). There is an observable decrease in the intensity and resolution/number of normal vibrations due to the ester. These variations are most apparent in the 1800 to 1300 cm^{-1} region, where the most intense $Ca(OCOOCH_3)_2$ ν_{CO2} and δ_{CH3} vibrations appear. Furthermore, there is no evidence of the previously seen calcium methoxide ($Ca(OCH_3)_2$) precursor. These variations can be attributed to the presence of the large volume of solvent (~750 ml), which in some cases masks the contribution of the solutes. As previously mentioned in section 3.4.3, mid-IR is very sensitive to contributions from solvents such as H_2O and CH_3OH (109, 110).

Hence, the methoxide ν_{OCH3} peak, which was previously seen at ~ 1049 cm^{-1} (*cf.* Figure 6.3) is masked by the strong CH_3OH ν_{CO} stretching vibration at 1026 cm^{-1}.

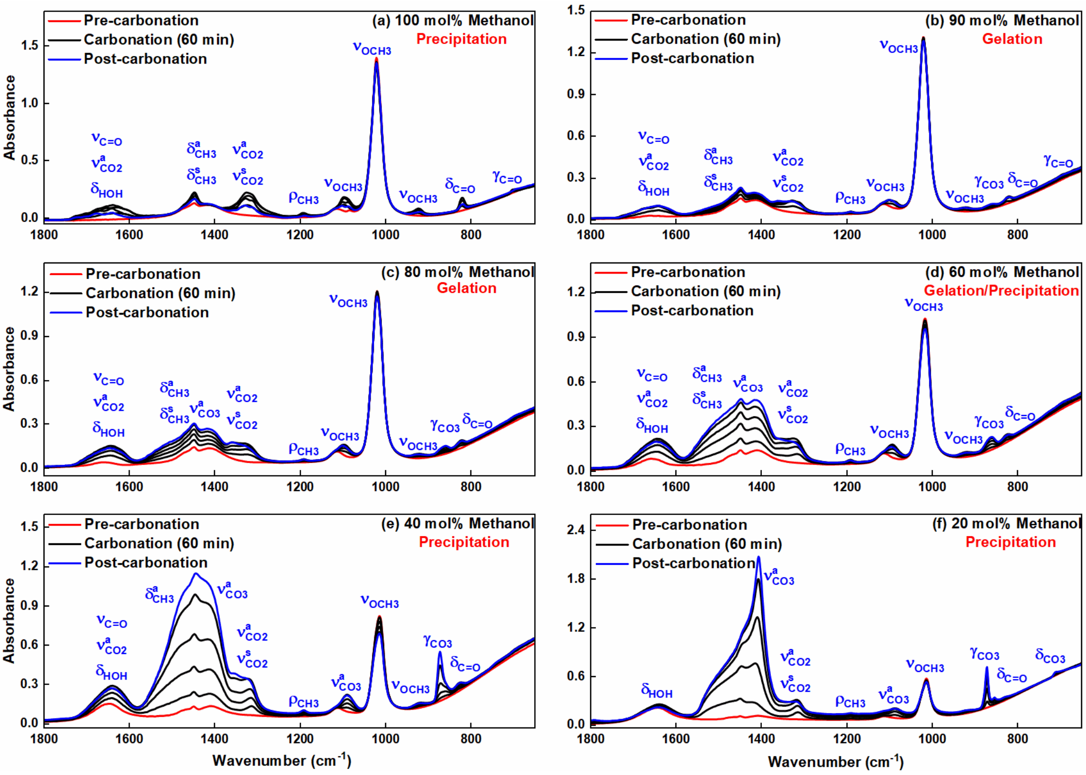

Figure 7.2. Time-resolved mid-IR plots showing the 60-minute carbonation of concentrated $Ca(OH)_2$ dispersions with varying CH_3OH content (20 to 100 mol%). Each black line represents 15 mins of carbonation. Vibrations due to $Ca(OH)_2$, CH_3OH, $Ca(OCOOCH_3)_2$, ACC, $CaCO_3$-α and $CaCO_3$-β have been highlighted.

Figure 7.2 and Table 7.1 show that above the 50 mol% threshold, CH_3OH dictates the reaction pathway *via* which calcium carbonate ($CaCO_3$) is formed. This correlates with the formation of $Ca(OCOOCH_3)_2$ and the gelation of the system up to ~60 mol%. A similar trend in gelation and precipitation has been reported (195) in relation to the formation of the ester intermediate. Based on the results it can be concluded that amorphous calcium carbonate (ACC) is the dominant polymorph at the end of carbonation in the 60, 80 and 90 mol% CH_3OH systems. This is evidenced by the appearance of the characteristic carbonate out-of-plane bending γ_{CO3} at 863 cm^{-1}. The assignment of this peak is still debatable since both $Ca(OCH_3)_2$ and $Ca(OCOOCH_3)_2$ sometimes display a methoxy stretch in this region. In the absence of definitive proof of this stretch (further investigation required), it is safe to assume that the observed peak is due to ACC. As was explained in section 6.4, the formation of the meta-stable ACC and vaterite ($CaCO_3$-γ) polymorphs from a gelatinous system is due to limited ion diffusion (221). The highly supersaturated environment created by the viscous gel media is akin to the 'solvent cages' created by the less polar ethanol (CH_3CH_2OH)

and isopropanol ($CH_3CH_2CH_2OH$). Notably, the reaction of $Ca(OH)_2$ and CH_3OH precludes the significant influence of such molecular interactions at the facets of the hydroxide. These interactions are reported to inhibit the precipitation of the thermodynamically stable calcite ($CaCO_3$-α) and aragonite ($CaCO_3$-β). The effects of the alcohol chain length on $CaCO_3$ crystallisation will be explored further in section 7.4.

Table 7.1. Mid-IR vibrational frequencies (cm^{-1}) for the CH_3OH, $Ca(OH)_2$, $Ca(OCOOCH_3)_2$, ACC, $CaCO_3$-α and $CaCO_3$-β involved in the carbonation of $Ca(OH)_2$ in the presence of CH_3OH (20 to 100 mol%).

Assignments	**Methanol Composition (mol%)**					
	100	**90**	**80**	**60**	**40**	**20**
ν_{OH}	3643	3643	3643	3643	3643	3643
ν_{OH}	3320	3320	3320	3320	3320	3320
$2\cdot\delta^{a}_{CH3}/\ \nu^{a}_{CH3}$	2982; 2944; 2915	2982; 2944; 2915	2982; 2944; 2915	2982; 2944; 2915	2982; 2953	2953
ν^{s}_{CH3}	2832	2832	2832	2832	2837	2844
$2\cdot\nu^{s}_{CO2}$	-	-	-	-	-	-
-	-	-	-	-	-	-
$\nu_{C=O}$	1721	-	-	-	-	-
ν^{a}_{CO2}	1680	-	-	-	-	-
δ_{HOH}	1643	1643	1643	1643	1643	1643
ν^{a}_{CO2}	-	-	1520	-	-	-
δ^{a}_{CH3}	1447	1448	1448	1448	1446	-
$\delta^{s}_{CH3}/\nu^{a}_{CO3}$	1412	1415	1415	1415		1408
ν^{s}_{CO2}	-	1360	1360	-	1355	-
ν^{s}_{CO2}	1330	1326	1322	1326	1322	1322
ν^{a}_{CO2}	1311	-	-	-	-	
ρ_{CH3}	1192	1192	1192	1192	1192	1190
ν_{OCH3}/ν^{s}_{CO3}	1103; 1087	1100	1100	1095	1090	1088
ν_{OCH3}	1022	1020	1020	1018	1015	-
ν_{OCH3}	918	924	924	924	924	-
ν_{OCH3}/γ_{CO3}	-	863	863	863	873	873; 854
$\delta_{C=O}$	820	825	825	825	823	830
$\gamma_{C=O}/\delta_{CO3}$	696	-	-	-	-	712
Initial State	**Precipitate**	**Gel**	**Gel**	**Gel/Precipitate**	**Precipitate**	**Precipitate**

Finally, the formation of crystalline $CaCO_3$ is evident in the mid-IR for the 20 and 40 mol% dispersions (Figures 7.2 e and f). The 20 mol% system shows the precipitation of $CaCO_3$-α (δ_{CO3} – 712 cm^{-1}; γ_{CO3} – 873 cm^{-1}) with traces of $CaCO_3$-β (γ_{CO3} – 854 cm^{-1}). Conversely, the 40 mol% IR is less definitive as to whether the product is $CaCO_3$-α or $CaCO_3$-γ. The distinguishing δ_{CO3} in-plane bending mode is absent, with the appearance of the common γ_{CO3} at 873 cm^{-1} (*cf.* Figure 5.6). Ultimately, this systematic *in situ* mid-IR study shows that three different $CaCO_3$ polymorphs can be formed in methanolic dispersions. Discrimination of these polymorphs is highly dependent on the composition of CH_3OH and the associated formation of a sol-gel.

7.4 Water and Methanol Systems

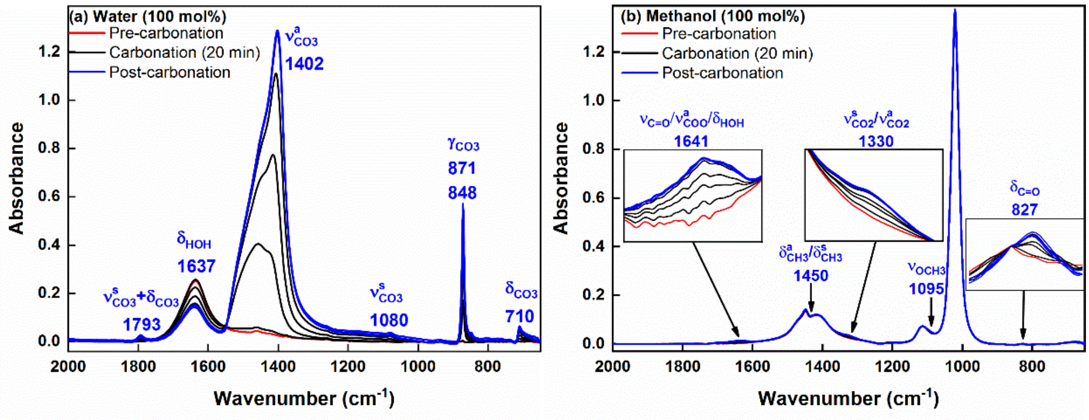

Figure 7.3. *In situ* mid-IR spectra showing the 20-minute carbonation of $Ca(OH)_2$ in 100 mol% (a) H_2O (product – $CaCO_3$-α) and (b) CH_3OH (product – $Ca(OCOCH_3)_2$). Each black line represents 5 mins of carbonation.

The capability of the continuous-flow liquid-jet PAT setup (shown in Figure 4.3) for simultaneous mid infrared (mid-IR) and X-ray absorption spectroscopy (XAS) analysis was explored. It was initially used to determine the time-resolved changes in the Ca speciation in dilute $Ca(OH)_2$-H_2O-CO_2 and $Ca(OH)_2$-CH_3OH-CO_2 systems. Fluorescence yield (FY) X-ray absorption near-edge structure (XANES) spectra were collected at the Ca K-edge before (pre-), during and after (post-) the 20-minute carbonation reactions. Both the mid IR (Figure 7.3) and the XANES (Figure 7.4) showed the formation of $CaCO_3$-α and $Ca(OCOOCH_3)_2$ in the pure H_2O and CH_3OH systems respectively. Inspection of the XANES for both systems revealed significant changes in the features due to the 1s → 4p electronic transitions.

Linear combination fitting (LCF) of the *in situ* XANES spectra (Figure 7.4) was performed using the previously collected references (Figures 5.9 and 6.8). LCF quantified the contributions of the different Ca species to the XANES as a function of time. Selection of reference spectra for LCF was informed by the results shown in Figure 7.3 of the well-defined mid IR. Fitting of the $Ca(OH)_2$-H_2O-CO_2 XANES (Figure 7.4a) using only the $Ca(OH)_2$ and $CaCO_3$-α references resulted in reasonable fits with marginally high residuals. Step-by-step analysis of the fits revealed that the theoretical spectra from 10 to 20 minutes during carbonation were underestimated. This was proven to be due to the exclusion of the reference spectrum for a hydrated Ca^{2+} cation. This spectrum was obtained by measuring the FY Ca K-edge of a calcium chloride solution (170). The Ca^{2+} cations are formed as a result of the dissociation of $Ca(OH)_2$ in water i.e. $Ca(OH)_2$ (s) ↔ Ca^{2+} (aq) + OH^- (aq). The effect of the Ca^{2+} on the XANES in the initial 5 minutes of the reaction is less apparent due to the low solubility of $Ca(OH)_2$ in water (*cf.* Table 3.1). However as the reaction progresses and $CaCO_3$-α forms, the forward $Ca(OH)_2$ dissociation reaction is favoured. Attempts to include the Ca^{2+} standard in the LCF of the pure methanol XANES (Figure 7.4b) yielded negative results. This in part proves that $CaCO_3$ in this system is obtained *via* the methoxylation and esterification reactions.

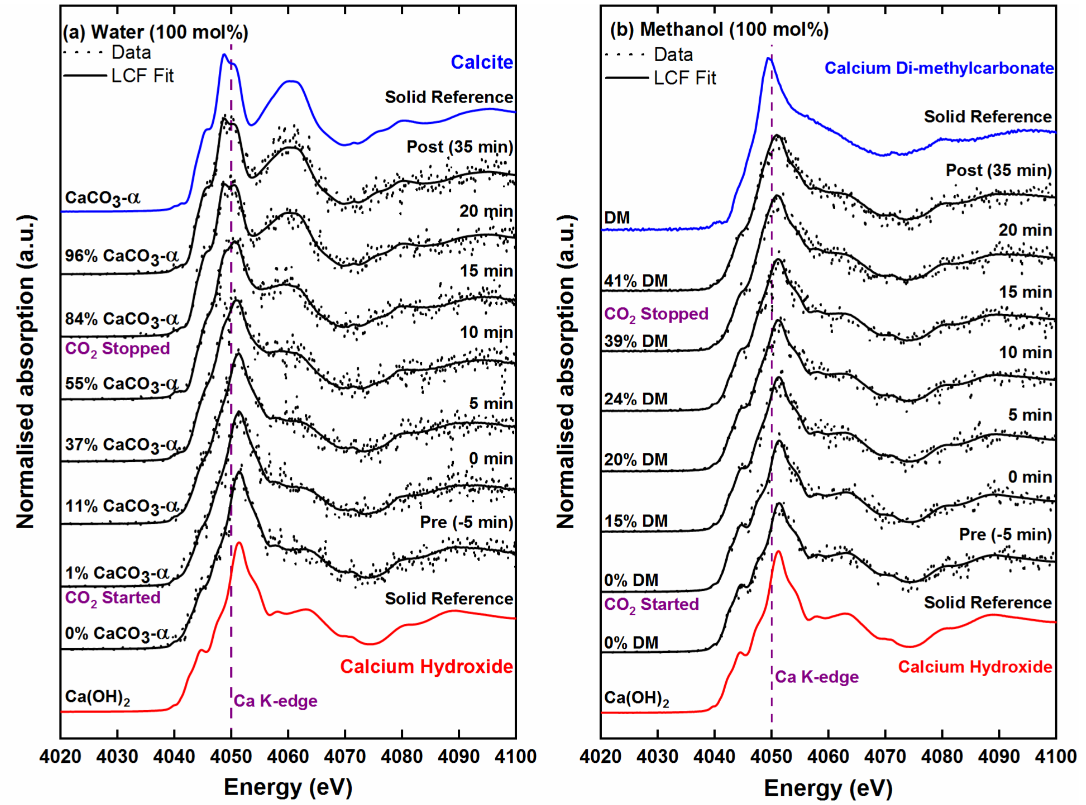

Figure 7.4. *In situ* Ca K-edge XANES spectra showing the 20-minute carbonation of $Ca(OH)_2$ in 100 mol% (a) H_2O (product – $CaCO_3$-α) and (b) CH_3OH (product – $Ca(OCOCH_3)_2$ (DM)).

In order to illustrate the accuracy of the LCF quantifications the stoichiometry for the formation of $CaCO_3$-α (Figure 7.4a) and $Ca(OCOCH_3)_2$ (Figure 7.4b) with respects to the reactants was determined. The extent of $Ca(OH)_2$ conversions were calculated based on the carbonation, methoxylation and esterification equations highlighted section 5.1. It's expected that the equimolar amount of carbon dioxide (CO_2) added to the two systems should result in hydroxide conversions of about 95 and 48 % in the aqueous and methanolic systems respectively. These are reasonably close to the LCF calculated values of 96(4) and 41(3) %. It is important to note that the slightly high standard deviation values are a factor noisy *in situ* data due to the pulsation of the liquid-jet flow.

7.3 Water-Methanol and Methanol-Toluene Systems

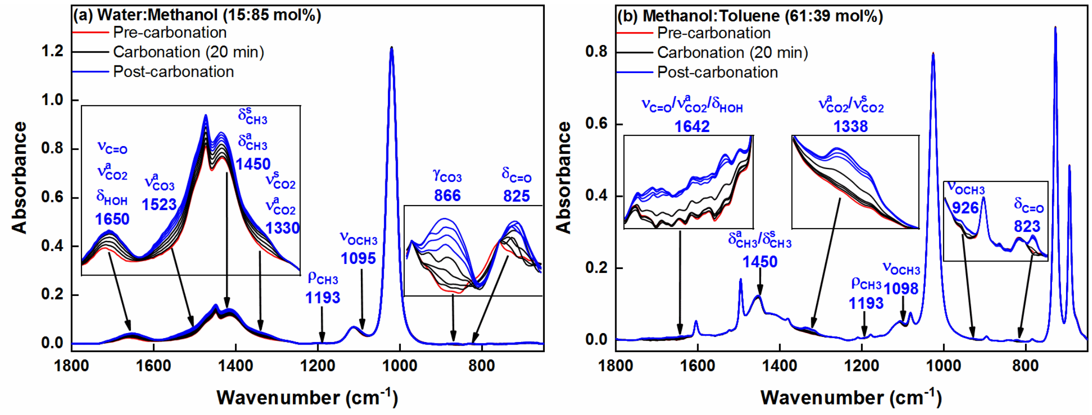

Figure 7.5. *In situ* mid-IR spectra following the 20-minute carbonation of $Ca(OH)_2$ in methanolic solutions with (a) 15 mol% H_2O (products – $Ca(OCOCH_3)_2$ and ACC) and (b) 39 mol% $C_6H_5CH_3$ (product – $Ca(OCOCH_3)_2$). Each black line represents 5 mins of carbonation time.

Comparison of the mid-IR (Figure 7.5) and XANES (Figure 7.6) *in situ* spectra for the water-methanol and methanol-toluene binary systems highlighted that carbonation can occur in the absence of H_2O. The $Ca(OCOOCH_3)_2$ ester intermediate was formed in both systems but ACC was only detected in water-methanol system (Figure 7.5a and 7.6a). As such, the subsequent LCF analysis for the H_2O-free system only accounted for the $Ca(OCOOCH_3)_2$ with a final composition of 60(3)% (Figure 7.6b). Conversely, the final product in the H_2O diluted system consisted of 32(7)% $Ca(OCOOCH_3)_2$ and 30(7)% ACC. Good LCF fits with R-factors of <2% were obtained in both cases. Post-synthesis *ex situ* mid-IR analysis of the water-methanol post-carbonation product (Figure E.1 in Appendix E) revealed that the mixed ester/ACC product converted into $CaCO_3$-α and $CaCO_3$-γ upon aging. This is similar to the conversion observed for the sol-gel in section 6.4. As was show in Figure 7.2 gelation occurs up to 80 mol% of water. Notably, the formation of $Ca(OCOOCH_3)_2$ in the methanol-toluene system proves that the postulation of no reaction occurring in the absence of H_2O is erroneous (16). The reaction in this particular non-aqueous binary system is solely due to the polar CH_3OH as proven by the lack of $Ca(OH)_2$ conversion in the non-polar pure toluene system (Figure E.2 in Appendix E).

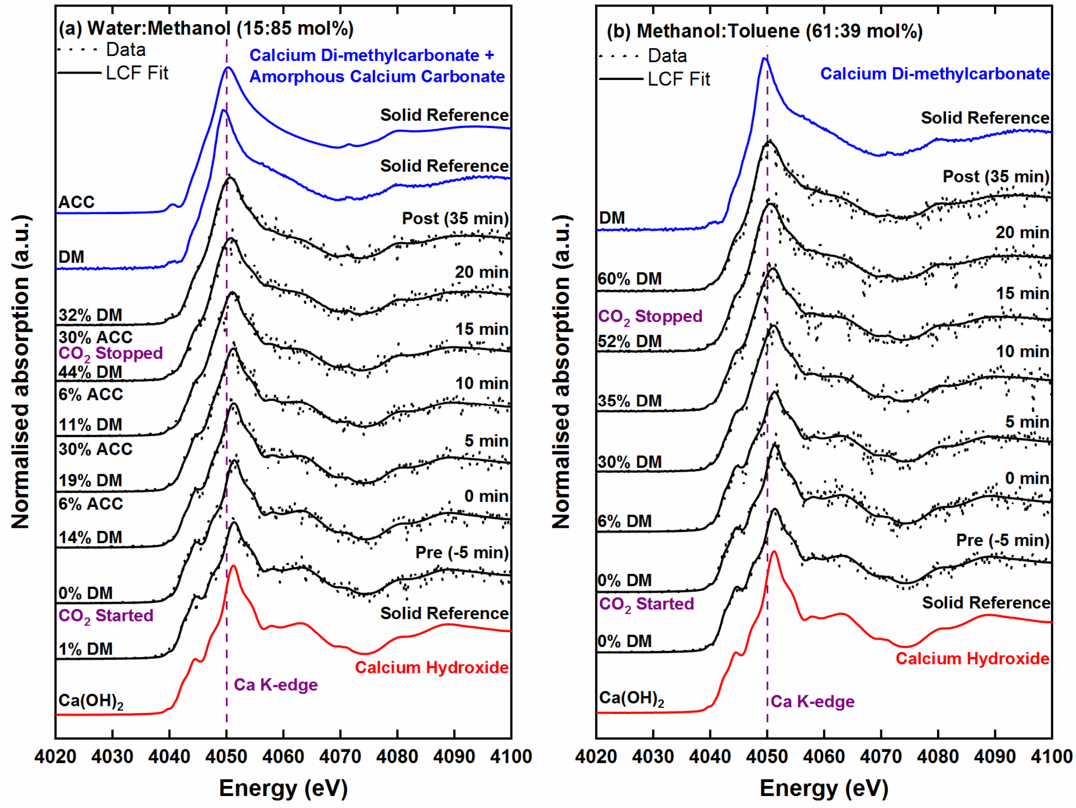

Figure 7.6. *In situ* Ca K-edge XANES spectra following the 20-minute carbonation of $Ca(OH)_2$) in methanolic solutions with (a) 15 mol% H_2O (products – $Ca(OCOCH_3)_2$ (DM) and ACC) and (b) 39 mol% $C_6H_5CH_3$ (product – $Ca(OCOCH_3)_2$ (DM)).

7.4 Water-Methanol-Toluene System

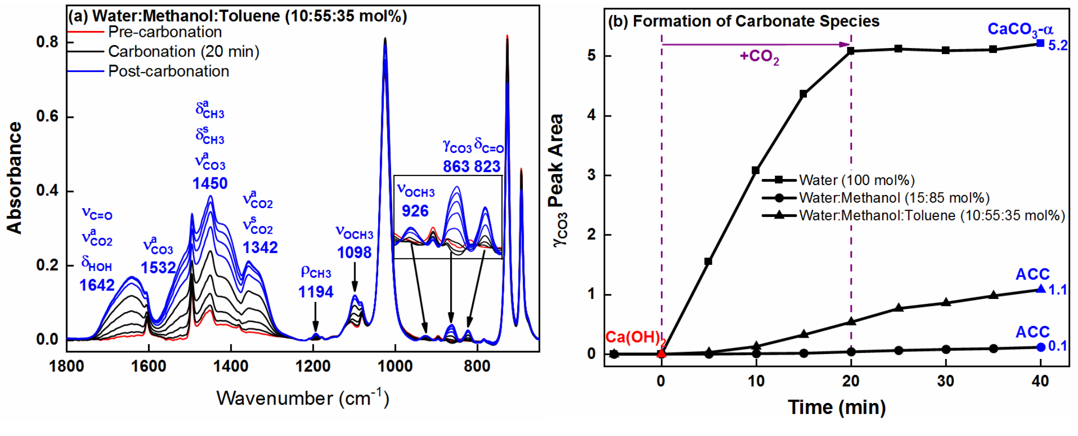

Figure 7.7. (a) *In situ* mid-IR spectra showing the 20-minute carbonation of $Ca(OH)_2$ in a H_2O-CH_3OH- $C_6H_5CH_3$ system (products – $Ca(OCOCH_3)_2$ (DM) and ACC). Each black line represents 5 mins of carbonation; and (b) quantitative analysis showing the formation of $CaCO_3$ based on the out-of-plane bending deformation (γ_{CO3}) peak area as a function of time.

A higher conversion from the $Ca(OH)_2$ to a carbonated species was observed in the mid-IR for the water-methanol-toluene (10:55:35 mol%) system (Figure 7.7a). This is in comparison with the pure methanol (Figure 7.3b) and the two binary (Figure 7.5) systems. The ternary system IR spectrum (Figure 7.7a) shows the formation of the

$Ca(OCOOCH_3)_2$ intermediate and what appears to be ACC. Quantitative analysis of the γ_{CO3} deformation peak area (Figure 7.7b) shows that ACC formed at a faster rate in the ternary system than the binary. This could be due to the fact that the toluene decreases the viscosity of the dispersion (3) and thus promotes diffusion/crystallisation. As can be seen in Figure 7.7b all of the $Ca(OH)_2$ in the pure water system converted into $CaCO_3$, whereas partial conversion was achieved in the presence of non-aqueous solvents.

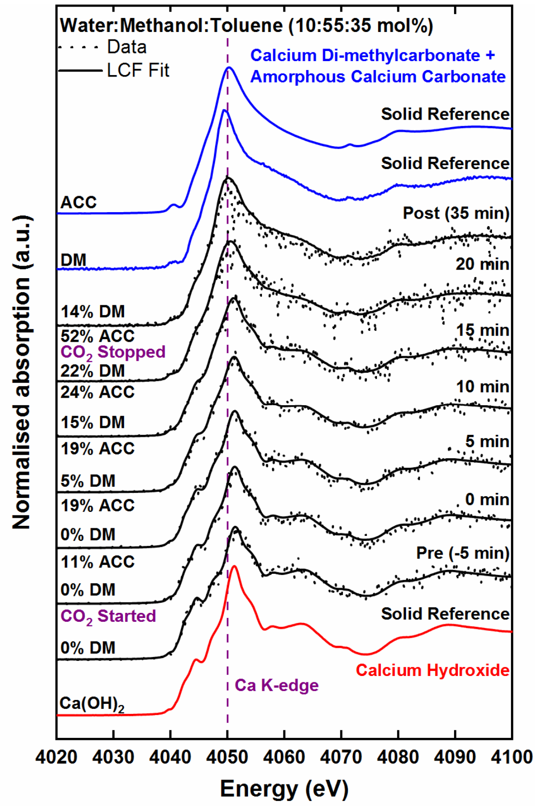

Figure 7.8. *In situ* Ca K-edge XANES spectra showing the 20-minute carbonation of $Ca(OH)_2$ in a H_2O-CH_3OH- $C_6H_5CH_3$ system (products – $Ca(OCOCH_3)_2$ (DM) and ACC).

According to the XANES (Figure 7.8), the final post-carbonation product from the ternary solvent system consists of 44% less $CaCO_3$ than the pure water dispersion (Figure 7.4a). The lower extent of conversion can again be attributed to diffusion-limited precipitation due to the presence of CH_3OH and the associated densification of the solvent media (221). Notably, an *ex situ* time-resolved PXRD study (Figure E.3 in Appendix E) on a concentrated system revealed that the presence of toluene reduced the stability of the gel formed. Peaks due to $CaCO_3$-α and $CaCO_3$-γ were present in the initial PXRD pattern of the gel. This is unlike the water-methanol sol-gel studied in section 6.4, which was stable in an amorphous form up to 90 mins (Figure 6.12).A similar de-stabilising effect of a hydrocarbon solvent was reported in relation to reducing the viscosity during the carbonation stage of the overbasing process (3)

Interestingly, the post-synthesis *ex situ* IR (Figure E.4 in Appendix E) for the ternary system showed that upon aging (60 h) the $Ca(OCOOCH_3)_2$ and ACC converted mainly into $CaCO_3$-β with traces of $CaCO_3$-α. Traces of $CaCO_3$-β have been detected previously, e.g. in the mid-IR of the aged pure methanol product in Figure 5.2b. However, this is the first reported instance that it has been detected in large quantities. Its presence is also evident in the time-resolved PXRD (Figure E.3 in Appendix E), along with $CaCO_3$-α and $CaCO_3$-γ. In this case, the formation of $CaCO_3$-β and $CaCO_3$-γ can be attributed to kinetic stabilisation induced by the chemisorption of the toluene. Kinetic stabilisation due to adsorption of organic compounds, such as ethanol, has been reported for these two polymorphs (24, 190, 216). Additionally, toluene has been shown to affect structure of $Ca(OH)_2$ (240). Hence, it can concluded that toluene behaves like Mg^{2+} ions in restricting crystal growth and preventing the formation of $CaCO_3$-α (24, 241).

7.5 Ethanol and Isopropanol Systems

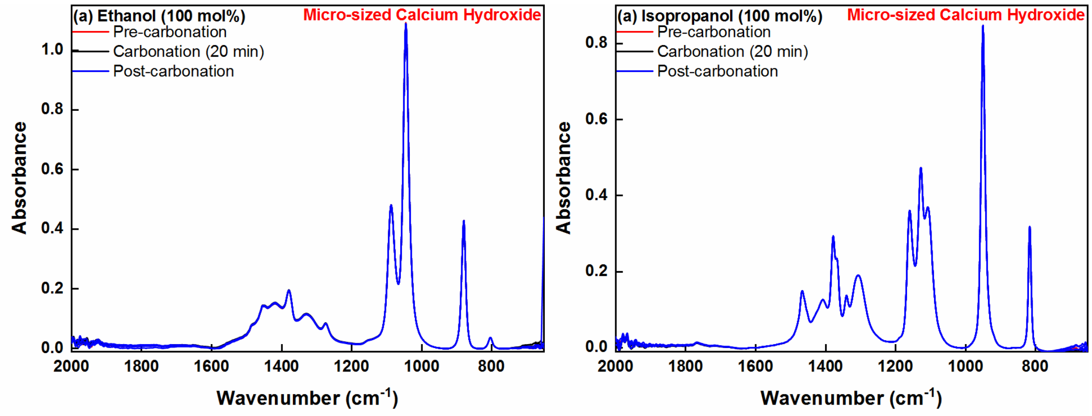

Figure 7.9. *In situ* mid-IR spectra showing the 20-minute carbonation of micro-sized $Ca(OH)_2$ in 100 mol% (a) CH_3CH_2OH and (b) $CH_3CH_2CH_2OH$ – no conversion. Each black line represents 5 mins of carbonation.

The effects of alcohol chain length on the reactive crystallisation of $CaCO_3$ were investigated. No changes were observed in the IR spectra (Figures 7.9) when micro-sized (~30 μm) $Ca(OH)_2$ was carbonated in the presence of pure ethanol (CH_3CH_2OH) and isopropanol ($CH_3CH_2CH_2OH$). Compared to CH_3OH, the ethyl and isopropyl alcohols are less polar (*cf.* Table 3.1). The difference in polarity is reflected in the decreasing solubility of the $Ca(OH)_2$ and CO_2 reactants from CH_3OH to

$CH_3CH_2CH_2OH$. This could account for the reduced reactivity in the CH_3CH_2OH and $CH_3CH_2CH_2OH$ systems.

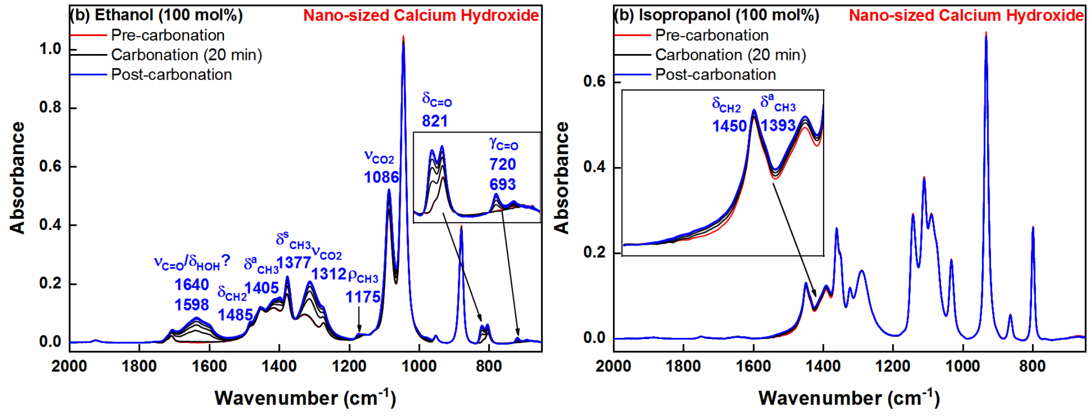

Figure 7.10. *In situ* mid-IR spectra following the 20-minute carbonation of nano-sized $Ca(OH)_2$ (nanolimes) in 100 mol% (a) CH_3CH_2OH (product – $Ca(OCOOCH_2CH_3)_2$) and (b) $CH_3CH_2CH_2OH$. Each black line represents 5 mins of carbonation.

The formation of calcium ethoxide and isopropoxide has been reported in alcoholic dispersions of nano-sized (~170 nm) $Ca(OH)_2$ (189-191). Much like the methanol systems reported here, these alkoxide salts were identified as precursors for ACC and $CaCO_3$-γ. Analysis of the time-resolved mid-IR (Figure 7.10) spectra for the CH_3CH_2OH nanolimes shows the conversion of the nano-sized $Ca(OH)_2$. Minor changes can also be observed in the isopropanol IR spectra (Figure 710b), however these changes were not reproducible. The post-carbonation product in the ethanol system was identified as calcium di-ethylcarbonate ($Ca(OCOOCH_2CH_3)_2$). This was determined from the peak assignments for the previously discussed $Ca(OCOOCH_3)_2$ ester and literature data on the ethoxycarbonyl ($-COOCH_2CH_3$) group (150).

LCF analysis of the *in situ* XANES (Figure 7.11) for the CH_3CH_2OH and $CH_3CH_2CH_2OH$ systems was precluded by the lack of reference spectra of the respective ester intermediates. However, a qualitative comparison of the pre- and post-carbonation spectra clearly shows that conversion from $Ca(OH)_2$ only occurred in the ethanol system with the nano-sized hydroxide particles. Ultimately, these results show that increasing the chain length decreases the reactivity of the alcohol and that formation of carbonated Ca species in the CH_3OH system is comparable to CH_3CH_2OH only when the $Ca(OH)_2$ particle size is significantly reduced (nano-scale). It might be worth investigating the effects of varying the particle size in the pure (100 mol%) methanol dispersion (Figure 7.3a) considering the relatively high extent of conversion observed in mid-IR of the ethanol nanolimes system (Figure 7.10a).

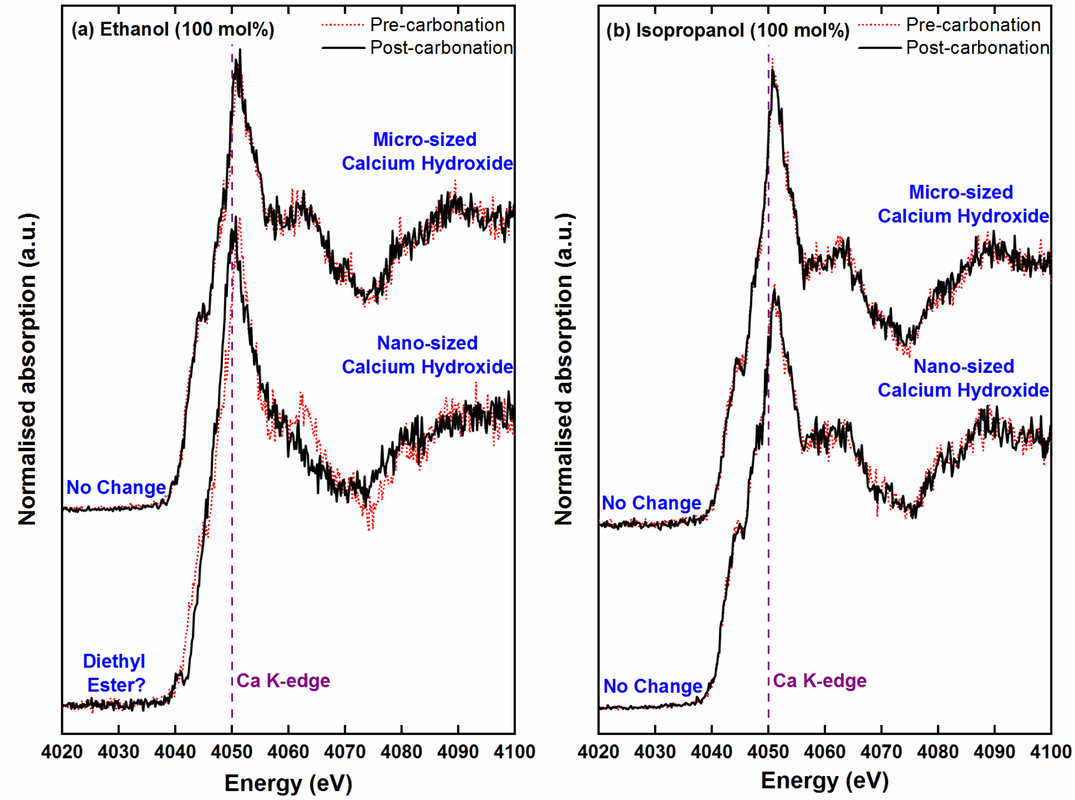

Figure 7.11. *In situ* Ca K-edge XANES spectra showing the 20-minute carbonation of micro-sized and nano-sized $Ca(OH)_2$ in pure (a) CH_3CH_2OH and (b) $CH_3CH_2CH_2OH$. Formation of $Ca(OCOOCH_2CH_3)_2$ is evident only in the spectrum for the CH_3CH_2OH nanolimes system.

7.6 Conclusions

A combined *in situ* mid infrared (mid-IR) and X-ray absorption spectroscopy (XAS) study of multiphase multicomponent calcium carbonate ($CaCO_3$) crystallisation processes was carried out. The synthesis of calcium carbonate ($CaCO_3$) *via* the carbonation of calcium hydroxide ($Ca(OH)_2$) in water (H_2O), methanol (CH_3OH), ethanol (CH_3CH_2OH), isopropanol ($CH_3CH_2CH_2OH$) and toluene ($C_6H_5CH_3$) environments has been successfully monitored. Real-time changes in structure from $Ca(OH)_2$ to different $CaCO_3$ polymorphic forms were monitored in the eight solvent systems. Calcite ($CaCO_3$-α) was confirmed to be the final product in the H_2O (100 mol%) and pure/binary/ternary methanolic (100, 85, 61 and 35 mol% of CH_3OH) systems. As was also shown in chapter 6, the presence of CH_3OH resulted in the formation of calcium methoxide ($Ca(OCH_3)_2$), calcium di-methylcarbonate ($Ca(OCOOCH_3)_2$), amorphous calcium carbonate (ACC) and vaterite ($CaCO_3$-γ). The presence of $C_6H_5CH_3$ led to a relatively higher viscosity in the ternary system, which consequently resulted in increased reaction rates and the crystallisation of aragonite ($CaCO_3$-β). Conversely, no $Ca(OH)_2$ conversion was initially observed in the pure CH_3CH_2OH and $CH_3CH_2CH_2OH$ systems. However, reduction in the $Ca(OH)_2$

particle size led to the formation of calcium di-ethylcarbonate ($Ca(OCOOCH_2CH_3)_2$) in the CH_3CH_2OH system. Suggesting that the CH_3OH used in the overbasing process can be replaced by CH_3CH_2OH if the $Ca(OH)_2$ particle size is significantly reduced (nano-scale). Further experimental work is required to determine whether overbased detergents can indeed be synthesised using CH_3CH_2OH nanolimes and how their structure differs from the CH_3OH-based detergents.

Chapter 8:
Overbased Calcium Sulphonate Detergents

8.1 Introduction

This chapter demonstrates that mid infrared (mid-IR) and X-ray absorption spectroscopy (XAS) can successfully be used to monitor chemical transformations in a multicomponent and multiphase industrial process using the novel continuous-flow liquid-jet process analytical technology (PAT) setup developed in this project (chapter 4). The PAT setup permits real-time analysis of the reaction mixture. The process chemistry investigated was a scaled-down version of the industrial manufacturing process for the synthesis of overbased calcium sulphonate detergents (12, 13, 15). The study presented in this chapter highlights the sensitivity of XAS to the crystal structure of calcium-containing materials in dilute dispersions, which becomes evident through the *operando* X-ray absorption near-edge structure (XANES) in the spectra.

The final products are lubricant oil additives for deposit control and protection against corrosion in combustion engines (5, 9, 10). The overbasing process is a complex four-phase system involving interfacial reactions between suspended solid and dissolved calcium hydroxide in a polar methanol/water phase, sulphonic acid solution in a non-polar organic solvent, and CO_2 gas (4, 7, 29, 30). The properties of the products formed are strongly dependent on temperature, mixing dynamics and the composition of the gas phase. Both water-in-oil and oil-in-water emulsions can be formed, and their balance can be affected by evaporation of volatile solvents (242). Ultimately particulate $CaCO_3$ products are generated, which can arise in at least six distinguishable crystalline or non-crystalline (‘amorphous’) forms (24). The final detergent products (Figure 8.1) contain colloidal nanoparticles of calcium carbonate stabilized by sulphonate surfactant.

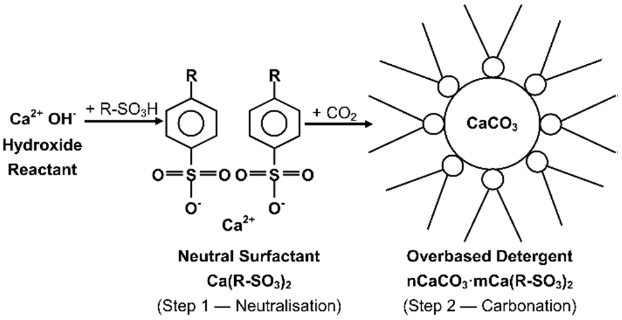

Figure 8.1. Schematic representation of the formation of a neutral calcium sulphonate surfactant ($Ca(R\text{–}SO_3)_2$) and overbased detergent ($nCaCO_3 \cdot mCa(R\text{–}SO_3)_2$) *via* sulphonic acid ($R\text{-}SO_3H$) neutralisation and calcium hydroxide ($Ca(OH)_2$) carbonation.

8.2 *Ex Situ* Characterisation of Overbased Detergents

Mid-infrared (mid-IR) spectroscopy. Mid-IR was used to distinguish between the two products from the overbasing process i.e. the neutral calcium sulphonate surfactant ($Ca(R–SO_3)_2$) and overbased calcium sulphonate detergent ($nCaCO_3{\cdot}mCa(R–SO_3)_2$). These were compared with the sulphonic acid ($R\text{-}SO_3H$) reactant and mineral oil dispersant. The mineral oil (Figure 8.2a), which has a similar structure to dodecane, is the main dispersant in the other three samples. The symmetric and asymmetric alkyl CH_2 and CH_3 stretching and deformations vibrations due to the oil are evident in all four spectra (Figure 8.2; Table 8.1). The $\nu^{a}_{CH2/CH3}$ and $\nu^{s}_{CH2/CH3}$ vibrations occur at about 2900 ± 46 cm^{-1}, whereas as the δ^{a}_{CH3} and δ^{s}_{CH3} appear at 1480 ± 23 cm^{-1} and 1370 ± 10 cm^{-1} respectively. Notably, there are some minor variations in these regions due to the additional alkyl chains (R group) in the $R\text{-}SO_2OH$, $Ca(R–SO_3)_2$ and $nCaCO_3{\cdot}mCa(R–SO_3)_2$. The IR spectra for the three sulphur-containing compounds also show peaks due to aromatic (C_6H_6) in-plane (δ_{C6H6}; 1000 to 1140 cm^{-1}) and out-of-plane (γ_{C6H6}; 834 cm^{-1}) deformations (243).

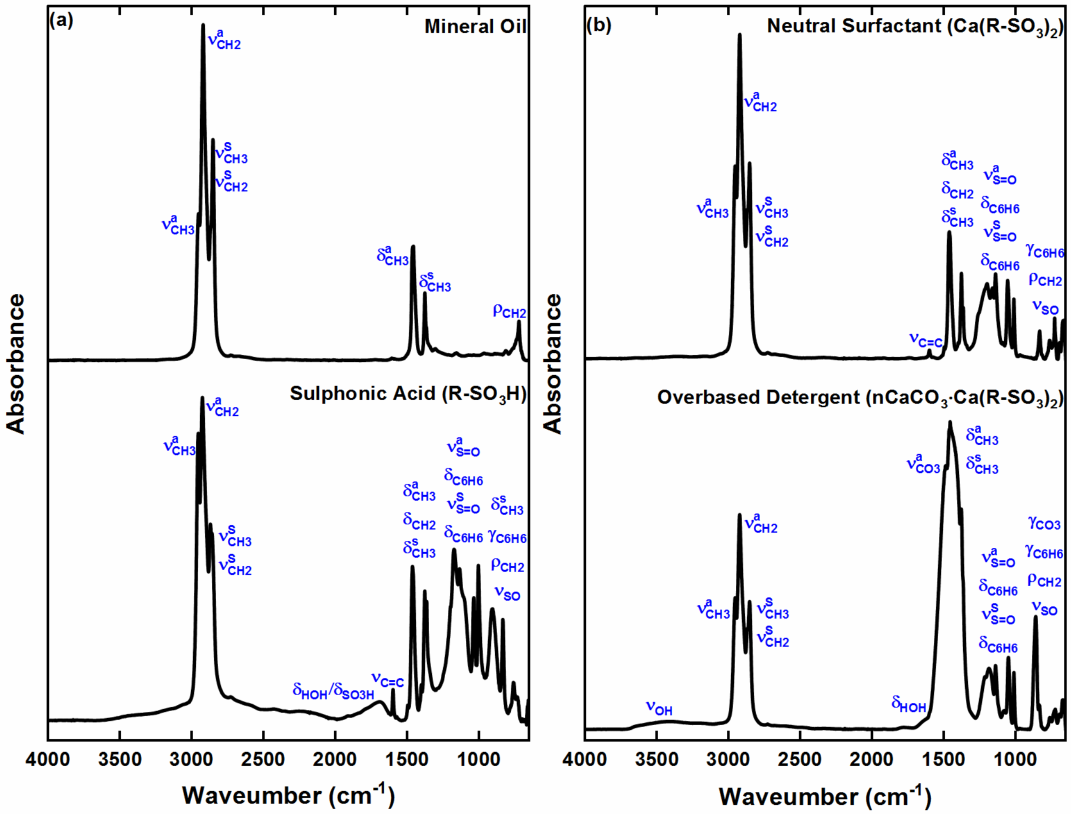

Figure 8.2. Mid-IR spectra for mineral oil, sulphonic acid ($R\text{-}SO_3H$), neutral calcium sulphonate surfactant ($Ca(R–SO_3)_2$) and overbased calcium sulphonate detergent ($nCaCO_3{\cdot}mCa(R–SO_3)_2$).

Table 8.1. Mid-IR vibrations (cm^{-1}) for mineral oil, sulphonic acid ($R\text{-}SO_3H$), neutral calcium sulphonate surfactant ($Ca(R–SO_3)_2$) and overbased detergent ($nCaCO_3 \cdot mCa(R–SO_3)_2$)

Assignments	Mineral Oil	Sulphonic Acid	Neutral Surfactant	Overbased Detergent
ν_{OH}	-	-	-	3450
ν^a_{CH3}	2955	2955	2955	2955
ν^a_{CH2}	2923	2927	2923	2923
ν^s_{CH3}	2871	2871	2871	2871
ν^s_{CH2}	2853	2856	2856	2856
$\delta_{HOH}/\delta_{SO3H}$	-	1685	-	-
δ_{HOH}	-	-	-	1646
$\nu_{C=C}$	-	1599; 1573	1599; 1573	-
δ^a_{CH3}	1460	1496; 1464	1496; 1464	1490
ν^a_{CO3}	-	-	-	1450
δ_{CH2}	-	1404	1404	-
δ^s_{CH3}	1378; 1364	1378; 1364	1378; 1364	1378; 1364
$\nu^a_{S=O}/\rho_{CH3}$	-	1200; 1174	1200; 1160	1215; 1185
δ_{C6H6}	-	1130;1100	1140	1140
ν_{OCH3}	-	-	-	1079
$\nu^s_{S=O}$	-	1036	1056	1050
δ_{C6H6}	-	1005	1012	1012
δ^s_{CH3}	-	906	-	-
γ_{CO3}	-	-	-	860
γ_{C6H6}	-	834	834	834
ν^s_{CO2}	-	760	762	762
ρ_{CH2}	722	727	727	723
ν_{SO}	-	663; 656	694; 667	694; 667

The main distinguishing features in the IR for the acid, surfactant and detergent (Figure 8.2) are due to the sulphonate ($R\text{-}SO_3^-$) and carbonate (CO_3^{2-}) anions. There is an observable change in the shape and intensity of the feature(s) in the region of the $\nu^a_{S=O}$ and $\nu^s_{S=O}$ vibrations (1030 to 1215 cm^{-1}). The difference between the acid (Figure 8.2a) and surfactant (Figure 8.2b) can be attributed to the varying effects of the monovalent H^+ and divalent Ca^{2+} cations on the electron density of sulphonyl oxygens. Conversely, there is a minor 5 cm^{-1} shift of the $\nu^s_{S=O}$ peak maxima to lower wavenumbers from the surfactant to the detergent. This negative shift suggests the possibility of a chemical interaction between the sulphonate and a constituent of the detergent core, such as the carbonate and/or water. In this case, it is most probably due to the trace amounts of water (δ_{HOH} – 1646 cm^{-1}; ν_{OH} – 3450 cm^{-1}), as similar shifts have been observed with increasing amounts of polar solvents (41, 244).

Evidently, the most prominent difference between the surfactant and detergent IR (Figure 8.2) is the strong asymmetric ν^a_{CO3} vibration (at ~1450 cm^{-1}) due the carbonate species in the detergent core. It could be assumed that the core is purely amorphous $CaCO_3$ (ACC) due to the complementary out-of-plane bending γ_{CO3} at 860 cm^{-1}. However, the results from the previous two chapters have highlighted the possibility of a methoxy stretching (ν_{OCH3}) contribution at ~860 cm^{-1} due to the presence of calcium methoxide ($Ca(OCH_3)_2$) and/or calcium di-methylcarbonate ($Ca(OCOOCH_3)_2$). A closer inspection of the IR (Table 8.1) reveals that there is a peak at 1079 cm^{-1} coupled with a red shift and an increase intensity at 1185 cm^{-1}. A previous study (245) states that this effect on the $\nu^{a}_{S=O}$ bands (at ~1200 cm^{-1}) is due to the formation of a bond between the sulphonate and carbonate. However, a comparison of the detergent IR with the *ex* (Figure 6.2) and *in situ* (Figure 7.1) IR for the formation of $Ca(OCOOCH_3)_2$ reveals that these peaks are most probably due to the ν_{OCH_3} and ρ_{CH_3} vibrations of the ester. This will be explored further in the mid-IR *operando* analysis of the overbasing process (section 8.3.1).

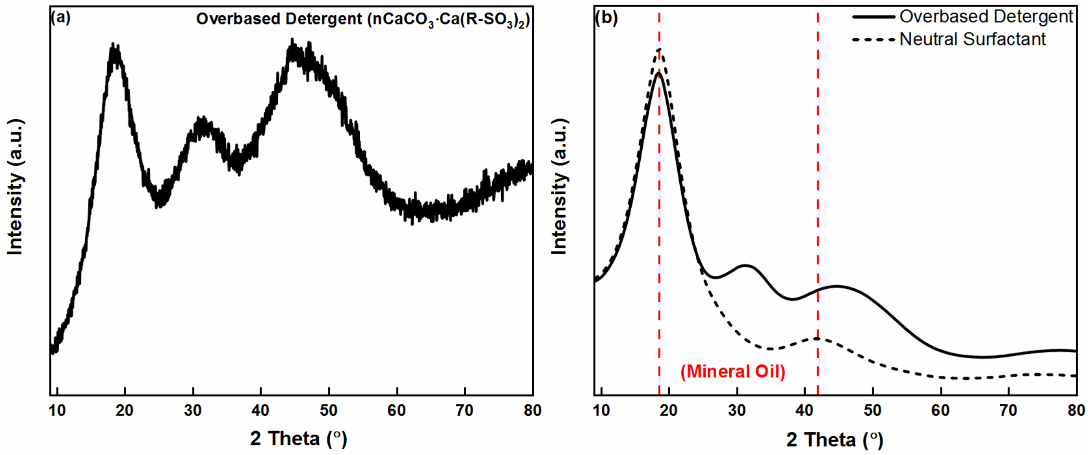

Figure 8.3. Plots showing the (a) PXRD and (b) WAXS patterns for the neutral calcium sulphonate surfactant ($Ca(R\text{–}SO_3)_2$) and overbased detergent ($nCaCO_3{\cdot}mCa(R\text{–}SO_3)_2$).

Powder X-ray Diffraction (PXRD) and Wide-angle X-ray Scattering (WAXS). The PXRD pattern for the overbased detergent (Figure 8.3a) is mainly dominated by diffraction from ordered alkyl chains in the dispersant (mineral oil). This is evidenced by the broad un-resolved peak at ~18 Å (42, 47, 81). The other two peaks have also been observed previously (42, 47, 81), where the peak at ~31 Å has been assigned to crystalline $CaCO_3$. Whereas all three polymorphs display peaks in this region (*cf.* Figure 5.8), diffraction from the 104 plane in calcite ($CaCO_3$-α) is the most prominent. Analysis of this second feature using wide-angle X-ray scattering (WAXS) (Figure 8.3b) shows that it is definitely not due to the mineral oil since it is absent in the surfactant pattern. Unfortunately, this region also encompasses peaks from the $Ca(OH)_2$ and $Ca(OCH_3)_2$ precursors which precludes unambiguous peak assignment. This issue could possibly be resolved by analysing variations in the short- and medium-range order of the X-ray pair distribution function (XPDF), as was done for the vaterite ($CaCO_3$-γ) structure in section 5.6. However, extraction of the XPDF for the detergent has proven difficult due to the lack of a definite structure.

Further analysis of the WAXS data (Figure 8.3b) shows that the area of the third peak in the detergent pattern is twice that of the surfactant. Comparison with a previous study (42) shows that the peak in the surfactant XRD (and partly in the detergent) is due to ordered alkyl chains. The remainder of the peak in the detergent XRD yet again falls in the same region as multiple peaks from the crystalline precursors and possible $CaCO_3$ polymorphs. Interestingly, the peaks observed at about 34, 45 and 51 degrees coincide with the $CaCO_3$-γ 114, 300 and 118 plane contributions (*cf.* Figure 5.8) that were also observed in the PXRD for the ACC/$CaCO_3$-γ intermediate (Figure 6.5) in the 100 mol% methanol system.

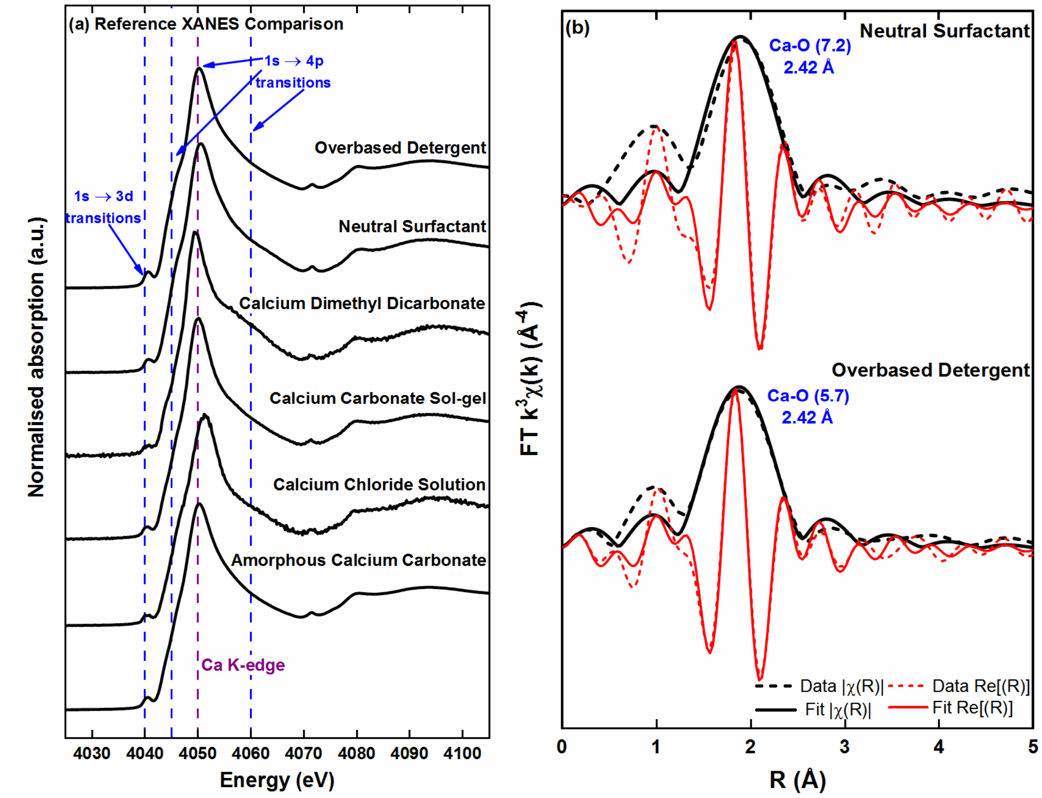

Figure 8.4. Ca K-edge reference (a) XANES and (b) EXAFS spectra for neutral calcium sulphonate surfactant ($Ca(R–SO_3)_2$) and overbased detergent ($nCaCO_3·mCa(R–SO_3)_2$).

X-ray absorption Near-Edge Structure (XANES). The electronic and local structure of the calcium sulphonate neutral surfactant and overbased detergent were investigated using Ca K-edge XANES and EXAFS. No significant differences were identified in the initial comparison of the XANES (Figure 8.4a) spectra for the two sulphonate products. The lack of a pronounced feature at 1s → 4p at 4060 eV in the detergent XANES, when compared to $CaCO_3$-α (*cf.* Figure 5.9b), has previously led to the conclusion that the core is ACC (17-19). However, as the extensive XANES comparison in Figure 8.4a shows, this 1s → 4p feature is not distinctive in the spectra for all the possible (in-process) products such as the $Ca(OCOOCH_3)_2$ ester and sol-gel. These results highlight two main issues relating to the qualitative XANES analysis i.e. (i) the detergent core can easily be ACC or any of the other in-process calcium species; and (ii) electronic transitions from the surfactant outer layer might have the ability to mask those from the core. These issues will be explored further in the *operando* XAS study in section 8.3.2.

Extended X-ray Absorption Fine Structure (EXAFS). A quantitative analysis of the EXAFS (Figure 8.4b) spectra for the two sulphonate products revealed only one major peak at 2.42 Å with varying coordination numbers (N_O) due to the first shell Ca-O scattering. The results for the detergent are in agreement with previous EXAFS studies (13, 18, 19). Interestingly, the N_O value of 5.7 for the detergent is similar to that for $CaCO_3$-α (Figure 5.13b), $CaCO_3$-γ (Figure 5.16) and ACC (Figure 6.8). The presence of the three polymorphs is possible as was suggested by the PXRD for the $Ca(OCOOCH_3)_2$ (Figure 6.5), sol-gel (Figure 6.12) and detergent (Figure 8.3). Ultimately, the *ex situ* PXRD , XANES and EXAFS results suggest the possibility of some crystallinity in the core.

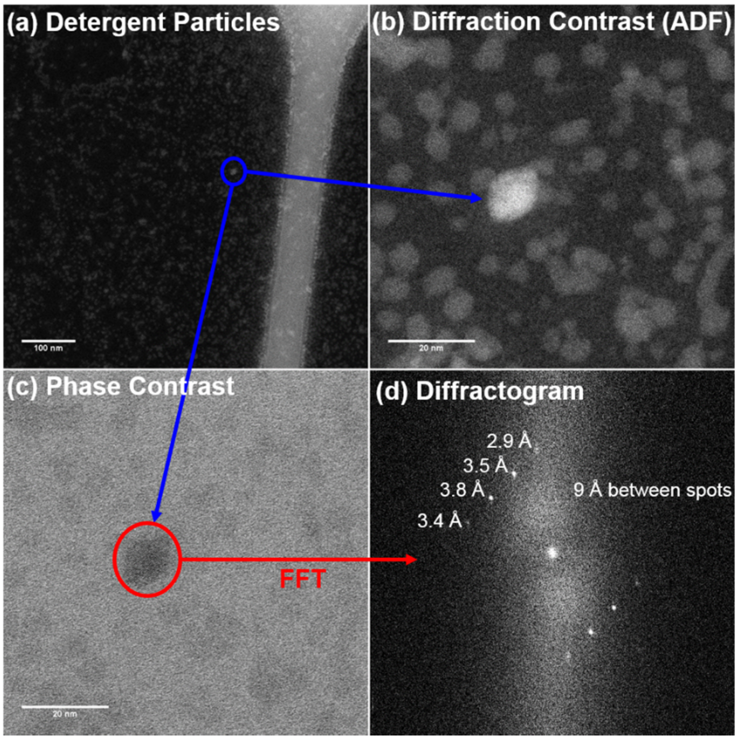

Figure 8.5. STEM images of the overbased detergent particles in (a and b) annular dark field (ADF) and (c) bright field (BF). The fast Fourier transform (FFT) of an isolated crystalline particle is also included (d) – images courtesy of Robert Hooley.

Transmission Electron Microscopy (TEM). The proposed discrete crystallinity in the core of the overbased detergents was further explored using low-dose TEM and STEM. Detergent particles with a core size of ~8 nm stabilised by a ~2 nm surfactant layer were identified (Figures 8.5 and F.1 in Appendix F). The particle sizing observed in the TEM and STEM images and the lack of crystallinity seen in the selected area diffraction pattern (Figure F.1) agree with previous studies (10, 19, 45-48). Further analysis using low angle annular dark field (ADF) and bright field (BF) STEM highlighted the presence of some crystalline particles (Figure 8.5). d-spacings of 2.9, 3.4, 3.5, 3.8 and 9 Å were observed in the fast Fourier transform (FFT) (Figure 8.5d). Most of these values can be linked to various $CaCO_3$-γ planes of the *C-1* model crystal structure by Mugnaioli *et al.* (164). Interestingly, the PXRD pattern for form III of calcium di-methylcarbonate ($Ca(OCOOCH_3)_2$) in Figure 6.5b contains minor peaks at all of these d-spacings. Further comparative diffraction analysis is required to determine the true structure of this crystalline carbonated species.

It is important to note that the appearance of the crystalline particles could be due to the destabilisation of the surfactant layer and subsquent precipitation. It has been shown that solvents affect the stability of such particles, most especially polar solvents such as water, methanol and acetone (34, 244, 246). Hence it is possible that the crystallinity is induced by the hexane used in the dialysis purification process., but the effect of non-polar solvents has been found to be negligible (244). Notably, previous TEM studies (3, 14) that have reported the presence of $CaCO_3$-α and $CaCO_3$-γ in the detergents induced precipitation by using acetone and/or methanol.

8.3 *Operando* Mid-IR and XAS of the Overbasing Process

In-line Mid-IR. The capability of the continuous-flow liquid-jet setup (*cf.* Figure 4.3) as a PAT tool was explored with a simultaneous *operando* mid-IR and XAS study of the synthesis of overbased calcium sulphonate detergents. Initially both techniques were used to monitor the time-resolved changes in a dilute overbasing system. However, no significant changes due to the formation of the surfactant or detergent were observed in the mid-IR. This can be attributed to the larger volume of solvents and surfactant compared to that of the calcium hydroxide ($Ca(OH)_2$). Hence, the standard concentrated process (211) (*cf.* section 3.3.4) was used for the mid-IR analysis (Figures 8.6 and 8.7). This highlighted the relatively higher sensitivity of XAS to changes in process chemistry even in dilute systems.

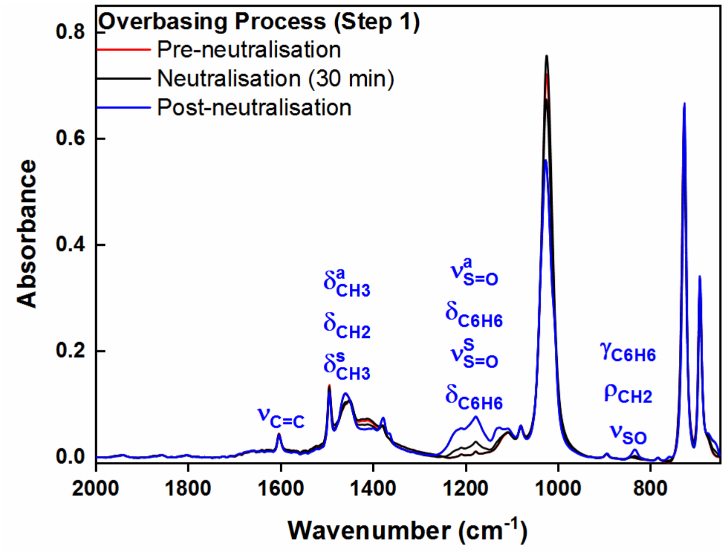

Figure 8.6. *Operando* mid-IR spectra of the calcium sulphonate detergent synthesis process. Time-dependent spectra during the neutralisation stage (step 1) – reaction of $Ca(OH)_2$ (base) and $R–SO_3H$ (acid) to form $Ca(R\text{-}SO_3)_2$ (surfactant).

Figure 8.6 shows the time-resolved neutralisation (step 1) of the sulphonic acid ($R–SO_3H$) to form of the neutral surfactant ($Ca(R\text{-}SO_3)_2$). The results agree with the vibrational frequencies identified in the previously discussed *ex situ* IR for the isolated surfactant (Figure 8.2b). Interestingly, there is an appreciable decrease in the intensity of the methanol (CH_3OH) ν_{OCH3} contribution at ~1026 cm^{-1} (Figure 8.6). This is probably due to a reaction between the $Ca(OH)_2$ with the CH_3OH to form calcium methoxide ($Ca(OCH_3)_2$) (*cf.* section 6.2).

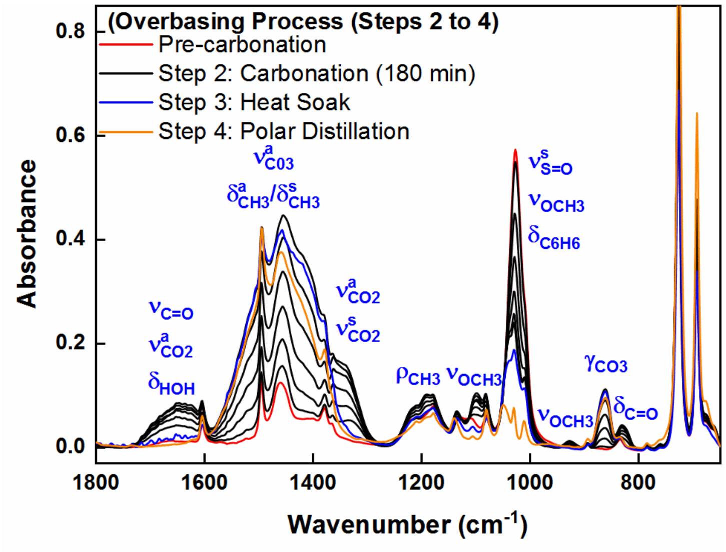

Figure 8.7. *Operando* mid-IR spectra of the calcium sulphonate detergent synthesis process. Time-dependent spectra during the carbonation stage (step 2) – reaction of a $Ca(OH)_2$ and $Ca(R\text{-}SO_3)_2$ mixture with CO_2 to form $nCaCO_3{\cdot}mCa(R–SO_3)_2$ (detergent). The heat soak and polar distillation steps have also been included.

A comparison with the IR of the carbonated dispersion (Figure 8.7) shows that the ν_{OCH3} intensity decrease continues up until the heat soak stage (step 3). As was discussed in section 6.3, the carbonation reaction promotes the formation of $Ca(OCH_3)_2$ as it converts into the $Ca(OCOOCH_3)_2$ ester intermediate. This intermediate then converts into ACC, mostly during the heat soak stage. This conversion is evidenced by the disappearance of the ester stretching and deformation vibrations (*cf.* Table 6.1) following heat soak and polar distillation (step 4). Notably, the *operando* mid-IR results seem to suggest that all of the intermediate is removed with the CH_3OH and H_2O during distillation. However, the previously discussed *ex situ* mid-IR spectrum (Figure 8.2b) shows that the detergent core has traces of $Ca(OCOOCH_3)_2$ and H_2O. This supports the theory that there is a polar interface between the carbonate core and the surfactant layer (10, 13, 34), which probably consists of the intermediate, CH_3OH and H_2O. Further analysis of this interface is required using surface techniques such as X-ray photoelectron spectroscopy (XPS) and time-of-flight secondary ion mass spectroscopy (ToF-SIMS) (10).

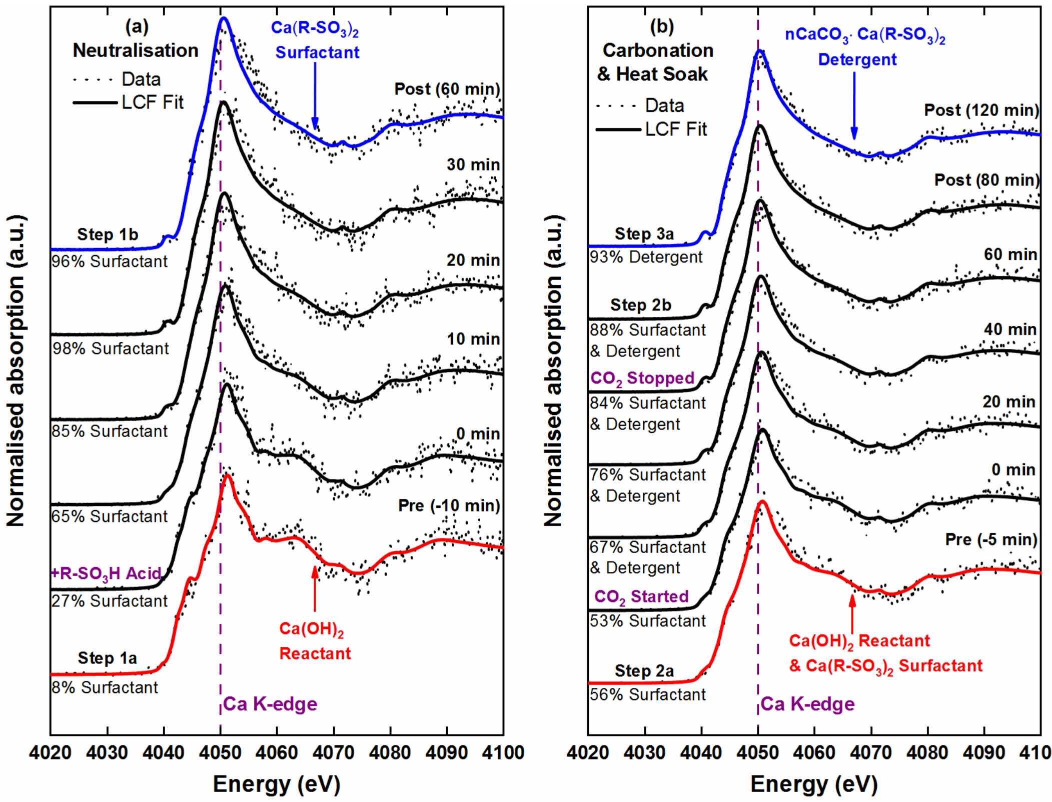

Figure 8.8. Ca K-edge FY XANES spectra of the calcium sulphonate detergent synthesis process. Time-dependent spectra during the (a) neutralisation stage (step 1) – reaction of $Ca(OH)_2$ (base) and $R–SO_3H$ (acid) to form $Ca(R\text{-}SO_3)_2$ (surfactant) and (b) the carbonation stage (step 2) – reaction of a $Ca(OH)_2$ and $Ca(R\text{-}SO_3)_2$ mixture with CO_2 to form $nCaCO_3 \cdot mCa(R–SO_3)_2$ (detergent).

On-line X-ray Absorption Spectroscopy (XAS). XAS was employed to determine $Ca(OH)_2$ dissolution, $CaCO_3$ crystallisation and polymorphic form, the effects of the surfactant on the electronic structure of the detergents, and composition of the reactants and products over time. Fluorescence-yield (FY) XANES spectra were collected at the Ca K-edge during the overbasing process (*cf.* section 3.3.4), and while dispersions were at equilibrium between individual steps of the overbasing process. Results from each of the three main steps of the detergent synthesis i.e. neutralisation (step 1), carbonation (step 2) and heat soak (step 3) are discussed separately below. Notably, the modified/dilute overbasing process with reduced (*cf.* section 3.3.4) sulphonic acid ($R–SO_3H$) and $Ca(OH)_2$ was used for the *operando* XAS experiments to allow for FY detection (*cf.* section 3.4.4).

Neutralisation (Step 1). The initial dispersion contains solid $Ca(OH)_2$ dispersed in water, methanol, toluene and mineral oil. The calcium sulphonate surfactant ($Ca(R-SO_3)_2$) was prepared by the slow addition of sulphonic acid ($R–SO_3H$) to the $Ca(OH)_2$ dispersion over a period of 30 minutes. The XANES spectrum of the pre-neutralisation dispersion (step 1a - Figure 8.8a and 8.9a) is identical to the *ex situ* reference spectrum of the solid phase $Ca(OH)_2$ reactant (*cf.* Figure 5.9a). This confirms that the calcium species in the dispersion is solely present as $Ca(OH)_2$. Following the complete addition of sulphonic acid ($R–SO_3H$), the post-neutralisation (step 1b) spectrum indicates the presence of the calcium sulphonate surfactant ($Ca(R-SO_3)_2$) 'in-process' product. The transformation from $Ca(OH)_2$ (step 1a) to $Ca(R-SO_3)_2$ (step 1b) is readily evident from changes in the XANES spectra from 4040 to 4060 eV (Figure 8.8a and 8.9a). The features at 4045 and 4060 eV in Figure 8.8a, which are generally attributed to $1s \rightarrow 4p$ electronic transitions (170, 172), are particularly diagnostic of changes in the local environment around Ca. Changes in these features can be attributed to the dissociation of the Ca^{2+} and OH^- ions in water and the subsequent formation of ionic bonds between Ca^{2+} and $R-SO_3^-$ ions. The reference XANES spectrum for hydrated Ca^{2+} ions is present in Figure 8.4 in the form of a $CaCl_2$ solution (170). Notably, the changes observed in the post-neutralisation XANES can also be attributed to $Ca(OCH_3)_2$ (*cf.* Figure 5.9a), which was detected in the *operando* mid-IR (Figure 8.6).

Linear combination fitting (LCF) was performed on the *operando* XANES spectra of the dispersion using reference spectra from solid $Ca(OH)_2$ and $Ca(R-SO_3)_2$. LCF showed that the $Ca(R\text{-}SO_3)_2$ present in the dispersion increased from about 8(3) to 96(4)% as $Ca(OH)_2$ content decreased (Figure 8.10a). LCF slightly underestimated the intensity of features present in the experimental spectra between 4050 – 4060 eV after 10 min of reaction (Figure 8.8a) highlighting the presence of Ca with a different local environment to that of the $Ca(OH)_2$ and $Ca(R\text{-}SO_3)_2$ references. The components that have not been accounted for in the LCF are most probably the hydrated Ca^{2+} ions and/or $Ca(OCH_3)_2$. The two references were not included the fits due to their similarity to the surfactant (Figure 8.4a) and hydroxide (*cf.* Figure 5.9a) respectively.

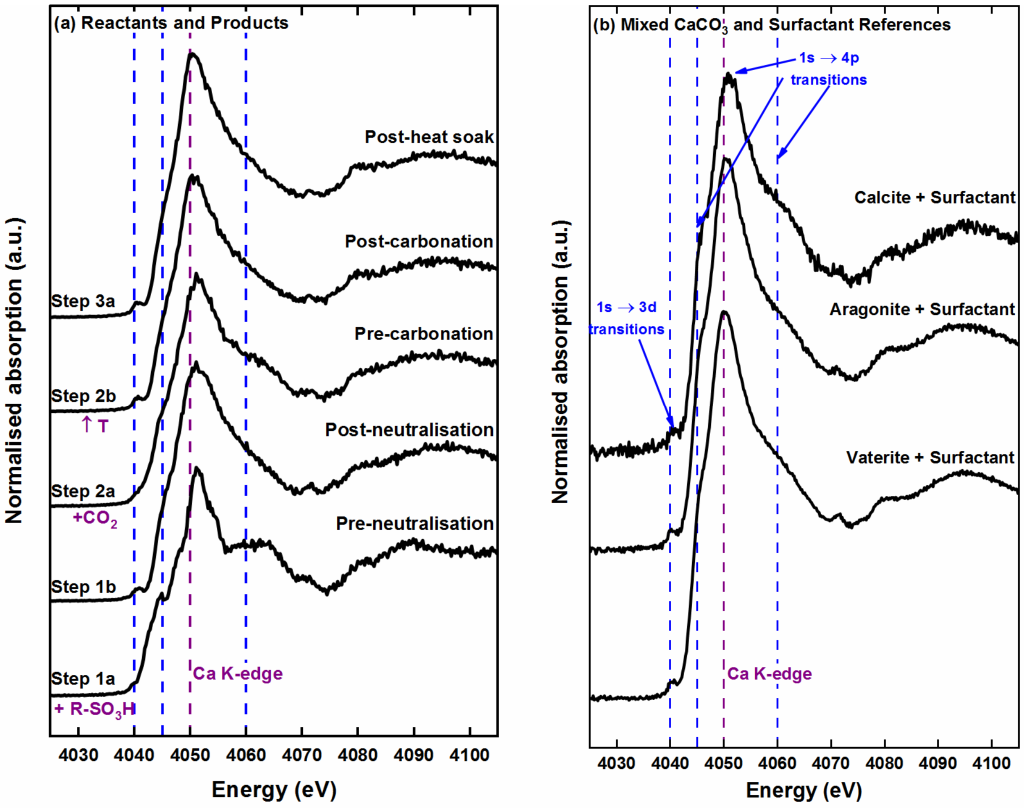

Figure 8.9. (a) Averaged *operando* Ca K-edge FY XANES spectra (of 10 scans) collected at equilibrium points between individual steps of the overbasing process; and (b) *ex situ* TEY reference spectra for mechanically mixed binary systems of $Ca(R\text{-}SO_3)_2$ (surfactant) and calcite/aragonite/vaterite.

Carbonation (Step 2). After neutralisation (step 1), a dispersion of $Ca(R\text{-}SO_3)_2$ surfactant (Figure 8.8a and 8.9a – post-neutralisation) was present in the baffled reactor. A second charge of solid $Ca(OH)_2$ was added to this dispersion immediately prior to carbonation. The presence of $Ca(OH)_2$ in the dispersion is readily evident from the Ca K-edge XAS (pre-carbonation – Figure 8.8b and 8.9a). The dispersion spectrum changes from being smooth and relatively featureless (post-neutralisation) to a spectrum with some defined 1s → 4p features at 4060 eV (pre-carbonation). This confirms that the dispersion contains a mixture of unreacted solid $Ca(OH)_2$ and the neutral $Ca(R\text{-}SO_3)_2$ surfactant.

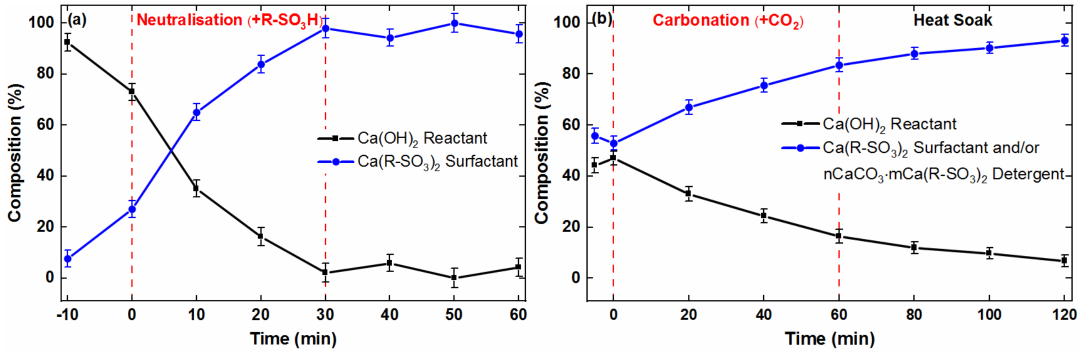

Figure 8.10. Linear combination fitting (LCF) results of the calcium-centric materials ($Ca(OH)_2$ reactant, $Ca(R\text{-}SO_3)_2$ surfactant and $nCaCO_3 \cdot mCa(R–SO_3)_2$detergent) present in the polyphasic dispersion during the (a) neutralisation (step 1) and (b) carbonation (step 2) and heat soak (step 3) reactions of the overbasing process.

Quantitative LCF analysis (Figure 8.10b) of the pre-carbonation spectrum in Figure 8.8b shows that the dispersion consists of 44(3) and 56(3)% of $Ca(OH)_2$ and $Ca(R\text{-}SO_3)_2$ surfactant respectively. Following the introduction of CO_2 flow, the composition of the hydroxide decreased with time as $nCaCO_3 \cdot mCa(R–SO_3)_2$ detergent formed (Figure 8.10b). The LCF shows that after the 60-minute carbonation reaction, more than 80% of the calcium-centric material present in the post-carbonation dispersion (Figure 8.8b) is the $nCaCO_3 \cdot mCa(R–SO_3)_2$ detergent. Due to the similarity of the $Ca(R\text{-}SO_3)_2$ surfactant and the $nCaCO_3 \cdot mCa(R–SO_3)_2$ detergent XANES spectra (Figure 8.4a), the percentages calculated by LCF using the detergent reference have been attributed to both components. Future measurements using C K-edge XAS could help distinguish the detergent and surfactant based on visible contributions from carbon present in CO_3^{2-}, which would only be present in the detergent spectra (19). Notably, preliminary XPS results (not presented here) show that the two sulphonate products are different with respects to their Ca 2p/$L_{2,3}$-edge contributions.

Heat Soak (Step 3). The spectra of the final steps in Figure 8.8b – post-carbonation (step 2b) and post-heat-soak (step 3a) – show the presence of the final product i.e. the calcium sulphonate detergent ($nCaCO_3 \cdot mCa(R–SO_3)_2$). During heat soak, process conditions are the same except that the reactor temperature is increased from 28 – 60 °C. There is an observable decrease in the width of the 1s → 4p feature at 4050 eV following heat soak (Figure 8.8b and 8.9a). This is most probably due to the same conversion of the $Ca(OCOOCH_3)_2$ intermediate into ACC that was observed in the *operando* mid-IR (Figure 8.7). This is supported by the LCF analysis (Figure 8.10b), which shows a slight increase in composition from 88(2)% (Figure 8.8b – post-carbonation) to the expected 93(2)% within 20 minutes of the heat soak stage. 100% conversion to detergent/surfactant is not expected as the amount $Ca(OH)_2$ that was added before carbonation (Figure 8.8b – pre-carbonation) was 5% in excess compared to the required stoichiometric amount.

As one progresses sequentially through the individual reaction steps, the number and intensity of the 1s → 4p pre- and post-edge features in the XANES (Figures 8.8a and 8.9a) decrease such that the spectrum of the $nCaCO_3{\cdot}mCa(R{-}SO_3)_2$ product is relatively featureless compared to the spectrum of the $Ca(OH)_2$ starting material. This lack of features has previously been associated with local disorder around the calcium atom (17, 19), and is reminiscent of the XANES spectrum of ACC (Figure 8.4a). However, there is a possibility of the core being $Ca(OCOOCH_3)_2$, $CaCO_3$-β or $CaCO_3$-γ (based on the presence of 1s → 3d transition feature at 4040 eV), whereby the 1s → 4p features related to crystallinity are being masked. It can be postulated that the (surface) Ca of the surfactant outer layer of the detergent reverse micelles makes up a significant fraction of the total signal such that it masks the signal of the very small (~8 nm) detergent core. This masking effect was observed when the three crystalline polymorphs are mechanically mixed with an equal wt% of surfactant (Figure 8.9b). It is clear to see that even the prominent $CaCO_3$-α 1s → 4p feature at 4060 eV is masked by the surfactant. This effect on the electronic structure can also be observed when the powders of the three crystalline polymorphs are mixed together (Figure F.2 in Appendix F). Interestingly, a reported XANES spectrum for a ternary powder consisting of all three polymorphs (247) is very similar to that of the detergent. This observation reinforces the need to further develop the liquid-jet cell to allow for TEY XAS measurements (Figure B.3 in Appendix B) of concentrated samples with extractable EXAFS data. A complementary *operando* XPDF study would also be beneficial to understanding the surfactant masking effect.

8.4 Conclusions

The results presented in this chapter demonstrate the ability of scanning transmission electron microscopy (STEM), mid-infrared (mid-IR) and Ca K-edge X-ray absorption spectroscopy (XAS) to determine the structure of calcium sulphonate overbased detergents ($nCaCO_3{\cdot}mCa(R{-}SO_3)_2$). Discrete crystallinity was observed in the mostly amorphous detergent core using STEM. Analysis of the fast Fourier transform STEM diffractogram of an isolated crystalline particle suggested that the crystals in the detergent were most probably vaterite ($CaCO_3$-γ). Notably, the STEM results did not exclude the presence of the calcium di-methylcarbonate ($Ca(OCOOCH_3)_2$) intermediate in the core. This intermediate was detected in the *ex situ* mid-IR spectrum of the detergent as well as the *operando* mid-IR and XAS spectra.

Real-time changes were evident in the mid-IR and X-ray absorption near-edge structure (XANES) spectra of the polyphasic dispersion during the neutralisation and carbonation stages of the synthesis. In both cases, analysis of the mid-IR and XANES spectra showed the conversion of $Ca(OH)_2$ to the $Ca(R\text{-}SO_3)_2$ surfactant and $nCaCO_3{\cdot}mCa(R–SO_3)_2$ detergent products as a function of time. Notably, the XAS was capable of simultaneously differentiating up to three different local environments present in the dispersion. However, elucidation of the $nCaCO_3{\cdot}mCa(R–SO_3)_2$ detergent structure was limited by a probable surfactant masking effect, which was evidenced by the similarity of surfactant and detergent XANES spectra. Hence, resolution of the detergent core structure requires additional structural analysis using other techniques such as X-ray photoelectron spectroscopy (XPS) and X-ray pair distribution function (XPDF). Ultimately, the *operando* mid-IR and XAS results confirmed that the detergent $CaCO_3$ core (most probably a mixture of amorphous calcium carbonate (ACC) and $CaCO_3$-γ) forms *via* a $Ca(OCOOCH_3)_2$ intermediate. This proves that structure of overbased calcium sulphonate detergents is highly dependent on the composition of methanol (CH_3OH).

Chapter 9:
Conclusions

9.1 Summary

The primary aim of this thesis was to determine what influences the structure of calcium carbonate ($CaCO_3$) in industrially-relevant overbased calcium sulphonate detergents ($nCaCO_3 \cdot mCa(R–SO_3)_2$). The various *ex* and *in situ* experiments characterised the structure of calcium species formed during the formation of $CaCO_3$ in different process environments to build up a picture of the influence of process parameters on process outcome.

The successful progression of this work was highly dependent on the development of a novel experimental setup, which is presented chapter 4. Figure 9.1 shows a simplified schematic of the continuous-flow liquid-jet experimental setup. This process analytical technology (PAT) system made *operando* monitoring of multiphase multicomponent syntheses possible with simultaneous mid-infrared (mid-IR) and X-ray absorption spectroscopy (XAS). Interpretation of the results of these experiments required a good understanding of the local and electronic structure of possible reagents, intermediates and products.

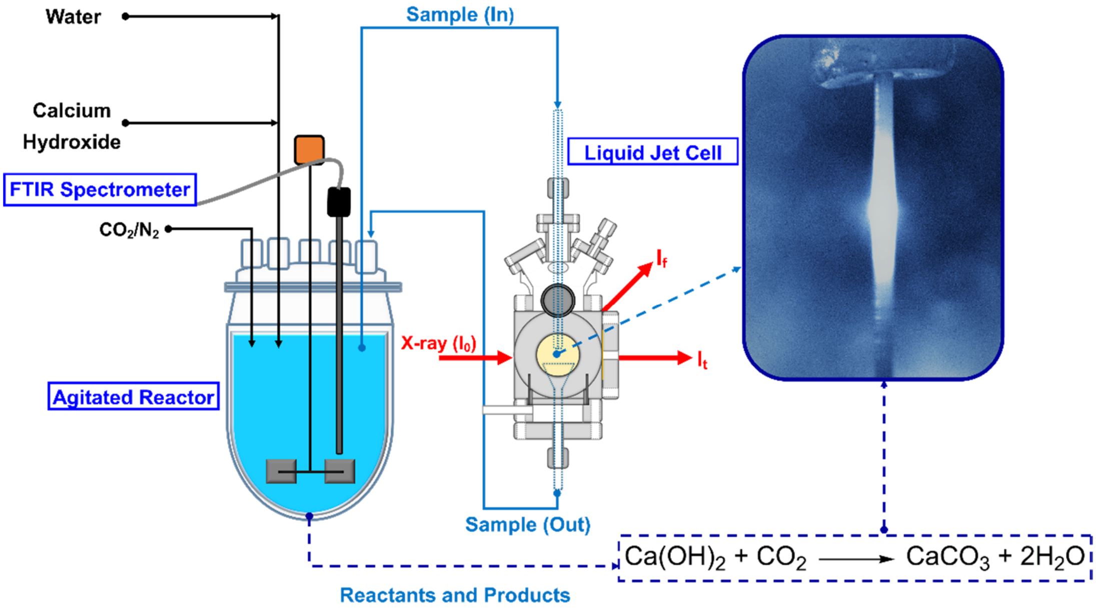

Figure 9.1. Simplified schematic of the continuous-flow liquid-jet PAT experimental setup for simultaneous *in situ/operando* mid-infrared (mid-IR) and X-ray absorption spectroscopy (XAS) measurements.

Table 9.1. Summary of the morphologies and crystal structures determined for the six reference calcium compounds.

Compound	Morphology	Crystal Structure
Calcium oxide (CaO)	-	Cubic – *Fm-3m* (89)
Calcium hydroxide ($Ca(OH)_2$)	-	Hexagonal – *P-3m1* (90)
Calcium methoxide ($Ca(OCH_3)_2$)	Plate-like	Hexagonal – *P-3m1* (91)
Calcite ($CaCO_3$-α)	Rhombohedral	Rhombohedral – *R-3c* (20)
Aragonite ($CaCO_3$-β)	Needle-like	Orthorhombic – *Pnma* (92)
Vaterite ($CaCO_3$-γ)	Spherical	Monoclinic – *C1* (95)

Chapter 5 explored multiple scattering and spectroscopic techniques, including mid-IR and XAS, which were found to be sensitive to calcium speciation of inorganic and metal-organic compounds. The results highlighted subtle structural differences induced by varying the type and unit cell orientation of the anion (Table 9.1). This was mainly illustrated by the two compounds with unconfirmed crystal structures i.e. calcium methoxide ($Ca(OCH_3)_2$) and vaterite ($CaCO_3$-γ). Notably, the sensitivity of the X-ray pair distribution function (XPDF) to variations in crystal structure models (*cf.* Figures 5.15 and 5.16) made it possible to resolve disagreements about the $CaCO_3$-γ structure (27, 93, 163). These experiments demonstrated that $CaCO_3$-γ consists of non-equivalent carbonate ions and that the monoclinic *C1* model structure (95) was the most probable. This work bridged results from powder X-ray diffraction (PXRD) to mid-IR and XAS which probe long- and short-range features respectively of the system.

A further part of the aims and objectives of this thesis was to understand the influence of methanol (CH_3OH) on the detergent core structure. In chapters 6 to 8, *ex* and *in situ* results led to the conclusion that that CH_3OH forms a complex intermediate with the calcium hydroxide ($Ca(OH)_2$) and carbon dioxide (CO_2) reagents (Figure 9.2). The intermediate was identified in chapter 6 as calcium di-methylcarbonate ($Ca(OCOOCH_3)_2$) (195, 196).

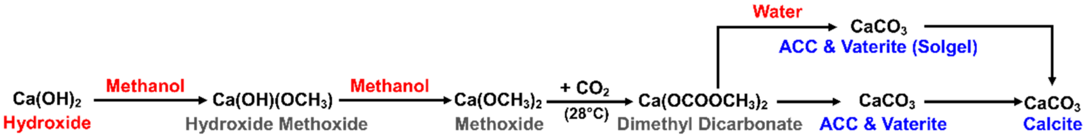

Figure 9.2. Summary of the reaction pathways for the precipitation of calcium carbonate ($CaCO_3$) in pure (100 mol%) and slightly diluted (10 mol% of H_2O) methanol systems.

As was determined in chapter 7 (Figure 9.3), depending on solvent composition this intermediate can transform into various forms of $CaCO_3$ *via* a diffusion-limited aggregation pathway (221). The most prevalent polymorphs were amorphous calcium carbonate (ACC), $CaCO_3$-γ and calcite ($CaCO_3$-α). Aragonite ($CaCO_3$-β) was mainly obtained in the presence of toluene. Notably, it was found that the size of $Ca(OH)_2$ particles influenced the outcome of the reaction in ethanol. Calcium di-ethylcarbonate ($Ca(OCOOCH_2CH_3)_2$) was formed from ethanolic nano-sized $Ca(OH)_2$.

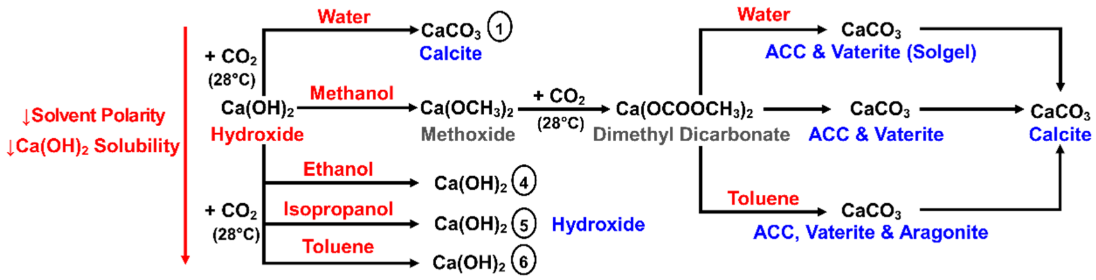

Figure 9.3. Summary of the reaction pathways for the precipitation of calcium carbonate ($CaCO_3$) in aqueous and non-aqueous systems. The formation of four $CaCO_3$ polymorphs is evident in the methanol-dependent routes.

The solvent dependence of the reactive crystallisation of the overbased detergent $CaCO_3$ core was also investigated (chapter 8). Variations in the Ca speciation as a function of time were monitored using the novel PAT system for simultaneous *operando* XAS and mid-IR analysis. The conversion of $Ca(OH)_2$ to $CaCO_3$ *via* the $Ca(OCH_3)_2$ and $Ca(OCOOCH_3)_2$ intermediates was also observed. This conversion was in tandem with the formation of the calcium sulphonate neutral surfactant and overbased detergent (Figure 9.4). The combined *operando* study has highlighted the benefits of using XAS as a PAT tool. XAS is comparatively more sensitive to Ca speciation than a conventional PAT technique such as mid-IR. This was demonstrated by its ability to detect and quantify contributions from intermediates in a very dilute system. Conversely, a concentrated dispersion was required for the mid-IR analysis due to the dominating vibrations of the solvents, acid and surfactant.

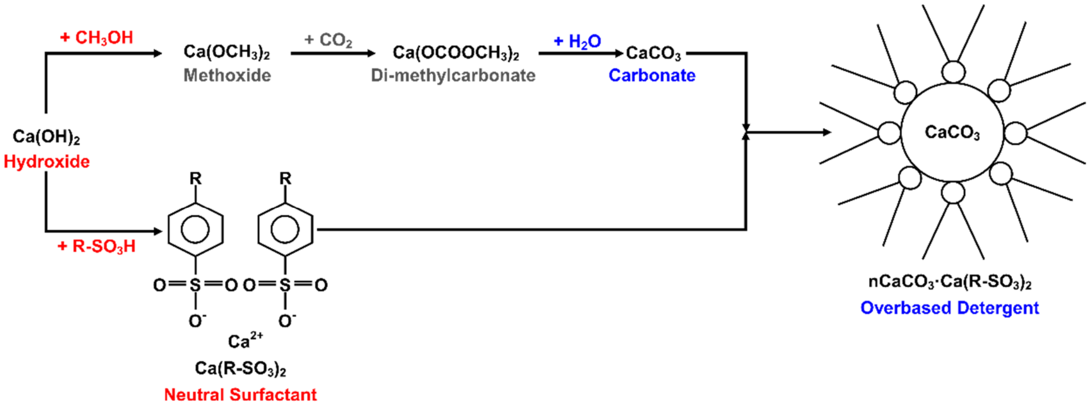

Figure 9.4. Summary of the proposed reaction pathways for the synthesis of overbased calcium sulphonate detergents.

Ultimately, the *ex situ* and *operando* results obtained for the detergents resonate the probability of discrete crystallinity in the core. This has previously been discounted without proper information about the effects of the solvents and surfactant shell on both the formation and detection of the detergent core. There is a high probability that the detergent core consists of more than one carbonated compound i.e. it might consist of a mixture $CaCO_3$ polymorphs (e.g. ACC and $CaCO_3$-γ) and/or the $Ca(OCOOCH_3)_2$ intermediate.

9.2 Recommended Future Work

In terms of future work, there is an inherent need to address the previously discussed limitations of the structural studies presented in this thesis. These limitations include the inability of XAS to distinguish between the neutral calcium sulphonate surfactant and the overbased detergent and the occurrence of a previously uncharacterised intermediate ($Ca(OCOOCH_3)_2$) with an undetermined molecular/crystal structure. Hence, the primary aims of follow-on studies should include: (i) definitive structural elucidation of the various intermediates and how they relate to the detergent core complex; and (ii) determination of the effects of the surfactant shell on the formation and detection of the core. The aims can be achieved by complementing the results presented in this thesis with computational modelling and further experimental work using other analytical techniques. These include X-ray photoelectron spectroscopy (XPS), time-of-flight secondary ion mass spectroscopy (ToF-SIMS), X-ray pair distribution function (XPDF) and solid-state nuclear magnetic resonance (NMR) spectroscopy. Further development of the liquid-jet PAT set-up to allow for TEY XAS measurements (Figure B.3 in Appendix B) of concentrated samples with extractable extended X-ray absorption fine structure (EXAFS) data is also recommended.

Appendix A:

Supplementary Information for Chapter 3

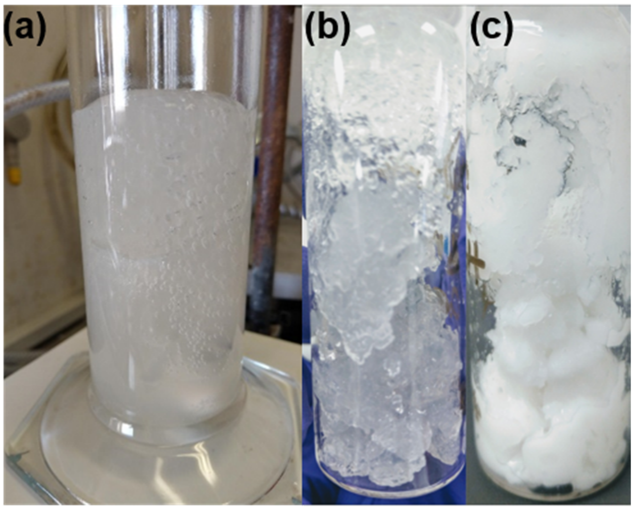

Figure A.1. The product from the carbonation of calcium hydroxide (Ca(OH)2) in 90 mol% methanol. Pictures show (a and b) an initial (~15 min) translucent sol-gel and (c) a sol-gel/white precipitate mixture (~1 h).

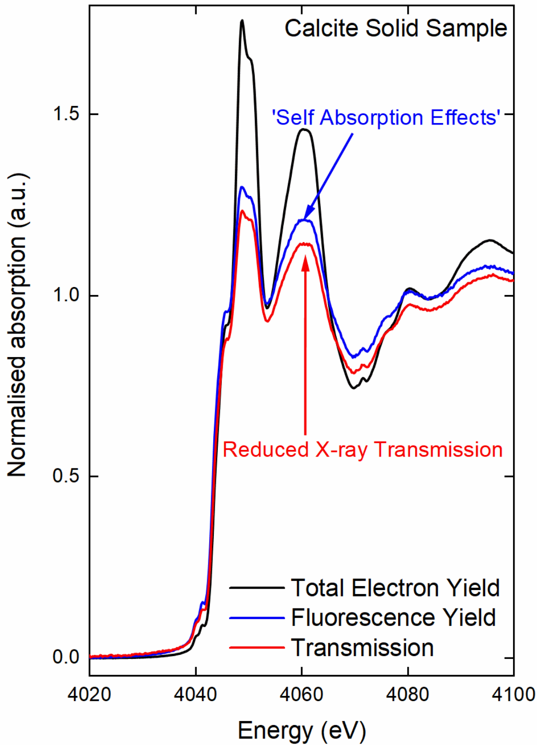

Figure A.2. X-ray absorption spectroscopy (XAS) plot of solid calcite highlighting the three X-ray absorption detection modes: transmission (I_t) or fluorescence yield (I_f; FY) and total electron yield (I_e; TEY).

Appendix B:

Supplementary Information for Chapter 4

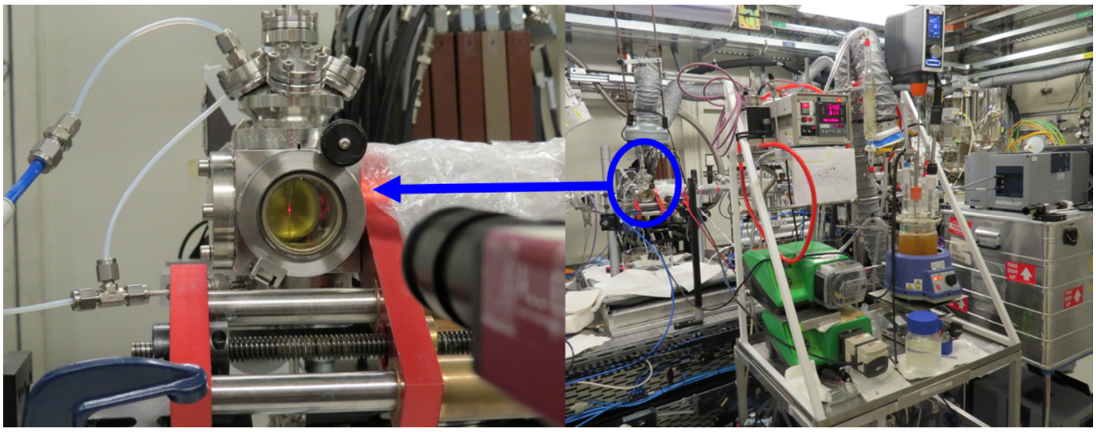

Figure B.1. Pictures of the continuous-flow liquid-jet PAT experimental setup at Beamline B18 (Diamond Light Source)

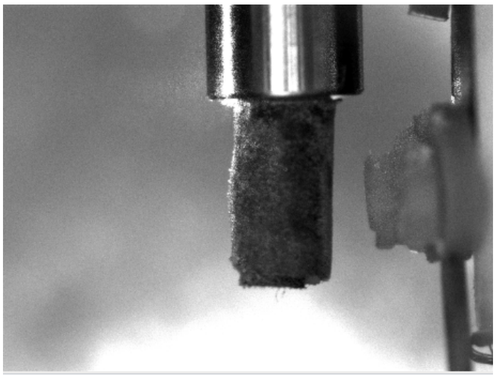

Figure B.2. Picture of the solid configuration of the cell (shown in Figure 4.2) for *ex situ* XAS measurements.

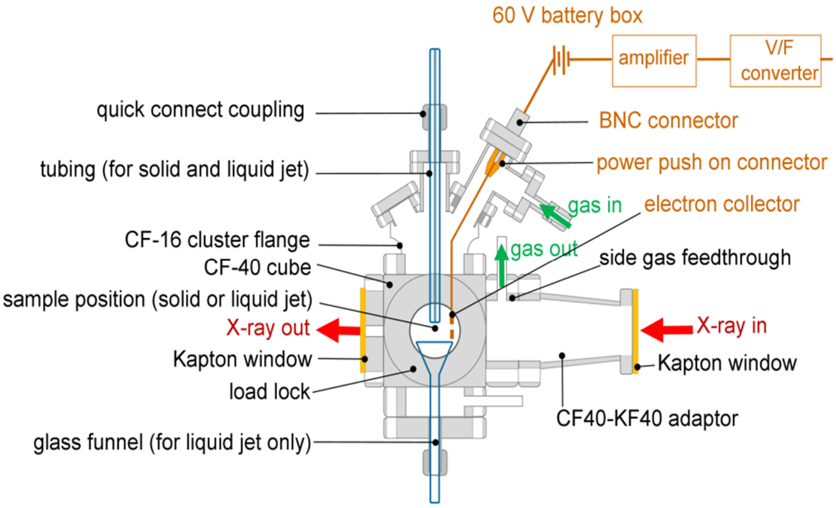

Figure B.3. Schematic of the reconfigured *in situ/operando* liquid-jet cell to include TEY detection for concentrated dispersion – updates courtesy of Sin-Yuen Chang.

Appendix C:

Supplementary Information for Chapter 5

Table C.1. Summary of lattice parameters of various vaterite model crystallographic structures

Reference	Crystal System	Space Group	Lattice Parameters					
			a	b	c	α	β	γ
Meyer, 1959 **(93)**	Orthorhombic	Pbnm	4.13	7.15	8.48	90.00	90.00	90.00
McConnell, 1960 **(160)**	Hexagonal	$P6_{3}22$	7.14	7.14	8.52	-	-	-
Kamhi, 1963 **(158)**	Hexagonal	$P6_{3}/mmc$	4.13	4.13	8.49	90.00	90.00	120.00
Bradley *et al.*, 1966 **(161)**	Hexagonal	$P6_{3}22$	7.14	7.14	8.52	-	-	-
Sato and Matsuda, 1969 **(154)**	Hexagonal	$P6_{3}/mmc$	4.13	4.13	8.49	-	-	-
Meyer, 1969 **(159)**	Hexagonal	$P6_{3}/mmc$	7.15	7.15	16.95	90.00	90.00	120.00
Lippmann, 1973 **(22)**	Hexagonal	$P6_{3}22$	7.15	7.15	8.47	-	-	-
Dupont, 1997 **(143)**	Hexagonal	$P6_{3}/mmc$	7.17	7.17	16.98	-	-	-
Gabrielli *et al.*, 2000 **(156)**	Hexagonal	$P6_{3}/mmc$	7.15	7.15	16.96	-	-	-
Medeiros, 2007 **(248)**	Orthorhombic	Pbnm	4.53	6.64	8.48	-	-	-
Wang and Becker, 2009 **(27)**	Hexagonal	$P6_{5}22$	7.29	7.29	25.30	90.00	90.00	120.00
Le Bail *et al.*, 2011**(94)**	Orthorhombic	Ama2	8.47	7.16	4.13	90.00	90.00	90.00
Demichelis *et al.*, 2012 **(163)**	Hexagonal	$P6_{5}$	7.11	7.11	25.41	90.00	90.00	120.00
Demichelis *et al.*, 2012 **(163)**	Hexagonal	$P3_{2}21$	7.12	7.12	25.32	90.00	90.00	120.00
Demichelis *et al.*, 2012 **(163)**	Orthorhombic	Ama2	8.49	6.39	4.50	90.00	90.00	90.00
Demichelis *et al.*, 2012 **(163)**	Orthorhombic	$P2_{1}2_{1}2_{1}$	4.37	6.58	8.43	90.00	90.00	90.00
Demichelis *et al.*, 2012 **(163)**	Monoclinic	$P112_{1}$	7.11	7.10	25.36	90.00	90.00	60.34
Mugnaioli *et al.*, 2012 **(164)**	Monoclinic	C2/c	12.17	7.12	9.47	90.00	115.37	90.00
Mugnaioli *et al.*, 2012 **(164)**	Monoclinic	C-1	12.17	7.12	25.32	90.00	99.22	90.00
Demichelis *et al.*, 2013 **(95)**	Monoclinic	C2	12.25	7.20	9.31	90.00	115.16	90.00
Demichelis *et al.*, 2013 **(95)**	Monoclinic	Cc	12.28	7.14	9.37	90.00	115.48	90.00
Demichelis *et al.*, 2013 **(95)**	Monoclinic	C1_1	12.36	7.11	25.74	90.43	99.88	90.29
Demichelis *et al.*, 2013 **(95)**	Monoclinic	C1_2	12.35	7.10	25.73	90.46	99.78	90.24

Appendix D:

Supplementary Information for Chapter 6

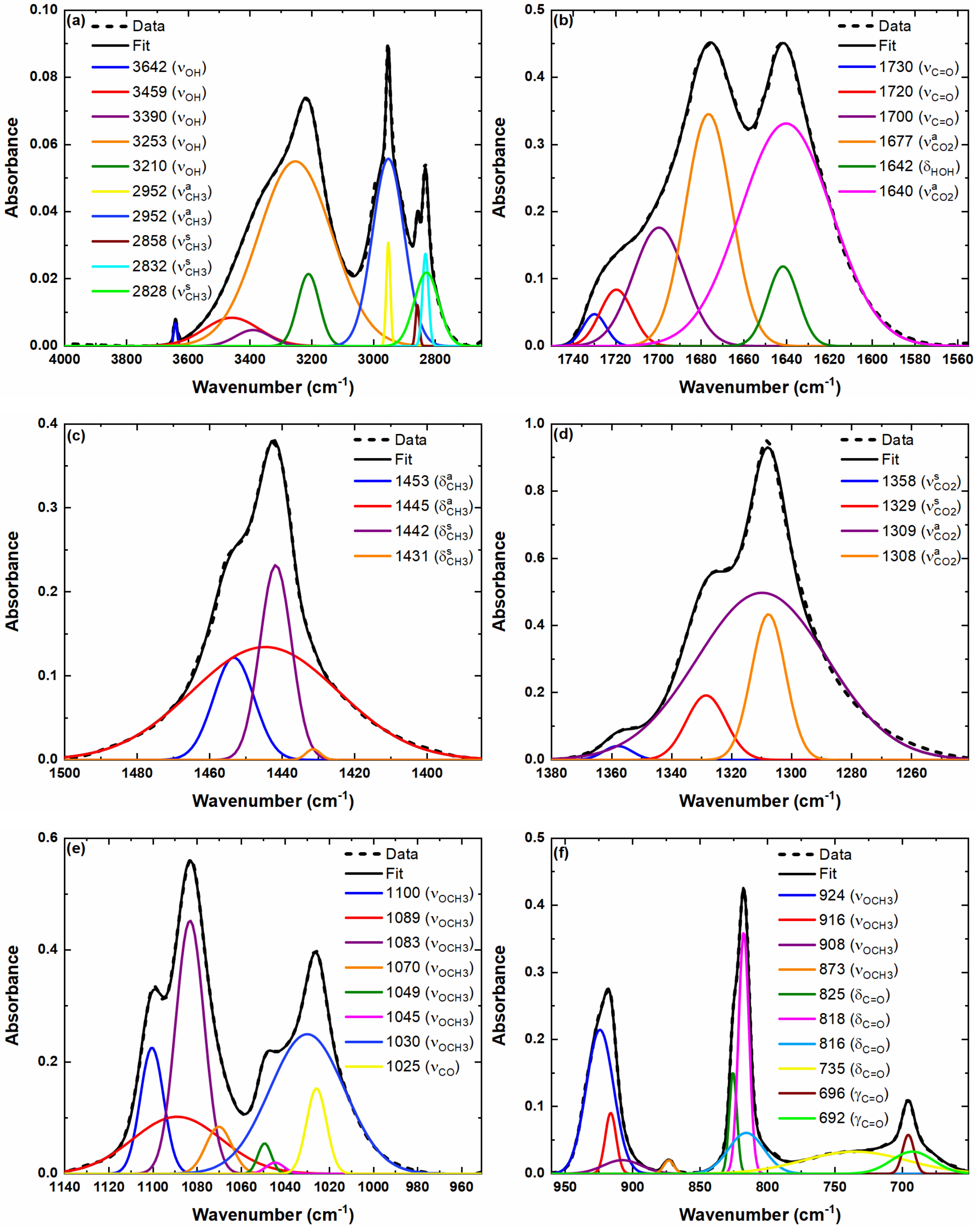

Figure D.1. Deconvoluted Mid-IR plots for the initial (15 minutes) post-carbonation product from the pure (100 mol%) methanolic dispersion from 4000 to 650 cm^{-1} (a to f). Vibrations due to methanol (CH_3OH), calcium methoxide ($Ca(OCH_3)_2$, calcium di-methylcarbonate ($Ca(OCOOCH_3)_2$) and water (H_2O) have been highlighted. All data is summarised in Table 6.1.

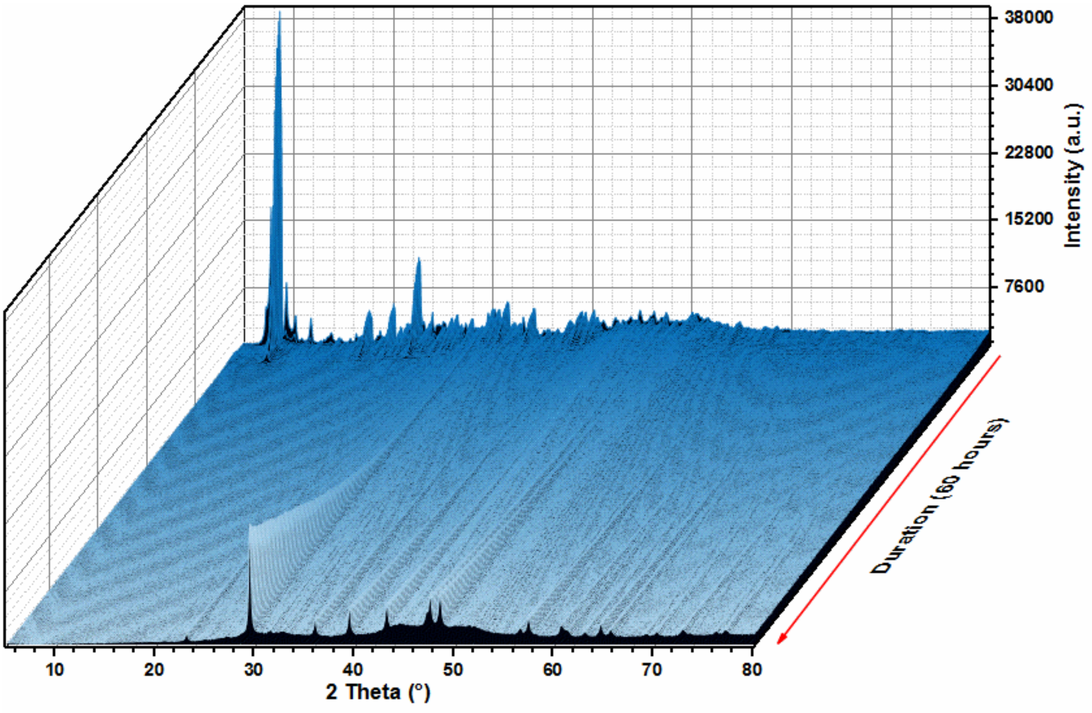

Figure D.2. Time-resolved PXRD plots showing the products precipitated from the carbonation of the pure (100 mol%) methanolic dispersion (experiment 2). Shows conversion from calcium hydroxide ($Ca(OH)_2$) to calcite ($CaCO_3$-α) via calcium methoxide ($Ca(OCH_3)_2$), calcium di-methylcarbonate ($Ca(OCOOCH_3)_2$), amorphous calcium carbonate (ACC) and vaterite ($CaCO_3$-γ).

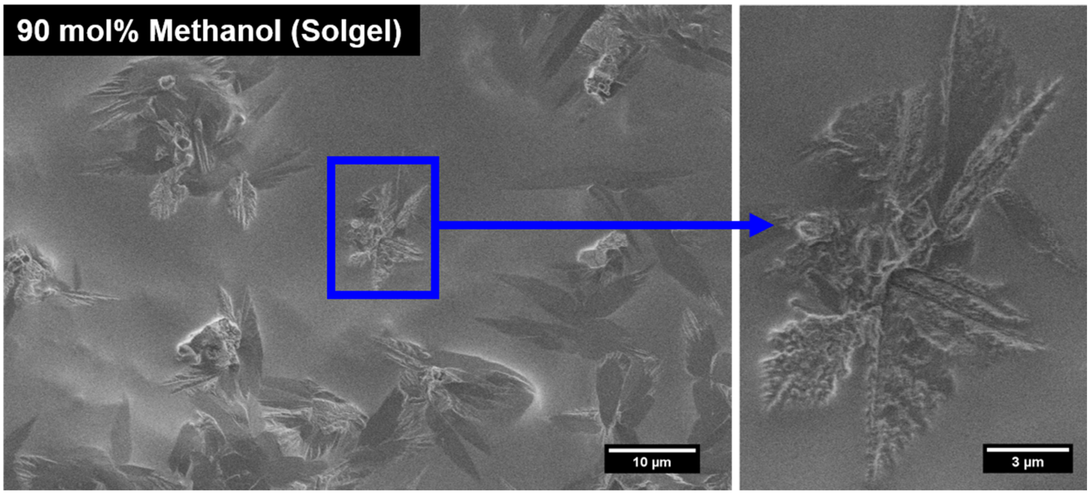

Figure D.3. Cryo-SEM micrographs of the sol-gel post-carbonation product from the diluted (90 mol%) methanolic calcium hydroxide ($Ca(OH)_2$) dispersion showing possible dendrites.

Appendix E:
Supplementary Information for Chapter 7

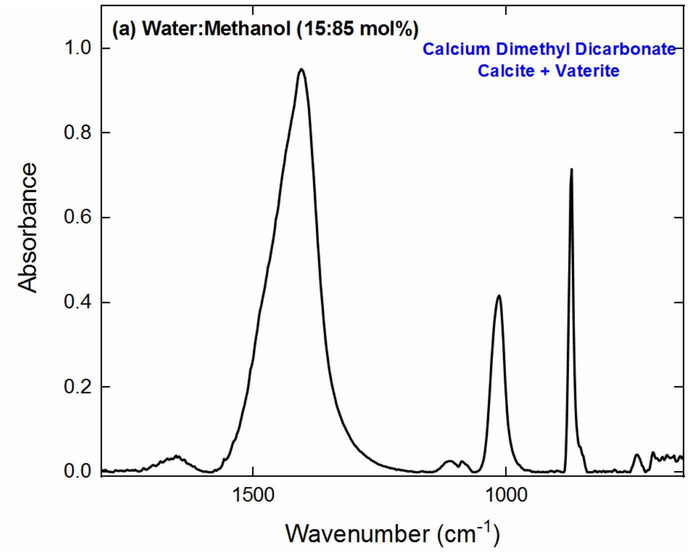

Figure E.1. Mid-IR spectrum of the aged post-carbonation product for the water-methanol system (*cf.* section 7.3).

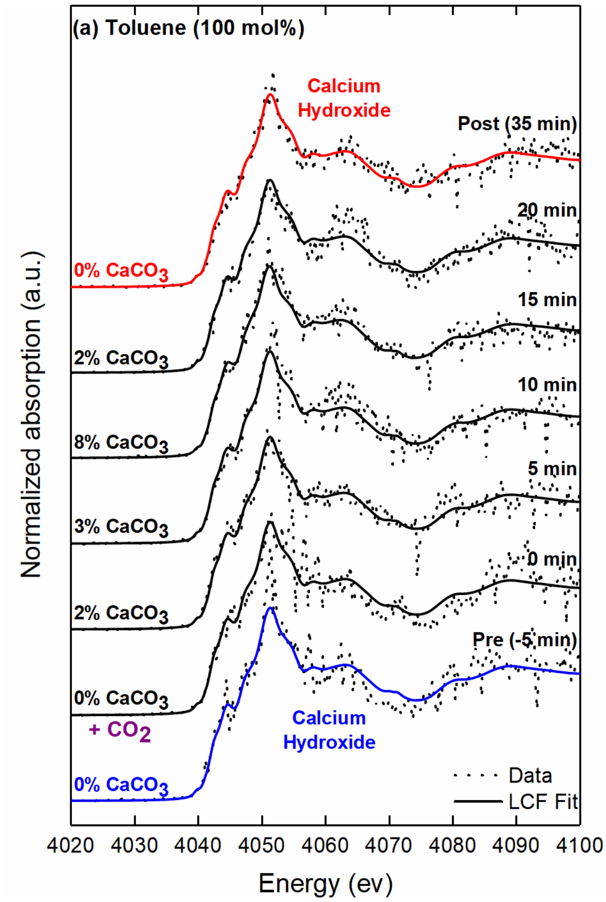

Figure E.2. Time-resolved Ca K-edge XANES of the 20-minute carbonation of calcium hydroxide ($Ca(OH)_2$) in pure toluene – no conversion observed.

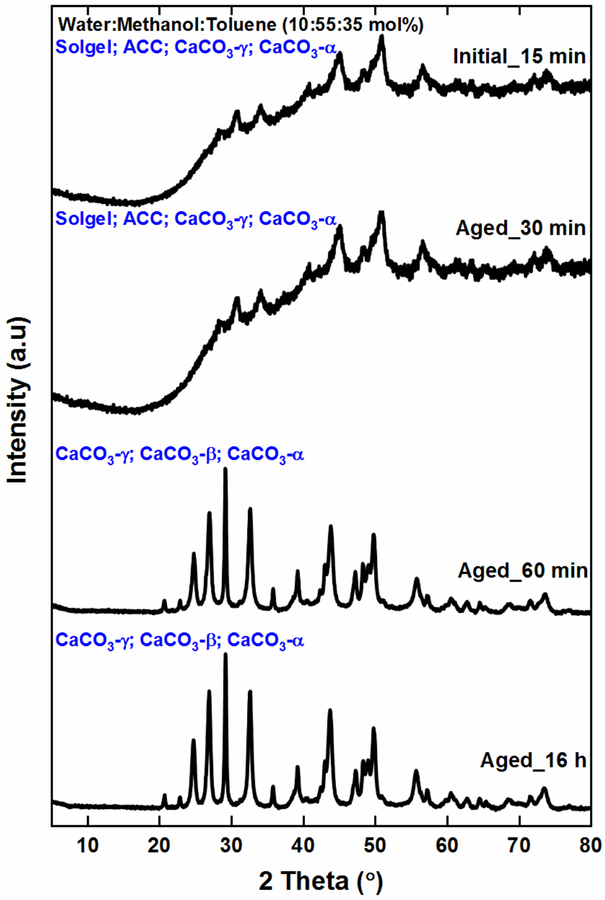

Figure E.3. Time-resolved PXRD plots following the aging of the post-carbonation product (15 mins to 16 hours) precipitated in a ternary water-methanol-toluene (10:55:35 mol%) system (*cf.* section 7.4). Transformation from a sol-gel with amorphous calcium carbonate (ACC) to a mixture of crystalline calcite ($CaCO_3$-α), aragonite ($CaCO_3$-β) and vaterite ($CaCO_3$-γ) observed.

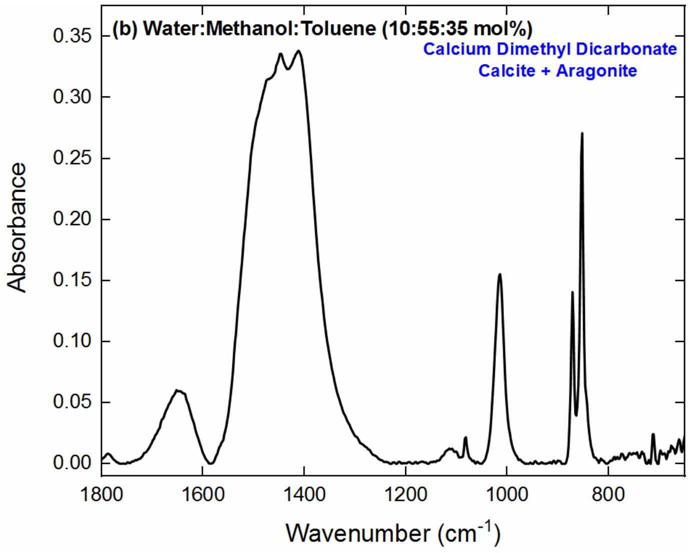

Figure E.4. Mid-IR spectrum of the aged (60 hours) post-carbonation products for the water-methanol-toluene system (*cf.* section 7.3). shows a mixture of calcite ($CaCO_3$-α) and aragonite ($CaCO_3$-β).

Appendix F:

Supplementary Information for Chapter 8

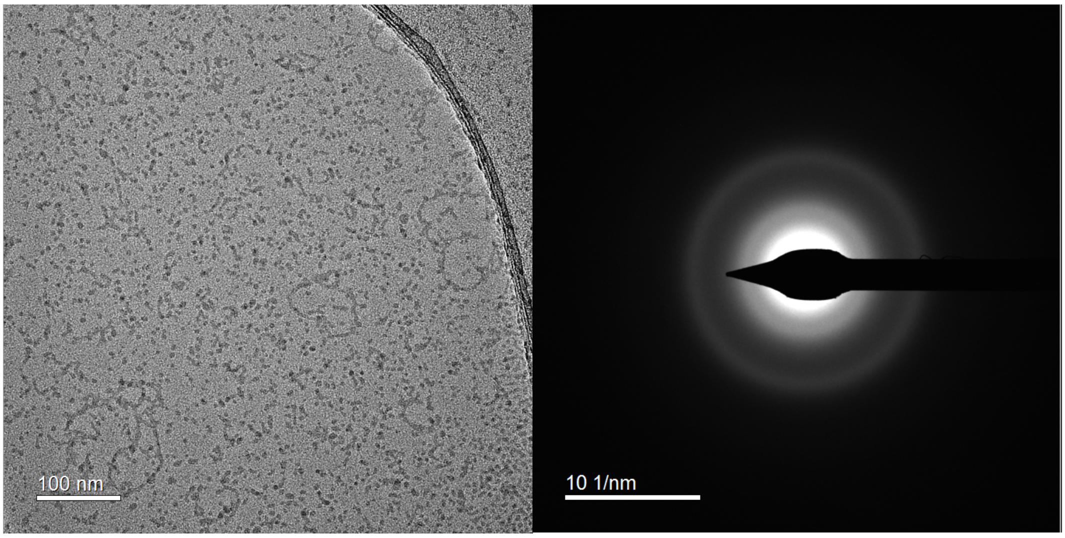

Figure F.1. TEM image and fast Fourier transform pattern of the overbased detergents dispersed in hexane.

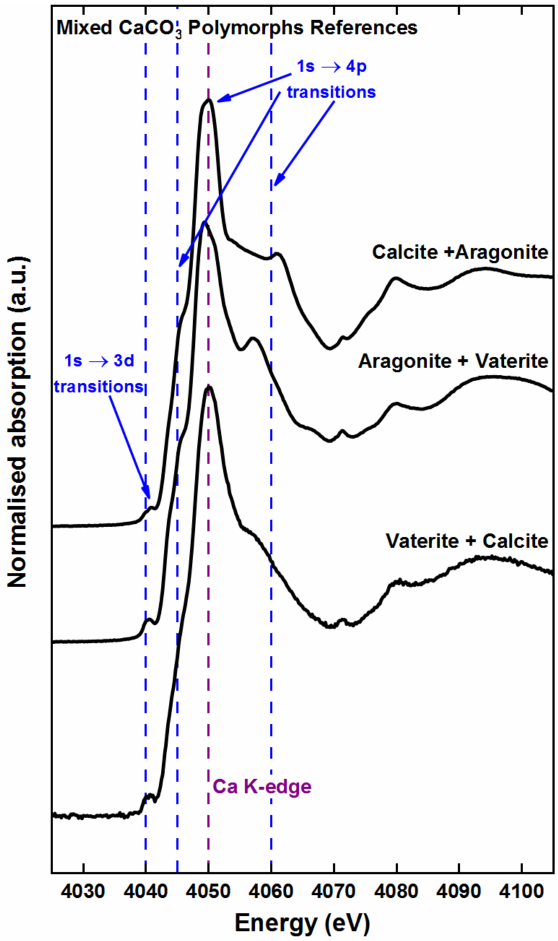

Figure F.2. Ca K-edge XANES of mechanically mixed binary systems containing calcite, aragonite and vaterite.

Appendix G:
Posters and Presentations

Conference Contributions:

1. Thokozile A. Kathyola, P. Mougoyannis, Elizabeth A. Willneff, and Sven L.M. Schroeder. Structural elucidation of calcium carbonate in industrial formulations with X-ray absorption spectroscopy. *ChemEng Day UK 2016, Bath, United Kingdom, 2016.* [Poster Presentation]
2. Thokozile A. Kathyola, Sin-Yuen Chang, Elizabeth A. Willneff, Giannantonio Cibin, Anna B. Kroner, Elizabeth J. Shotton and Sven L.M. Schroeder. XAS as a PAT tool: monitoring a multi-phase multi-component crystallisation process with a liquid-jet system. *Crystallize COST Action Meeting, Prague, Czech Republic, 2018.* [Oral Presentation]

   Extra Funding – Received a travel bursary to attend the COST Action meeting (Prague, Czech Republic) from the European Cooperation in Science and Technology (COST).
3. Thokozile A. Kathyola, Sin-Yuen Chang, Elizabeth A. Willneff, Colin Willis, Giannantonio Cibin, Paul Wilson, Anna B. Kroner, Elizabeth J. Shotton, Peter J. Dowding and Sven L.M. Schroeder. In situ monitoring of the reactive crystallisation of calcium carbonate in multiphase systems. *255th ACS National Meeting, New Orleans, USA, 2018.* [Oral Presentation]

   Extra Funding: Overseas Conference Travel Grant (2018) – Received a travel bursary to attend the 255th ACS National Meeting (New Orleans, USA) from the Analytical Chemistry Trust Fund of the Royal Society of Chemistry.
4. Thokozile A. Kathyola, Elizabeth A. Willneff, Sin-Yuen Chang, and Sven L.M. Schroeder. Combined EXAFS and X-ray Pair Distribution Function (XPDF) analysis of local structure in calcium carbonates. *ChemEng Day UK 2018, Leeds, United Kingdom, 2018.* [Oral Presentation]
5. Thokozile A. Kathyola, Sin-Yuen Chang, Elizabeth A. Willneff, Colin Willis, Arturs Pugejs, Giannantonio Cibin, Paul Wilson, Anna B. Kroner, Elizabeth J. Shotton, Peter J. Dowding and Sven L.M. Schroeder. Combined operando X-ray absorption and infrared spectroscopy of multiphase multicomponent calcium carbonate crystallisation processes. *BACG Annual Meeting, Limerick, Ireland, 2018.* [Poster Presentation]

6. Thokozile A. Kathyola, Sin-Yuen Chang, Elizabeth A. Willneff, Colin Willis, Arturs Pugejs, Giannantonio Cibin, Paul Wilson, Anna B. Kroner, Elizabeth J. Shotton, Peter J. Dowding and Sven L.M. Schroeder. Combined operando X-ray absorption and infrared spectroscopy of multiphase multicomponent calcium carbonate crystallisation processes. *17th International Conference on X-ray Absorption Fine Structure, Krakow, Poland, 2018.* [Oral Presentation]
   Extra Funding: Conference Travel Grant (2018) – Received a travel bursary to attend the 17th International Conference on X-ray Absorption Fine Structure (Krakow, Poland) from the Atomic Spectroscopy Group of the Royal Society of Chemistry.
7. Thokozile A. Kathyola, Andrew Britton, Elizabeth A. Willneff, Sin-Yuen Chang, Laila Al-Madhagi, Bethan Evans, Giannantonio Cibin, Philip Chater, Anna B. Kroner, Elizabeth J. Shotton, Colin Willis, Peter J. Dowding, and Sven L.M. Schroeder. Combined EXAFS and X-ray Pair Distribution Function (XPDF) analysis of local structure in calcium carbonates and ferroelectric relaxors. *17th International Conference on X-ray Absorption Fine Structure, Krakow, Poland, 2018.* [Poster Presentation]
8. Sin-Yuen Chang, Thokozile A. Kathyola, Arturs Pugejs, Elizabeth A. Willneff, Colin Willis, Paul Wilson, Peter J. Dowding, Giannantonio Cibin, Anna B. Kroner, Elizabeth J. Shotton, and Sven L.M. Schroeder. A versatile liquid (liquid-macrojet and droplet) cell for in situ monitoring of multiphase systems using XAS: design considerations and advantages. *17th International Conference on X-ray Absorption Fine Structure, Krakow, Poland, 2018.* [Poster Presentation]
9. Sin-Yuen Chang, Giannantonio Cibin, Thokozile A. Kathyola, Arturs Pugejs, Elizabeth A. Willneff, Colin Willis, Peter J. Dowding, Anna B. Kroner, Elizabeth J. Shotton, and Sven L.M. Schroeder. Ambient pressure gas-flow total electron-yield cell for operando XAFS studies of liquid-jets with soft and tender X-rays. *17th International Conference on X-ray Absorption Fine Structure, Krakow, Poland, 2018.* [Poster Presentation]

References

1. Rizvi, S.Q.A. Lubricant Additives. In: *Comprehensive Review of Lubricant Chemistry, Technology, Selection, and Design*. ASTM International, 2009, pp.100 - 159.
2. Baker, H.R., Singleterry, C.R. and Solomon, E.T. Neutral and basic sulfonates - corrosion-inhibiting and acid-deactivating properties. *Industrial & Engineering Chemistry.* 1954, **46**(5), pp.1035-1042.
3. Bray, U.B., Dickey, C.R. and Voorhees, V. Dispersions of insoluble carbonates in oils. *Industrial & Engineering Chemistry Product Research and Development.* 1975, **14**(4), pp.295-298.
4. Assef, P.A., Mastin, T.W. and Rhodes, A. *Organic Alkaline Earth Metal Complexes and Method of Making Same*. 1952.
5. O'Connor, S.P., Crawford, J. and Cane, C. Overbased lubricant detergents – a comparative study. *Lubrication Science.* 1994, **6**(4), pp.297-325.
6. Bearchell, C.A., Danks, T.N., Heyes, D.M., Moreton, D.J. and Taylor, S.E. Experimental and molecular modelling studies of overbased detergent particles. *Physical Chemistry Chemical Physics.* 2000, **2**(22), pp.5197-5207.
7. Marsh, J.F. Colloidal lubricant additives. *Chemistry & Industry.* 1987, (14), pp.470-473.
8. Hone, D.C., Robinson, B.H., Steytler, D.C., Glyde, R.W. and Galsworthy, J.R. Mechanism of acid neutralization by overbased colloidal additives in hydrocarbon media. *Langmuir.* 2000, **16**(2), pp.340-346.
9. Galsworthy, J., Hammond, S. and Hone, D. Oil-soluble colloidal additives. *Current Opinion in Colloid & Interface Science.* 2000, **5**(5-6), pp.274-279.
10. Cizaire, L., Martin, J.M., Le Mogne, T. and Gresser, E. Chemical analysis of overbased calcium sulfonate detergents by coupling XPS, ToF-SIMS, XANES, and EFTEM. *Colloids and Surfaces a-Physicochemical and Engineering Aspects.* 2004, **238**(1-3), pp.151-158.
11. Langevin, D. Technological Relevance of Microemulsions and Reverse Micelles in Apolar Media. In: Luisi, P.L. and Straub, B.E. eds. *Reverse Micelles: Biological and Technological Relevance of Amphiphilic Structures in Apolar Media*. New York: Plenum Press, 1984, pp.287 - 303.

12. Markovic, I., Ottewill, R.H., Cebula, D.J., Field, I. and Marsh, J.F. Small-angle neutron-scattering studies on non-aqueous dispersions of calcium-carbonate .1. the guinier approach. *Colloid and Polymer Science.* 1984, **262**(8), pp.648-656.

13. Roman, J.P., Hoornaert, P., Faure, D., Biver, C., Jacquet, F. and Martin, J.M. Formation and structure of carbonate particles in reverse microemulsions. *Journal of Colloid and Interface Science.* 1991, **144**(2), pp.324-339.

14. Glavati, O.L., Fialkovskii, R.V., Marchenko, A.I., Premyslov, V.K. and Alekseev, O.L. Stabilization of colloidal $CaCO_3$ dispersions in hydrocarbons containing anionic surfactants. *Colloid Journal of the Ussr.* 1980, **42**(1), pp.20-24.

15. Alcock, K. *Preparation of overbased calcium sulphonates*. Google Patents. 1984.

16. Robbins, M.L., Leder, F., Chludzinski, E. and Chludzinski, G.R. *Preparation of Overbased Sulfonates*. 1969.

17. Martin, J.M., Belin, M. and Mansot, J.L. EXAFS of calcium in overbased micelles. *Journal De Physique.* 1986, **47**(C-8), pp.354-357.

18. Mansot, J.L., Martin, J.M., Dexpert, H., Faure, D., Hoornaert, P. and Gallo, R. Local-structure analysis in overbased reverse micelles. *Physica B.* 1989, **158**(1-3), pp.237-239.

19. Mansot, J.L., Hallouis, M. and Martin, J.M. Colloidal antiwear additives .1. structural study of overbased calcium alkylbenzene sulfonate micelles. *Colloids and Surfaces a-Physicochemical and Engineering Aspects.* 1993, **71**(2), pp.123-134.

20. Markgraf, S.A. and Reeder, R.J. High-temperature structure refinements of calcite and magnesite. *American Mineralogist.* 1985, **70**(5-6), pp.590-600.

21. Devillie.Jp. Crystal structures of aragonite, strontianite, and witherite. *American Mineralogist.* 1971, **56**(5-6), pp.758-&.

22. Lippmann, F. Crystal Chemistry of Sedimentary Carbonate Minerals. In: Lippmann, F. ed. *Sedimentary Carbonate Minerals*. Berlin, Heidelberg: Springer Berlin Heidelberg, 1973, pp.5-96.

23. Behrens, G., Kuhn, L.T., Ubic, R. and Heuer, A.H. Raman-spectra of vateritic calcium-carbonate. *Spectroscopy Letters.* 1995, **28**(6), pp.983-995.

24. Meldrum, F.C. Calcium carbonate in biomineralisation and biomimetic chemistry. *International Materials Reviews.* 2003, **48**(3), pp.187-224.

25. Addadi, L., Raz, S. and Weiner, S. Taking advantage of disorder: Amorphous calcium carbonate and its roles in biomineralization. *Advanced Materials.* 2003, **15**(12), pp.959-970.

26. Maslen, E.N., Streltsov, V.A. and Streltsova, N.R. X-ray study of the electron-density in calcite, $CaCO_3$. *Acta Crystallographica Section B-Structural Science.* 1993, **49**, pp.636-641.

27. Wang, J.W. and Becker, U. Structure and carbonate orientation of vaterite (CaCO3). *American Mineralogist.* 2009, **94**(2-3), pp.380-386.

28. Hudson, L.K., Eastoe, J. and Dowding, P.J. Nanotechnology in action: Overbased nanodetergents as lubricant oil additives. *Advances in Colloid and Interface Science.* 2006, **123**, pp.425-431.

29. Hunt, M.W. *Highly Basic Magnesium Containing Additive Agent*. 1960.

30. Sabol, A.R., Blaha, E.W. and Brannen, C.G. *Methods of Preparing Over-based Alkaline Earth Sulfonates*. 1970.

31. Ellis, G., Hartley, J. and Moseley, J.C. *Improvements in or relating to the Preparation of Basic Oil-Soluble Polyvalent Metal Salts of Organic Acids and Solutions of said Basic Salts in Oils, and the Resulting Salts*. 1957.

32. Ottewill, R.H., Sinagra, E., Macdonald, I.P., Marsh, J.F. and Heenan, R.K. Small-angle neutron-scattering studies on nonaqueous dispersions .5. magnesium carbonate dispersions in hydrocarbon media. *Colloid and Polymer Science.* 1992, **270**(6), pp.602-608.

33. Griffiths, J.A., Bolton, R., Heyes, D.M., Clint, J.H. and Taylor, S.E. Physicochemical characterization of oil-soluble overbased phenate detergents. *Journal of the Chemical Society-Faraday Transactions.* 1995, **91**(4), pp.687-696.

34. Belle, C., Gallo, R., Jacquet, F., Hoornaert, P. and Roman, J.P. The overbasing of detergent additives: The behaviour of promoters and determination of factors controlling the overbasing reaction. *Lubrication Science.* 1992, **5**(1), pp.11-31.

35. Kandori, K., Kon-no, K. and Kitahara, A. Formation of ionic water/oil microemulsions and their application in the preparation of CaCO3 particles. *Journal of Colloid and Interface Science.* 1988, **122**(1), pp.78-82.

36. van Wijngaarden, G.D. and Brons, H.M.J. *Preparation of a Basic Salt*. 1989.

37. Jao, T.C. and Kreuz, K.L. Rigidity of alkylaryl sulfonate micelles monitored by intrinsic fluorescence probes. *Journal of Colloid and Interface Science.* 1988, **126**(2), pp.622-628.

38. Jao, T.C. and Kreuz, K.L. Characterization of inverted micelles of calcium alkaryl-sulfonates by some pyrene fluorescence probes. *Acs Symposium Series.* 1986, **311**, pp.90-99.

39. Markovic, I. and Ottewill, R.H. Small-angle neutron-scattering studies on nonaqueous dispersions of calcium-carbonate .3. concentrated dispersions. *Colloid and Polymer Science.* 1986, **264**(5), pp.454-462.

40. Kandori, K., Shizuka, N., Konno, K. and Kitahara, A. Preparation of caco3 particles in water pool in nonaqueous nonionic surfactant solutions. *Journal of Dispersion Science and Technology.* 1987, **8**(5-6), pp.477-491.

41. Tavacoli, J.W., Dowding, P.J., Steyder, D.C., Barnes, D.J. and Routh, A.F. Effect of water on overbased sulfonate engine oil additives. *Langmuir.* 2008, **24**(8), pp.3807-3813.

42. Osullivan, T.P., Vickers, M.E. and Heenan, R.K. The characterization of oil-soluble calcium-carbonate dispersions using small-angle x-ray-scattering (SAXS) and small-angle neutron-scattering (SANS). *Journal of Applied Crystallography.* 1991, **24**, pp.732-739.

43. Jao, T.C. and Kreuz, K.L. Solubility of oxygen in inverted micelles of calcium alkylbenzene sulfonates. *Journal of Colloid and Interface Science.* 1984, **102**(1), pp.308-310.

44. Kandori, K., Kon-no, K. and Kitahara, A. Dispersion stability of nonaqueous calcium carbonate dispersion prepared in water core of WO microemulsion. *Journal of Colloid and Interface Science.* 1987, **115**(2), pp.579-582.

45. Martin, J.M., Mansot, J.L. and Hallouis, M. Energy filtered electron-microscopy (EFEM) of overbased reverse micelles. *Ultramicroscopy.* 1989, **30**(3), pp.321-327.

46. Martin, J.M., Mansot, J.L., Hallouis, M. and Tenailleau, H. High-resolution electron spectroscopic imaging (ESI) of reverse micelles. *Microscopy Microanalysis Microstructures.* 1990, **1**(2), pp.93-102.

47. Giasson, S., Espinat, D., Palermo, T., Ober, R., Pessah, M. and Morizur, M.F. small-angle x-ray-scattering (SAXS) on calcium sulfonate dispersions - effects of friction on microstructure. *Journal of Colloid and Interface Science.* 1992, **153**(2), pp.355-367.

48. Makhloufi, R., Mansot, J.L., Hirsch, E., Wery, J., Candau, S.J., Thomas, D. and Rolland, J.P. Electron-microscopy and light-scattering STUDY OF

organometallic inverse micellar systems. *Colloid and Polymer Science.* 1995, **273**(3), pp.242-251.

49. Mansot, J.L., Hallouis, M. and Martin, J.M. Colloidal antiwear additives .2. tribological behavior of colloidal additives in mild wear regime. *Colloids and Surfaces a-Physicochemical and Engineering Aspects.* 1993, **75**, pp.25-31.

50. Cabos, C., Delord, P. and Rouviere, J. Dimensions of mixed micelles of para-alkylbenzene sulfonates determined by x-ray small-angle scattering. *Journal of Applied Crystallography.* 1977, **10**(FEB1), pp.37-44.

51. Tze-Chi, J. and Kenneth, L.K. Characterization of inverted micelles of calcium alkarylsulfonates by some pyrene fluorescence probes. In: *Phenomena in Mixed Surfactant Systems*. American Chemical Society, 1986, pp.90-99.

52. Geere, R.G., Gaskell, P.H., Greaves, G.N., Greengrass, J. and Binstead, N. EXAFS and XANES spectra of calcium silicate glasses. In: Bianconi, A. et al. eds. *EXAFS and Near Edge Structure*. Springer Berlin Heidelberg, 1983, pp.256-260.

53. Taylor, M.G., Simkiss, K., Greaves, G.N., Okazaki, M. and Mann, S. An X-ray absorption spectroscopy study of the structure and transformation of amorphous calcium carbonate from plant cystoliths. *Proceedings of the Royal Society B-Biological Sciences.* 1993, **252**(1333), pp.75-80.

54. Levi-Kalisman, Y., Raz, S., Weiner, S., Addadi, L. and Sagi, I. X-Ray absorption spectroscopy studies on the structure of a biogenic "amorphous" calcium carbonate phase. *Journal of the Chemical Society-Dalton Transactions.* 2000, (21), pp.3977-3982.

55. Becker, A., Bismayer, U., Epple, M., Fabritius, H., Hasse, B., Shi, J.M. and Ziegler, A. Structural characterisation of X-ray amorphous calcium carbonate (ACC) in sternal deposits of the crustacea Porcellio scaber. *Dalton Transactions.* 2003, (4), pp.551-555.

56. Marxen, J.C., Becker, W., Finke, D., Hasse, B. and Epple, M. Early mineralization in Biomphalaria glabrata: Microscopic and structural results. *Journal of Molluscan Studies.* 2003, **69**, pp.113-121.

57. Politi, Y., Levi-Kalisman, Y., Raz, S., Wilt, F., Addadi, L., Weiner, S. and Sagi, I. Structural characterization of the transient amorphous calcium carbonate precursor phase in sea urchin embryos. *Advanced Functional Materials.* 2006, **16**(10), pp.1289-1298.

58. Lam, R.S.K., Charnock, J.M., Lennie, A. and Meldrum, F.C. Synthesis-dependant structural variations in amorphous calcium carbonate. *Crystengcomm.* 2007, **9**(12), pp.1226-1236.

59. Gunther, C., Becker, A., Wolf, G. and Epple, M. In vitro synthesis and structural characterization of amorphous calcium carbonate. *Zeitschrift Fur Anorganische Und Allgemeine Chemie.* 2005, **631**(13-14), pp.2830-2835.

60. Neumann, M. and Epple, M. Monohydrocalcite and its relationship to hydrated amorphous calcium carbonate in biominerals. *European Journal of Inorganic Chemistry.* 2007, (14), pp.1953-1957.

61. Michel, F.M., MacDonald, J., Feng, J., Phillips, B.L., Ehm, L., Tarabrella, C., Parise, J.B. and Reeder, R.J. Structural characteristics of synthetic amorphous calcium carbonate. *Chemistry of Materials.* 2008, **20**(14), pp.4720-4728.

62. Ravel, B. and Newville, M. ATHENA, ARTEMIS, HEPHAESTUS: data analysis for X-ray absorption spectroscopy using IFEFFIT. *Journal of Synchrotron Radiation.* 2005, **12**, pp.537-541.

63. Newville, M. Fundamentals of XAFS. In: Henderson, G.S. et al. eds. *Spectroscopic Methods in Mineralology and Materials Sciences.* Chantilly: Mineralogical Soc Amer, 2014, pp.33-74.

64. Hasse, B., Ehrenberg, H., Marxen, J.C., Becker, W. and Epple, M. Calcium carbonate modifications in the mineralized shell of the freshwater snail Biomphalaria glabrata. *Chemistry-a European Journal.* 2000, **6**(20), pp.3679-3685.

65. Lam, R., Charnock, J.M., Lennie, A. and Meldrum, F.C. Synthesis-dependant structural variations in amorphous calcium carbonate. *Crystal Engineering Communications.* 2007, (9), pp.1226-1236.

66. Tobler, D.J., Blanco, J.D.R., Sorensen, H.O., Stipp, S.L.S. and Dideriksen, K. Effect of pH on Amorphous Calcium Carbonate Structure and Transformation. *Crystal Growth & Design.* 2016, **16**(8), pp.4500-4508.

67. Goodwin, A.L., Michel, F.M., Phillips, B.L., Keen, D.A., Dove, M.T. and Reeder, R.J. Nanoporous Structure and Medium-Range Order in Synthetic Amorphous Calcium Carbonate. *Chemistry of Materials.* 2010, **22**(10), pp.3197-3205.

68. Kitamura, M., Konno, H., Yasui, A. and Masuoka, H. Controlling factors and mechanism of reactive crystallization of calcium carbonate polymorphs from calcium hydroxide suspensions. *Journal of Crystal Growth.* 2002, **236**(1-3), pp.323-332.

69. Shivkumara, C., Singh, P., Gupta, A. and Hegde, M.S. Synthesis of vaterite CaCO3 by direct precipitation using glycine and L-alanine as directing agents. *Materials Research Bulletin.* 2006, **41**(8), pp.1455-1460.

70. Koga, N., Nakagoe, Y.Z. and Tanaka, H. Crystallization of amorphous calcium carbonate. *Thermochimica Acta.* 1998, **318**(1-2), pp.239-244.

71. Williams, D.B. and Carter, C.B. The transmission electron microscope. In: *Transmission electron microscopy: A textbook for materials science.* Boston, MA: Springer US, 2009, pp.3-22.

72. Bell, D.C. and Erdman, N. Introduction to the theory and advantages of low voltage electron microscopy. In: Brooks, S. et al. eds. *Low voltage electron microscopy.* 2012.

73. Hooley, R., Brown, A. and Brydson, R. Factors affecting electron beam damage in calcite nanoparticles. *Micron.* 2019, **120**, pp.25-34.

74. Schneider, C.A., Rasband, W.S. and Eliceiri, K.W. NIH Image to ImageJ: 25 years of image analysis. *Nature Methods.* 2012, **9**(7), pp.671-675.

75. Sader, K., Brown, A., Brydson, R. and Bleloch, A. Quantitative analysis of image contrast in phase contrast STEM for low dose imaging. *Ultramicroscopy.* 2010, **110**(10), pp.1324-1331.

76. Bragg, W.H. and Bragg, W.L. The reflection of X-rays by crystals. *Proceedings of the Royal Society of London Series a-Containing Papers of a Mathematical and Physical Character.* 1913, **88**(605), pp.428-438.

77. Reeder, R.J. and Michel, F.M. Chapter twenty - Application of total x-ray scattering methods and pair distribution function analysis for study of structure of biominerals. In: De Yoreo, J.J. ed. *Methods in enzymology.* Academic Press, 2013, pp.477-500.

78. Takeshi, E. and Billinge, S.J.L. Chapter 3 - The method of total scattering and atomic pair distribution function analysis. In: Egami, T. and Billinge, S.J.L. eds. *Pergamon Materials Series.* Pergamon, 2012, pp.55-111.

79. Takeshi, E. and Billinge, S.J.L. Chapter 2 - Crystallographic analysis of complex materials. In: Egami, T. and Billinge, S.J.L. eds. *Pergamon Materials Series.* Pergamon, 2012, pp.27-54.

80. Reeder, R.J., Tang, Y.Z., Schmidt, M.P., Kubista, L.M., Cowan, D.F. and Phillips, B.L. Characterization of structure in biogenic amorphous calcium carbonate:

pair distribution function and nuclear magnetic resonance studies of lobster gastrolith. *Crystal Growth & Design.* 2013, **13**(5), pp.1905-1914.

81. Costello, M.T. X-ray diffraction of amorphous and crystalline overbased sulphonates. *Tribotest.* 2006, **11**(3), pp.207-212.

82. Degen, T., Sadki, M., Bron, E., Konig, U. and Nenert, G. The HighScore suite. *Powder Diffraction.* 2014, **29**, pp.S13-S18.

83. Bergerhoff, G., Hundt, R., Sievers, R. and Brown, I.D. The inorganic crystal-structure data-base. *Journal of Chemical Information and Computer Sciences.* 1983, **23**(2), pp.66-69.

84. Filik, J., Ashton, A.W., Chang, P.C.Y., Chater, P.A., Day, S.J., Drakopoulos, M., Gerring, M.W., Hart, M.L., Magdysyuk, O.V., Michalik, S., Smith, A., Tang, C.C., Terrill, N.J., Wharmby, M.T. and Wilhelm, H. Processing two-dimensional X-ray diffraction and small-angle scattering data in DAWN 2. *Journal of Applied Crystallography.* 2017, **50**, pp.959-966.

85. Hannon, A.C., Howells, W.S. and Soper, A.K. ATLAS - A suite of programs for the analysis of time-of-flight neutron-diffraction data from liquid and amorphous samples. *Institute of Physics Conference Series.* 1990, (107), pp.193-211.

86. Farrow, C.L., Juhas, P., Liu, J.W., Bryndin, D., Bozin, E.S., Bloch, J., Proffen, T. and Billinge, S.J.L. PDFfit2 and PDFgui: computer programs for studying nanostructure in crystals. *Journal of Physics-Condensed Matter.* 2007, **19**(33), p.7.

87. Downs, R.T. and Hall-Wallace, M. The American mineralogist crystal structure database. *American Mineralogist.* 2003, **88**(1), pp.247-250.

88. Wojdyr, M. Fityk: a general-purpose peak fitting program. *Journal of Applied Crystallography.* 2010, **43**, pp.1126-1128.

89. Wong-Ng, W., McMurdie, H.F., Hubbard, C.R. and Mighell, A.D. JCPDS-ICDD Research Associateship (cooperative program with NBS/NIST). *Journal of Research of the National Institute of Standards and Technology.* 2001, **106**(6), pp.1013-1028.

90. Busing, W.R. and Levy, H.A. Neutron diffraction study of calcium hydroxide. *Journal of Chemical Physics.* 1957, **26**(3), pp.563-568.

91. Staeglich, H. and Weiss, E. Crystal-structures of alkaline-earth methanolates $M(OCH_3)_2$,M=Ca,Sr,Ba. *Chemische Berichte-Recueil.* 1978, **111**(3), pp.901-905.

92. Pilati, T., Demartin, F. and Gramaccioli, C.M. Lattice-dynamical estimation of atomic displacement parameters in carbonates: Calcite and aragonite $CaCO_3$,

dolomite CaMg(CO_3)(2) and magnesite $MgCO_3$. *Acta Crystallographica Section B-Structural Science Crystal Engineering and Materials.* 1998, **54**, pp.515-523.

93. Meyer, H.J. Uber vaterit und seine struktur. *Angewandte Chemie-International Edition.* 1959, **71**(21), pp.678-678.

94. Le Bail, A., Ouhenia, S. and Chateigner, D. Microtwinning hypothesis for a more ordered vaterite model. *Powder Diffraction.* 2011, **26**(1), pp.16-21.

95. Demichelis, R., Raiteri, P., Gale, J.D. and Dovesi, R. The Multiple structures of vaterite. *Crystal Growth & Design.* 2013, **13**(6), pp.2247-2251.

96. Bhagavantam, S. and Venkatarayudu, T. Raman effect in relation to crystal structure. *Proceedings of the Indian Academy of Sciences - Section A.* 1939, **9**(3), pp.224-258.

97. Herzberg, G. *Molecular spectra and molecular structure. II. Infrared and Raman spectra of polyatomic molecules.* Van Nostrand, 1939.

98. Workman, J. *The Concise Handbook of Analytical Spectroscopy: Theory, Applications, and Reference Materials.* WORLD SCIENTIFIC, 2016.

99. Amma, S., Luo, J.W., Pantano, C.G. and Kim, S.H. Specular reflectance (SR) and attenuated total reflectance (ATR) infrared (IR) spectroscopy of transparent flat glass surfaces: A case study for soda lime float glass. *Journal of Non-Crystalline Solids.* 2015, **428**, pp.189-196.

100. Wojdyr, M. Fityk: a general-purpose peak fitting program. *Journal of Applied Crystallography.* 2010, **43**(5), pp.1126-1128.

101. Koningsberger, D.C. Extended x-ray-absorption fine-structure - physical principles and data-analysis. *Synchrotron Techniques in Interfacial Electrochemistry.* 1994, **432**, pp.181-198.

102. Koningsberger, D.C., Mojet, B.L., van Dorssen, G.E. and Ramaker, D.E. XAFS spectroscopy; fundamental principles and data analysis. *Topics in Catalysis.* 2000, **10**(3-4), pp.143-155.

103. Bordiga, S., Groppo, E., Agostini, G., van Bokhoven, J.A. and Lamberti, C. Reactivity of Surface Species in Heterogeneous Catalysts Probed by In Situ X-ray Absorption Techniques. *Chemical Reviews.* 2013, **113**(3), pp.1736-1850.

104. Booth, C.H. and Bridges, F. Improved self-absorption correction for fluorescence measurements of extended X-ray absorption fine-structure. *Physica Scripta.* 2005, **T115**, pp.202-204.

105. Hahn, T., Klapper, H., Müller, U. and Aroyo, M.I. Point groups and crystal classes. *International Tables for Crystallography.* 2016.

106. Chen, L.X. X-Ray transient absorption spectroscopy. In: *X-ray absorption and X-ray emission spectroscopy.* John Wiley & Sons, Ltd, 2016, pp.213-249.

107. Yael, P. and Ivo, Z. Local structure development. In: *Biomineralization sourcebook.* CRC Press, 2014, pp.95-113.

108. Martens, G., Rabe, P. and Wenck, P. Destructive interference and multiple-scattering effects observed in Ca K-edge EXAFS spectra. *Physica Status Solidi a-Applied Research.* 1985, **88**(1), pp.103-111.

109. Yu, L.X., Lionberger, R.A., Raw, A.S., D'Costa, R., Wu, H.Q. and Hussain, A.S. Applicatlons of process analytical technology to crystallization processes. *Advanced Drug Delivery Reviews.* 2004, **56**(3), pp.349-369.

110. Skibsted, E. and Engelsen, S.B. Spectroscopy for Process Analytical Technology (PAT) A2 - Lindon, John C. In: Tranter, G.E. and Koppenaal, D.W. eds. *Encyclopedia of spectroscopy and spectrometry (Third Edition).* Oxford: Academic Press, 2017, pp.188-197.

111. Cornel, J., Lindenberg, C. and Mazzotti, M. Quantitative application of in situ ATR-FTIR and Raman spectroscopy in crystallization processes. *Industrial & Engineering Chemistry Research.* 2008, **47**(14), pp.4870-4882.

112. Chang, S.Y., Grunder, Y., Booth, S.G., Molleta, L.B., Uehara, A., Mosselmans, J.F.W., Cibin, G., Pham, V.T., Nataf, L., Dryfe, R.A.W. and Schroeder, S.L.M. Detection and characterisation of sub-critical nuclei during reactive Pd metal nucleation by X-ray absorption spectroscopy. *Crystengcomm.* 2016, **18**(5), pp.674-682.

113. Seidler, G.T., Mortensen, D.R., Remesnik, A.J., Pacold, J.I., Ball, N.A., Barry, N., Styczinski, M. and Hoidn, O.R. A laboratory-based hard x-ray monochromator for high-resolution x-ray emission spectroscopy and x-ray absorption near edge structure measurements. *Review of Scientific Instruments.* 2014, **85**(11), p.12.

114. Dent, A.J., Cibin, G., Ramos, S., Smith, A.D., Scott, S.M., Varandas, L., Pearson, M.R., Krumpa, N.A., Jones, C.P. and Robbins, P.E. B18: A core XAS spectroscopy beamline for Diamond. In: *14th International Conference on X-Ray Absorption Fine Structure (XAFS14)*, *Jul 26-31*, *Camerino, ITALY.* BRISTOL: Iop Publishing Ltd, 2009.

115. Ulrich, J. and Frohberg, P. Problems, potentials and future of industrial crystallization. *Frontiers of Chemical Science and Engineering.* 2013, **7**(1), pp.1-8.

116. Workman, J., Lavine, B., Chrisman, R. and Koch, M. Process Analytical Chemistry. *Analytical Chemistry.* 2011, **83**(12), pp.4557-4578.

117. Chang, S.-Y., Kathyola, T.A., Willneff, E.A., Willis, C., Cibin, G., Wilson, P., Kroner, A., Shotton, E., Dowding, P.J. and Schroeder, S.L.M. Versatile liquid jet/sessile droplet system for *operando* studies of liquid phase reactions by x-ray absorption spectroscopy. *(submitted to Reaction Chemistry & Engineering).* 2018.

118. Shi, H., Lercher, J.A. and Yu, X.Y. Sailing into uncharted waters: recent advances in the in situ monitoring of catalytic processes in aqueous environments. *Catalysis Science & Technology.* 2015, **5**(6), pp.3035-3060.

119. Kaito, T., Mitsumoto, H., Sugawara, S., Shinohara, K., Uehara, H., Ariga, H., Takakusagi, S. and Asakura, K. A new spectroelectrochemical cell for in situ measurement of Pt and Au K-edge X-ray absorption fine structure. *Review of Scientific Instruments.* 2014, **85**(8), p.8.

120. Uehara, A., Chang, S.Y., Booth, S.G., Schroeder, S.L.M., Mosselmans, J.F.W. and Dryfe, R.A.W. Redox and ligand exchange during the reaction of tetrachloroaurate with hexacyanoferrate(ii) at a liquid-liquid interface: voltammetry and x-ray absorption fine-structure studies. *Electrochimica Acta.* 2016, **190**, pp.997-1006.

121. Booth, S.G., Uehara, A., Chang, S.Y., Mosselmans, J.F.W., Schroeder, S.L.M. and Dryfe, R.A.W. Gold deposition at a free-standing liquid/liquid interface: evidence for the formation of au(i) by microfocus X-ray spectroscopy (μXRF and μXAFS) and cyclic voltammetry. *Journal of Physical Chemistry C.* 2015, **119**(29), pp.16785-16792.

122. Chang, S.Y., Uehara, A., Booth, S.G., Ignatyev, K., Mosselmans, J.F.W., Dryfe, R.A.W. and Schroeder, S.L.M. Structure and bonding in Au(I) chloride species: a critical examination of X-ray absorption spectroscopy (XAS) data. *Rsc Advances.* 2015, **5**(9), pp.6912-6918.

123. Uehara, A., Booth, S.G., Chang, S.Y., Schroeder, S.L.M., Imai, T., Hashimoto, T., Mosselmans, J.F.W. and Dryfe, R.A.W. Electrochemical insight into the brust-schiffrin synthesis of Au nanoparticles. *Journal of the American Chemical Society.* 2015, **137**(48), pp.15135-15144.

124. Grunder, Y., Mosselmans, J.F.W., Schroeder, S.L.M. and Dryfe, R.A.W. In situ spectroelectrochemistry at free-standing liquid-liquid interfaces: UV-vis spectroscopy, microfocus X-ray absorption spectroscopy, and fluorescence imaging. *Journal of Physical Chemistry C.* 2013, **117**(11), pp.5765-5773.

125. Booth, S.G., Chang, S.Y., Uehara, A., La Fontaine, C., Cibin, G., Schroeder, S.L.M. and Dryfe, R.A.W. In situ XAFS study of palladium electrodeposition at the liquid/liquid interface. *Electrochimica Acta.* 2017, **235**, pp.251-261.

126. Nagasaka, M., Hatsui, T., Horigome, T., Hamamura, Y. and Kosugi, N. Development of a liquid flow cell to measure soft X-ray absorption in transmission mode: A test for liquid water. *Journal of Electron Spectroscopy and Related Phenomena.* 2010, **177**(2-3), pp.130-134.

127. Lange, K.M., Kothe, A. and Aziz, E.F. Chemistry in solution: recent techniques and applications using soft X-ray spectroscopy. *Physical Chemistry Chemical Physics.* 2012, **14**(16), pp.5331-5338.

128. Northrup, P., Leri, A. and Tappero, R. Applications of "tender" energy (1-5 kev) X-ray absorption spectroscopy in life sciences. *Protein and Peptide Letters.* 2016, **23**(3), pp.300-308.

129. Dey, A., de With, G. and Sommerdijk, N. In situ techniques in biomimetic mineralization studies of calcium carbonate. *Chemical Society Reviews.* 2010, **39**(2), pp.397-409.

130. Zhang, Q., Jiang, Y., Gou, B.D., Huang, J., Gao, Y.X., Zhao, J.T., Zheng, L., Zhao, Y.D., Zhang, T.L. and Wang, K. In situ detection of calcium phosphate clusters in solution and wet amorphous phase by synchrotron x-ray absorption near-edge spectroscopy at calcium k-edge. *Crystal Growth & Design.* 2015, **15**(5), pp.2204-2210.

131. Wolf, S.E., Leiterer, J., Kappl, M., Emmerling, F. and Tremel, W. Early homogenous amorphous precursor stages of calcium carbonate and subsequent crystal growth in levitated droplets. *Journal of the American Chemical Society.* 2008, **130**(37), pp.12342-12347.

132. Polte, J., Ahner, T.T., Delissen, F., Sokolov, S., Emmerling, F., Thunemann, A.F. and Kraehnert, R. Mechanism of gold nanoparticle formation in the classical citrate synthesis method derived from coupled in situ XANES and SAXS evaluation. *Journal of the American Chemical Society.* 2010, **132**(4), pp.1296-1301.

133. Polte, J., Erler, R., Thunemann, A.F., Emmerling, F. and Kraehnert, R. SAXS in combination with a free liquid jet for improved time-resolved in situ studies of the nucleation and growth of nanoparticles. *Chemical Communications.* 2010, **46**(48), pp.9209-9211.

134. Yao, T., Sun, Z.H., Li, Y.Y., Pan, Z.Y., Wei, H., Xie, Y., Nomura, M., Niwa, Y., Yan, W.S., Wu, Z.Y., Jiang, Y., Liu, Q.H. and Wei, S.Q. Insights into initial kinetic nucleation of gold nanocrystals. *Journal of the American Chemical Society.* 2010, **132**(22), pp.7696-7701.

135. Chao, Y.J., Horner, O., Vallee, P., Meneau, F., Alos-Ramos, O., Hui, F., Turmine, M., Perrot, H. and Ledion, J. In situ probing calcium carbonate formation by combining fast controlled precipitation method and small-angle x-ray scattering. *Langmuir.* 2014, **30**(12), pp.3303-3309.

136. Meldrum, F.C. and Colfen, H. Controlling mineral morphologies and structures in biological and synthetic systems. *Chemical Reviews.* 2008, **108**(11), pp.4332-4432.

137. Gryglewicz, S. Alkaline-earth metal compounds as alcoholysis catalysts for ester oils synthesis. *Applied Catalysis a-General.* 2000, **192**(1), pp.23-28.

138. Liu, X.J., Piao, X.L., Wang, Y.J., Zhu, S.L. and He, H.Y. Calcium methoxide as a solid base catalyst for the transesterification of soybean oil to biodiesel with methanol. *Fuel.* 2008, **87**(7), pp.1076-1082.

139. Teo, S.H., Taufiq-Yap, Y.H., Rashid, U. and Islam, A. Hydrothermal effect on synthesis, characterization and catalytic properties of calcium methoxide for biodiesel production from crude Jatropha curcas. *Rsc Advances.* 2015, **5**(6), pp.4266-4276.

140. Withum, J.A. and Yoon, H.Y. Treatment of hydrated lime with methanol for in-duct desulfurization sorbent improvement. *Environmental Science & Technology.* 1989, **23**(7), pp.821-827.

141. Parakhonskiy, B.V., Haase, A. and Antolini, R. Sub-micrometer vaterite containers: Synthesis, substance loading, and release. *Angewandte Chemie International Edition.* 2012, **51**(5), pp.1195-1197.

142. Trushina, D.B., Bukreeva, T.V., Kovalchuk, M.V. and Antipina, M.N. $CaCO_3$ vaterite microparticles for biomedical and personal care applications. *Materials Science and Engineering: C.* 2014, **45**, pp.644-658.

143. Dupont, L., Portemer, F. and Figlarz, M. Synthesis and study of a well crystallized $CaCO_3$ vaterite showing a new habitus. *Journal of Materials Chemistry.* 1997, **7**(5), pp.797-800.

144. Xu, A.W., Antonietti, M., Colfen, H. and Fang, Y.P. Uniform hexagonal plates of vaterite $CaCO_3$ mesocrystals formed by biomimetic mineralization. *Advanced Functional Materials.* 2006, **16**(7), pp.903-908.

145. Ryskin, Y.I. The Vibrations of protons in minerals: hydroxyl, water and ammonium. In: Farmer, V.C. ed. *The Infrared Spectra of Minerals.* Mineralogical Society of Great Britain and Ireland, 1974.

146. Grigorev, A.I. and Turova, N.Y. Infrared absorption spectra of alcoholates of beryllium magnesium and alkali earth metals. *Doklady Akademii Nauk Sssr.* 1965, **162**(1), pp.98-101.

147. Lutz, H.D. Zur kenntnis der erdalkalimethylate - ir-spektroskopische und rontgenographische untersuchungen an $Mg(OCH_3)_2$ $Ca(OCH_3)_2$ $Sr(OCH_3)_2$ und $Ba(OCH_3)_2$. *Zeitschrift Fur Anorganische Und Allgemeine Chemie.* 1967, **353**(3-4), pp.207-215.

148. Arai, Y., Yasue, T. and Wakui, Y. Methoxidation of calcium hydroxide and characteristics of its compound. *Nippon Kagaku Kaishi.* 1981, (9), pp.1402-1408.

149. Beaudoin, J.J. Validity of using methanol for studying the microstructure of cement paste. *Materials and Structures.* 1987, **20**(1), pp.27-31.

150. Roeges, N.P.G. Normal vibrations absorption regions of oxy compounds. In: *Guide to the complete interpretation of infrared spectra of organic structures.* - Lobachev, A. N. ed. Chichester, England: John Wiley & Sons Ltd., 1994, pp.263-269.

151. Adler, H.H. and Kerr, P.F. Infrared study of aragonite and calcite. *American Mineralogist.* 1962, **47**(5-6), pp.700-717.

152. Andersen, F.A. and Brecevic, L. Infrared-spectra of amorphous and crystalline calcium-carbonate. *Acta Chemica Scandinavica.* 1991, **45**(10), pp.1018-1024.

153. White, W.B. The carbonate minerals. In: Farmer, V.C. ed. *The infrared spectra of minerals.* Mineralogical Society of Great Britain and Ireland, 1974.

154. Sato, M. and Matsuda, S. Structure of vaterite and infrared spectra. *Zeitschrift Fur Kristallographie Kristallgeometrie Kristallphysik Kristallchemie.* 1969, **129**(5-6), pp.405-410.

155. Anderson, A. Group theoretical analysis of the $\nu_1(CO_3^{2-})$ vibration in crystalline calcium carbonate. *Spectroscopy Letters.* 1996, **29**(5), pp.819-825.

156. Gabrielli, C., Jaouhari, R., Joiret, S. and Maurin, G. In situ Raman spectroscopy applied to electrochemical scaling. Determination of the structure of vaterite. *Journal of Raman Spectroscopy.* 2000, **31**(6), pp.497-501.

157. Wehrmeister, U., Soldati, A.L., Jacob, D.E., Hager, T. and Hofmeister, W. Raman spectroscopy of synthetic, geological and biological vaterite: a Raman spectroscopic study. *Journal of Raman Spectroscopy.* 2010, **41**(2), pp.193-201.

158. Kamhi, S. On the structure of vaterite $CaCO_3$. *Acta Crystallographica.* 1963, **16**(8), pp.770-772.

159. Meyer, H.J. Structure and disorder in vaterite. *Zeitschrift Fur Kristallographie Kristallgeometrie Kristallphysik Kristallchemie.* 1969, **128**(3-6), pp.183-212.

160. McConnell, J.D.C. Vaterite from ballycraigy, larne, northern ireland. *Mineralogical Magazine and Journal of the Mineralogical Society.* 1960, **32**(250), pp.535-544.

161. Bradley, W.F., Graf, D.L. and Roth, R.S. The vaterite-type ABO_3 rare-earth borates. *Acta Crystallographica.* 1966, **20**(2), pp.283-287.

162. Tao, J. Chapter Twenty-Two - FTIR and Raman studies of structure and bonding in mineral and organic–mineral composites. In: De Yoreo, J.J. ed. *Methods in Enzymology*. Academic Press, 2013, pp.533-556.

163. Demichelis, R., Raiteri, P., Gale, J.D. and Dovesi, R. A new structural model for disorder in vaterite from first-principles calculations. *Crystengcomm.* 2012, **14**(1), pp.44-47.

164. Mugnaioli, E., Andrusenko, I., Schuler, T., Loges, N., Dinnebier, R.E., Panthofer, M., Tremel, W. and Kolb, U. Ab initio structure determination of vaterite by automated electron diffraction. *Angewandte Chemie-International Edition.* 2012, **51**(28), pp.7041-7045.

165. Christy, A.G. A review of the structures of vaterite: The impossible, the possible, and the likely. *Crystal Growth & Design.* 2017, **17**(6), pp.3567-3578.

166. Lekgoathi, M.D.S. and Kock, L.D. Effect of short and long range order on crystal structure interpretation: Raman and powder X-ray diffraction of LiPF6. *Spectrochimica Acta Part a-Molecular and Biomolecular Spectroscopy.* 2016, **153**, pp.651-654.

167. Ogino, T., Suzuki, T. and Sawada, K. The formation and transformation mechanism of calcium carbonate in water. *Geochimica et Cosmochimica Acta.* 1987, **51**(10), pp.2757-2767.

168. Calvin, S. *XAFS for everyone.* Taylor & Francis, 2013.

169. Sowrey, F.E., Skipper, L.J., Pickup, D.M., Drake, K.O., Lin, Z., Smith, M.E. and Newport, R.J. Systematic empirical analysis of calcium-oxygen coordination environment by calcium K-edge XANES. *Physical Chemistry Chemical Physics.* 2004, **6**(1), pp.188-192.

170. Fulton, J.L., Heald, S.M., Badyal, Y.S. and Simonson, J.M. Understanding the effects of concentration on the solvation structure of Ca^{2+} in aqueous solution. I: The perspective on local structure from EXAFS and XANES. *Journal of Physical Chemistry A.* 2003, **107**(23), pp.4688-4696.

171. Gomilsek, J.P., Kodre, A., Arcon, I. and Preseren, R. K-edge x-ray-absorption spectrum of potassium. *Physical Review A.* 2001, **64**(2), pp.art. no.-022508.

172. D'Angelo, P., Petit, P.E. and Pavel, N.V. Double-electron excitation channels at the Ca2+K-edge of hydrated calcium ion. *Journal of Physical Chemistry B.* 2004, **108**(31), pp.11857-11865.

173. Stöhr, J. Experimental and calculated K-shell spectra of simple free molecules. In: Stöhr, J. ed. *NEXAFS Spectroscopy.* Berlin, Heidelberg: Springer Berlin Heidelberg, 1992, pp.79-113.

174. Penner-Hahn, J.E. X-ray absorption spectroscopy. *eLS.* 2005.

175. Bodeur, S., Millie, P., Alugrin, E.L., Nenner, I., Filipponi, A., Boscherini, F. and Mobilio, S. Double-core-vacancy excited-states in the photoabsorption spectrum of SiH_4, $Si(CH_3)_4$, SiF_4, $SiCl_4$, $SiBr_4$ at the silicon 1s edge. *Physical Review A.* 1989, **39**(10), pp.5075-5081.

176. Cabaret, D., Emery, N., Bellin, C., Herold, C., Lagrange, P., Wilhelm, F., Rogalev, A. and Loupias, G. Nature of empty states in superconducting CaC6 and related Li-Ca ternary graphite intercalation compounds using polarized x-ray absorption near-edge structure at the Ca K edge. *Physical Review B.* 2013, **87**(7), p.9.

177. Henderson, G.S., de Groot, F.M.F. and Moulton, B.J.A. X-ray Absorption Near-Edge Structure (XANES) spectroscopy. In: Henderson, G.S. et al. eds. *Spectroscopic methods in mineralology and materials sciences.* Chantilly: Mineralogical Soc Amer, 2014, pp.75-+.

178. Wolf, S.E., Muller, L., Barrea, R., Kampf, C.J., Leiterer, J., Panne, U., Hoffmann, T., Emmerling, F. and Tremel, W. Carbonate-coordinated metal complexes precede the formation of liquid amorphous mineral emulsions of divalent metal carbonates. *Nanoscale.* 2011, **3**(3), pp.1158-1165.

179. Masadeh, A.S., Bozin, E.S., Farrow, C.L., Paglia, G., Juhas, P., Billinge, S.J.L., Karkamkar, A. and Kanatzidis, M.G. Quantitative size-dependent structure and strain determination of CdSe nanoparticles using atomic pair distribution function analysis. *Physical Review B.* 2007, **76**(11), p.11.

180. Dmitrienko, V.E., Ishida, K., Kirfel, A. and Ovchinnikova, E.N. Polarization anisotropy of X-ray atomic factors and 'forbidden' resonant reflections. *Acta Crystallographica a-Foundation and Advances.* 2005, **61**, pp.481-493.

181. Kokubun, J. and Dmitrienko, V.E. Anisotropic resonant X-ray scattering: Beauty of forbidden reflections. *European Physical Journal-Special Topics.* 2012, **208**(1), pp.39-52.

182. Bordet, P. Local structure studies using the pair distribution function. In: *Neutrons and Materials for Energy Conference (JDN)*, *Jun 21-25*, *Sete, FRANCE.* CEDEX A: E D P Sciences, 2013.

183. Taylor, M.G., Simkiss, K., Greaves, G.N., Okazaki, M. and Mann, S. An X-ray-absorption spectroscopy study of the structure and transformation of amorphous calcium-carbonate from plant cystoliths. *Proceedings of the Royal Society B-Biological Sciences.* 1993, **252**(1333), pp.75-80.

184. Kabalah-Amitai, L., Mayzel, B., Kauffmann, Y., Fitch, A.N., Bloch, L., Gilbert, P. and Pokroy, B. Vaterite crystals contain two interspersed crystal structures. *Science.* 2013, **340**(6131), pp.454-457.

185. Berner, E. The effect of earth alkaline oxide on alcohols. *Berichte Der Deutschen Chemischen Gesellschaft.* 1938, **71**, pp.2015-2021.

186. Kubo, T., Uchida, K., Tsubosaki, K. and Hashimi, F. Studies of reactions between metal hydroxides and alcohols .2. Reactions between CdI_2 structured metal(ii) hydroxides and CH_3OH. *Kog Kagaku Zasshi.* 1970, **73**(1), pp.75-+.

187. Day, R.L. Reactions between methanol and portland-cement paste. *Cement and Concrete Research.* 1981, **11**(3), pp.341-349.

188. Beaudoin, J.J., Gu, P., Marchand, J., Tamtsia, B., Myers, R.E. and Liu, Z. Solvent replacement studies of hydrated portland cement systems: The role of calcium hydroxide. *Advanced Cement Based Materials.* 1998, **8**(2), pp.56-65.

189. Rodriguez-Navarro, C., Suzuki, A. and Ruiz-Agudo, E. Alcohol dispersions of calcium hydroxide nanoparticles for stone conservation. *Langmuir.* 2013, **29**(36), pp.11457-11470.

190. Rodriguez-Navarro, C., Elert, K. and Sevcik, R. Amorphous and crystalline calcium carbonate phases during carbonation of nanolimes: implications in heritage conservation. *Crystengcomm.* 2016, **18**(35), pp.6594-6607.

191. Rodriguez-Navarro, C., Vettori, I. and Ruiz-Agudo, E. Kinetics and mechanism of calcium hydroxide conversion into calcium alkoxides: implications in heritage conservation using nanolimes. *Langmuir.* 2016, **32**(20), pp.5183-5194.

192. Turova, N.Y., Popovkin, B.A. and Novoselo.Av. X-ray study of alkali-earth metal methoxides. *Doklady Akademii Nauk Sssr.* 1966, **167**(3), pp.604-&.

193. Schlosberg, R.H. and Scouten, C.G. Organic chemistry of calcium: a new phenol separation/recovery approach. In: *ACS Fuels*, *Seattle, United States of America*. American Chemical Society, 1983, pp.180-187.

194. Schlosberg, R.H. and Scouten, C.G. Organic-chemistry of calcium - formation and pyrolysis of hydroxycalcium phenoxides. *Energy & Fuels.* 1988, **2**(4), pp.582-585.

195. Buzágh, A. Ueber kolloide Lösungen der Erdalkalikarbonate. *Kolloid-Zeitschrift.* 1926, **38**(3), pp.222-226.

196. Plank, J., Hoffmann, H., Schlkopf, J., Seidl, W., Zeitler, I. and Zhang, Z. Preparation and characterization of a calcium carbonate aerogel. *Research Letters in Materials Science.* 2009, **2009**.

197. Witkamp, G.J., Escobar, S.A.P. and Gaertner, R.S. *Method for producing calcium carbonate gel and product obtained thereby*. 2015.

198. Clifford, A.F. The electronegativity of groups. *Journal of Physical Chemistry.* 1959, **63**(8), pp.1227-1231.

199. Huheey, J.E. The electronegativity of groups. *The Journal of Physical Chemistry.* 1965, **69**(10), pp.3284-3291.

200. Gebauer, D., Gunawidjaja, P.N., Ko, J.Y.P., Bacsik, Z., Aziz, B., Liu, L.J., Hu, Y.F., Bergstrom, L., Tai, C.W., Sham, T.K., Eden, M. and Hedin, N. Proto-calcite and proto-vaterite in amorphous calcium carbonates. *Angewandte Chemie-International Edition.* 2010, **49**(47), pp.8889-8891.

201. Chen, S.F., Colfen, H., Antonietti, M. and Yu, S.H. Ethanol assisted synthesis of pure and stable amorphous calcium carbonate nanoparticles. *Chemical Communications.* 2013, **49**(83), pp.9564-9566.

202. Ito, K. and Bernstein, H.J. The vibrational spectra of the formate, acetate, and oxalate ions. *Canadian Journal of Chemistry-Revue Canadienne De Chimie.* 1956, **34**(2), pp.170-178.

203. Musumeci, A.W., Frost, R.L. and Waclawik, E.R. A spectroscopic study of the mineral paceite (calcium acetate). *Spectrochimica Acta Part a-Molecular and Biomolecular Spectroscopy.* 2007, **67**(3-4), pp.649-661.

204. Valor, A., Reguera, E. and Sanchez-Sinencio, F. Synthesis and X-ray diffraction study of calcium salts of some carboxylic acids. *Powder Diffraction.* 2002, **17**(1), pp.13-18.

205. Mattes, R. and Scholten, K. Vibrational-spectra and force constants in monoalkylcarbonates and monoalkylthiocarbonates. *Spectrochimica Acta Part a-Molecular and Biomolecular Spectroscopy.* 1975, **31**(9-10), pp.1307-1315.

206. Matsuta, S., Asada, T. and Kitaura, K. Vibrational assignments of lithium alkyl carbonate and lithium alkoxide in the infrared spectra - An ab initio MO study. *Journal of the Electrochemical Society.* 2000, **147**(5), pp.1695-1702.

207. Zhuang, G.V., Yang, H., Ross, P.N., Xu, K. and Jow, T.R. Lithium methyl carbonate as a reaction product of metallic lithium and dimethyl carbonate. *Electrochemical and Solid State Letters.* 2006, **9**(2), pp.A64-A68.

208. Katon, J.E. and Cohen, M.D. The vibrational spectra and structure of dimethyl carbonate and its conformational behavior. *Canadian Journal of Chemistry.* 1975, **53**(9), pp.1378-1386.

209. Lang, P.L. and Katon, J.E. The vibrational-spectra, structure, and conformational behavior of dimethyl dicarbonate. *Journal of Molecular Structure.* 1988, **172**, pp.113-128.

210. Bauer, J., Spanton, S., Henry, R., Quick, J., Dziki, W., Porter, W. and Morris, J. Ritonavir: An extraordinary example of conformational polymorphism. *Pharmaceutical Research.* 2001, **18**(6), pp.859-866.

211. Markovic, I., Ottewill, R.H., Cebula, D.J., Field, I. and Marsh, J.F. Small angle neutron scattering studies on nonaqueous dispersions of calcium carbonate. Part I. The Guinier approach. *Colloid and Polymer Science.* 1984, **262**(8), pp.648-656.

212. Radha, A.V., Forbes, T.Z., Killian, C.E., Gilbert, P. and Navrotsky, A. Transformation and crystallization energetics of synthetic and biogenic amorphous calcium carbonate. *Proceedings of the National Academy of Sciences of the United States of America.* 2010, **107**(38), pp.16438-16443.

213. Ma, Y.F. and Feng, Q.L. A crucial process: organic matrix and magnesium ion control of amorphous calcium carbonate crystallization on beta-chitin film. *Crystengcomm.* 2015, **17**(1), pp.32-39.

214. Ihli, J., Wong, W.C., Noel, E.H., Kim, Y.Y., Kulak, A.N., Christenson, H.K., Duer, M.J. and Meldrum, F.C. Dehydration and crystallization of amorphous calcium carbonate in solution and in air. *Nature Communications.* 2014, **5**, p.10.

215. Chen, S.F., Yu, S.H., Jiang, J., Li, F.Q. and Liu, Y.K. Polymorph discrimination of $CaCO_3$ mineral in an ethanol/water solution: Formation of complex vaterite superstructures and aragonite rods. *Chemistry of Materials.* 2006, **18**(1), pp.115-122.

216. Sand, K.K., Rodriguez-Blanco, J.D., Makovicky, E., Benning, L.G. and Stipp, S.L.S. Crystallization of $CaCO_3$ in water-alcohol mixtures: spherulitic growth, polymorph stabilization, and morphology change. *Crystal Growth & Design.* 2012, **12**(2), pp.842-853.

217. Seo, K.S., Han, C., Wee, J.H., Park, J.K. and Ahn, J.W. Synthesis of calcium carbonate in a pure ethanol and aqueous ethanol solution as the solvent. *Journal of Crystal Growth.* 2005, **276**(3-4), pp.680-687.

218. Yamashita, H., Nomura, M. and Tomita, A. local structures of metals dispersed on coal .4. Local-structure of calcium species on coal after heat-treatment and CO_2 gasification. *Energy & Fuels.* 1992, **6**(5), pp.656-661.

219. Guo, X.X., Wu, J., Yiu, Y.M., Hu, Y.F., Zhu, Y.J. and Sham, T.K. Drug-nanocarrier interaction-tracking the local structure of calcium silicate upon ibuprofen loading with X-ray absorption near edge structure (XANES). *Physical Chemistry Chemical Physics.* 2013, **15**(36), pp.15033-15040.

220. Odin, G.P., Vanmeert, F., Farges, F., Gand, G., Janssens, K., Romero-Sarmiento, M.F., Steyer, J.S., Vantelon, D. and Rouchon, V. Alteration of fossil-bearing shale (Autun, France; Permian), part II: Monitoring artificial and natural ageing by combined use of S and Ca K-edge XANES analysis, Rock-Eval pyrolysis and FTIR analysis. *Annales De Paleontologie.* 2015, **101**(3), pp.225-239.

221. Oaki, Y. and Imai, H. Experimental demonstration for the morphological evolution of crystals grown in gel media. *Crystal Growth & Design.* 2003, **3**(5), pp.711-716.

222. Green, D. and Perry, R. *Perry's Chemical Engineers' Handbook, Eighth Edition.* McGraw-Hill Education, 2007.

223. Danks, A.E., Hall, S.R. and Schnepp, Z. The evolution of 'sol-gel' chemistry as a technique for materials synthesis. *Materials Horizons.* 2016, **3**(2), pp.91-112.

224. Cushing, B.L., Kolesnichenko, V.L. and O'Connor, C.J. Recent advances in the liquid-phase syntheses of inorganic nanoparticles. *Chemical Reviews.* 2004, **104**(9), pp.3893-3946.

225. Hench, L.L. and West, J.K. THE SOL-GEL PROCESS. *Chemical Reviews.* 1990, **90**(1), pp.33-72.

226. Bots, P., Benning, L.G., Rodriguez-Blanco, J.D., Roncal-Herrero, T. and Shaw, S. Mechanistic insights into the crystallization of amorphous calcium carbonate (ACC). *Crystal Growth & Design.* 2012, **12**(7), pp.3806-3814.

227. Rodriguez-Blanco, J.D., Shaw, S. and Benning, L.G. The kinetics and mechanisms of amorphous calcium carbonate (ACC) crystallization to calcite, via vaterite. *Nanoscale.* 2011, **3**(1), pp.265-271.

228. Nielsen, M.H., Aloni, S. and De Yoreo, J.J. In situ TEM imaging of CaCO3 nucleation reveals coexistence of direct and indirect pathways. *Science.* 2014, **345**(6201), pp.1158-1162.

229. Yasue, T., Mamiya, A., Takahashi, Y., Tsukisaka, R. and Arai, Y. Synthesis and characteristics of amorphous calcium-carbonate. *Nippon Kagaku Kaishi.* 1984, (7), pp.1107-1113.

230. Yasue, T., Mamiya, A., Fukushima, T. and Arai, Y. Synthesis and characteristics of amorphous calcium carbonate in ethanol. *Gypsum & Lime.* 1985, **1985**(198), pp.245-252.

231. Ueda, Y., Komatu, K., Shimizu, S., Nishioka, H., Hanazaki, M. and Minayoshi, S. Formation and coagulation processes of vaterite in the reaction of the system $Ca(OH)_2$-CH_3OH-H_2O-CO_2. *Gypsum & Lime.* 1994, **1994**(249), pp.105-114.

232. Manoli, F. and Dalas, E. Spontaneous precipitation of calcium carbonate in the presence of ethanol, isopropanol and diethylene glycol. *Journal of Crystal Growth.* 2000, **218**(2-4), pp.359-364.

233. Dickinson, S.R. and McGrath, K.M. Switching between kinetic and thermodynamic control: calcium carbonate growth in the presence of a simple alcohol. *Journal of Materials Chemistry.* 2003, **13**(4), pp.928-933.

234. Park, J.-K., Ahn, J.-W., Park, Y.-S. and Han, C. Characteristic of crystal transition of amorphous calcium carbonate in H_2O, ethyl and propyl alcohol system. *Geosystem Engineering.* 2004, **7**(4), pp.89-94.

235. Lee, H.S., Ha, T.H. and Kim, K. Fabrication of unusually stable amorphous calcium carbonate in an ethanol medium. *Materials Chemistry and Physics.* 2005, **93**(2-3), pp.376-382.

236. Hu, Y.D., Zhou, Y.H., Xu, X.R. and Tang, R.K. Phase-controlled crystallization of amorphous calcium carbonate in ethanol-water binary solvents. *Crystal Research and Technology.* 2015, **50**(4), pp.312-318.

237. Magnabosco, G., Polishchuk, I., Pokroy, B., Rosenberg, R., Colfen, H. and Falini, G. Synthesis of calcium carbonate in trace water environments. *Chemical Communications.* 2017, **53**(35), pp.4811-4814.

238. Farhadi-Khouzani, M., Chevrier, D.M., Zhang, P., Hedin, N. and Gebauer, D. Water as the key to Proto-Aragonite amorphous $CaCO_3$. *Angewandte Chemie-International Edition.* 2016, **55**(28), pp.8117-8120.

239. Nakashima, Y., Takai, C., Razavi-Khosroshahi, H., Suthabanditpong, W. and Fuji, M. Synthesis of ultra-small hollow silica nanoparticles using the prepared amorphous calcium carbonate in one-pot process. *Advanced Powder Technology.* 2018, **29**(4), pp.904-908.

240. Pashalidis, I. and Theocharis, C.R. The effect of sorbed toluene on the surface properties of calcium hydroxide. *Journal of Chemical Technology and Biotechnology.* 1998, **71**(3), pp.223-226.

241. Kitano, Y., Hood, D.W. and Park, K. Pure aragonite synthesis. *Journal of Geophysical Research.* 1962, **67**(12), pp.4873-&.

242. Khopkar, A.R. and Ranade, V.V. Stirred vessels: Computational modeling of multiphase flows and mixing. In: *Chemical Engineering in the Pharmaceutical Industry.* John Wiley & Sons, Inc., 2010, pp.269-297.

243. Roeges, N.P.G. *Guide to the complete interpretation of infrared spectra of organic structures.* - Lobachev, A. N. ed. Chichester, England: John Wiley & Sons Ltd., 1994.

244. Sun, J.X., Hu, Z.S. and Hsu, S.M. The effect of concentration, solvent, and temperature on aggregation of a commercial calcium sulfonate additive as studied by FTIR and light scattering techniques. *Tribology Transactions.* 1997, **40**(4), pp.633-638.

245. Kotova, G.G. and Zimina, K.I. Composition of overbased sulfonates. *Chemistry and Technology of Fuels and Oils.* 1973, **9**(3), pp.204-206.

246. Stawski, T.M., Roncal-Herrero, T., Fernandez-Martinez, A., Matamoros-Veloza, A., Kroger, R. and Benning, L.G. "On demand" triggered crystallization of CaCO3 from solute precursor species stabilized by the water-in-oil microemulsion. *Physical Chemistry Chemical Physics.* 2018, **20**(20), pp.13825-13835.

247. Hayakawa, S., Hajima, Y., Qiao, S., Namatame, H. and Hirokawa, T. Characterization of calcium carbonate polymorphs with Ca K-edge X-ray absorption fine structure spectroscopy. *Analytical Sciences.* 2008, **24**(7), pp.835-837.

248. Medeiros, S.K., Albuquerque, E.L., Maia, F.F., Caetano, E.W.S. and Freire, V.N. First-principles calculations of structural, electronic, and optical absorption properties of CaCO3 Vaterite. *Chemical Physics Letters.* 2007, **435**(1-3), pp.59-64.